2015

Advanced microstructural characterisation of insulated rail joints

Chandrahas Ramappa Rathod
University of Wollongong

Advanced Microstructural Characterisation of Insulated Rail Joints

A thesis submitted in fulfilment of

the requirements for the award of the degree

Master of Philosophy

by

Chandrahas Ramappa Rathod, M.Eng

School of Mechanical, Materials and Mechatronics Engineering

Faculty of Engineering

University of Wollongong

2015

THESIS CERTIFICATION

I, Chandrahas R Rathod, declare that this thesis, submitted in fulfilment of the requirements for the award of Master of Philosophy, in the school of Mechanical, Material and Mechatronic Engineering, University of Wollongong, is wholly my own work and that, to the best of my knowledge and belief, it contains neither material previously published or written by another person nor material which has been accepted for the award of any other degree or diploma of a university or other institution, except where explicitly specified and referenced.

Chandrahas.R.Rathod, B.E, M.E

August 2015

ACKNOWLEDGEMENT OF COUNTRY

I would like to acknowledge the traditional custodians of the lands on which I am allowed to stay and complete this project. I would also like to pay my respects to their elders both past and present, and all aboriginal peoples within this land.

This dissertation is dedicated to the

Late Dr APJ Abdul Kalam

Thank you for giving us insight and vision.

Righteousness is the beginning

Where there is righteousness in the heart

There is beauty in the character.

When there is beauty in the character,

There is harmony in the home.

When there is harmony in the home.

There is an order in the nation.

When there is order in the nation,

There is peace in the world.

- DR. APJ Abdul Kalam

ACKNOWLEDGEMENTS

My Sincere thanks to the following people for their valuable assistance:

I would like to give my heartfelt thanks to my supervisors, Dr. David Wexler and Honorary Professor Tara Chandra, for their time, interest, expertise, kind guidance, encouragement and support during the whole course of this research study, without this project would not have been completed. It gives me a great comfortable and pleasure to interact with David, which most of the time turns out to be an interesting and engaging conversations for hours, in and outside of the project. Thanks for organising the trips to Rockhampton and Brisbane for conducting the experiments and to attend project related committee meetings. Sincere thanks to my Supervisor Dr. David Wexler for his abundance of patience, wise guidance and constant encouragement during the entire project.

I am grateful to Cooperative Research Centre CRC for Rail Innovation for providing the scholarship enabling me to undertake and finally complete this research work. I also would like to thank the research teams at Queensland University of Technology (QUT) and Centre of Queensland University (CQU) for their advice and insights during the course of project work. I thank Professor Manicka Dhanasekar (QUT), Paul Boyd (CQU) Ian Marks (QR) and Ph.D. students Nannan Zong (QUT), Thaminda BandulaHeva (QUT) and Hossein Askarinejad (CQU). We gratefully acknowledge the expertise and assistance of Dr. Paul Boyd in conducting the full-scale wheel-rail test rig.

Special thanks to Dr. Enda Crossin (QR) and Mr. Steve Selby (UOW) for carrying out initial welding trails.

In addition, A special thanks and gratitude to Dr. Vladimir Luzin (Australian Nuclear Science and Technology Organisation) who helped with Neutron diffraction experiments and invaluable guidance during entire course of my time at ANSTO the experimental period, and also like to thank ANSTO Bragg Office, for the in-kind grants for beam time proposals P-1972, P-2206, P-2258 and P-3526.

I also wish to take the opportunity to thank the staff the School of Materials, Mechanical and Mechatronics Engineering for all the assistance and help provided. In particular, big thanks to a very kind and humble person Mr. Greg Tillman for his great helping hand in assistance for metallographic preparation. I also wish to take this opportunity to thank Mr. Ron Marshall, Mr. Stuart Rodd, and Engineering workshop staff for their great help in numerous sample preparations and assisting in conducting welding experiment and BlueScope Steel Australia for carrying out Non-destructive testing for initial weld rail samples.

I acknowledge the University of Wollongong, Electron Microscopy centre for using FEG-SEM JSM 7001-F (LE00ss2813) funded by Australian research Council Grant(s) for SEM and JEOL JEM-2011 for TEM and also like to Thank Mr. Nick Mackie and Dr. Azdiar Gazder for SEM training.

I would like to thank Professor Druce Dunne for his expert guidance and suggestion on welding experiments and Dr. Huijun Li, Mr. Nathan Lan, Dr. Lenka Kuzmikova, and Dr. Zengxi Pan for their helpful and critical assistance in operating the welding experiments.

Thanks to Robert Taylor (ARTC) for arranging the rail-end samples. Thankful to ESAB, Australia for supplying welding feed wire. And also like to thank Dr.

Buyung Kosasih, Dr. Hongtao Zhu and their Ph.D. students for helping us to conduct the CETR ball-on-disk test.

I would like to thank Dr. Charlie Kong from the University of New South Wales, an expert on FIB-SEM and TEM, for his assistance in the preparation of TEM samples.

I will always be grateful to the University of Wollongong for providing IPTA scholarships and time extension to finish my Thesis, and also big thanks to UOW library for conducting and providing series of regular seminar and classes for HDR students, and, to Mrs .R. Cambareri and EIS for assistance with official matters.

Thanks also go to UOW colleagues; Dr. Lihong Su, Theo Sinkovits and Dr. Mansur Ahmed for encouragement and giving suggestions and help. Finally, friends who became part of my life by contributing their time and experiences to get me going and finish the thesis, Dr. Wenxu li, Shiran, Chao Wang and Niroshan. We shared our thoughts, feelings and support each other during the M.Phil process. I feel lucky and privileged to have such good friends.

Finally, I would like to express my appreciation to my encouraging family, my outrageously loving and supportive wife and my in-law family for their tremendous patience, support and encouragement.

ABSTRACT

Insulated Rail Joints (IRJs) experience a much shorter fatigue life than continuous rail sections, especially IRJs located in heavy haul rail corridors. IRJs are one of the most critical components of the rail system since their failure can lead to multiple catastrophic consequences, including; malfunctioning of the track signalling system due to metal contact across the insulating rail gap and, in cases where joints are damaged at the fishplate or rail bolt holes, derailment of railway vehicles.

A literature review on the topic revealed that these joints suffer from a wide range of damage, predominately resulting from either the gradual accumulation of metal under plastic flow across the railhead in the vicinity of the rail end post, or rail end spalling and/or rail end post insulation damage. Other failure modes relate to problems with fishplates/joint bar and rail bolt holes. These include: fishplate cracking, delamination of fishplates, bolt looseness and bolt hole cracking. Therefore, IRJs are regarded as high-risk component and are maintained via expensive maintenance programs requiring high standards. Every year rail operators around Australia and the world install tens of thousands of rail joints, due to their early failure, or the risk of failure of either the signalling system and/or the structural track integrity. For the Australian heavy haul rail industry, the economic costs of IRJ maintenance are very high.

In this study, approaches to both advanced characterisation of IRJ damage and to improving IRJs service lifetimes were investigated. Damage accumulation in the vicinity of the joint was characterised by advanced metallographic (optical microscopy, SEM and TEM) and neutron diffraction techniques. In the early stage of the project, surface hard facing was selected as a potential approach to improving IRJ

lifetimes, and surface clad rail samples were produced and studied via simulation testing and testing of ex-service rails.

The initial hard facing experiments involved comparison of the performance of ex-service laser clad IRJ samples (431 stainless steel cladding produced by Jarvie Engineering Private Limited) with that of uncoated IRJ samples manufactured from normal head hardened 60kg grade rail. The results indicated IRJ lifetimes can be improved by a hard facing of rail ends. Follow-up investigations were performed using both robots TIG MMAW hard facing deposition approach, and experimentation with a choice of cladding metal and geometry of the hard-face rail surface. Experimentation included advanced metallography and electron microscopy, and limited wear testing of cladding materials. Full-scale wheel on track rig testing was also performed on both coated and uncoated samples, which involves cyclic rolling contact loading on railhead surface was the main objective to investigate the railhead damage.

It was concluded that ferritic type commercial hard facing alloys, and maraging steels, appear good candidate materials for hard facing by weld deposition in the vicinity of IRJs. They also appear more suitable than the initial 431 stainless steel used in the laser cladding experiments as deleterious effects of thermal contraction during cooling are less in the ferritic alloys. It was also concluded and that geometry of the hard facing profile should include a steep angle of hard facing with the rail surface where it intersects the top surface of the rail head.

Neutron diffraction analysis of ex-service IRJs revealed significant stress evolution in the vicinity of the top surfaces of the rail ends abutting the insulating gap. This distribution is characterised by a compressive layer of approximately 5mm

deep and a counterbalanced tensile layer located 5-15mm at the sub-surface region. It exceeded the distribution along the continuous rail. Residual stresses analysis for the laboratory rig tested rail ends revealed similar characteristic to those found in ex-service rail ends. However, in contrast to the ex-service rail ends, the stress distributions in the test rig samples were slightly different and this difference was attributed to the localization of wheel load under the particular test conditions. A separate neutron diffraction examination of residual stresses near bolt-holes across ex-service IRJ fishplates revealed a stress evolution characterised by both compressive and tensile stresses, extended in a 90^0 and 45^0 angles to the longitudinal plane. The later results were consistent with a common observation of fishplate fracture originating at bolt holes at 45^0 to the running rail surface.

Keywords: *Insulated rail joint, full-scale wheel-railhead test rig, residual stresses, rail surface cladding.*

LIST OF PUBLICATIONS DURING M.PHIL COURSE

A. C Rathod, D Wexler, T Chandra, H Li. Microstructural characterisation of railhead damage in insulated rail joint. *Materials Science Forum* 2012 (706-709) pp. 2937-2942.

B. D Wexler, C Rathod, H Li, M Dhanasekar, V Luzin. An investigation of residual stresses in insulated rail joints. *Ansto Research Selections*, *Materials Engineering* 2012 pp. 86-89.

C. V Luzin, H J Prask, T Gnaupel-Herold, J Gordon, D Wexler, C Rathod, S Pal, W Daniel, AAtrens. Neutron residual stress measurements in rails. *Neutron News*, 2013 (24-3) pp. 9-13.

D. V Luzin, C Rathod, D Wexler, P Boyd, M Dhanasekar. Residual stresses in rail ends from the in-service insulated rail joints using neutron diffraction. *Materials Science forum* 2014 (768-769) pp. 741-746.

E. C Rathod, D Wexler, V Luzin, P Boyd, M Dhanasekar. A Neutron Diffraction investigation of residual stresses using neutron diffraction in rail ends after severe deformation of rail surfaces *Materials Science Forum*2014(768-769), pp.741-746.

My contribution to advanced characterisation of insulated rail joints has been incorporated into a Manual, which is a major outcome of this CRC project #R3.100 on longer life insulated rail joints: "*Manual for the Design, Installation and Maintenance of Insulated Rail Joints*".

TABLE OF CONTENTS

Thesis certification i

Acknowledgement of Country ii

Acknowledgements iv

Abstract vii

List of Publications during M.Phil course x

Table of Contents xi

List of Figures xvi

List of Tables xxiv

List of Abbreviations and Symbols xxvi

1 Introduction to CRC Project 1

1.1 Program of CRC Research and Investigation 1

1.2 Outcomes of a previous related CRC project on IRJs 2

1.3 Residual Stress Analysis in Collaboration with the ANSTO Bragg Institute 4

2 Introduction to Insulated Rail Joints and scope of investigations 5

2.1 Insulated rail joints 5

2.2 Scope of investigations and project overview 8

2.3 Outline of Thesis Structure 10

3 Literature review 12

3.1 Insulated Rail Joint Design 12

3.2 Rail head defect of IRJs 14

3.2.1 Variations in configuration and support structures 16

3.3 Common IRJ designs and failures: Local and Global perspectives 22

3.4 IRJ Failure Mechanisms 24
3.4.1 Overview of failure modes 27
3.5 Previous studies on IRJs 30
3.6 Major rail accidents due to failure of IRJs 33
3.6.1 Rail Head Cracks with Internal Origin 38
3.6.2 Rail Web Cracks 39
3.7 Stages of Rail Fatigue 42
3.8 Crack Initiation 46
3.9 Material response and shakedown maps: 48
3.10 Crack Propagation 50
3.11 IRJ Design and Failure SUMMARY 52
3.12 The origin of residual stresses 52
3.13 Residual Stress contributions to IRJ degradation 53
3.13.1 Residual stresses and degradation of rail surface and rail end 54
3.13.2 Degradation of the IRJ fishplate supports 54
3.14 Diffraction techniques for determination of stress field in IRJs 58
4 Experimental Methodology 60
4.1 Introduction 60
4.2 Welding Trails 62
4.2.1 Manual Metal Arc Welding (MMAW) welding trails 63
4.2.2 Gas Metal Arc Welding (GMAW) 64
4.3 Ball on disc wears test 69
4.4 Full-scale wheel-rail simulation rig test 71
4.5 Neutron Samples Preparation and Experimental 74
4.5.1 Rail ends obtained from the ex-serviced rails 75

4.5.2 Rail ends obtained from the laboratory serviced wheel-on-rail rig test 76
4.5.3 Samples from Fish-plates 78
5 Microstructural characterisation of railhead damage in insulated rail joints 80
5.1 A coated rail approach to improvement of IRJ 80
5.2 Uncoated Raul (Rail U) 81
5.3 Coated Rail (Rail C) 82
5.4 Hardness 84
5.5 Microhardness results 85
5.6 Summary and discussion 86
5.7 Grounds for Follow-up investigations 87
5.7.1 Morphology of worn surfaces 88
5.7.2 Wear response 89
5.8 Conclusions and discussion 92
5.8.1 Initial comparison of ex-service head hardened Rail and ex-service Laser clad IRJs 92
5.8.2 Improved hard-facing design approaches and new hard-facing trials 93
5.8.3 Conclusions of Improved hard-facing design approaches and new hard-facing trials 95
6 Residual stresses in rail-ends from the in-service insulated rail joints using neutron diffraction 96
6.1 Microstructures of damaged rail samples 96
6.2 Microstructure 97
6.3 Residual stress in longitudinal slice 98

6.3.1 Unused rail L-slice 99
6.3.2 Severely deformed rail L-slice 100
6.3.3 Partially deformed rail L-slice 102
Longitudinal component 102
Vertical component 103
6.3.4 Residual stresses for centre line 104
6.4 Residual stress in transverse slice 105
6.4.1 Unused rail T-Slice 107
6.4.2 Partially damaged rail T-Slice 108
6.4.3 Severely damaged rail T-Slice 109
6.5 A neutron diffraction investigation of rail ends deformed in full-scale wheel on track rig testing device 111
6.5.1 Tests of R1 & R2 for longitudinal component of accumulated residual stress 114
6.5.2 Test R1 & R2 for vertical component 115
6.5.3 Unused rail for longitudinal and vertical component 116
6.6 Residual stress summary 117
6.6.1 Residual stress for serviced rail 117
6.6.2 Deformation, Residual stresses and microstructural changes 118
6.7 Residual stress for wheel rail rig test rails 120
6.8 Residual stress mapping for bolt holes 121
6.8.1 Results - Rail web bolt holes 122
6.8.2 Rail web bolt holes 124
6.8.3 Fishplate bolt holes 125
6.9 Conclusion and discussions 127

6.9.1 Residual stress for bolt holes 127
6.9.2 Rail web bolt holes 127
6.9.3 Fishplate bolt hole nearest to IRJ endpost 128
7 Summary, Conclusions and Recommendations for future work 130
7.1 Scope and Limitations 133
7.2 Recommendations for Further Research Investigating on IRJs 135
8 References 138
9 Appendices 153
9.1 Paper A: Microstructural characterisation of railhead damage in insulated rail joints 153
9.2 Paper B: Residual stresses in rail ends from the in-service insulated rail joints using neutron diffraction 159
9.3 Paper C: A neutron diffraction investigation of residual stresses in rail ends after severe deformation of rail surfaces 167
9.4 Paper D: An investigation of residual stresses in insulated rail joints . 173
9.5 Paper E: Neutron residual stress measurements in rails 177
9.6 Non-destructive testing results from maraging cladded rail sample 183
9.7 Welding procedure specification 184

LIST OF FIGURES

Figure 2-1 A 6-bolt straight cut IRJ on a suspended sleeper support 5

Figure 2-2 Circuit diagram of insulated joints showing its role in traffic signalling system..... 6

Figure 2-3 (a) A straight cut IRJ displaying evidence of gap narrowing; (b, c & d) rail head squashing, air gap formation, and spalling for one side of a rail joint 7

Figure 2-4 Surface coated IRJ with martensitic stainless steel 9

Figure 3-1 Typical insulated joint assembly. (A) Cross section, (B) Exploded view of IRJ 13

Figure 3-2 An insulated rail joint with 6-bolt joint bars used in Australia 13

Figure 3-3 (a) Metal flow across the rail end post of IRJ (b) sketch of sectional view through line A-B at railhead end..... 15

Figure 3-4 Contact Pressure Singularity 16

Figure 3-5 Types of IRJ (a) supporting system: 6-bolt suspended IRJ (b) shape of fishplate: 12-bolt supported IRJ (c) insulation material: poly-insulated joint (d) Shape and cross section: mitre-cut/long-angle cut IRJ 17

Figure 3-6 (a) Inserted, straight cut 4-boltjoint (b) Glued joint 18

Figure 3-7 Discrete concrete sleeper supported 6-bolt IRJ..... 19

Figure 3-8 (a) Square cut IRJ (b) Inclined cut IRJ..... 20

Figure 3-9 (a) Inclined IRJ the endpost is positioned at 75^{O} to the longitudinal axis of the rail (b) sketch of Inclined IRJ -Top view..... 21

Figure 3-10 Conventional ballasted track employed in Australia..... 21

Figure 3-11 High modulus IRJs: 1.2m long joint bars on test with TTCI,(A) 275mm wide ties and insulated three-tie plate, (B) 1.2m long joint with centre liner 22

Figure 3-12 (A) Lap joint detail design components, (B) mitre-cut/long-angle cut insulated rail joint 23
Figure 3-13 “Hercules” series insulated rail joints from NorFast Inc 24
Figure 3-14 Ishikawa diagram (cause and effect diagram) for the factors influencing rail degradation 25
Figure 3-15 Different types of loading cycles related to fatigue: perfectly elastic (A), elastic shakedown (B), cyclic plasticity (plastic shakedown) (C) and incremental (ratcheting) (D) 26
Figure 3-16 Behaviour of suspended (top) and supported (bottom) IRJs in response to wheel loading 28
Figure 3-17 “Step” mechanism of wheel-rail impact 29
Figure 3-18 Brazing joint, cross-sectional SEM image of brazed PSZ/rail steel joint 31
Figure 3-19 Surface coated IRJs with high yield strength steel 31
Figure 3-20 Typical 3D view of the arc shaped railhead in the proximity of the gap 32
Figure 3-21 Von Mises stresses in the current and Non-ratcheting IRJs design 32
Figure 3-22 Railhead damaged at the vicinity of rail joint in Rockhampton, Queensland 33
Figure 3-23 (a) Hither Green rail crash 1967 (b &c) fatigue crack growth at first bolthole of IRJ and detached portion of railend broken out (d) underside of the rail foot 34
Figure 3-24 Frequency and severity graph of class I main-line freight train derailments 35
Figure 3-25 Flaw types in rail and in rail joint that can cause broken rails 36

Figure 3-26 (a) Transverse section of a rail head containing hydrogen shatter cracks (‘‘flakes”), (b) Kidney shaped or Tache Ovale crack in a rail head. 39
Figure 3-27 Longitudinal vertical web crack "piping, Horizontal web crack..... 40
Figure 3-28 Web cracks originating from a fishbolt hole..... 40
Figure 3-29 The most common failure modes of IRJs (a) Rail end battering (b) Rail end shelling (c) Rail end spalling (d) Rail end crushing and metal flow..... 41
Figure 3-30 Propagation stages of a squat-like fatigue crack 43
Figure 3-31 Effect of a liquid entrapped in a squat-like crack on the mode I and mode II stress intensity ranges DK 44
Figure 3-32 Formation and development of a surface crack from an internal horizontal defect (shelling) as a function of service time and passed tonnage at a Japanese Shinkansen rail..... 46
Figure 3-33 Principle of material response from repeated stress cycles having constant non-zero mean level..... 49
Figure 3-34 Shakedown map for general three-dimensional rolling-sliding contact. 50
Figure 3-35 Three phases of life of a (rolling contact) fatigue crack initiated at the surface of a rail..... 51
Figure 3-36 (a) Typical star crack and (b) horizontal crack for rail web bolt holes .. 56
Figure 3-37 (a) Schematic diagram of wheel-rail contact and (b) Rail end battering and metal flow over the gap..... 57
Figure 3-38 Classification of residual stress measurements techniques into destructive and non-destructive..... 58
Figure 4-1 Preliminary trail welding of Maraging steel on the rail head in the shape of bathtub dimension..... 64

Figure 4-2 (a) ABB ARB 4400-60-6 axis industrial robot carrying weld gun used for GMAW on high precision work table with set of clamps (b) wire feed source 65

Figure 4-3 Welding table with a set of clamps and accessories. Electric resistance heating blanket used to preheat the rail head 66

Figure 4-4 (a) Run-on plate (b) weld run (c & d) Completion of weld 68

Figure 4-5 (a) Hacksaw cut for extra weld run at the rail end (b, c &d) grinding and polishing the rail surface and rail end 68

Figure 4-6 (a) Uncoated rail end (b, c and d) rail surface coated after grinding and polishing..... 69

Figure 4-7 Ball on disc instrument setup. Ball-on-disc samples extracted from the rail head and schematic wear test configuration..... 70

Figure 4-8 Full-scale wheel-on-rail track rail rig set-up 72

Figure 4-9 Schematic of wheel-on-rail simulation rig, in top, side and front view ... 73

Figure 4-10 (a) front view of wheel-on-rail rig (b) schematic of wheel contact on rail surface (c) run-on wheel patch on rail surface (d) schematic of coating approach to the rail end surface 74

Figure 4-11 Schematics of sample section for neutron diffraction analysis longitudinal (L-Slice)..... 75

Figure 4-12 (a) Laboratory wheel-on-rail simulation rig (b) schematic diagram of wheel movement (c) In general, load-cycle plot for the rail sample carried out for both 600cycles and 1000 cycles using cyclic wheel-on-track simulation test rig (d) schematic of L-slice 77

Figure 4-13 Schematic of sample geometry and mesh, left hole corresponds to Hole #1 near to rail end and right hole to Hole#2..... 79

Figure 5-1 Martensitic stainless steel IRJ, (a) top view of ex-service IRJ fabricated with a 15-degree angle cut, (b) section showing bathtub shape of metal deposit. 81

Figure 5-2 Head hardened rail - Damaged rail end with both spalling and metal flow. (a) side view, (b) top view, (c) top view of squat before removal showing crack directions (d) same region as (c) after removal of surface squat and (e) high mag suspected region. 81

Figure 5-3 Laser surface coated rail – (a) rail end (b) top view, (c) SEM image of metal flow at rail end on wheel side of track (d) polished section 10 mm back from the rail end, (e) SEM image of void formation at interface between stainless and rail steel 83

Figure 5-4 Cracks formation around the edges of the weld interfaces. 84

Figure 5-5 Surface hardness profiles for coated and uncoated head hardened rail for the first 10mm below the top surfaces and around 10 mm back from the rail ends. 85

Figure 5-6 Micro hardness profiles as functions of depth below the surface near the rail end. 86

Figure 5-7 Different Weld profiles on the rail head surface; (a) profile for Martensitic stainless steel coating, (b) maraging steel weld deposit in a shallow groove, (c, d) redesigned bathtub groove on the rail head. 87

Figure 5-8 SEM micrographs of worn surface of (a) rail samples (b) martensitic stainless steel samples (c) maraging steel specimens undergone for two wear cycles 88

Figure 5-9 Coefficient of friction graph showing sliding friction coefficient vs sliding time for different cycle of wear test run (A, B, C) pearlitic rail steel (I, II, III) martensitic stainless steel (a,b,c) Maraging steel 90

Figure 5-10 Surface roughness on the worn tracks of (a) pearlitic rail steel (b) maraging steel (c) martensitic stainless steel 91

Figure 6-1 Optical images of (a) moderately deformed rail and (b) severely deformed rail ends 96

Figure 6-2 SEM images of rail end in longitudinal direction shows evolution of specifically deformed microstructures along the wheel rolling direction 97

Figure 6-3 Schematics of sample section for neutron diffraction analysis longitudinal (L-Slice). 98

Figure 6-4 2D stress and d0 maps for the L-slices. Compressive forces are blue, tensile forces are red. Square L-slice patch is 60mm in size 99

Figure 6-5 Residual stress variation for unused rail sample along the rail length of 60 mm. Measurements point from 2 mm from the rail surface to 20 mm in depth (a & b) – for Longitudinal (I & II) – for Vertical component 100

Figure 6-6 Rail #1, severely deformed used rail residual stress variation along the length of 60mm. Measurement points are from 2mm from the rail surface to 20mm in depth. (a& b) for the longitudinal component, (I & II) for the vertical component 101

Figure 6-7 Rail #2 partially deformed rail. Residual stress variation for used rail sample along the rail length of 60mm. Measurement points from 2mm from the rail surface to 20mm in depth. (c& d) for the longitudinal component, (III & IV) for the vertical component 103

Figure 6-8 Comparison of residual stresses measured at central line from the rail end along the rail depth for Rail #5 unused rail (a, I), Rail #1 severely deformed rail (b, II) and Rail #2 partly deformed rail (c, III)..... 105

Figure 6-9 2D stress and d_0 maps for the T-slices. Compressive forces are blue, tensile forces are red..... 106

Figure 6-10 Residual stress variations for unused rail sample across the rail head for a transverse slice. Measurements point from 2.5 mm from the rail surface to 29.5 mm in depth (a & b) – for Transverse (I & II) – for Vertical component 108

Figure 6-11 Residual stress variations for partially damaged rail sample across the rail head for a transverse slice. Measurements point from 2.5mm from the rail surface to 29.5mm in depth. (a & b) for the transverse component, (I & II) for the vertical component 109

Figure 6-12 Residual stress variations for severely damaged rail sample across the rail head for a transverse slice. Measurements point from 2.5mm from the rail surface to 29.5mm in depth. (C & d) for the transverse component, (III & IV) for the vertical component 110

Figure 6-13 Residual stress maps in the longitudinal slices from the rails contact loaded in the rig tester. Variation in d0 is also shown in the bottom..... 111

Figure 6-14 Longitudinal component for Rail #1 & Rail #2. Residual stress distributions on the rail head across the rail length to the depth of 20mm from the rail surface 114

Figure 6-15 Vertical component for Rail #1 & Rail #2. Residual stress distributions on the rail head across the rail length to the depth of 20mm from the rail surface 115

Figure 6-16 Residual stress variation for unused rail sample along the rail length of 60 mm. Measurements point from 2 mm from the rail surface to 20 mm in depth (a & b) – for Longitudinal (I & II) – for Vertical component..... 116
Figure 6-17 Schematic of sample geometry and mesh left hole corresponds to Hole #1 near to rail end and right hole to Hole#2..... 121
Figure 6-18 Residual stress maps from the rail web sections for rail #1 and rail #2. Compressive stress is blue, tensile stress is red. Map patch is 40mm in size .. 123
Figure 6-19 Radial and Hoop component stress map from the rail web sections for rail #1 and rail #2 124
Figure 6-21 Residual stress maps for fishplate section. Stress representation across the lines as shown in schematic diagram 126

LIST OF TABLES

Table 1-1 List of ANSTO proposal beam time for neutron strain investigations 4

Table 3-1 Description of the flaw types in rail joints and in general rails. 37

Table 4-1 Chemical composition of Pearlitic rail steel AS 1085.12. 61

Table 4-2 Mechanical properties of Pearlitic rail steel AS 1085.12. 61

Table 4-3 Chemical composition of UTP-702 63

Table 9-1 Gas metal Arc Welding procedure specification 184

LIST OF ABBREVIATIONS AND SYMBOLS

Abbreviation's

2D	Two-Dimensional
3D	Three-Dimensional
b.c.c	Body Centred Cubic
f.c.c	Face Centred Cubic
h.c.p	Hexagonal Close-Packed
ABB	ASEA Brown Boveri
AC	Alternating Current
ANSTO	Australian Nuclear Science and Technology organisation
ARTC	Australian Rail Track Corporation
AS	Australian Standard
BM	Base Metal
CE	Carbon Equivalent
COF	Coefficient of Friction
CRC	Cooperative research Centre
CQU	Central Queensland University
CRE	Centre for Railway Engineering
CWR	Continuously Welded Rail
EBSD	Electron Backscatter Diffraction
EDM	Electric Discharge Machine
EDS	Energy Dispersive X-Ray Spectroscopy
EIS	Engineering and Information Sciences

ESAB	Elektriska Svetsnings-Aktiebolaget (Electric Welding Limited Company)
FEG-SEM	Field Emission Gun Scanning Electron Microscope
FEM	Finite Element Method
FGM	Functionally Graded Materials
FIB-SEM	Focused Ion Beam- Scanning Electron Microscope
GMAW	Gas Metal Arc Welding
Gpa	Gigapascal
H	Hardness
HAZ	Heat Affected Zone
HCT	Hertz Contact Theory
HV	Vickers Hardness
IRB	Industrial Robots
IRJ	Insulated Rail Joint
k	Material Yield Stress
L	Longitudinal
MGT	Million Gross Tons
MMAW	Manual Metal Arc Welding
MPa	Megapascal
MSS	Martensitic Stainless steel
NDT	Non-Destructive Testing
NSW	New South Wales
OM	Optical Microscope
PIV	Particle Image Velocimetry
P0	Maximum Hertzian Pressure

PSZ	Partially Stabilized Zirconia
PWHT	Post-Weld Heat Treatment
QUT	Queensland University of Technology
Rail C	Rail Coated
Rail U	Rail Uncoated
RCF	Rolling Contact Fatigue
SEM	Scanning Electron Microscope
T	Transverse
TEM	Transmission Electron Microscope
TIG	Tungsten Inert Gas
TTCI	Transportation Technology Centre Inc
UMT	Universal Mechanical Tester
V	Vertical
Wt%	Weight Percent

1 INTRODUCTION TO CRC PROJECT

1.1 Program of CRC Research and Investigation

The Australian CRC for Rail Innovation (2007-2014) is a collaborative research venture between Australian Rail operators and Universities, which provides extensive assistance and advanced information to railway engineers and researchers via a range of dedicated research programs. The current M.Phil program on the advanced characterization of Insulated Rail Joints (IRJs) forms a component of a larger specific research project awarded by the Australian Cooperative Research Centre (CRC) for Rail Innovation, to meet the needs of the Australian heavy-haul track industry with a view to improving the service life's of current IRJs. The CRC project, entitled 'longer life insulated rail joints' (CRC Project R3.100) was awarded to a group of researchers from Queensland University of Technology, Central Queensland University, University of Wollongong as core participants, and Industrial partners Australian Rail and Track Cooperation, Rio Tinto (Pilbara Iron), Queensland Rail, and additional industrial support from Thermit Australia, Brisbane, & Jarvey Industries, Newcastle as manufacturer of Insulated Rail Joints with required design criteria as specified in AS 1085.12. This project is strategically divided among researchers which include aspects of structural design and material innovation, FEM models for IRJ designs were developed by researchers at QUT and CQU, microstructural characterisation of rail joints were carried out at UOW.

The original steering committee members included: the project was headed by Prof. Manicka Dhanasekar as Project leader, QUT, Robert Taylor (Chair) (ARTC), Enda Crossin (QR), David Wexler (UOW), Paul Boyd (CQU), Scott Simpson (CQU) and Wirtu Bayissa (QUT).

In addition to the advanced characterisation of IRJs performed at Wollongong University, Project R3.100 included advanced modelling, field testing, damage simulation testing, and alternative design approaches. One primary outcome of this project was a Best Practice Manual; CRC Rail project R3.100 had its foundations in a previous project over the period of 2001 to 2007. This project, Rail CRC Project #75, included design improvements, including a reduction of the gap size of the glued end-post. Additional experimentation involved the application of advanced materials processing methods, such as functionally graded materials (FGM) and advanced metal to ceramic brazing technology to totally eliminate the required soft polymer insulation at the rail ends. During the course of the earlier project, laser welded rail joints were developed by the Australian Rail and Track Corporation (ARTC) in Hunter Valley and by QR. To investigate the feasibility of increasing the rail end properties by means of mitigating problems in metal flow across the rail end. Initial trials of laser welded deposition of 431 martensitic stainless steel inserts of 8mm depth on standard Australian rail steel were manufactured. Characterisation of these laser clad joints formed a part of the current investigation.

1.2 Outcomes of a previous related CRC project on IRJs

The outcomes of a previous related Rail CRC project for the period of 2001 to 2007 (CRC Project #75) to address the problem of shorter life of Insulated Rail Joints are described below.

1: Rail CRC Project #75 developed a new generation IRJ design by reducing the gap size of the glued end-post.

The project also involved the application of advanced materials processing methods, including as the use of functionally graded materials (FGM), and advanced metal to ceramic brazing technology to totally eliminate the required polymer electrical insulation. The latter approach offered the opportunity to provide new, reliable and longer life insulated rail joints by increasing the hardness of the insulating layer while providing a continuous joint across the metal/ceramic/metal interface. However, there was still a challenge to meet the requirements for shear stress and fatigue resistance of the ceramic insulating material. The interface between the two dissimilar materials of the ceramic layer the rail metal leads to a crucial area of stress concentration near the interface resulting in failure of joints.

2: The functionally graded materials approach included the experimental development of a surfaced hard-faced IRJ, produced by Laser Weld Deposition. This was developed by ARTC and Jarvie Industries and tested in the Hunter Valley and by QR. The general approach involved increasing the rail end properties by means of mitigating against metal flow across the rail end. Initial trials of laser welded deposition of 431 martensitic stainless steel inserts of 8mm depth on standard Australian rail steel were manufactured. The applicability of inserting a surface layer through laser welding was believed to be an effective approach in rendering the rail joint problems with high properties of martensitic stainless steel in effectively delaying the failure mechanism of the railhead. During the current project, the approach of surface hard facing was further investigated in some detail, including evaluation of ex-service IRJ samples prepared by Jarvie Industries.

1.3 Residual Stress Analysis in Collaboration with the ANSTO Bragg Institute

During the course of this research work, a program of residual stress analysis of IRJ regions commenced. Significant in-kind support came from the Australian Nuclear Science and Technology Organisation Bragg Centre with 3 in-kind grants for beam time on the Kowari instrument for neutron strain investigations. List of proposal details here mentioned below and significant theoretical and invaluable practical support from Dr Vladimir Luzin:

Table 1-1 List of ANSTO proposal beam time for neutron strain investigations

Proposal ID	Proposal Title
P 1792	An investigation of residual stresses in insulated rail joints
P 2206	An investigation of residual stresses in rail ends after severe deformation of rail surfaces
P 2528	An investigation of residual stresses in fish-plate/joint bars from insulated rail joints
P 2822	An investigation of residual stresses in rail-web bolt holes of insulated rail joints
P 3526	Further investigation of residual stresses in rail-web bolt-holes of insulated rail joints

2 INTRODUCTION TO INSULATED RAIL JOINTS AND SCOPE OF INVESTIGATIONS

2.1 Insulated rail joints

Insulated Rail Joints (IRJs) play a key role in signalling systems in rail networks. End-to-end track sections are separated by a short insulating gap, often called an end post, while rigidity of IRJ components is obtained by bolted side joint bars, called fishplates, which are also electrically isolated from the track by a layer of composite material (Peltier et al., 2004, Huang et al., 2007) as shown in Figure 2-1.

Figure 2-1 A 6-bolt straight cut IRJ on a suspended sleeper support

IRJ assemblies enable electrical isolation of track sections by a small voltage difference between the rails; a travelling train conducts current between the two rails Figure 2-2, so that an electrical signal passing through a train's wheels can be used for a variety of functions including signalling the train's position to activate the initiation of events such as the closing of level crossing boom gates (Wu and Thompson, 2003). IRJs also play a secondary role as an aid to the detection of rail

fractures in track segments. However, as one of the weakest components of the rail track systems (Yasuhara, 1984), IRJ's pose a significant impact on maintenance costs due to their low and fluctuating service lives compared to continuously welded rail sections. The poor service reliability of IRJs is a particular problem in heavy haul rail corridors (Dhanasekar and Ding, 2013). Within Australia, 4-bolt and 6-bolt joint bars are the two most common IRJ assembly designs (Askarinjejad et al., 2010). The fishplate/bolt assemblies insulation is achieved by plastic liners for the fishplate, or by fully insulated fishplate encased by plastic liners/phenolic resins or/and by glued joints (Hojo et al., 1965).

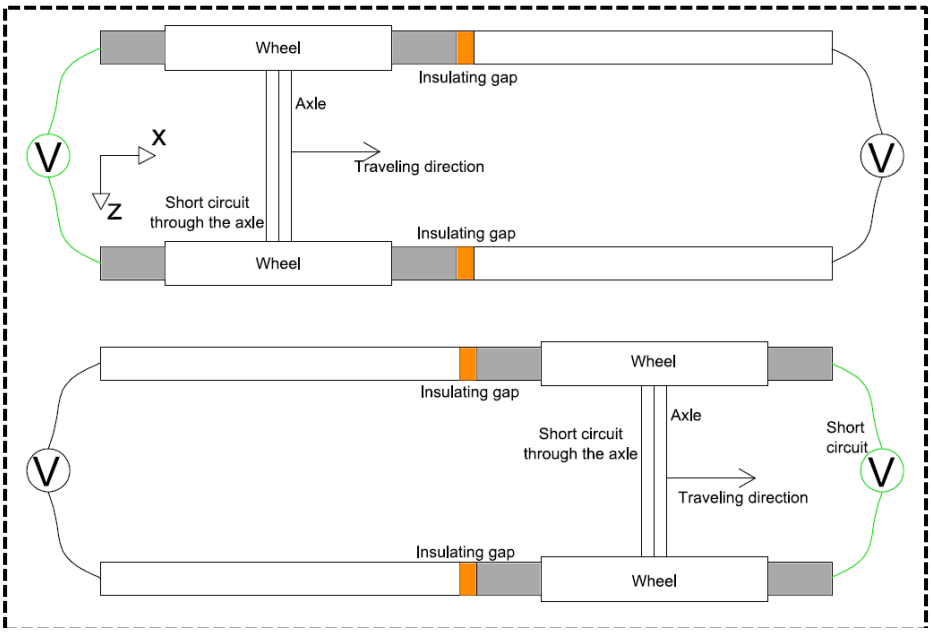

Figure 2-2 Circuit diagram of insulated joints showing its role in traffic signalling system

A majority of IRJ failures in Australian heavy haul rail corridors are caused by the flow of steel over the rail end-posts (Clinton, 2009) Figure 2-3(a). High impact forces cause rail damage such as spalling, and squashing Figure 2-3(b &d) and wear (Wen et al., 2005). Deterioration of the integrity of the bolt, fishplate, epoxy bonding and support configurations, which themselves experience combined lateral and

vertical bending stresses, leads to a vicious circle accelerating the failure at the joint (Barkan et al., 2009, Igwemezie and Nguyen, 2009b, Igwemezie and Nguyen, 2010). Failure itself is generally characterised by either an unsafe gap or other evidence of defects which might result in catastrophic failure (Cannon et al., 2003). Grinding out track surface can mitigate problems associated with the metal flow over the gap (Magel and Kalousek, 2002). However, eventually, the IRJ assembly must be replaced and this involves cutting out of a section of track, around 1.5-2.5 m in length, and re-welding a new length of the track containing the new IRJ (Igwemezie and Nguyen, 2010).

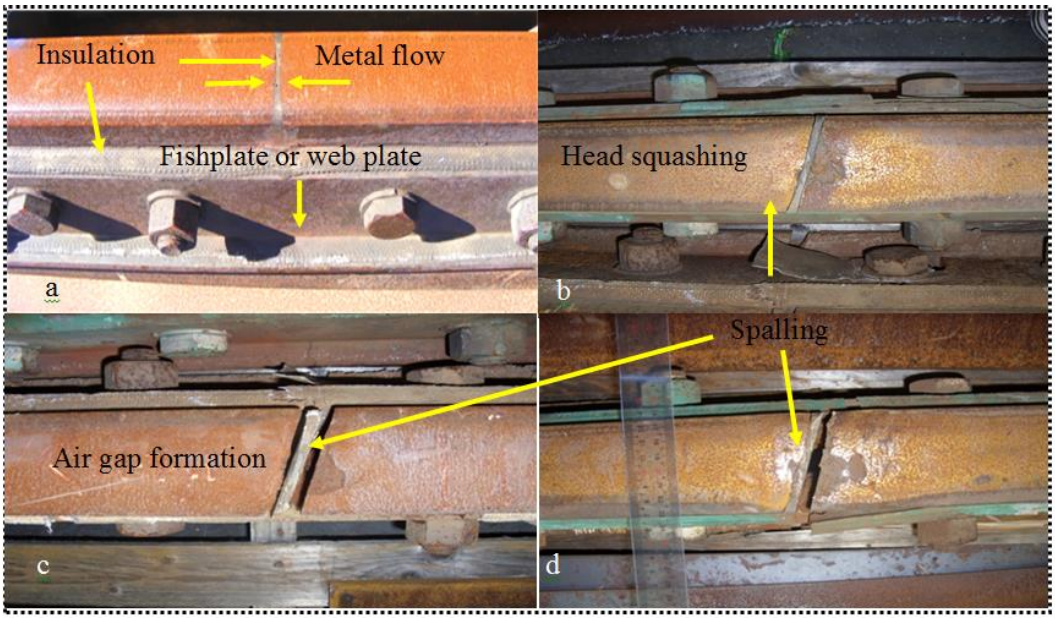

Figure 2-3 (a) A straight cut IRJ displaying evidence of gap narrowing; (b, c & d) rail head squashing, air gap formation, and spalling for one side of a rail joint

2.2 Scope of investigations and project overview

This current investigation falls into three areas; (i) advanced studies of microstructural changes during degradation of IRJs, (ii) investigations of the rail surface hard facing as an approach to mitigating IRJ degradation near rail ends and (iii) a detailed series of neutron diffraction investigations to determine residual stress development in both ex-service IRJs and IRJs subject to controlled rolling deformation in a dedicated full-scale wheel on track test rig.

(i) Studies of microstructural changes during degradation of IRJs As part of our initial efforts to increase understanding of relationships between IRJ design and lifetime employed advanced methods of metallography and electron microscopy were used to study degradation mechanisms in damaged IRJs.

(ii) Investigation of the rail surface hard facing as an approach to mitigating IRJ degradation near rail ends. Initial work included comparative studies of coated and uncoated IRJs, one made from head hardened rail and deemed to be a failed joint due to metal flow, and the second, an IRJ surface coated by laser deposition with martensitic stainless steel Figure 2-4. Both joints were removed from service after the same period of operation under heavy haul rail traffic. As the project progressed another surface hard facing metals, including maraging steels, were investigated, with the production of the hard facing surface via standard weld deposition methods, to enable the possibility of in-situ repair of damaged IRJs via weld deposition methods. Optimum design of the hard facing profile was one outcome.

Figure 2-4 Surface coated IRJ with martensitic stainless steel

(iii**) Neutron diffraction investigations of residual stress development.** The third component of the investigation involved residual stress analysis, in both regions of the track in the vicinity of IRJ rail ends, and in selected critical fishplate and associated fishplate boltholes components. These studies of residual stress evolution in IRJs were the first ever of this type and provide fundamental information about the degradation mechanism of IRJs. The neutron diffraction investigations were been supported by the Australian Nuclear Science and Technology Organisation (ANSTO) via a series of in-kind grants for beam time, and scientific and technical assistance from ANSTO beamline scientists. More details of these are found in the section 1.3 of Chapter 1.

2.3 Outline of Thesis Structure

This thesis is laid out in a progressive manner that further introduces the reader to the problem at hand, by addressing the objectives mentioned above. The results from the study are elucidated and followed by discussions and conclusions.

The contents of each Chapter are highlighted below:

Chapter 1: "Introduction to CRC project"

A brief introduction to the Australian CRC for Rail Innovation (2007-2014) project ventured between Australian Rail operators and Universities.

Chapter 2: "Introduction to Insulated Rail Joints and scope of investigations"

This Chapter outlines further general information about the research. Initially, research background and existing research gaps are discussed and presented. This is followed by the specific objectives of this research to minimize the identified gaps. In the following, the scope and the limitations of this research are pointed out. Finally, the thesis structure is presented by summarising all of the Chapters.

Chapter 3: "Literature review"

The literature review comprehensively presents the background for this research. The Chapter describes different types of rail joint designs and provides an overview of rail joint failure modes. The remaining parts of this Chapter provide the current strategies used for IRJ maintenance, replacement and repair technology.

Chapter 4: "Experimental methodology"

The Chapter presents details of the investigated materials, the history of the rail samples, specimen's fabrication and preparation with regard to hard facing by welding and procedures and for microstructural characterisation.

Chapter 5: "Microstructural characterisation of railhead damage in insulated rail joints"

The Chapter disseminates the initial results obtained from ex-service control samples of IRJs and clad IRJs using a type 431 martensitic stainless steel laser surface coating. The results are split into two sections followed by discussion or approaches to the improvement in the cladding profile design and improvements in the selection of candidate material for future cladding experiments.

Chapter 6: "Residual stresses in rail-ends from the in-service insulated rail joints using neutron diffraction

This Chapter describes a comprehensive series of neutron diffraction investigations of both ex-service and simulation tested rail ends and IRJs. From these investigations insights are obtained concerning a strain accumulation in the vicinity of IRJs resulting from both rail production and damage accumulation during service.

Chapter 7: "Summary, conclusions and recommendations for future work"

In this Chapter, the conclusions obtained from this thesis will be listed, as well as the recommendations to which the future work should be focused on.

3 LITERATURE REVIEW

3.1 Insulated Rail Joint Design

Insulated rail joints (IRJs) are used in the rail industry to serve the following two main functions:

1) To join two sections of rail end-to-end while providing adequate strengths and stiffness for supporting the moving traffic;

2) To prevent electrical current from flowing between the two rails section with a view to isolating sections of the track, this allows for identifying train locations and controlling signalling.

Electrical isolation of track sections enables electrical current to flow from trains into the track signalling system allowing the identification of train locations, the control of specific signalling operations and certain track fault finding operations to be performed, such as identification of fractured rail sections (Esveld, 2001). The conventional model of Insulated rail joints consists of bars to connect the two rails, one on each side of the rail. Coatings of fabric to insulate are placed under the bars; and screws that are secluded from the rails and bars by ferrules, which keeps the joint connected. A conventional joint assembly that is insulated is depicted in Figure 3-1, which was described in a previous report (Mandal and Peach, 2010).

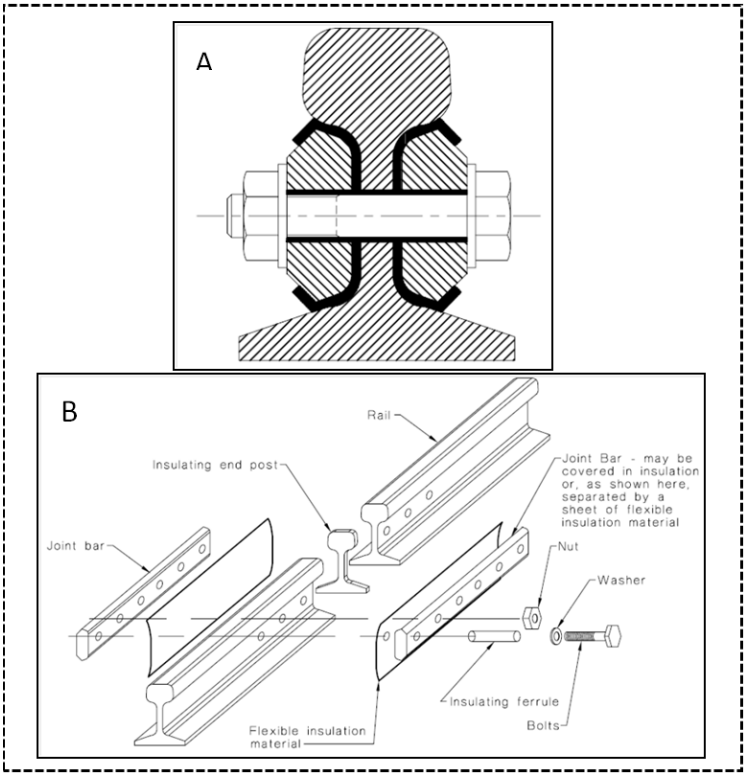

Figure 3-1 Typical insulated joint assembly. (A) Cross section, (B) Exploded view of IRJ

A part of the insulating fabric shaped identically to the rail is put under the ends of the rail. Typically, either 4-bolt or 6-bolt assemblies of bars to join are most frequently used in Australia; Figure 3-2 shows a common design of insulated rail joints with 6-nut assemblies of bars to join.

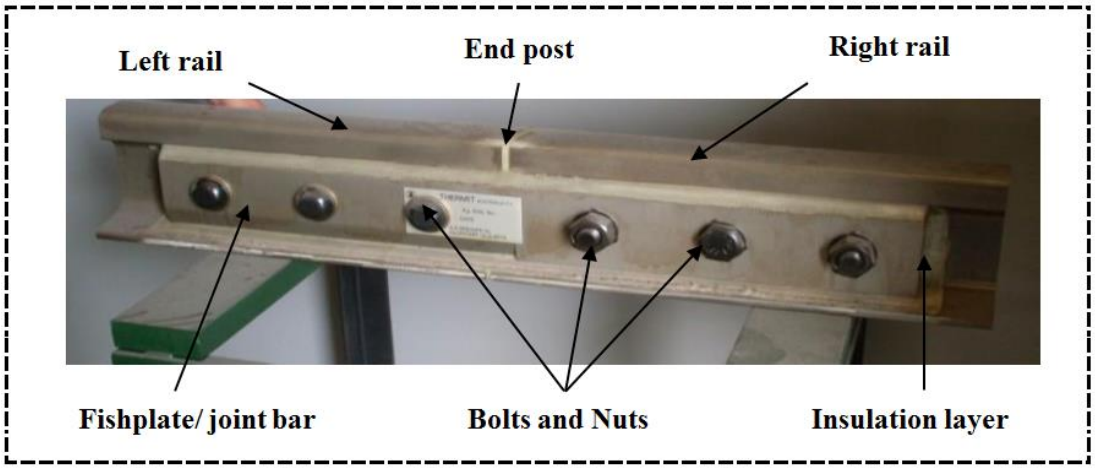

Figure 3-2 An insulated rail joint with 6-bolt joint bars used in Australia

The present model of insulated rail joints (IRJs) fulfils all the aforementioned factors. Although, there is still significant room available for improvement in the area of connectivity and support in the insulated rail joint (IRJ) assembly.

Following are the listed modes of malfunction in the insulated rail joint (IRJ) assemblies:

1) Fracture of fishplates/ joint bars;
2) Loosening of nuts;
3) Failure of the coating of material or metal on the railhead.
4) Railhead metal flows across the joint
5) Breakdown of insulating end post
6) Ballast settlement

3.2 Rail head defect of IRJs

The IRJs exhibit many failure modes. It Is believed that railhead metal flow is the most common mode of malfunction in the insulated rail joints (IRJs) in Australia as depicted in Figure 3-3 (Dhanasekar, 2009). Cumulative accumulation of metal flow under plastic flow of the railhead material in the vicinity of the gaps of the rail joint is a failure mode of significant concern to the heavy haul rail industry as it has the potential to short-circuit due to imminent metal contact culminating in signalling complications. The strong force of wheel/rail contact impact and the associated rate to the metal plasticity of the rail steel is the major reason for the initiation of this mode (Olofsson and Lewis, 2006). This metal flow on the railhead generally starts with a minor defect on the rail head; if not treated early, it can result in electrical

problems and other detrimental situations leading to errors on the subsurface failures of the rail head (Ekberg et al., 2002).

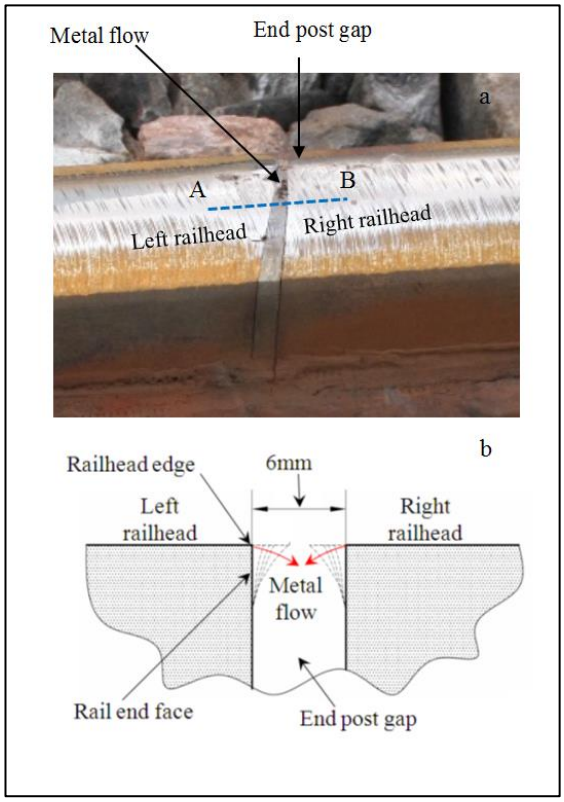

Figure 3-3 (a) Metal flow across the rail end post of IRJ (b) sketch of sectional view through line A-B at railhead end

Ratchetting is affected by the wheel-rail rolling contact pressure singularity (which is a theoretical 'infinite pressure peak' that can cause damage to any engineering material available in the industry) as shown in Figure 3-4. It can be seen that the wheel-rail contact away from the railhead edge produces pressure defined by the Hertzian theory (with no singularities); the same wheel when approaching the railhead edge unfortunately does not obey the theory and causes contact pressure singularity (Ringsberg and Lindbäck, 2003, Kabo, 2002). The pressure singularity leads to high levels of stress concentration at the corners defined by the rail end and railhead top (adjacent to the gap) as shown in Figure 3-4. It can also be seen from the

figure that away from the gap, the stress concentration exists below the railhead. Migration of stress concentration from below the railhead top to the top of the gap is the major reason for the onset of ratchetting in the current design of IRJs.

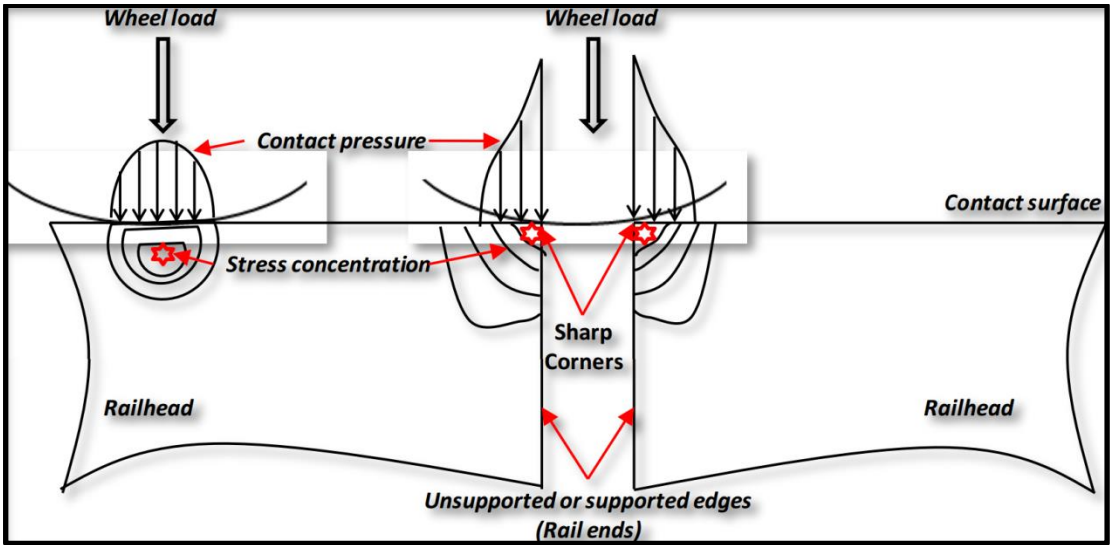

Figure 3-4 Contact Pressure Singularity

3.2.1 Variations in configuration and support structures

(Pang, 2007) presented several IRJ designs divided into categories of suspended or supported joints, and supported joints may be classified as either continuously or discretely supported. This classification is based on the position of the endpost of the IRJ in relation to the sleepers of the rail track.

Designs differ in different aspects which include, accompanying supporting system, the shape of fishplates, insulation material and shape of the cross section, as shown in Figure 3-5, respectively (Plaut et al., 2007b). Nowadays, the poly-insulated joint, the bonded insulated joint and fibreglass joints are used; formerly insulation consists of a coating of insulation material between the surface of metal joints and ends of rail (Wen et al., 2005). In both of these joints, the bars are held to the rail by bolts, similar to the ordinary rail joint. In bonded insulated joints, the steel joint-bars

are insulated by a thin layer of "fibreglass material and are attached to the rail ends by bolts and an epoxy adhesive.

Two steel bars, coated entirely by polyurethane that acts as an insulation material, are used in the poly-insulated joint. The fibreglass joint is extracted out of a fibreglass matter that is in the form of a complete solid bar/block. As in the common rail joint, both of these joints use bolts and nuts to keep the fishplate attached to the rails. The end-post is one of the major constituents of an insulated rail joint (IRJ) and it significantly affects the performance of IRJs. The way that end-posts fit between the rails also distinguishes different IRJs.

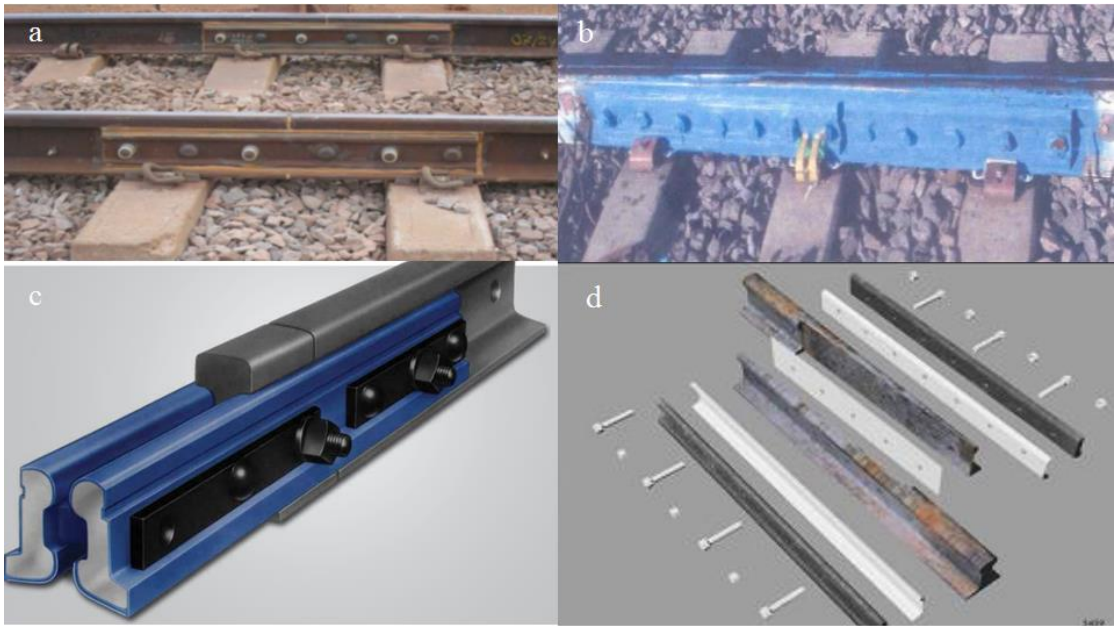

Figure 3-5 Types of IRJ (a) supporting system: 6-bolt suspended IRJ (b) shape of fishplate: 12-bolt supported IRJ (c) insulation material: poly-insulated joint (d) Shape and cross section: mitre-cut/long-angle cut IRJ

Two common types are the inserted IRJ (non-glued) and the glued IRJ end post, as shown in Figure 3-6(a) (Davis and Akhtar, 2005b). The width of end –post (size of opening) varies between 5mm and 20mm, which pose a major impact on IRJ models. The inserted IRJs (non-glued) uses the insertion of the insulated element into the end

post opening via heat technique without any adhesion material (Mandal and Dhanasekar, 2013). Adhesive material (epoxy) is used to strengthen the bond between the fishplates to join and the rail web whilst stay electrically insulated in the glued IRJs Figure 3-6(b) (Davis and Akhtar, 2005a).

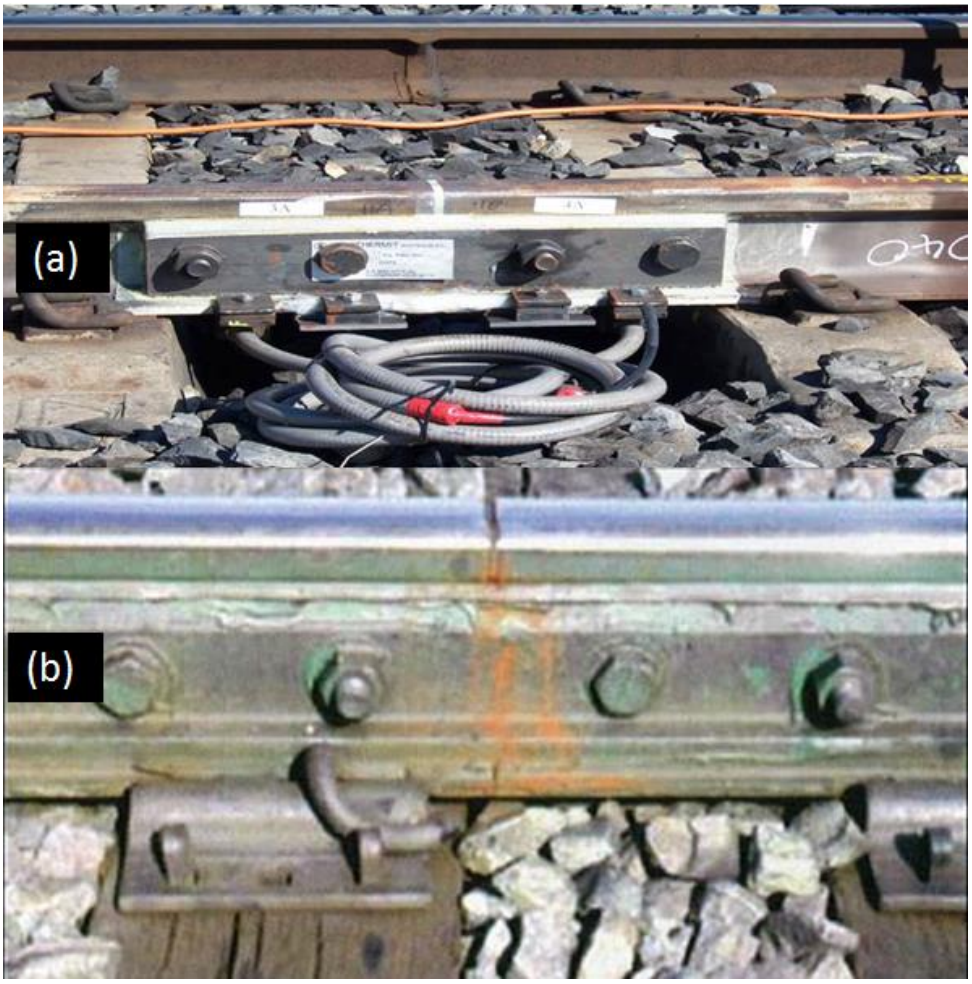

Figure 3-6 (a) Inserted, straight cut 4-boltjoint (b) Glued joint

The joint-bar designs are characterised by various cross-section designs and the length of joint bar, namely 4-bolt joint bar and 6-bolt joint bar. In practice, 4-bolt joint bars Figure 3-6(a) and 6-bolt joint bars Figure 3-7 are most popular. Because of the higher number of bolts, the latter joint bar is also longer. As per the Australian

Standard (AS 1085, 2002), lengths of 4-bolt joint bars and 6-bolt joint bars are 576 mm and 830 mm respectively.

Six-bolt bonded glued IRJ designs are the most recently used in the Australia heavy haul track system shown in Figure 3-7. These designs comprise bonded, double butt-strap joints containing two steel joint bars fixed to the rails and an epoxy adhesive, insulating endpost, high-tensile bolts, absorption materials (Australian Standard AS 1085.12–2002). The insulated joint assemblies can be supplied as square- and inclined-cut designs with field-assembled capability, as described by AS 1085.12 provisions.

Figure 3-7 Discrete concrete sleeper supported 6-bolt IRJ

Two common end-to-end rail configurations are employed in IRJ designs and this can be described accordingly as, square cut and inclined cut. Figure 3-8(a) shows a square cut joint, which is transverse or at right angles to the travel direction or long axis of the rail. The impact distance over this type of joint shorter compared to the inclined joint, shown in Figure 3-8(b). A benefit of the inclined joint is that the

impact tends to be less and spread over a larger distance. However, a problem with inclined cut joints is that the railhead in the vicinity of the IRJ suffers biaxial twists due to the odd nature of the load shift onto the railheads from the interaction area in angled-cut joints (Dhanasekar, 2009).

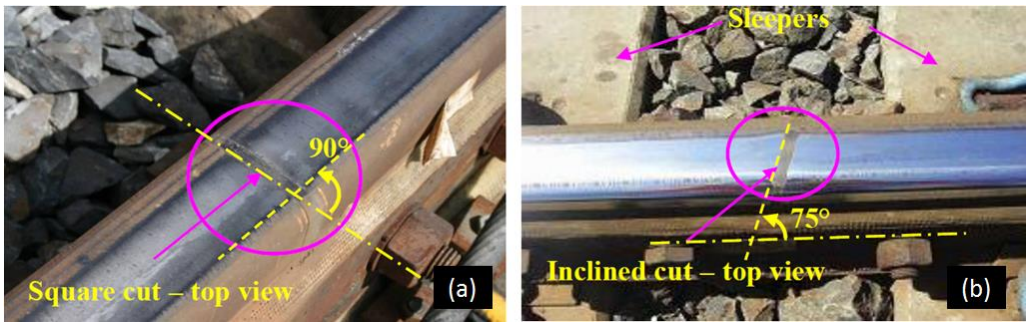

Figure 3-8 (a) Square cut IRJ (b) Inclined cut IRJ

Various approaches have been employed to increase the lifetimes of IRJs. These include; decreasing the gap size, from 7-8 mm to around 5-6 mm, which results in less impact on rail ends; experimentation with the suspension and support configuration to give high deflections and lower impact loads (Pang, 2007, Himebaugh et al., 2008); and altering the length of the joint bars according to whether they are 4-bolt or 6-bolt joints (Talamini et al., 2007). One to reducing the wheel-rail impact over joints has been to change from straight/conventional IRJs to 15 degrees inclined cut IRJs Figure 3-9. However, even after changing to tapered cut joint, metal flow at the surface is not completely eliminated (Plaut et al., 2007a).

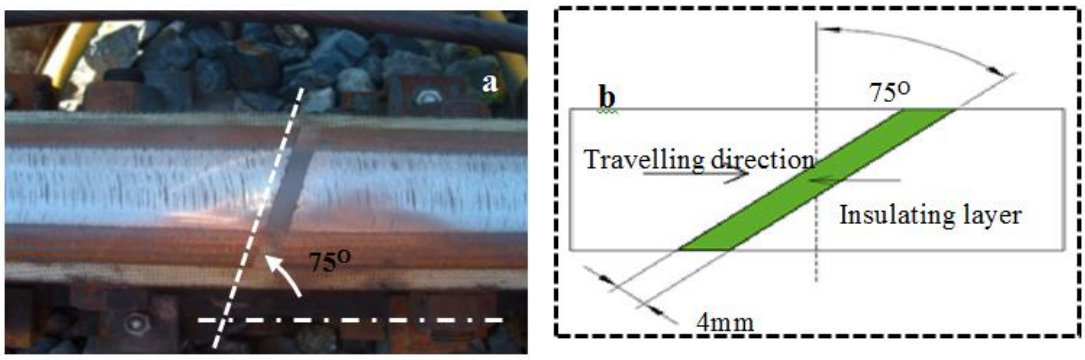

Figure 3-9 (a) Inclined IRJ the endpost is positioned at 75^{O} to the longitudinal axis of the rail (b) sketch of Inclined IRJ -Top view

Similar to all other railroad structures, the IRJs are supported on a bed which contains several flexible layers: sleepers, pads and ballasted structures. The ballast structure possesses three surfaces called ballast layer, sub-ballast layer and subgrade. This is the most conventional track structure employed in Australia. The IRJ is placed onto the top of the structure fastened onto the sleepers. Figure 3-10 depicts the traditional type of track employed in Australia (Pang, 2007). The performance and behaviour of IRJs depend not only on the IRJ but also on the stiffness and damping of the rail support structures.

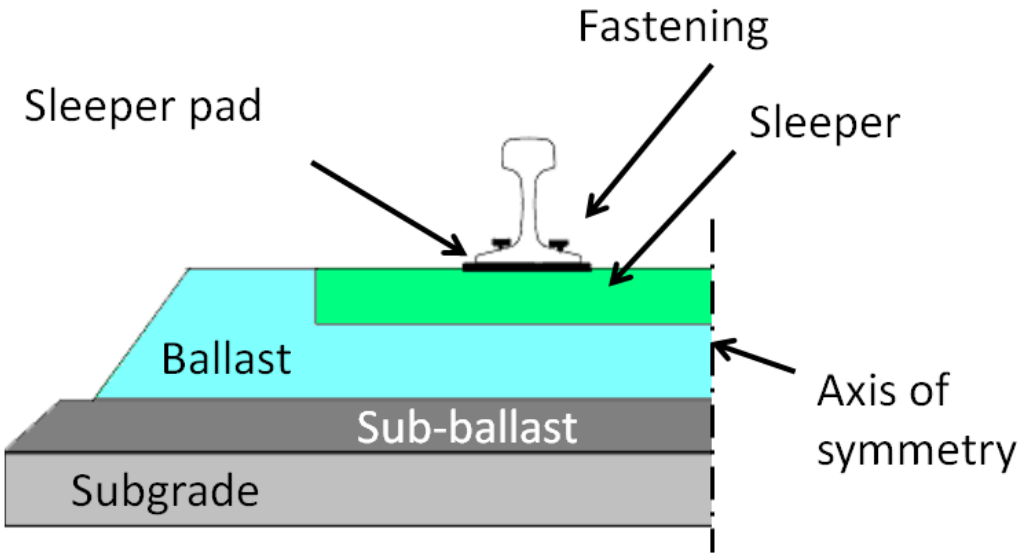

Figure 3-10 Conventional ballasted track employed in Australia

3.3 Common IRJ designs and failures: Local and Global perspectives

New designs for IRJs have become an emerging topic for many projects in the USA. Original IRJ prototypes, which exhibit adhesive debonding and joint bar cracking failures, have been recently modified for stiffness and strength against heavy axle loads by using special stiffening materials for centre liner insulators (Davis et al., 2005). New designs of IRJs also focus on extending service life by enhancing the length and cross-sectional dimensions of joint bars, increasing the width of sleepers, applying stronger and tougher insulating materials as well as various supports underneath the IRJs (Steenbergen, 2008). Two most noticeable designs of IRJs are shown in Figure 3-11 (Akhtar et al., 2008).

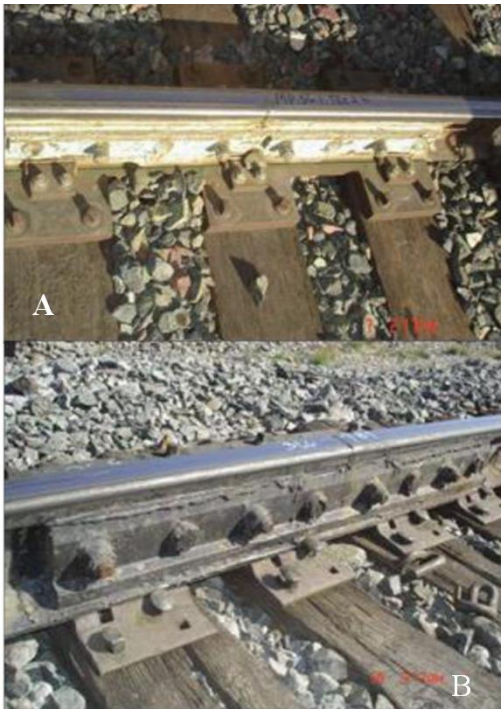

Figure 3-11 High modulus IRJs: 1.2m long joint bars on test with TTCI,(A) 275mm wide ties and insulated three-tie plate, (B) 1.2m long joint with centre liner

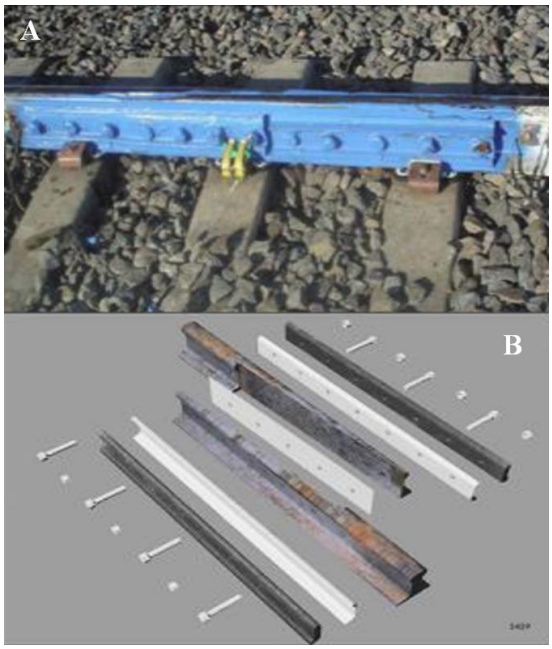

Figure 3-12 (A) Lap joint detail design components, (B) mitre-cut/long-angle cut insulated rail joint

A newly introduced advanced design of IRJs, known as the Mitre Cut Insulated Joint Figure 3-12 is a long-angle cut/lap joint. This joint performed poorly during field testing on the mainline track, mainly as a result of railhead material failure (Akhtar and Davis, 2008, Akhtar et al., 2008).

A new IRJ type described as the “Hercules”, has been recently introduced in Canada by NorFast. It has been demonstrated to have heavy-haul railway applications due to the longer service life of this type of joint. Also, of benefit is the high-speed installation, high signal reliability, and improved economics of field installation (Australian Rail Track Corporation, 2010). Compared with TTCI designs, the “Hercules” IRJs is claimed to cope with higher wheel loads without the requirement of glued bonds, and can be field-assembled without field welding. In addition, it is claimed that the field assembly process can be performed with straightforward and versatile properties on either tangent track or at turnouts/corners, Figure 3-13 (Australian Rail Track Corporation, 2010).

Figure 3-13 “Hercules” series insulated rail joints from NorFast Inc

3.4 IRJ Failure Mechanisms

It is well known that wear and fatigue are considerable problems for the rail industry. Rail deterioration is related to operational conditions including; train speed, axle load, rail-wheel material type, size and profile, track construction, wagon, Million Gross Tonnes (MGT), curvature, traffic type, and the environment. Wear and fatigue significantly impact on rail quality (Kumar, 2006). Although rails are designed to fit the shape of the wheels and, therefore, limit contact stresses, longitudinal compressive and tensile stresses, as well as shear forces, are inevitable in the rails (Kalousek and Bethune, 1978). While the former mainly occurs at the head and foot of the rail, the latter induces shear stresses in the rail web. It is important that the rail has a sufficient mechanical property to resist the bending moment at the head and foot of the rail (Cope, 1993).While wheel-on-track wear results in significant damage to the rail head, abrasive contact with the base plate or sleeper also cause rail deterioration (Sheng et al., 2006).

In addition, loss of rail section is caused by corrosion, and the fatigue resistance of the rail is suppressed by the occurrence of surface cracks. Increasing problems of modern rail system include rail wear, rolling contact fatigue and plastic flow.

Surface-initiated cracks are also the result of increased speed, higher axle loads, heavy traffic and freight (Reddy, 2004). The Ishikawa diagrams in Figure 3-14 general factors responsible for rail degradation are; design, manufacturing, operation and maintenance.

In the first stage, rail/wheel material type, rail size and rail profile are selected based on operating conditions such as axle load, traffic type and density. (Kumar et al., 2008). Track geometry (elevation and curvature) decides the selection of track construction model whose design should have less degradation and longer rail life. Figure 3-14 show that manufacturing process may potentially generate rail defects. Moreover, it demonstrates that different factors from manufacturing process as well as operational and maintenance elements can induce rail degradation.

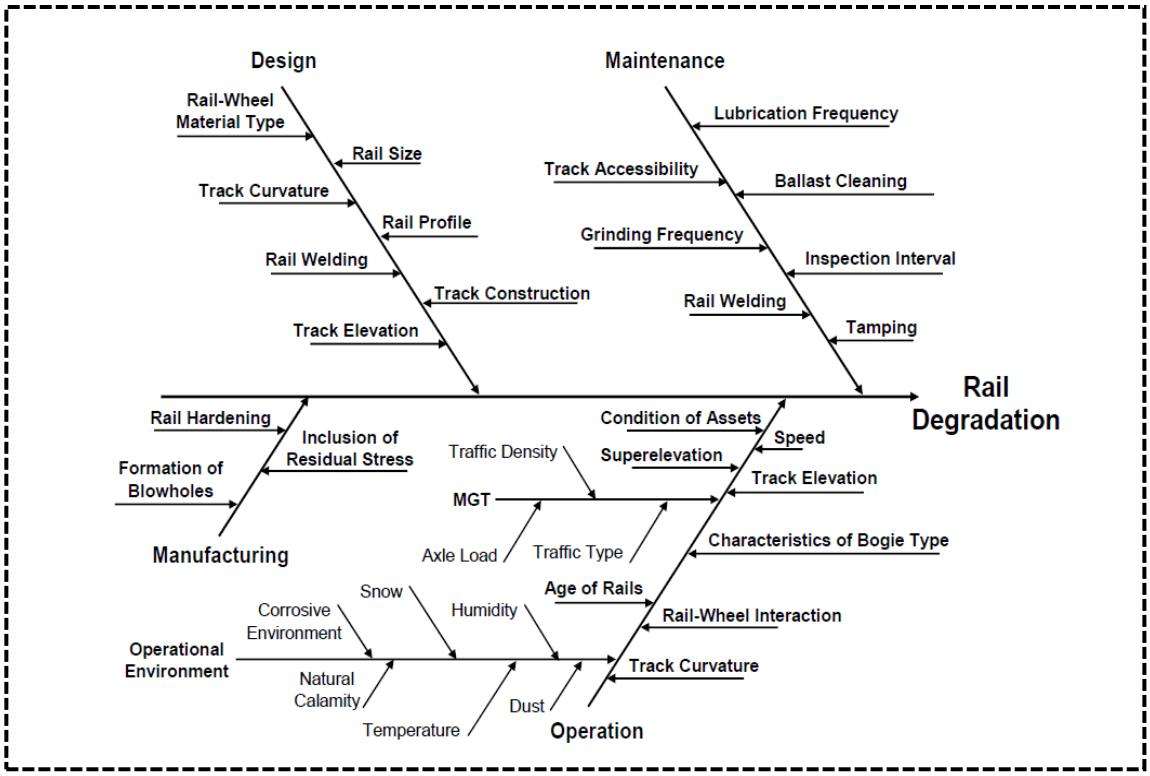

Figure 3-14 Ishikawa diagram (cause and effect diagram) for the factors influencing rail degradation

Four different responses of a structure or element to cyclic loading on a macro-scale have been identified regarding stress level (Jiang and Sehitoglu, 1996, McDowell, 1995). Details about that respondent behaviour are described from a previous study (Bower and Johnson, 1989), Figure 3-15. Firstly, there is completely elastic and reversible response when the load is sufficiently low. Secondly, plastic deformation is induced by the excessive yield stress in the first loading cycles, followed by strain hardening, geometry change and residual stress and elastic shakedown. Thirdly, plastic shakedown is performed associated with closed-cycle plastic deformation occurring in every loading cycle. Lastly, ratcheting response is created when there are repeated increments of unidirectional plastic deformation (Bower and Johnson, 1991).

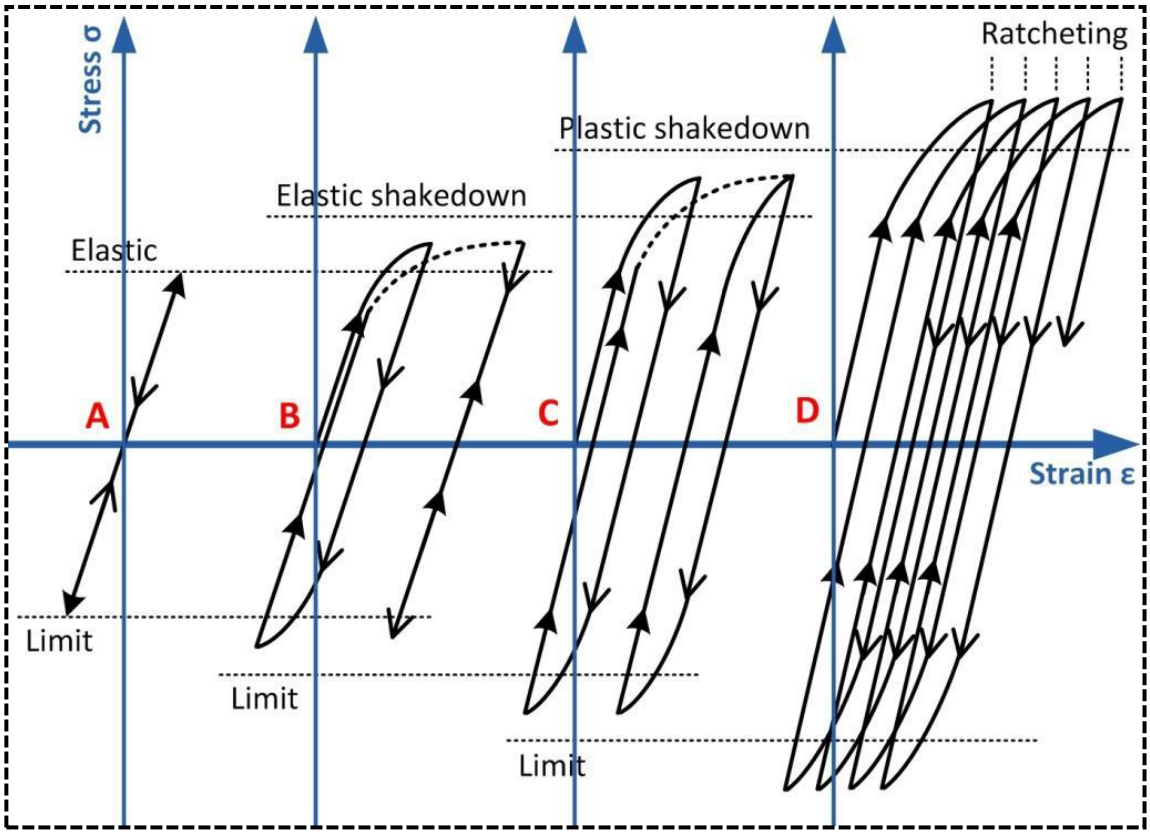

Figure 3-15 Different types of loading cycles related to fatigue: perfectly elastic (A), elastic shakedown (B), cyclic plasticity (plastic shakedown) (C) and incremental (ratcheting) (D)

3.4.1 Overview of failure modes

For the Australian IRJs, two key factors lead to the failure of IRJs.

1) Wheel/rail contact impact force;
2) Material ratcheting.

The wheel/rail impact force is excited by the IRJ structural/geometry discontinuity. Under severe wheel/rail loading, the material ratcheting/fatigue is initiated and causes metal flow on the railhead. The initiation and progression of the failure are considered concentrated on the railhead in the vicinity of end post. It is worth noting that, although the wheel/rail interaction force has components in both the vertical and the horizontal planes, the vertical contact-impact force is believed to play the major role. This failure mechanism of IRJs has been widely acknowledged by Australian practicians. As part of a project for a longer life of IRJs, this thesis tries to conduct the design optimization of IRJs from not only the angle of its contact forces and different responses but also the issue of material fatigue.

Rolling contact fatigue of rails is a severe and increasing problem for many railways all over the world (Cannon and Pradier, 1996). The annual cost for rail re-profiling and repairing is very high. Two types of surface initiated cracks that appear on the rail due to rolling contact fatigue are commonly described as head checks and squats (Li et al., 2008). This type of damage does not result from metallurgical defects, but seems to be the result of an increasing traffic density and increased axle loads on the railway lines. Wheel/rail contact may also lead to the initiation of subsurface fatigue cracks which are closely associated with metallurgical faults, for example, gauge corner shelling and the detailed fracture (Zerbst et al., 2009). Modelling the initiation and growth of these types of cracks, which are expected to

decrease in number owing to improved rail making and maintenance technologies, is not the main objective of this work. Rolling contact fatigue has been extensively studied in the literature (Johnson and Johnson, 1987) and is overviewed in the textbook, (Suresh, 1998).

At any given instance, only one wheel can be located within the span of a sleeper, as the sleeper spacing is kept smaller than the wheelset spacing in the wagon structure. Therefore, an examination of the behaviour of IRJs (either suspended between sleepers or supported on a sleeper) is essential to an understanding of their performance. Figure 3-16 illustrates the deformation of a suspended and a supported IRJ when subjected to wheel loading. It is clear that the edge of a rail end (point of stress concentration zones/ singularities) on a supported joint is more vulnerable to direct impact from the running wheels. Limited finite element (FE) from a previous study (Pang and Dhanasekar, 2006) has confirmed that supported joints exhibit higher impact than their suspended counterparts.

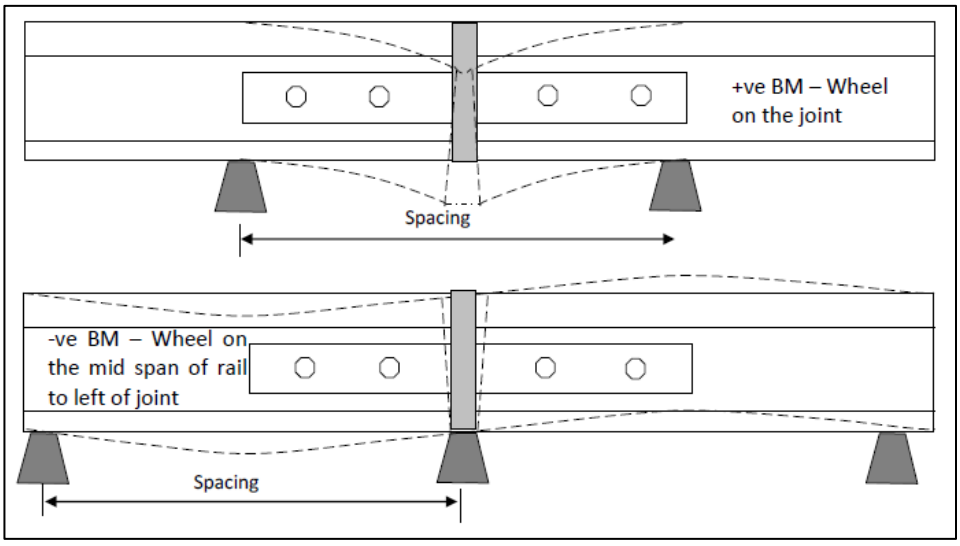

Figure 3-16 Behaviour of suspended (top) and supported (bottom) IRJs in response to wheel loading

At the foot and at the web, low energy cracks in rails can be initiated at the head of the rail. Their enlargement can originate spalling of material wreckage which will influence the travelling ease, sound and, in addition, the vibrant weight exaggeration for the track as well as rolling stock (Koh et al., 1993). In case, if the fatigue cracks are not detected in due time, they can result in fracturing the rail or can cause derailment (Zerbst et al., 2005). So, for evaluation of tolerating damage, enlargement of possible fatigue cracks and nucleation are likely the failure scenarios.

Globally, due to the low bending stiffness of the joint-bars at the gap during the wheel passage, the rail ends in the IRJs are subjected to wheel impact due to 'step' mechanism (Wen et al., 2005) illustrated schematically in Figure 3-17. With the uneven vertical deformation of the top rail surface at either side of the rail gap shown as dotted profile, the wheel momentarily experience double point contact whilst crossing the rail gap from Rail 1. Subsequently it would hit the "rise" of Rail-2 resulting in an impact load. The 'step' forms due to the difference in the elastic behaviour (predicted by Young's Modulus) of the railhead steel and the endpost material (generally nylon), and the type of contact between the two materials. To minimise the 'step', one should ideally use a material that is as stiff as that of steel.

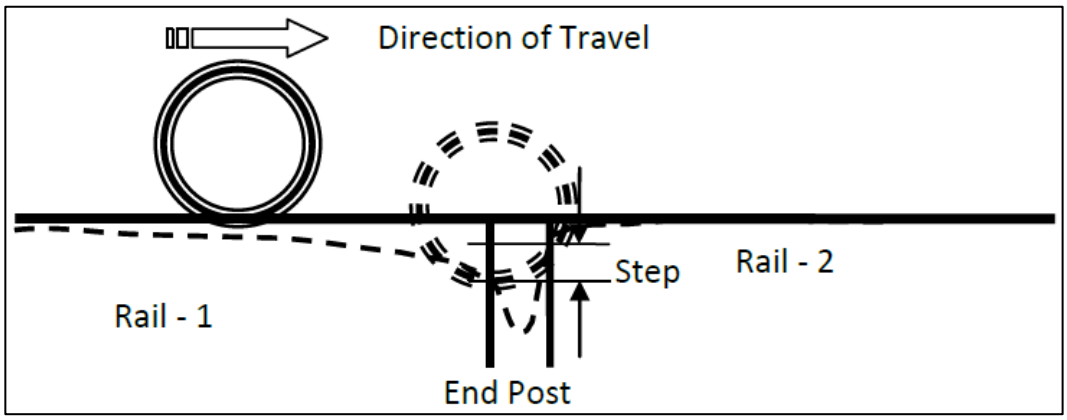

Figure 3-17 "Step" mechanism of wheel-rail impact

3.5 Previous studies on IRJs

With a view to increasing the axle loads and the annual operational throughput, many improved structural designs of IRJs have emerged in the market. A patent search on rail joints found hundreds of designs. An analysis of the collection reveals that, from 1903 to 2011 (Akhtar and Davis, 2011, Nelson and Goken, 1976, Hamilton Jr William, 1968, Page, 1903), the primary focus of the rail joint design remained unchanged with the concept being centred on 'strengthening/ stiffening' of the components/ assembly. Transport Technology Corporation Inc., USA (Davis and Akhtar, 2006) have developed designs that possess either increased tie-plate length and number of bolts or a more supporting mechanism using an additional saddle design (a design trialled at TTCI is shown in Figure 3-12a).

The ARTC conducted an unsuccessful field trial of a ceramic (zirconia) endpost in a heavy-haul corridor. Although zirconia and railhead steel exhibit similar E-values (between 190 and 240GPa), the zirconia ultimately proved too brittle in this application. The brazing technique with partially stabilized zirconia (PSZ) to a rail steel has been previously conducted under CRC Rail project-75 in order to totally eliminate the joint with providing electrical insulation being obtained through graded conductivity of the material in it, Figure 3-18. Irrespective of promising new design (Huang et al., 2007), it faces a great challenge to meet the requirements for shear stress and fatigue properties of the ceramic material as it outweighs the mechanical properties of pearlitic rail steel and thus leading to undesired failure of ceramic insert.

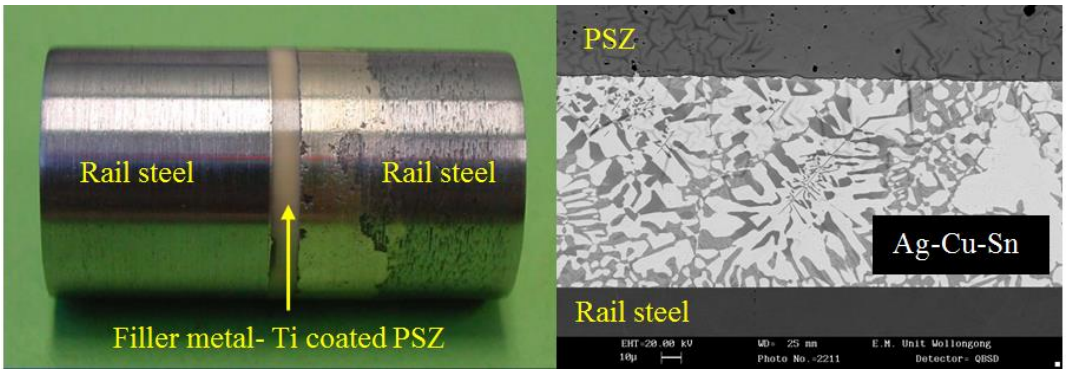

Figure 3-18 Brazing joint, cross-sectional SEM image of brazed PSZ/rail steel joint

The early damage at the rail end due to localised stress concentration are being solved by the engineering industry such as ARTC in Hunter Valley and by QR and also practiced by the in USA, Figure 3-19. Preliminary evidence shows that the selection of high yield strength steel e.g. martensitic stainless steel as a rail surface coating material and coating design has resulted in cracking along the rail weld interface contact area.

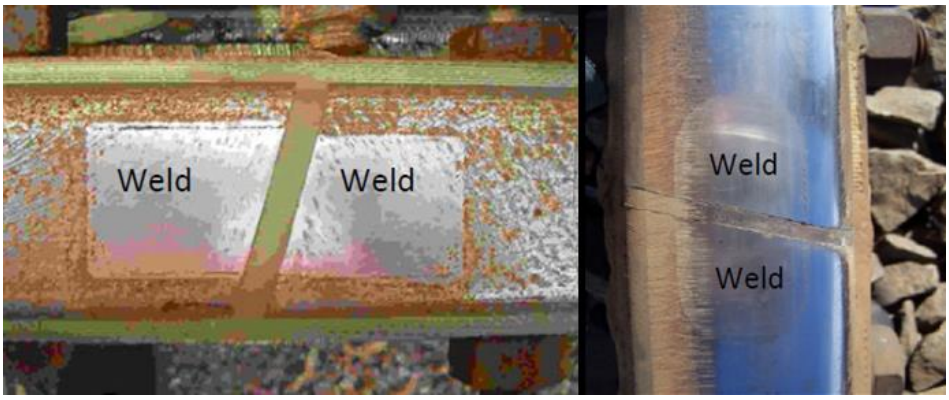

Figure 3-19 Surface coated IRJs with high yield strength steel

Another design emerged recently is reported in a previous study (Zong, 2013) from the CRC R3.100 rail innovation project. This joint introduces a new rail end joint. According to the author stress/contact concentration at the “critical” zone of the rail end, it cannot solve the global failure modes (joint bar cracking/bolt hole cracking and bolt loosening) due to the existing complexity of the design. To solve this problem (Zong, 2013) has developed non-ratcheting IRJ in such a manner that

the stress concentration at the rail end migrates to the underside of the railhead similar to the stress distribution in a continuous rail Figure 3-20.

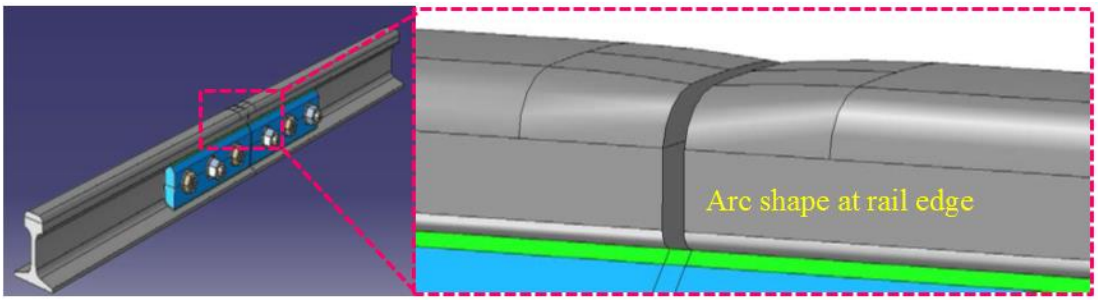

Figure 3-20 Typical 3D view of the arc shaped railhead in the proximity of the gap

With the non-ratcheting IRJ design for both 6mm and 2mm gapped IRJs, it can be seen in the Figure 3-21, and that the stresses are just below the yield point of rail steel for non-ratcheting IRJ design compared to current IRJ design and also (Zong, 2013) suggests that with this design it is possible for IRJ to have smaller gap (2mm) without any risk of electrical short-circuiting, which couldn't be possible for current design to be brought that close to eliminating the ratcheting problem Figure 3-21.

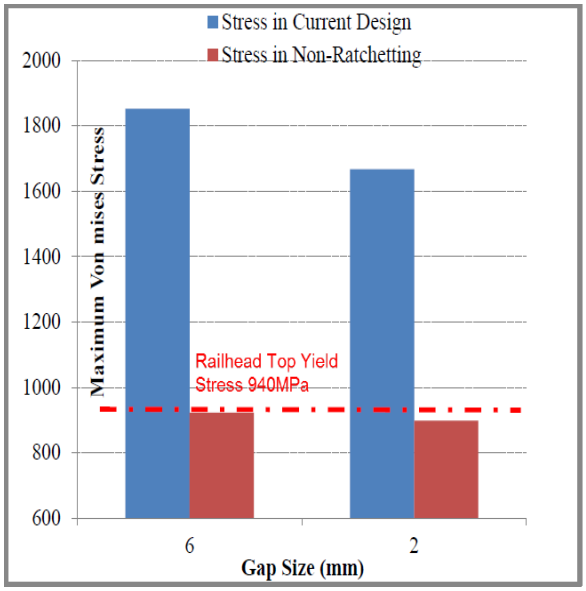

Figure 3-21 Von Mises stresses in the current and Non-ratcheting IRJs design

3.6 Major rail accidents due to failure of IRJs

The majority of failures of IRJs in Australia are related to railhead surface defects in the crown or shoulder of the rail running surface. Two key factors relevant to the failure of Australian IRJs are wheel/rail contact impact force and metal plasticity.

Established research shows that severe plastic flow is generated when the wheel-rail contact points traverse the IRJ. In addition, the shear strength ratio (*P0/k*) is a parameter for the metal plasticity. Together with the nature of contact (line or point), *the P0/k* value is associated with material behaviour such as plastic shakedown or ratcheting. Damage happens when there is a peak of contact pressure *P0,* which is a result of wheel load and the impact force from the structural discontinuity at the IRJ, and on surface asperity (Kapoor et al., 2002).

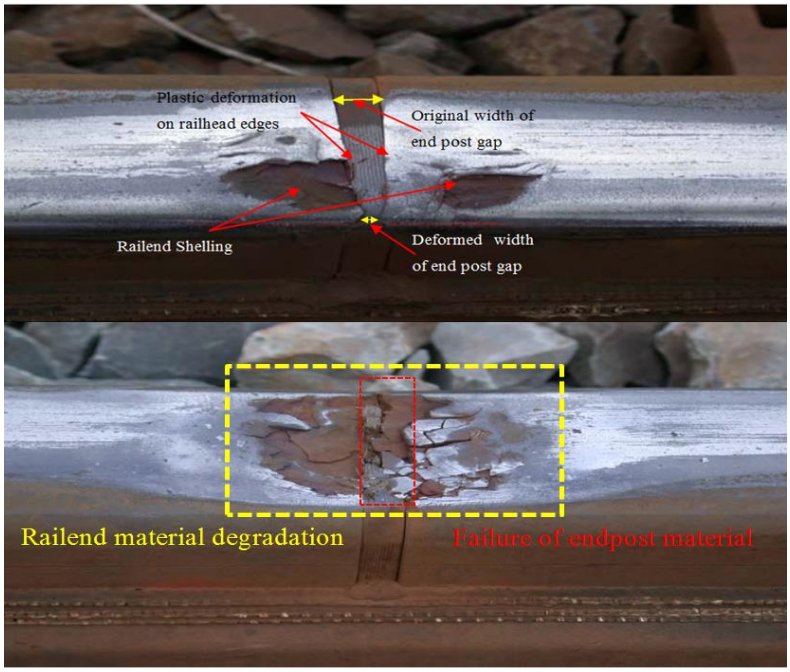

Figure 3-22 Railhead damaged at the vicinity of rail joint in Rockhampton, Queensland

In Figure 3-23a, the Hither Green rail derailment of an express passenger train caused on November 1967 resulted as per broken rail at a rail joint, the fishplate of this joint had a fatigue crack through the first bolt hole which had propagated vertically from the rail running surface. Figure 3-23(b & c) shows the triangular piece of rail fracture and fatigue crack in the fishplate (Liu et al., 2012).

Analysis on the train derailment shows that the number of rail failure occurrence are those with rail joints (Liu et al., 2012). Also, three major causes are joint bar defects, rail defects at bolted joints and rail joint defects. Figure 3-24 enables an easy comparison of the severity of rail derailment and its frequencies of occurrence.

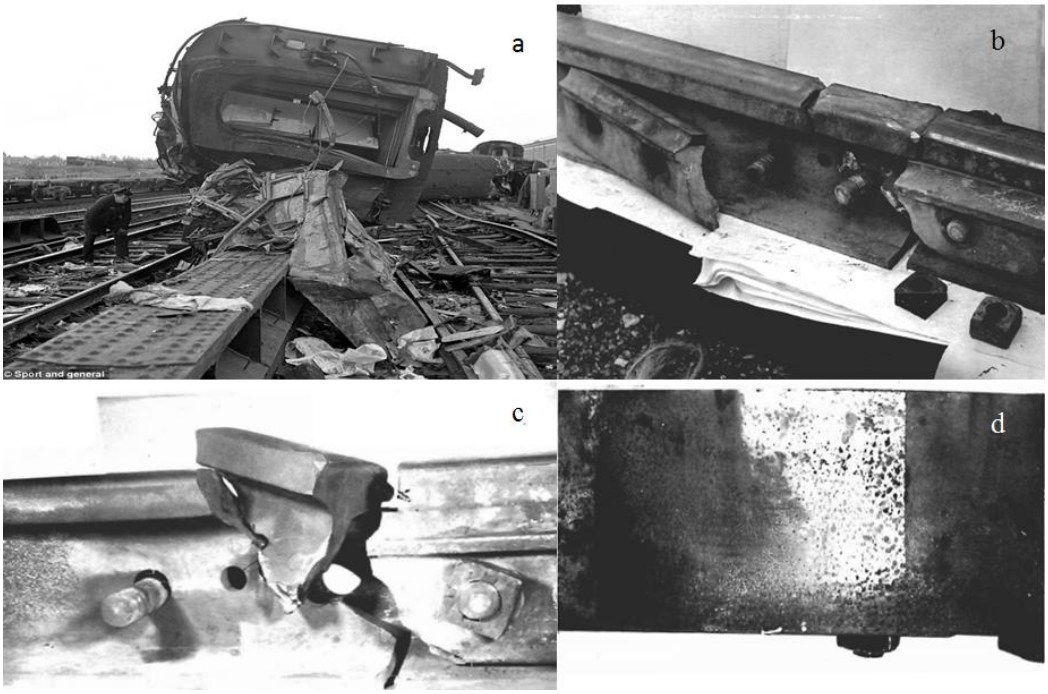

Figure 3-23 (a) Hither Green rail crash 1967 (b &c) fatigue crack growth at first bolthole of IRJ and detached portion of railend broken out (d) underside of the rail foot

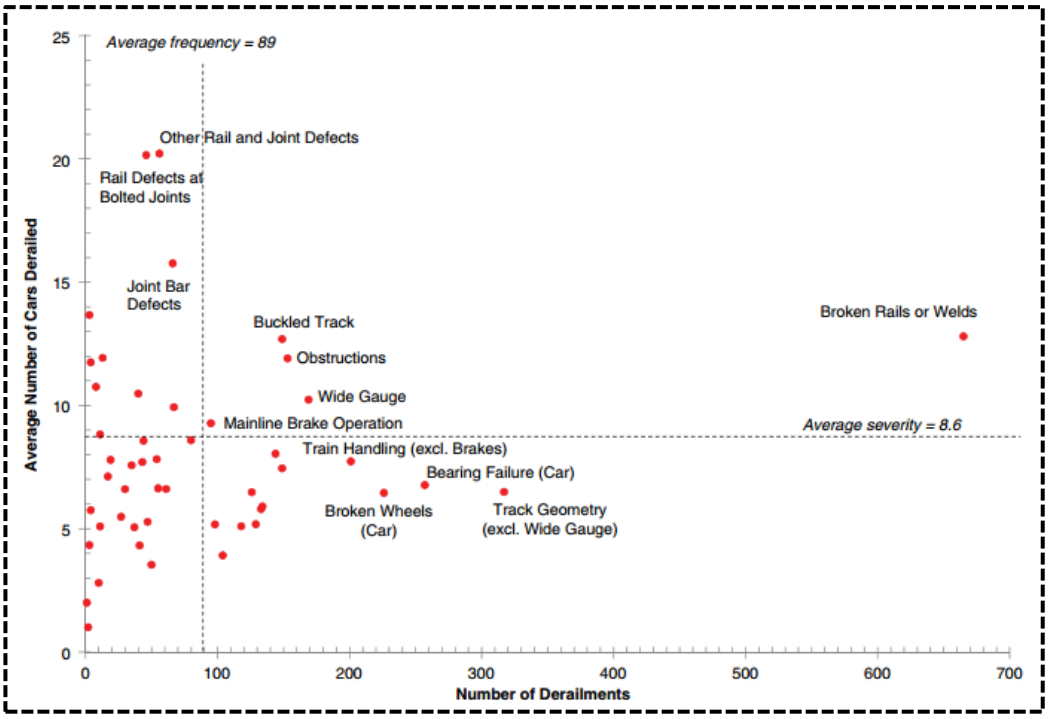

Figure 3-24 Frequency and severity graph of class I main-line freight train derailments

The multi-occurrence of the Head checks makes them very dangerous and this we can easily find by the example of Hatfield Accident, 17th October 2000 (Smith, 2002a). The Head checks are the groups of the fine surface cracks at the gauge or running corner of rails and having distinctively interspaced at 0.5 – 10 millimetres. An effect called knock-on effect was observed after the first crack. Following the first crack, the damage occurring at rail section running adjacently spread so briskly that it resulted in the derailment, causing unaffordable loss as discussed. The process of head checking generally takes place on outer rail tracks at the curves and track crossings at the gauge corners (Heckl and Abrahams, 2000). This is because of uninvited deformation of plastic corresponding to the frictional force with the wheels.

Rail degradation is processed with the failure of microstructure and macrostructure in addition to the relative interaction of wear rates and mechanism, fatigue crack initiation and shorter rail life (Reddy et al., 2008, Eden et al., 2005). Squats and wheel burns are common defects in most of the rail network Figure 3-25. The frequency of each failure occurs on annually and every two kilometres on every network. For example, 4000 of rail fractures have been reported each year in at least one railway network in Europe. This disruptive factor of rail track dramatically increases replacement cost although it is less dangerous after an associated repair (Telliskivi and Olofsson, 2001). The replacement of this defect is calculated based on each short rail section due to its expensive cost. For instance, the average cost for this replacement may up to thousands of dollars. However, the design of this repair is out of expectation as there is the generation of new discontinuities of defect of the aluminothermic weld (Lonsdale and Engineer, 1999). This reduces the production of a long hot-rolled rail plus to wheel-rail defects. Thus high cost of replacement encourages researcher in this field to find alternative methods for rail defect.

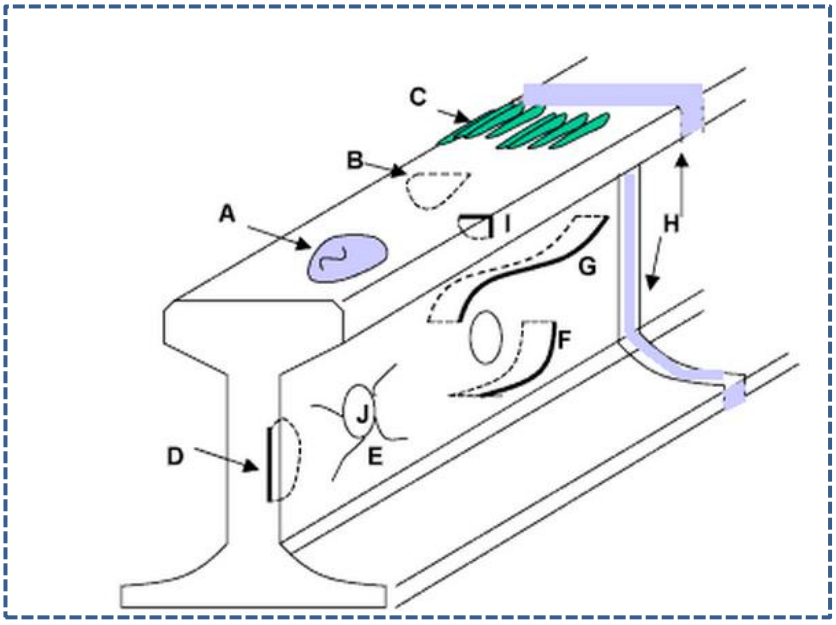

Figure 3-25 Flaw types in rail and in rail joint that can cause broken rails

Table 3-1 Description of the flaw types in rail joints and in general rails.

Key	Description
A	Head surface flaws
B	Squat flaws running parallel to the rail surface
C	Roughness of the rail head due to missing material (caused by breaking/slipping wheels)
D	Vertical longitudinal split flaws
E	Star cracks at bolt holes
F	Diagonal crack in web of rail
G	Horizontal flaws
H	Flaws in thermit welds
I	Gauge Corner Crack
J	Bolt holes (although not flaws) can provide initiation points for star cracks

Cracks extend along the vector in the direction of traffic on the track, which is efficiently controlled by lubrication (Bogdanski S, 2002). Cracks are often filled with material deposits over time, moreover, when the cracks size up to millimetre range, transverse cracks start to develop which eventually lead to structural damage to the rail. Following figure pictures the transverse parts of head checks.

Squats: squats are weaknesses induced due to rolling contacts similar to head checks. Generally, they may occur in linear, transverse or curved cracks however they are present at the top surface or rail (Magel et al., 2005). They develop at random locations unlike head checks (Lewis and Olofsson, 2009). Squats and head

checks both occur due to inevitable characteristic plasticity and not due to metallurgic reasons. Squats gradually spread into transverse direction after growing initially at a right angle to the surface. Squats are visible on the rails and appear as depressions on the rail surface (Li et al., 2008). They are also called ‘dark spots’. It is observed that frequency of head cracks induced on the rail surfaces is high on high-speed railway tracks. This is due to innovation in steel wear resistance in the modern form of rail. It is interesting to know that two factors come at par with each other in this context: wear resistance metal removal and early stress crack spread. Improved wear resistance can have dual effects which can either result in an increase in grinding interval thereby increasing rail life as well as a decrease in maintenance costs. Besides, it can simultaneously allow smaller cracks that are not damaged away, to grow to a significant size (Kalousek et al., 1989, Magel et al., 2003).

3.6.1 Rail Head Cracks with Internal Origin

Kidney-shaped crack: In former times rail cracks with internal origin rather than surface induced cracks, were dominating the failure statistics. This type of cracks usually initiates from manufacturing defects, e.g. hydrogen shatter cracks, so-called ‘‘flakes” Figure 3-26(a). This shatter crack defects originates as a series of small hydrogen inclusions/cracks in the head of a rail and is characterized by a series of closely spaced internal defects that occur within the head of the rail. The pre-existent flaw is the nucleus for a so-called ‘‘kidney-shaped” crack or ‘‘tache ovale” Figure 3-26(b). However, that sub-surface cracks can also initiate in the virtually defect-free material (Frederick, 1993, Masumoto et al., 1978).

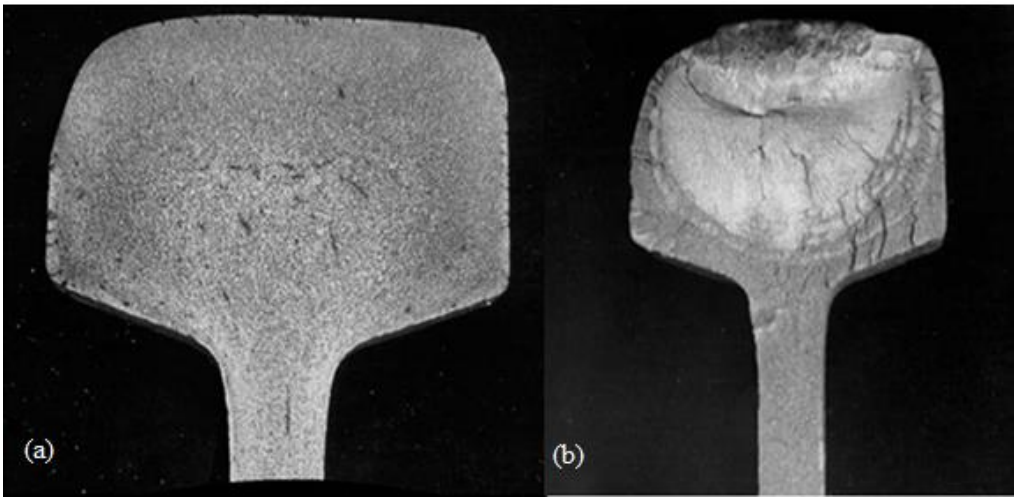

Figure 3-26 (a) Transverse section of a rail head containing hydrogen shatter cracks (‘‘flakes”), (b) Kidney shaped or Tache Ovale crack in a rail head.

***Longitudinal cracks*:** horizontal cracks are unique kind of subsurface induced cracks that are present beneath the gauge corner (Zerbst et al., 2009). These can result in the breakdown of material, known as gauge corner shelling as well as transverse crack propagation, called as detail fracture as shown in Figure 3-27. Transverse crack propagation can occur on either one end or both of a surface “shell”. The crack is attached to a band of non-metallic inclusions that is present 10mm under the surface.

3.6.2 Rail Web Cracks

***Longitudinal horizontal and vertical cracks*:** These cracks present in web generally result from manufacturing defects. Consider Figure 3-27 that depicts longitudinal vertical crack called as “piping” (Vitez et al., 2007). Figure 3-28 contains a demonstration of the horizontal crack. These two kinds of web cracks eventually result in fracturing the rail.

Machine holes in the web are an origin of web cracks. These cracks usually extend in the direction of 45^{o} with respect to the horizontal and tend to deviate further as they gradually grow Figure 3-28.

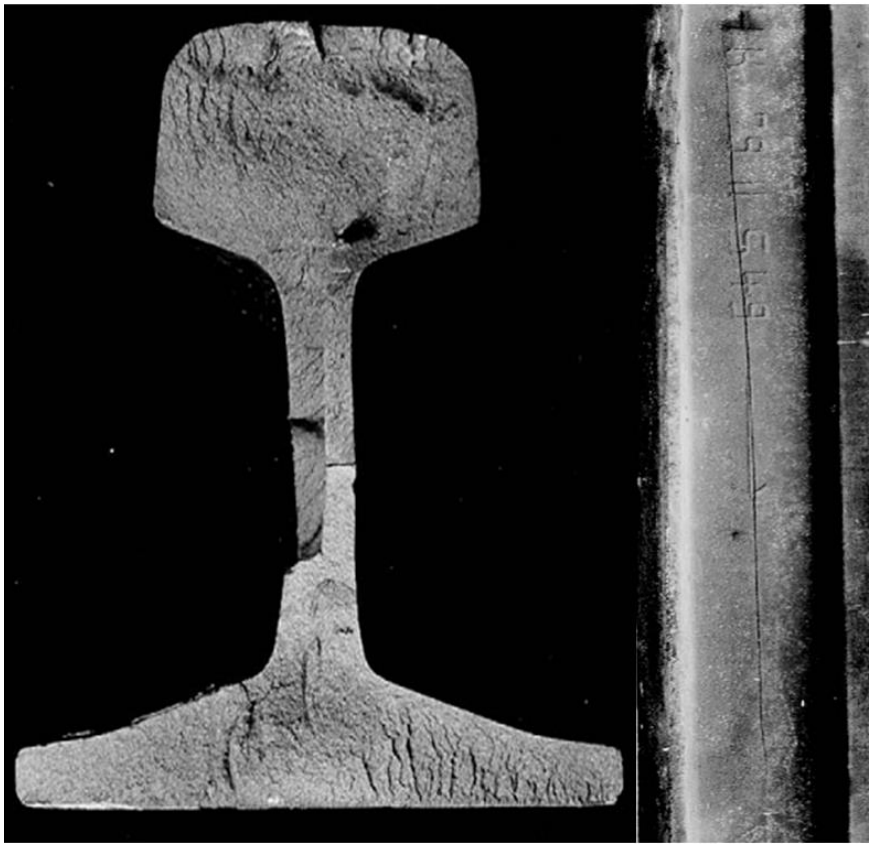

Figure 3-27 Longitudinal vertical web crack "piping, Horizontal web crack

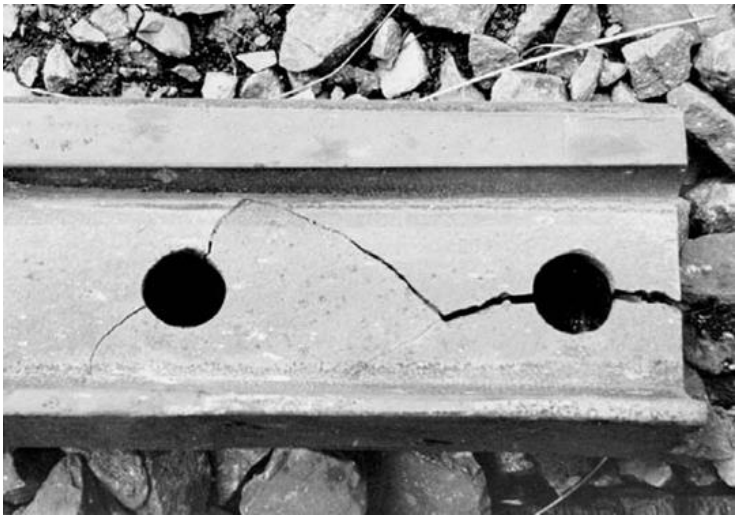

Figure 3-28 Web cracks originating from a fishbolt hole

Cracks can be introduced due to vertically downward fatigue caused by fishplate restraint, in which cases they can also grow in the direction along the rail. If the cracks start forming at the holes at the ends of rails, they become highly hazardous, similar to the fish bolt holes. These cracks start to initiate near the bolt holes at 45° due to higher stress amplitude caused by combined shear and bending condition of wheel loading (Mayville and Stringfellow, 1995). Reverse bending stress as wheel leaves the joint, propagates the crack in fatigue mode and causes the joint bar failure.

The IRJs fail due to a large number of failure mechanisms. Each component which forms the IRJ (fish-plate, bolts, insulating material) fails under severe wheel-rail contact impact loading. Some of the major failures reported in Australian IRJs are related to railhead failure in the vicinity of endpost. Development of plastic deformation and accumulation of residual stress near the rail end are severe because of its discontinuity in joint design (Mandal, 2014). Examples of some of the major failure modes of IRJs reported in the literature are shown in Figure 3-29.

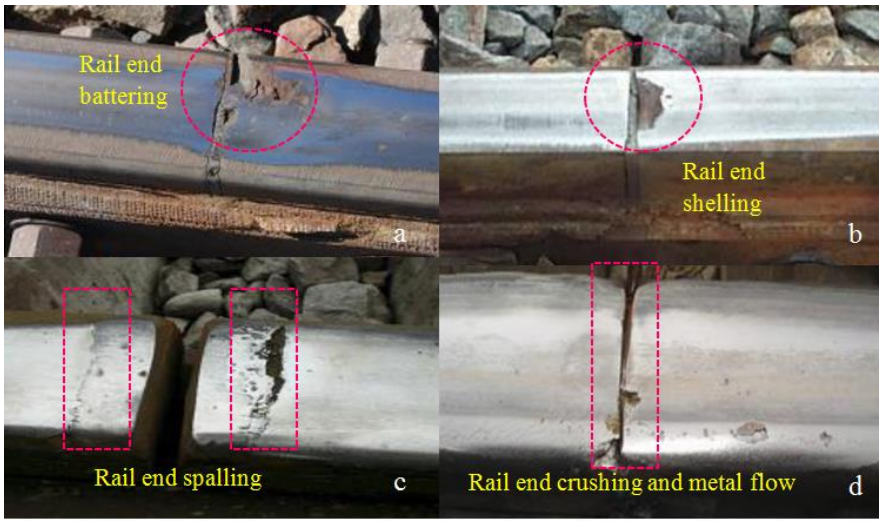

Figure 3-29 The most common failure modes of IRJs (a) Rail end battering (b) Rail end shelling (c) Rail end spalling (d) Rail end crushing and metal flow

High axle longitudinal force and thermal effects contribute to bolt loosening which generates severe geometry discontinuity and exhibits higher impact contact

forces. This leads to bolt-hole failure and battering/crushing and metal flow at the end post, Figure 3-29. Subsurface cracks grow horizontal along the running surface about 10mm (Gullers et al., 2008) from the railhead usually associated with residual stresses field and interface region of deformed and undeformed subsurface level. These cracks can grow vertical up towards the rail head or downwards, leading to dislocation of the rail head section (Fischer and Daves, 2011), Figure 3-29. Railhead shelling in operational rails is known to result from high axle load. Shelling occurs originally about 4 to 6 mm below the running service of the rails (Ekberg and Kabo, 2005). These fatigue ruptures are caused by the long-term effects of fatigue strength of the overload rails. All these modes of failure aggregating each other causing critical electrical isolation of signal and failure of the IRJs (Nicoli et al., 2011).

3.7 Stages of Rail Fatigue

Propagation of squat-like cracks in the rail can be divided into three phases which support the extension and growth. In these phases different mechanical variables catalyse and control the crack growth in Figure 3-30.

A. Ratcheting is affected that occurs due to plastic accumulation under cyclic contact loading (Sandström and Ekberg, 2009). Initially, surface cracks are originated as a result of ratcheting. Once the crack is developed, it is resisted by the normal structure and tends to stop extending initially, especially in the case of minor cracks. This process can be related to a possible crack closure mechanism which could not resist crack formation initially. Interestingly, this closure mechanism (Ringsberg, 2001) is so evident that it plays its part in removing or adjusting minor surface cracks gradually as a result of metallic wear. However, modern technology

has the vision to provide alternatives with better wear resistance which will eliminate the possibility of this benefit.

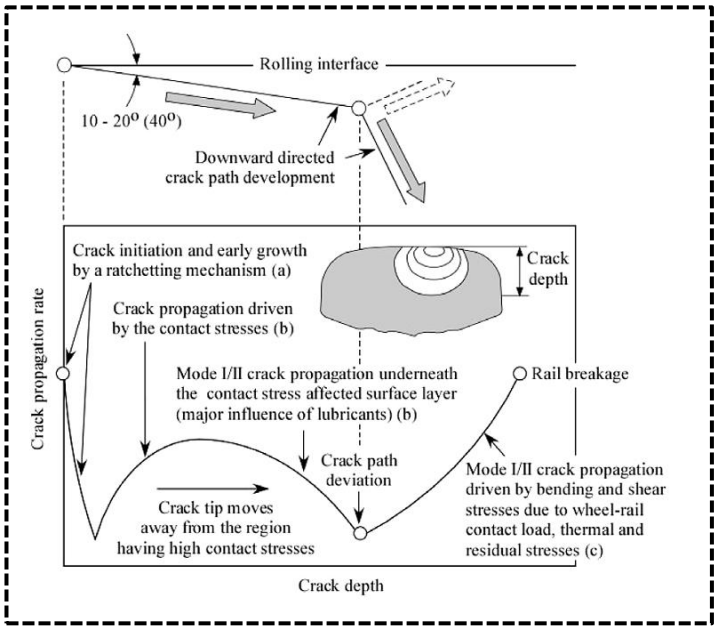

Figure 3-30 Propagation stages of a squat-like fatigue crack

B. The second phase starts whenever a crack reaches a certain threshold of depth. This threshold represents certain values of variables like stress, ductile strength and yield strength of the material of the rail. Once a crack reaches this value, it starts growing at a steady increasing exponential. Two modes assist crack propagation namely combined opening and sliding mechanisms called mode I and mode II respectively (Wong et al., 2000). The steady increase still largely depends on the vertical stresses due to the wheels. This is followed by crack expansion to a certain level after which cracks spread through unstressed parts and extension is decreased again. Moisture levels in the rail material are an effective determinant of crack behaviour (Olver, 2005).

The decreasing growth is actually due to lesser friction quotient between the rails and the wheels due to the presence of liquid compounds which support the crack

extension of mode II and III. Moreover, a negligible effect of this liquid is also seen when stress due to wheels, cause minor extensions in the cracks, which are filled by liquid content. Figure 3-31 depict stress intensity behaviours in ranges DKI and DKII, according to (Donzella et al., 2005) simulation. Where DKI and DKII are stress intensity factor for mode I and mode II fracture mechanics. DK I is applied for the tensile crack opening mode and DK II is applied for crack sliding mode in a direction perpendicular to the leading edge of the crack (Hutchinson and Suo, 1992).

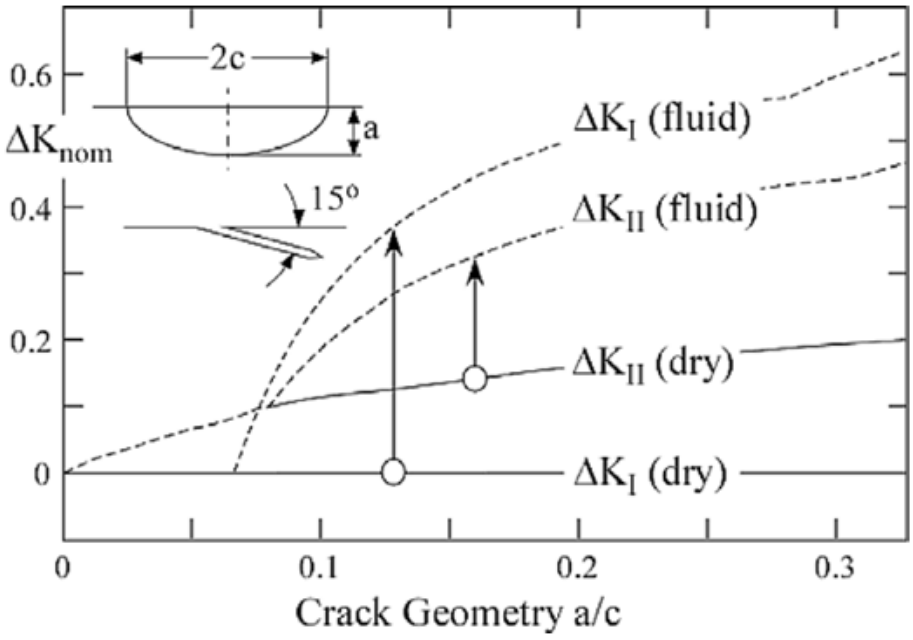

Figure 3-31 Effect of a liquid entrapped in a squat-like crack on the mode I and mode II stress intensity ranges DK

Stress intensity in mode II cracks often creates a tree of secondary cracks at the edges of parent cracks. The newborn cracks rise forward in the direction of traffic or tend to make smaller trees in the opposite direction tilted towards a downward direction. This tree effect is resisted by the moisture filled in the cracks due to lubrication on the edges of the cracks which limits wear due to surface cracks of the

rail. It is assumed that the first two stages have a mild angular propagation of cracks reaching up to 10-20^{o} up to the tangential maximum (Masse et al., 2011).

Crack propagation under stress reaches its third stage threshold once an acute tree of cracks is formed. It is evident from the picture of tree cracks that secondary cracks are inclined away from the normal from the parent cracks, as the parent cracks are aligned to the surface Figure 3-32. Hence, the angle which the secondary cracks propagate is around two times the original angle. The combination of modes determines the extension of cracks however mode I happen to be more prominent compared to prior stages.

The extension is catalysed and controlled by stresses due to the wheel, while frictional forces, stray losses and thermal elements support the propagation. The final stage of crack propagation persists till the 'breaking point' of the material. After this point, the point of material fracture stress is surpassed and the material becomes completely brittle and unusable (Magel and Kalousek, 2002, Ekberg and Sotkovszki, 2001).

The difference of stress behaviour will determine the crack scatter pattern on the rail surface between different materials, with different fracture points. Figure 3-32 exhibits the stages of crack development from above to the inside of the surface due to stage 2 tree development (Kondo et al., 1996). The numeric figures are not general and refer to results of the specific application, however, similar characteristics are observed. (Liu et al., 2007) defines the propagation of shelling shorter secondary cracks tend to propagate with steeper angles while long cracks extend along the direction of the surface.

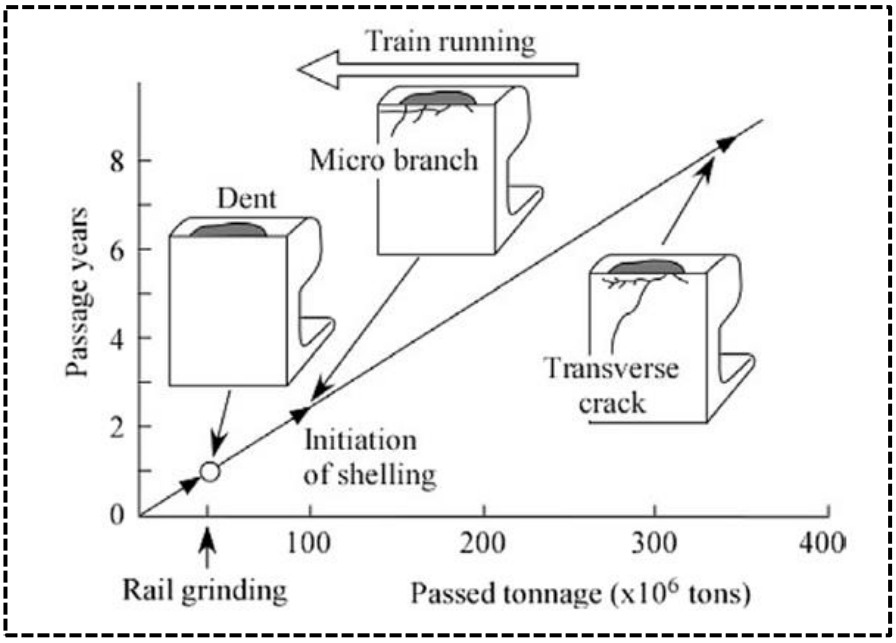

Figure 3-32 Formation and development of a surface crack from an internal horizontal defect (shelling) as a function of service time and passed tonnage at a Japanese Shinkansen rail

3.8 Crack Initiation

***Nucleation process*:** As discussed above, the squat cracks on the edge of railheads are excited by deforming plastics and stress hence induced near the railhead. Hertzian type wheel stresses both normal and shear, stray strains and frictional stresses due to crack edges, induce this combined strain effect.

According to (Ringsberg, 2000, Suresh, 1998) the fatigue initiation process starts with nucleation within the metal grains and is affected by the presence of grain boundaries, precipitates, impurities and inclusions. Cyclic shear-induced dislocations in the grains cause plastic deformations at high enough stress levels. Continued plastic deformations give rise to slip bands surrounded by less affected material. Repeated deformation of such a slip band makes a crack form. A small grain size will suppress dislocations and will therefore contribute to higher fatigue strength.

However, material imperfections lead to stress concentrations that will nucleate cracks and thereby reduce the fatigue strength (Liu C D, 1995).

A fatigue crack can be considered to have been initiated when the nucleation and formation of slip bands is completed. An initiated crack is physically quite short; in the order of 0.1 mm. In numerical modelling work the complex process of initiation must be ‘‘summed up” into a macroscopic level. For the fatigue life models discussed in the following the initiation is thus described by material parameters obtained by employing standardized material testing methods.

It should be noted that the fatigue problem under contact loads is quite different from a conventional fatigue problem, e.g. in a railway axle. In an axle, bending stresses and surface characteristics are dominating factors and the fatigue cracks always initiate at the surface, normally at fillets with stress concentration, and propagate perpendicularly to the surface. In the rolling contact fatigue problem, important factors are largly hydrostatic stresses and rotating stress fields (Sato et al., 2002, Hirakawa and Kubota, 2001).

Residual stresses formed by plastification will suppress further plastification. The initiation could start at the surface or at a subsurface position depending on the loading, although squat-like cracks normally initiate at the surface and propagate into the rail at a shallow angle to the surface. The hydrostatic stresses (compressive) mean that material imperfections will have less influence on the fatigue life than in a conventional fatigue problem (Bogdański et al., 1999).

Initiation of crack takes place from the surface and usually at fillets having stress focus which then proliferate vertically to the surface. Fields of rotating stress and hydrostatic stress are two important factors present in the fatigue problem of rolling contact (Bower, 1988). Plastification itself produces residual stresses which further

suppress plastification. The origination occurs at the upper plane or at times from subsurface, totally depending on loading. The cracks which are bending occur usually at the surface and then propagate at a low angle with the surface into a rail. Hydrostatic stress means that significant level of imperfections has less impact on fatigue as compared to conventional fatigue problems.

3.9 Material response and shakedown maps:

The stress which is provoked in the railhead due to rolling contact will lead to an unusual reaction to the materials depending on the stage of nature (Ringsberg, 2000), see Figure 3-33. When the load is not that heavy then the reaction is absolutely elastic and no everlasting bend takes place when continuous over rolling occurs.

A small plastification will take place at a certain level of the load; this plastification will get suppressed after a few cycles of the residual stress which is produced by plastification itself and then subsequent cycles would take place elastically (Bodner and Partom, 1975). Such a process is known as an elastic shakedown. When the load is increased then frequent cyclic plastification takes place every time the over rolling occurs, this type of a process is known as a plastic shakedown. If the load is increased beyond the above-mentioned level then the material undergoes a growth of strain and if this strain continues to grow, then a time will come when the material will finally break down. This phenomenon is further demonstrated in Figure 3-33.

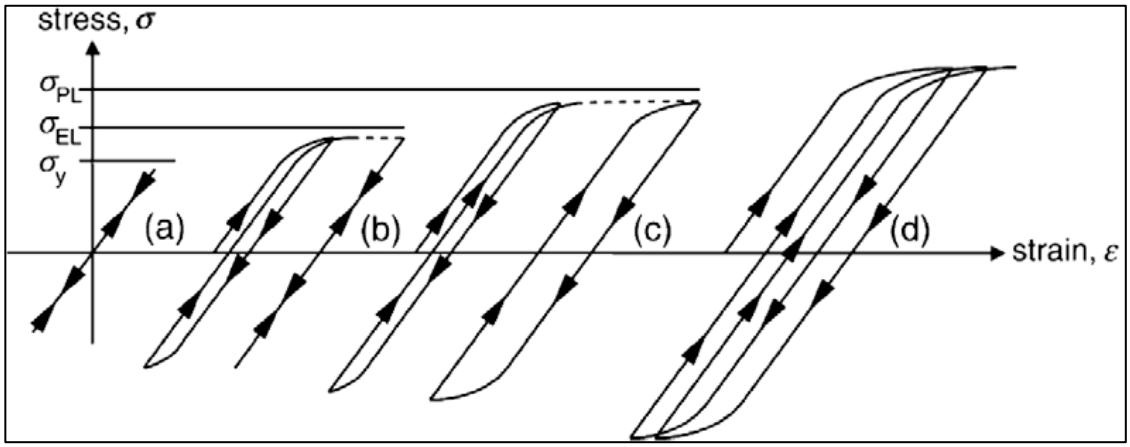

Figure 3-33 Principle of material response from repeated stress cycles having constant non-zero mean level

Figure 3-34 describes the shakedown maps that have been recognized for common non-conforming rolling contacts, adopted from a previous research (Ringsberg, 2000, Ponter et al., 1985). The rolling friction, contact geometry, size of usual contact pressure and flexibility of the material is used in the derivation of the curves. The fatigue damage takes place usually at the surface or at the sub-surface. On the vertical axis, the load factor is p_0/k. Here p_0 is maximum Hertzian pressure e and k is the material yield stress. K is also the factor that relies on the form of the contact ellipse. Friction on contact is specified as 1 on the abscissa. For the initial evaluation of fatigue's impact on predictable positions, for a certain level of load and geometry, shakedown maps are used (Ringsberg, 2000).

In short there are three common mechanisms that contribute to shakedown in rolling contacts of wheel-rail and they are:

1. Due to plastification and wear, surfaces widen more, thus confirming contacts.

2. Due to plastification which produces residual stresses which further restrain plastification.

3. When plastic deformation takes place then the material gets harder.

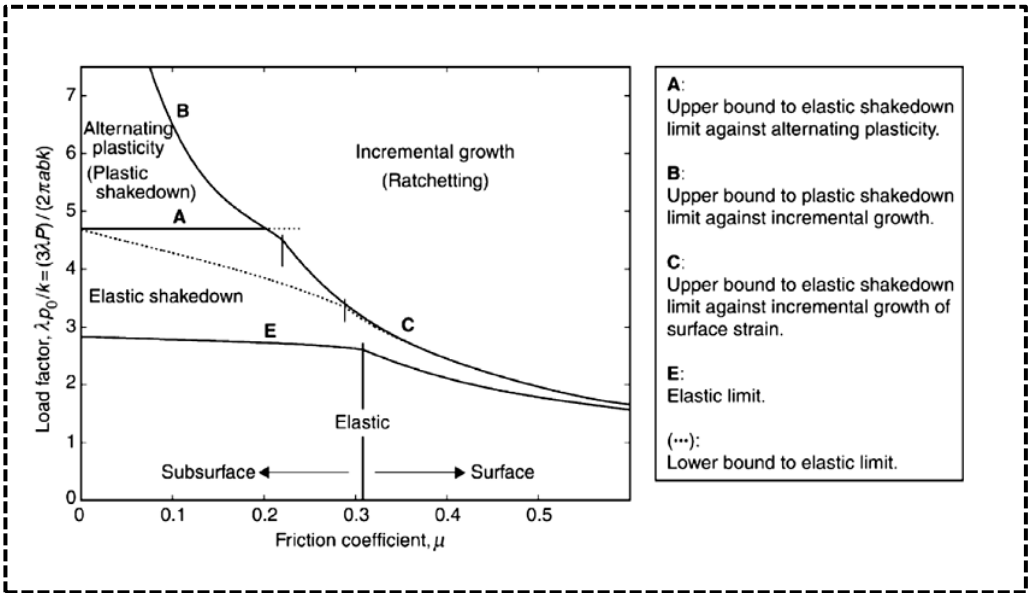

Figure 3-34 Shakedown map for general three-dimensional rolling-sliding contact

3.10 Crack Propagation

In the early stages of crack development in rails, when continuous rolling contact occurs, then RCF is generated on the railhead. High levels of tangential forces along with surface irregularity encourage uniaxial plastic bending to take place in a slim surface layer. Rail and squat fracture are later seen on the surface of the rail or at the corner of the gauge. Initially, one crack is produced which is a minor one, typically around 0.1 mm in length. This crack then grows at a low angle (10–25 ^{o}) from the face in the path of a plastically distorted anisotropic material, until the time it gets to a critical length (~ 1-2 mm), as shown in Figure 3-35. When this critical length is reached then the strains present at the tip of the crack continues to grow upward or downward. Further description of the crack development and propagation can be found in the literature review (Ringsberg J W, 2003).

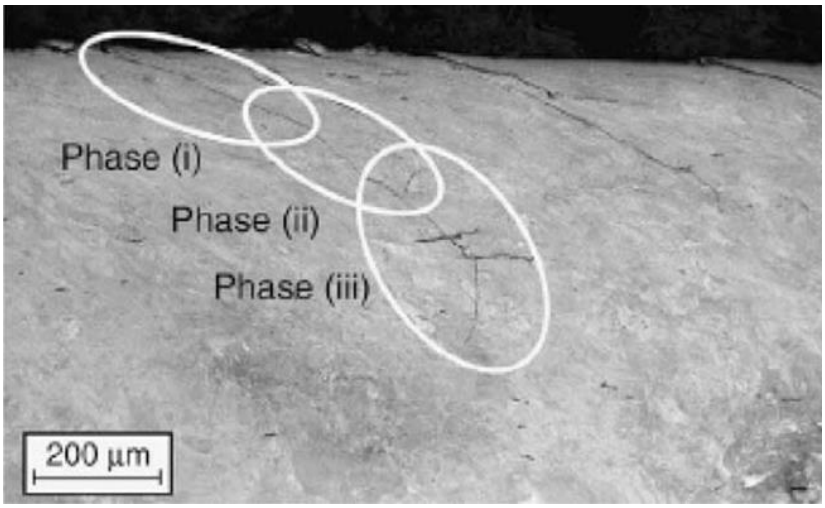

Figure 3-35 Three phases of life of a (rolling contact) fatigue crack initiated at the surface of a rail

An important role is played by fluids when crack proliferation takes place in rails. Fluids provide lubrication to the cracked surfaces and stop the crack from getting closed. Lubrication is very necessary for the small cracks, but it is ambiguous, whether liquid entrapment will take place or not (Ringsberg and Lindbäck, 2003).

A railway accident that took place in October of 2000 at Hatfield had its foundation in the head checks on the rail (Smith, 2002b). Identification, as well as the elimination of such types of cracks, is essential. For the safety of life and rolling stock economics, one should be aware of not only the presence of cracks but also about their growth rate. Continuous maintenance strategies are required to be undertaken so that the means of wear and tear, as well as the growth of cracks, can be considered.

3.11 IRJ Design and Failure Summary

This Chapter discussed stress and failure of IRJs considering static and dynamic wheel loadings. Different designs of IRJs and related support conditions were used as a background for analysis. Modes of failure of IRJs in Australian and overseas contexts were illustrated. The following content is key aspects of this Chapter:

• The design of IRJs: The designs of IRJs includes of symmetrical or non-symmetrical, supportive or suspended which can be differentiated by concrete or timber sleeper and either square or inclined type joints respectively.

• Types of failure of IRJs: The failure modes of IRJs include glued bond failure, endpost crush and delamination; joint bar failures including bolt-hole failure due to shear, pull-apart failure or fatigue failure; railhead damage in the vicinity of the endpost including dipping, squashing and chipping out of railhead material.

From the stress analysis point of view, it can be stated that only limited studies on IRJs have been carried out to date. Detailed knowledge of the failure modes of the railhead material in the vicinity of the endpost is essential to ensure the correct tolerance design and a safe load limit for IRJs. Regarding that review, the current study includes degradation of railhead materials in the vicinity of the endpost to examine.

3.12 The origin of residual stresses

Residual stresses in rail materials are common and an inevitable problem in each step of material processing. The causative factors of this kind of problem may be mechanical, thermal or chemical. The first refers to manufacturing processes that produce non-uniform plastic deformation (Webster et al., 1989). This issue may

naturally happen during processing or treatment or be deliberately induced to develop a particular stress profile in a component (Schleinzer and Fischer, 2001).

Rod or wire drawing, welding, machining and grinding are examples of operations that produce undesirable surface tensile stresses or residual stress gradients. Conventional and highly abrasive grinding produces more tensile stresses near the surface than those produced by compressive stresses with gentle grinding (Clayton, 1996). The gentle grinding is induced by shot peening, toughening of glass or cold expansion of holes resulting in performance benefits.

On a macroscopic level, thermally generated residual stresses are often the consequence of non-uniform heating or cooling operations. Coupled with the material constraints in the bulk of a large component, this induced stresses can lead to severe thermal gradients and the development of large internal stresses. An example is the quenching of steel or aluminium alloys, which leads to surface compressive stresses, balanced by tensile stresses in the bulk of the component (Totten, 2002).

3.13 Residual Stress contributions to IRJ degradation

As rail joints undergo plastic deformation during cyclic stress under rolling contact loading condition which results in a complex residual stress state near the surface and subsurface area of the rail head (Sasaki et al., 2008). Stresses are even more complex and intertwined near the rail joint due to its discontinuity in structure, and it is important to understand the stress development near the vicinity of rail joints and in the subsurface region of the rail head (Johnson and Wise, 1970). Stresses developed from a wheel/rail contact in service, exceeding the material yield point, can cause spalling fatigue cracking and can also produce head checking fatigue

cracks. The lifespan of joined rails is mainly governed by the failures/damage at the rail head, most commonly manifest as rail end battering. This is because the end of rail head surface near the rail ends is the part where the highest concentrations of defects occur as a result of train passage over the IRJ gap (Luzin et al., 2013b, Rathod et al., 2014). However, during the complex loading regime undergone by IRJs failures also happen in other regions, and are particularly common through the mechanism of fatigue fracture around the bolt holes in rail webs and fishplates.

3.13.1 Residual stresses and degradation of rail surface and rail end

Residual stresses in the subsurface region of the rail head are induced due to manufacturing processes and, subsequently, by train movement over the IRJ (Papaelias et al., 2008). Understanding the evolution of residual stresses in the vicinity of IRJ rail ends is a complex task as damage accumulates under different modes, with one aggravating to the other. The combination of cyclic stresses under rolling contact (Davis and Akhtar, 2005b, Kerr and Cox, 1999), impact stresses associated with the structural discontinuity of the joint (Wen et al., 2005), and severe macroscopic rail deflections all contribute to the accumulation of stresses during service. Severe stress concentrations occurring at the rail-end and causes plastic deformation across the joint near the joint surface (Kerr and Cox, 1999).

3.13.2 Degradation of the IRJ fishplate supports

Rail web defects include vertical and longitudinal cracking, cracking occurring at fishplate bolt holes, cracking at adjacent holes found in the web of the type which generally classified as star cracks, and transverse fatigue cracking(Zong et al., 2013) . The regions around bolt holes, in particular, become weak points and are regions

vulnerable to crack initiation as they face very high-stress concentrations and web shear stresses. However, low bending stiffness of the fishplates at rail joints comparing to the rail section results in higher vertical deflection and dynamic forces under passing trains. This damages the fishplates, bolt holes and will lead to deterioration of rail head (Kataoka et al., 2005).

Moreover, it decays the ballast and damages the area of the rail joints at the same time. The need for electrical insulation of some sections of the track is expected to keep the insulated rail joints in track for several decades, as fully replacing the current signalling system will be a major cost to the rail infrastructure industry.

Stress accumulation near the bolt-hole surface is explained via two mechanisms: Firstly, low amplitude stresses are introduced during manufacture and installation of joints and during the high lateral load from wheel rolling service (Orringer, 1990). The behaviour of a rail joint under the load is different and more complicated compared to a continuous rail because of its structural discontinuity. Secondly, the conditions are compounded by in-service problems associated with factors including; joint dip, loose joint sleepers, settlement of ballast support system, loosening of fish bolts or stresses associated with over tight fish bolts, wearing out of the fish plate planes, battering of rail ends and excessive expansion of rail gaps (Wilson et al., 2012).

Two scenarios of rail web failure have been suggested. (1) During the passage of wheel, under flexural loading, the joint undergoes bending; with bolts loading mode changing from pure shear to complex/combined shear and bending while a significant deformation causes the rail end gap to open wider (Igwemezie and Nguyen, 2009a).With this reason, there will be a development of stress concentration caused by the notch effect at the bottom and top of the bolt-hole surface of the rail

web and fishplates, which will initiate two diametrically opposite cracks at 45^{O} (star crack). The cracks will grow during the reversal of loading when a wheel passes the joint as shown in Figure 3-36 (Zerbst et al., 2009). Once this process begins, the benefits gained from an ideal support condition are lost and the system reverts back to the unsupported state.

(2) Bolt-hole cracks/cracks in the web region are also caused by loosening of ballast elasticity underneath the tracks, giving a higher vertical displacement at the joint which causes fretting between the fishplate and rail web. Eventually, this leads to dislocation of rail web section by fracture (Igwemezie and Nguyen, 2009b). As the wheel approaches rail 1 Figure 3-37a, firstly, the dynamic wheel load increases towards the railend before the joint gap and decreases once in the vicinity of the centre of the joint gap and finally, as the wheel moves to the rail 2 the wheel load increases again (Suzuki et al., 2005).

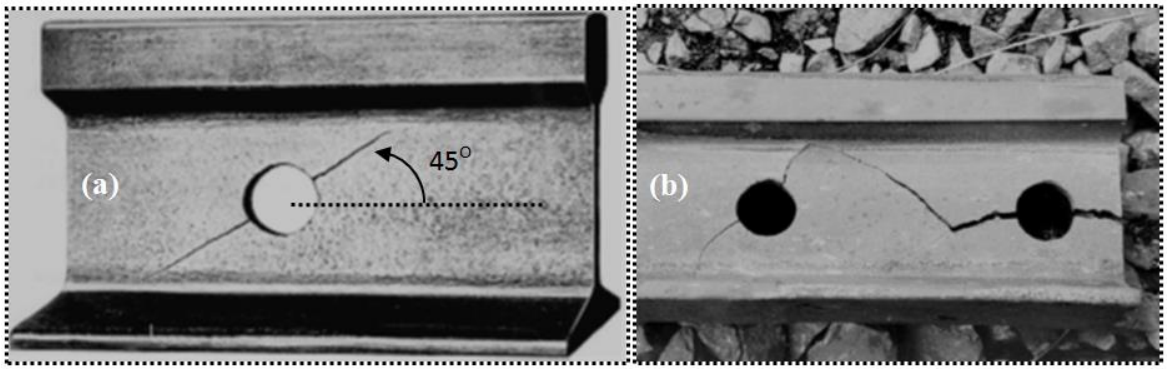

Figure 3-36 (a) Typical star crack and (b) horizontal crack for rail web bolt holes

Due to a combination of the discontinuity in joint designs and higher dynamic performance of the wheel, high-frequency excitation of stress distributions occurs in irregular fashions, which can cause a recoverable dip as illustrated in Figure 3-37a,

and metal flow, as observed at the surface of the rail head end as shown in Figure 3-37b.

Rail joints undergo bending stresses which cause fretting between the bottom of the rail head and top of fishplate surface and this creates very high and complex contact stresses at the top of the fishplate bar. As a result, fishplates suffer a contact fatigue (Chen and Kuang, 2002). In addition, as the fishplate resists longitudinal movement of the rail, there will be a concentrations of stresses developing at the bolt hole surfaces (Igwemezie and Nguyen, 2009b).

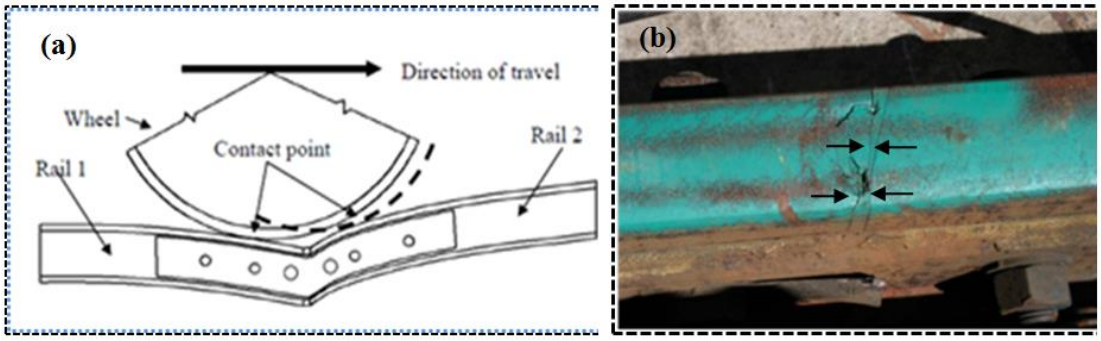

Figure 3-37 (a) Schematic diagram of wheel-rail contact and (b) Rail end battering and metal flow over the gap

Depending on whole rail support system (including supporting sleepers and subgrade structures), fatigue cracks can develop from either 90^{O} to top or bottom for rail bolt holes, or at 45^{O} for a fishplate bolt hole. These initial cracks will lead to the crack propagation when subjected to reversal bending cycles and this process eventually causes the fishplate to fail, either by straight vertical crack or star cracks in the rail web bolt hole (Salehi et al., 2011).

3.14 Diffraction techniques for determination of stress field in IRJs

Many techniques exist for the measurement of residual stresses within engineering components; however it is the effects of the residual stresses that are actually measured not the stresses themselves. The techniques are generally classified into destructive and non-destructive techniques see Figure 3-38.

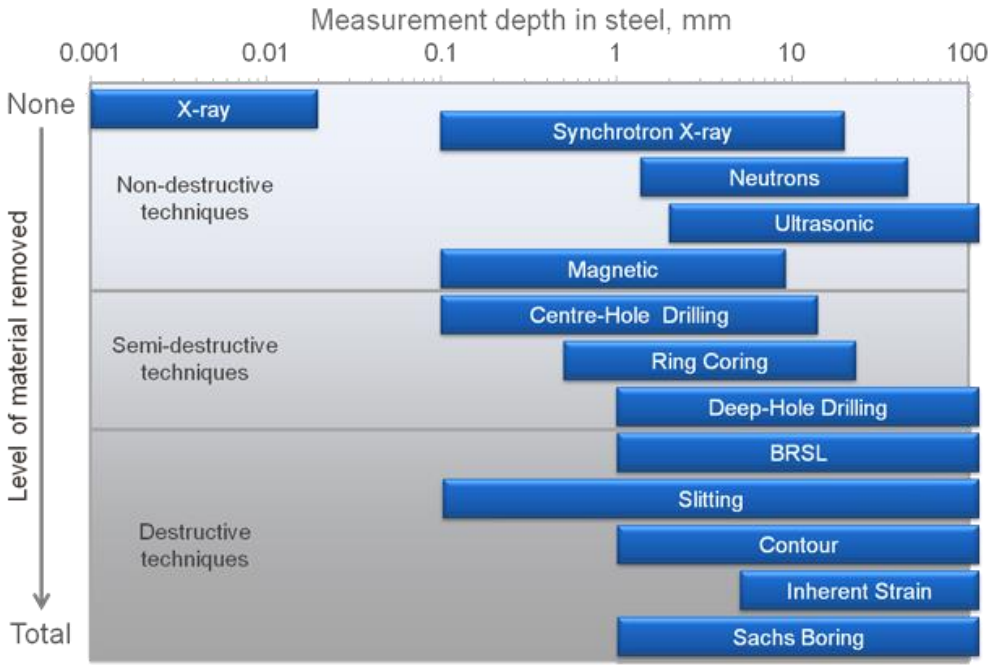

Figure 3-38 Classification of residual stress measurements techniques into destructive and non-destructive

Diffraction techniques are particularly suited to the non-destructive mapping of complex stress fields. Traditionally, neutron diffraction has been used to determine residual stresses internally in denser materials such as steel, where penetration depths are orders of magnitude greater than those of X-rays. Detailed 2-D and 3-D maps enable railway engineers to model and to better understand how residual stress fields

are generated and to determine the most appropriate rail maintenance and replacement schedules for safe and economic operation.

There are a handful of examples in the literature of the use of neutron diffraction to investigate residual stresses in rail, (Webster et al., 1992, Webster, 1993, Gnäupel-Herold, 1999, Luzin et al., 2004). These investigations usually involve measurements of slices out of rails, like in the study on comparison of rails (slices) produced under different production conditions and investigations of residual stresses in wheel damaged track (Luzin et al., 2004).

Residual stresses result in changes in atomic spacing's of α -Fe phase within the pearlitic matrix of medium carbon rail steel. With spatial resolutions of around 0.5 mm and penetration depths up to 60-100 mm compared to less than 3 μm for x-rays, neutron diffraction is an attractive option for internal strain measurements and subsequent calculation of residual stress in such steels. Compared to destructive relaxation methods that involve cutting and drilling, neutrons are also the preferred non-destructive method to determine the whole strain. The first reported neutron diffraction investigation of residual strain in full rail sections (Luzin et al., 2004) involved significant beam time, and this has been followed up by less time-consuming neutron diffraction investigations of strain in rail slices (Gnäupel-Herold, 1999). Recent investigation of strain in rail ends of ex-service IRJs (Luzin et al., 2013b) form a component of the current M.Phil investigation.

4 EXPERIMENTAL METHODOLOGY

In this Chapter, the experimental instruments and methodologies used in this study are introduced briefly. These include macro and microstructural investigations, hardness testing, neutron residual stress analyses and full-scale laboratory wheel on rail rig testing. The associated sample preparation methods for each investigation will also be introduced.

4.1 Introduction

In the current investigation, microstructural changes in the vicinity of end-posts of IRJs made from both surface-coated and uncoated rail are investigated using techniques of optical and scanning electron microscopy. Damaged IRJs made from pearlitic head hardened rail steel are compared with head hardened rail steel laser coated with martensitic stainless steel, the latter having an increased service life. Problems associated with the surface coating are identified and approaches to further improving IRJ resistance to rolling contact fatigue are suggested.

Both the coated and uncoated angle cut, 6-bolt, IRJs were fabricated from Australian standard 60g grade head-hardened steel AS 1085.12 with composition as listed in Table 4-1.

Table 4-1 Chemical composition of Pearlitic rail steel AS 1085.12.

Element	AS 1085.12 (Wt%)
C	0.53-0.69
Si	0.15-0.58
Mn	0.6-0.95
P	0.025 max.
Ni	0.10 max.
Cr	0.15 max.
Mo	0.02 max.
Cu	0.15 max.
Al	0.005 max.
Sn	0.04 max.

Table 4-2 Mechanical properties of Pearlitic rail steel AS 1085.12.

Nominal rail size	0.2% proof stress MPa	Tensile strength MPa	Elongation %	Surface hardness HB
60kg-Head-hardened rail	780	905min-1130max	9-10	340-620

The test piece for surface coating with MSS was prepared by machining a "bathtub" shape into the head of the rail and then powder laser depositing of a 431 Martensitic Stainless Steel (MSS), as shown in Figure 2-4. Laser deposition has chosen over other deposition technique because of the finer microstructure and smaller heat affected zones compared to that resulting from deposition techniques

such as hard facing by stick weld deposition. Full details are on the deposition methodology are commercial-in-confidence.

Macro optical imaging and both optical and scanning electron microscopes were used as the principal analytical techniques for this investigation. Specimens of rail head in the vicinity of the rail ends were sectioned in transverse and longitudinal directions to the long axis of the rail. Macro images were obtained from separated rail ends with no cleaning or chemical treatment. Samples prepared for microscopy and hardness testing were ground and polished to a 1μm finish and etched with 2% nital solution and 10% oxalic acid. A Leica DMRM was used for optical microscopy.

Microhardness in the transverse section was performed using LECO M-400-H1 Hardness machine at 500gram load. Hardness values associated with a particular region were taken as an average of 8-10 readings. A JEOL JSM-6490LA model scanning electron microscope equipped with JEOL x-ray energy dispersive analysis system was used for secondary electron and backscattered electron SEM imaging.

4.2 Welding Trails

A number of welding techniques can be used for welding rail surfaces. The main problem in welding pearlitic rail steels is their poor weldability, i.e. susceptibility to welding defects, due to its high carbon equivalent. Pearlitic rail end surface can be welded, in spite of their poor weldability, and properly choice of welding material and welding technology, it is possible to get an improved structure with dominant properties comparing to the original (Popovic and Prokic-Cvetkovic, 2012).

The practical objectives of this work are to utilize the welding methodology on rail head to increase the service lifespan of rail joints. Experimental welding trials were carried out at Queensland Rails, Brisbane and at the University of Wollongong

and are divided into two separate segments as initial trail welding and optimising the inlay design for welding on rail head.

4.2.1 Manual Metal Arc Welding (MMAW) welding trails

The base material for welding is same as mentioned in Table 4-1pearlitic rail steel. The filler material UTP-702 is used for welding whose chemical compositions and mechanical properties are mentioned in Table 4-3.

Table 4-3 Chemical composition of UTP-702

Element	C	Si	Mn	Ni	Co	Mo	Fe
Wt%	0.025	0.2	0.6	20.0	12.0	4.0	Rest

Welding consumable UTP-702 is age-hardenable martensitic steel. The filler material is free from titanium, so titanium carbide formation at the interface with the rail steel is absent. Rail steel is preheated by oxy-acetylene torch to a temperature of 350-400^{o}C, as the hardenability of rail steel is high, making it highly susceptible to hydrogen cracking. The toughness of the maraging steel is maintained by preheating the filling material to just above M_s Temperature, as heating to a high temperature will result in the maraging steel losing toughness and becoming susceptible to cracking under traffic. The trial tests were prepared by machining out the head of the rail and then depositing maraging steel using various initial preheats shown in Figure 4-1. The area to be welded and surrounding area are preheated to a required temperature. The preheat temperature is maintained till the welding is completed, and the rail are preheated if the temperature falls below. The preheat temperatures are

tested before welding commences using a thermocouple near the rail head. The purposes of this assessment were to examine for weld defects, determine the hardnesses of the inlay and the HAZ, and general metallurgical qualities of the different test pieces.

Figure 4-1 Preliminary trail welding of Maraging steel on the rail head in the shape of bathtub dimension

4.2.2 Gas Metal Arc Welding (GMAW)

The welding robot used in this thesis is an Industrial robot system (IRB 4400 robot on linear rail from ABB). The robot consisted of two main parts; the manipulator or robot arm and the robot controller. The manipulator had six independently controlled axes driven by electric motors and was used to hold and drive the welding torch to the desired locations and along the desired paths.1.6mm hard-facing wire supplied by ESAB was used for the welds. The welding parameters are presented in Appendix 9.7. Welding work carried using the Lean Automation

Robotic Work cell at the University of Wollongong, which equipped with an industrial robot system (ABB IRB 4400 robot on the linear rail), equipped with a high precision table, a flexible tool changer, and advanced welding machines and multiple laser and vision sensors. Figure 4-2 shows the robotic system welding setup. 1.6 mm diameter filler was used for all welds.

4.2.2.1 Consumables

GMAW trials were performed using flux-cored wire for hard facing applications. The diameter of wire was 1.6mm. The flux-cored consumable OK Tubrod 15.73 is a versatile, gas shielded, seamed wire (Fe, C, Mn, Cr, Ni, Mo, Nb, V based) designated for welding in down hand position.

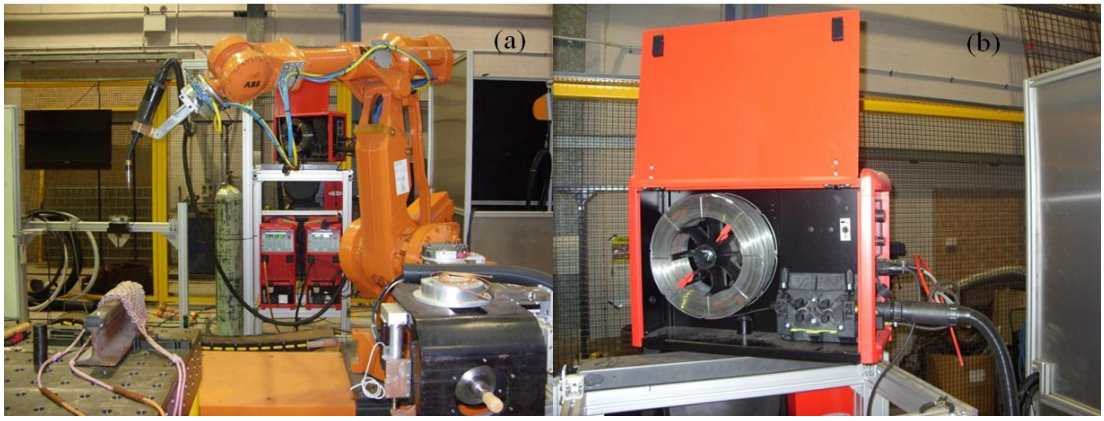

Figure 4-2 (a) ABB ARB 4400-60-6 axis industrial robot carrying weld gun used for GMAW on high precision work table with set of clamps (b) wire feed source

4.2.2.2 Welding Table

A high precision welding table with a set of clamps and accessories shown in Figure 4-3 was used to position and secure the samples at the exact locations defined in the robot programmes to ensure excellent repeatability and accuracy of the produced welds.

4.2.2.3 Robot Carrying Welding Torch

Welding applications are ideal candidates for automation because they are repetitive, require high-quality and consistent results. Robots are also extremely helpful when access to a part is limited or difficult to reach. Implementing robots into manufacturing process brings many advantages like enhanced repeatability, increased output, reduced costs and improved safety. The 6-axis industrial robot ABB ARB 4400-60 shown in Figure 4-2 was used for all GMAW trails. Robot programmes in the generic programming language were written defining the number of weld passes, exact weld path location, travel and wire feed speed, torch angle, stick out. A touch-sensing function was introduced to compensate for the geometrical variations of the steel plates to be welded in order to achieve excellent repeatability of the weld seam positioning for all the weldments.

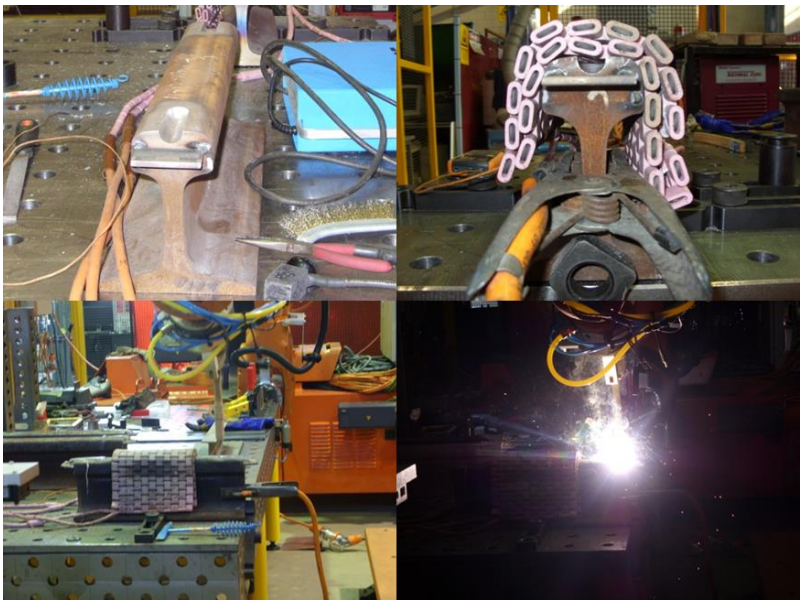

Figure 4-3 Welding table with a set of clamps and accessories. Electric resistance heating blanket used to preheat the rail head

During operation, the robot moves the welding torch in the horizontal direction towards one end of the vertical rail head. The welding power source is inactive state

sending a very low current to the filler wire. When the tip of welding wire touches the plate the electrical circuit closes and the location of the welding torch at that point is identified as an x coordinate of the start of the weld seam. The same process is repeated at the other end to acquire the x coordinate of the end of the weld seam. Y coordinates of the start and end of the weld seam are obtained in the same manner touch-sensing the horizontal rail head. For multiple passes, the position of the start and end of the subsequent passes are offset from the coordinates of the first pass. The example of the robot program used in the welding trials investigating optimal of the interpass temperature for an 18-22 pass bath-tub configuration utilising a flux-cored consumable is shown in Appendix 9.7.

Photographs of the rail end welding are shown in Figure 4-4, showing the location where the rail specimen was sectioned for surface welding. To prevent the defect at the rail end, run-on plate tab was used during welding. Rail samples for rail rig test was prepared by cutting the extra weld run at the rail end using an automatic hacksaw cut. In finishing, surface grinding and polishing were done to get a desired surface finish of rail end surface shown in Figure 4-5.

Figure 4-4 (a) Run-on plate (b) weld run (c & d) Completion of weld

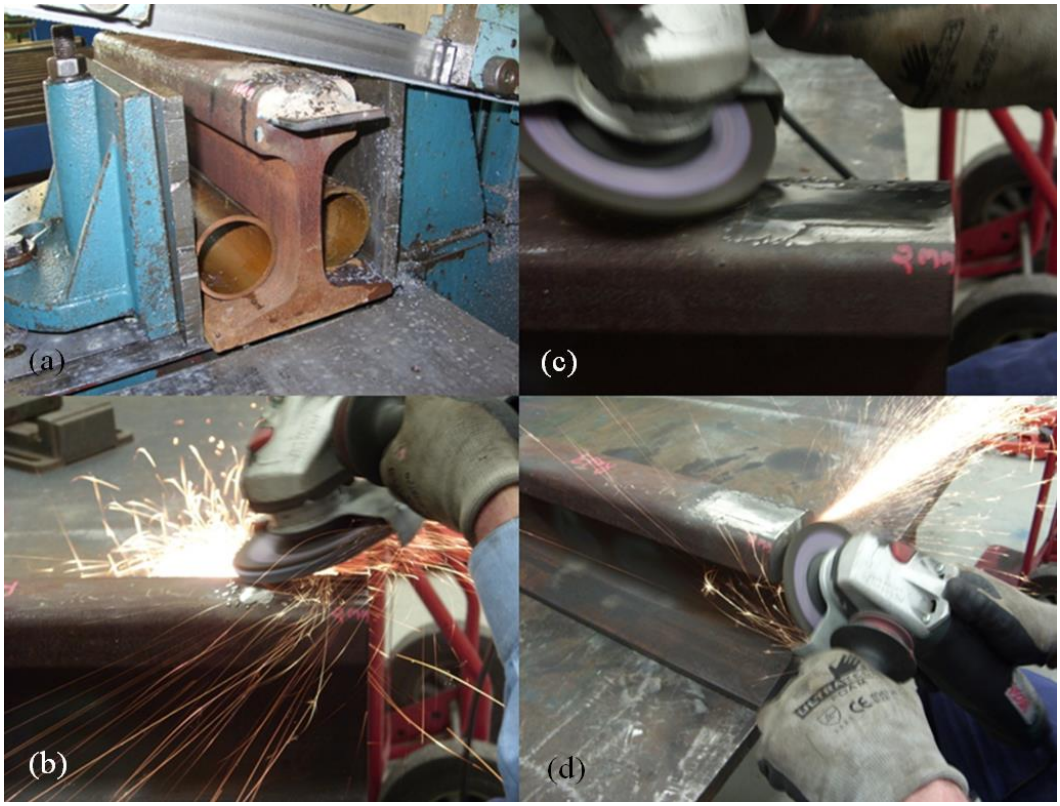

Figure 4-5 (a) Hacksaw cut for extra weld run at the rail end (b, c &d) grinding and polishing the rail surface and rail end

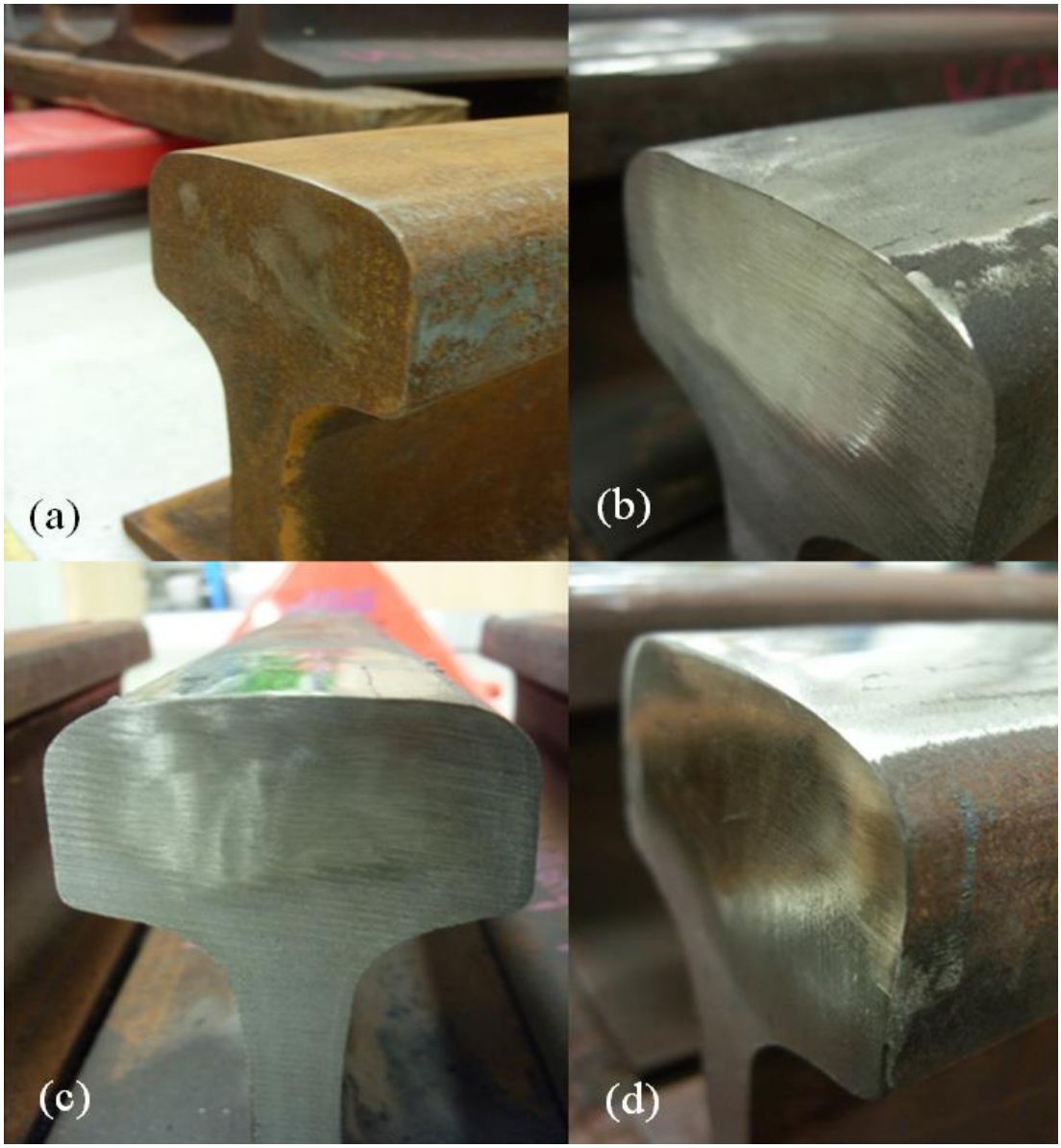

Figure 4-6 (a) Uncoated rail end (b, c and d) rail surface coated after grinding and polishing

4.3 Ball on disc wears test

Laboratory scale investigations were performed on rail steel and coating materials using a non-lubricated ball-on-disk wear tester. Both metallographic and wear damage investigations will be presented and compared with the aim of evaluating both the performance of the surface coating and design the surface coated rail ends.

A Ball-on-disc tribometer was used to study the wear rate and frictional behaviour of a wheel–rail contact. This type of tribometer is assembled from a rotating disc and a stationary dead-weight-loaded ball. The sliding velocity is determined by the radius and angular velocity of the disc while the contact pressure is determined by the radius of the spherical tip of the pin and the normal load. The setup used in this study was located in a climate chamber in which the temperature could be varied from (0 to 40°C) and the relative humidity from 20 to 100%. The coefficient of friction was calculated from the constant normal load and the tangential load, which were measured using a load cell.

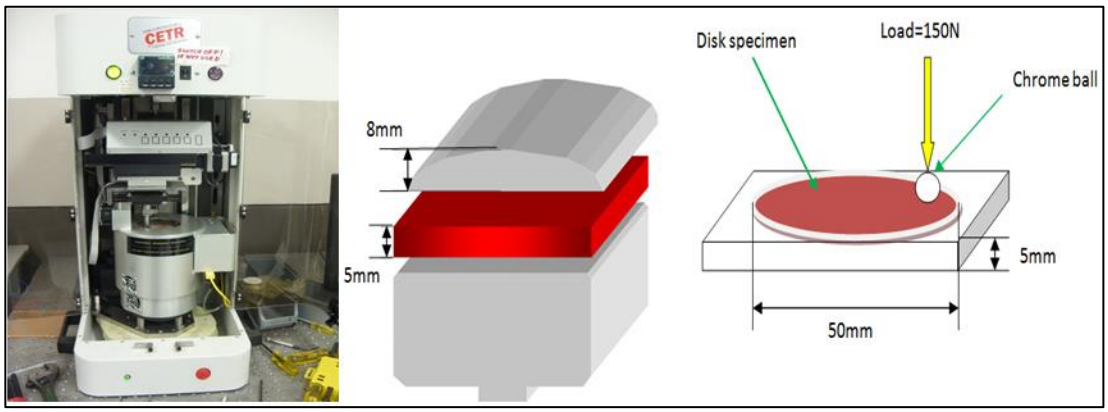

Figure 4-7 Ball on disc instrument setup. Ball-on-disc samples extracted from the rail head and schematic wear test configuration

The ball/pin-on-Disc system setup was selected in this study to carry out the un-lubricated unidirectional sliding wear test. This method involves a ball-shaped upper specimen that slides against a rotating disk as a lower specimen under a prescribed set of conditions. The UMT allows for monitoring during the test the actual dynamic normal load, friction force and coefficient of friction, and depth of wear. A schematic of ball-on-Disc system setup is shown in Figure 4-7.The ball specimen used in this work is a common high chrome ball with a diameter of 6.35 mm with a pre-set load as a normal load, pressed onto the disc material to be slid. The samples were,

respectively, mounted and fixed on a disc holder on the specimen table of the rig in each wear test. In the sliding test, which included four rounds from beginning to end, all the balls were pressed against a rotating disk with a pre-set load. The wear test parameters selected were as follows: 44mm/s and 60mm/s for the equivalent unidirectional sliding speeds, 50N and 60N of normal loads, respectively for each round of the whole wear testing. The disks tested were sliding against the static upper balls at a constant speed of 191 rpm in the whole tests. Before each new test, the old ball-shaped pin was replaced with a new one. All the tests were conducted at a room temperature of about 20^{o}C. After the test, worn surfaces were observed using scanning electron microscopy JEOL.

4.4 Full-scale wheel-rail simulation rig test

In this investigation, we compare wear damage to the surfaces of rail ends with and without a secondary metallurgical hard facing surface coating. Full-scale wheel-on-track rail rig testing was performed on rail ends designed for service as 60kg grade freight rail. In addition, laboratory-scale investigations were performed on rail steel and coating materials using a non-lubricated ball-on-disk wear tester. In the case of ball-on-disk testing, the crack formation was induced in the rail steel, and was recognisable after a small number of cycles but not evident in the hard facing material. Both metallographic and wear damage investigations will be presented and compared with the aim of evaluating both the performance of the surface coating and design the surface coated rail ends.

Figure 4-8 Full-scale wheel-on-rail track rail rig set-up

For the tests at CQU, full-scale rail-wheel test rigs were employed while those at the UOW used a ball-on-disc test facility. Full-scale testing is carried in order to understand the deformation in terms of metal flow and damage for resurfaced rails while the small scale is carried out to compare the wear mechanism for three different steels. Although ball on disc tests are not able to mimic the reality of wheel-rail wear condition in complete detail as there is a great variety of different parameters which cannot be reproduced in laboratories, in many cases the lab tests are able to give an indication of the rail performance in track with good accordance to track test results (Clayton and Hill, 1987).

The quantification of Maraging, Hard-facing Steel and railhead steel metal flow in the vicinity of end post is very important in this research. The plastic strain is a good indicator for the railhead metal flow. The strain gauges can be used to measure

strains at the rail end face. However, it has been observed that the strain gauges are deboning close to the railhead due to the higher strains and vibrations. Therefore, it is decided to use optical measurement technique to quantify the rail head strains. In order to cope with the optical measuring technique, half IRJ will be used instead of full IRJ. During the test a series of high-quality photos of rail end surface close to the rail, top are captured.

The following sections of this Chapter describe the welding power supply, the welding consumables, and the weld monitoring system, the welding cell computer control system and various other articles of equipment used for robot welding.

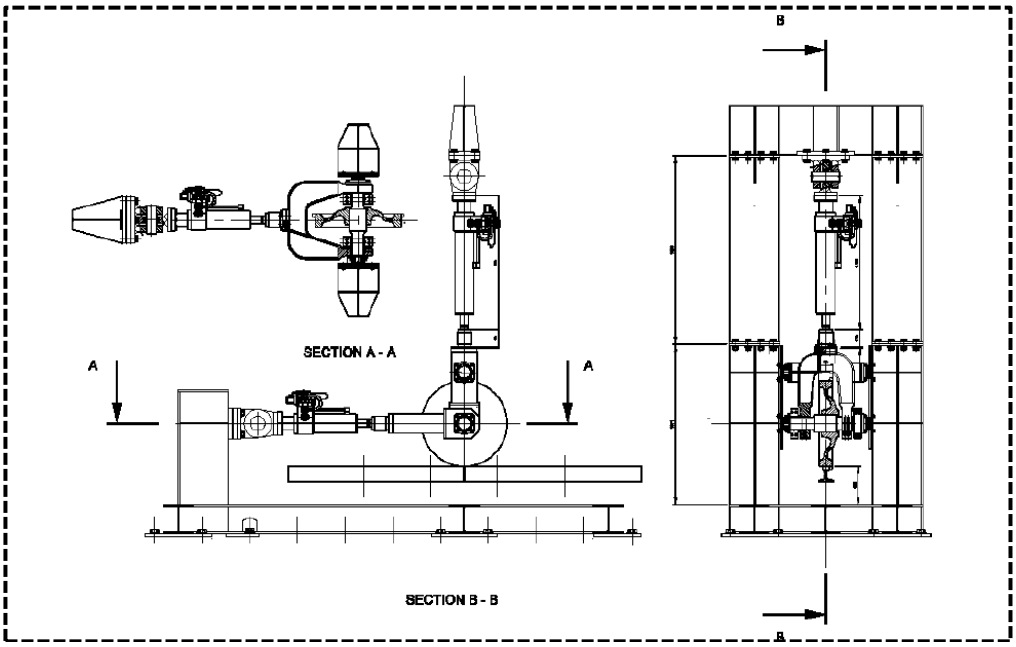

Figure 4-9 Schematic of wheel-on-rail simulation rig, in top, side and front view

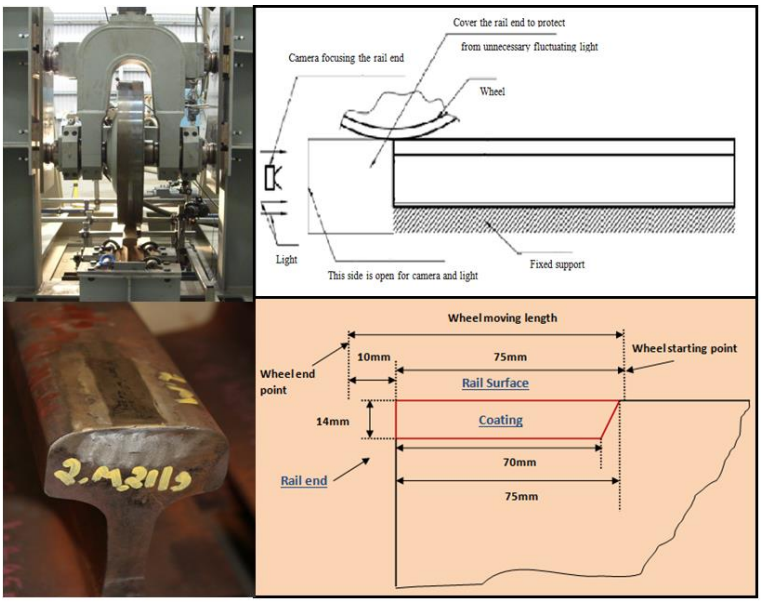

Figure 4-10 (a) front view of wheel-on-rail rig (b) schematic of wheel contact on rail surface (c) run-on wheel patch on rail surface (d) schematic of coating approach to the rail end surface

4.5 Neutron Samples Preparation and Experimental

Three sets of samples were studied for residual stress investigations:

(1) Rail ends obtained from the ex-serviced rails.

(2) Rail ends obtained from the laboratory serviced wheel-on-rail rig test which had undergone controlled amounts of surface plastic deformation.

(3) Samples of ex-service IRJ fishplates

Residual stress measurements were carried out using the Kowari neutron residual stress scanner using 0.1672nm neutron wavelength, Si (400) monochromator at $2\Theta_M = 76^o$. In slices, the experiments were carried out using a gauge volume of $3\times3\times3$ $mm^3$and the Fe (211) reflection with the detector at the Bragg angle $2\theta_B$ of 90^o. The measuring time of 30 secs per point was typical to achieve accuracy of~$5x10^{-5}$μstrains in strain scale and it was short enough to allow detailed stress mapping with a large number of mesh points, 400 for L-slice and 355 for T-slices.

4.5.1 Rail ends obtained from the ex-serviced rails

Rail heads were analysed using the dedicated neutron residual stress diffractometer Kowari at the Australian Nuclear Science and Technology Organisation (ANSTO). In the current investigation, two IRJs with different rail service histories and accumulated damage were selected from the Queensland (Australia) heavy haul track service line. In addition, an unused IRJ fabricated from standard head hardened pearlitic steel track, was employed as a reference sample in order to differentiate the stresses developed during rail manufacturing and those developed during rail service.

The end rail samples used for residual stress investigations are comprised of 400mm lengths of head-hardened rail, obtained from disassembled 6-bolt square ended insulated rail joints. Three IRJs used are described as being in 'as-manufactured', condition, 'partly damaged' and 'badly damaged', the latter having enough damage on inspection to require immediate removal from the Australian heavy haul rail track system. The 60 kg grade medium carbon rail steel is designated by Australian standard AS1085.12, with carbon content 0.65-0.82 wt%.

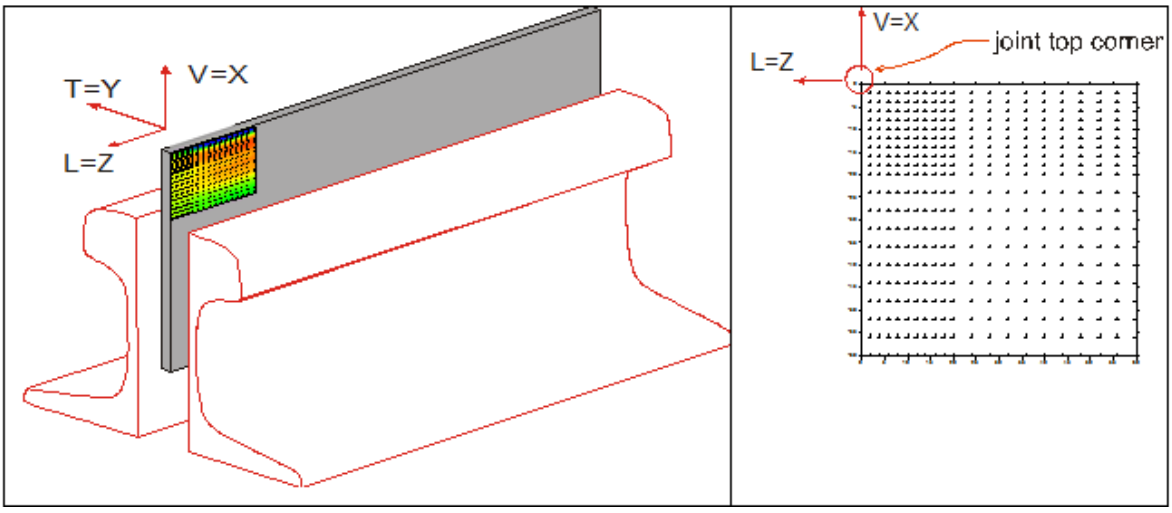

Figure 4-11 Schematics of sample section for neutron diffraction analysis longitudinal (L-Slice)

Measurements were made from intact rail ends in the transverse (T) and longitudinal (L) directions at depths of 2, 4 and 6 mm from the top rail surfaces adjoining the rail ends. After that, 5mm thick slices were cut using electric discharge machining (EDM): transverse slices were cut from the middle part of the rail section while longitudinal slices were taken from ends of the rail section, as shown in Fig.4.

Sectioned and polished samples were also examined using standard methods of reflected light microscopy, micro hardness measurements (Leco Device) and secondary electron imaging (JEOL JSM 2001F instrument). Micro hardness measurements were carried out along running surface of the rail head and across the gauge corner to access the extent of compressive stress shown in the transverse residual maps. A test load of 500g was selected, to measure the hardness distribution in the in-depth direction to about 20mm below the rail surface and at the gauge corner of the rail.

4.5.2 Rail ends obtained from the laboratory serviced wheel-on-rail rig test

In this investigation, residual stress measurements were obtained from rail-ends which had undergone controlled amounts of surface plastic deformation using a full-scale wheel-on-track simulation test rig.

Rail ends of the same steel type as above, which had undergone controlled amounts of surface plastic deformation, using cyclic wheel-on-track simulation test rig illustrated in Figure 4-12. This testing regime was carried out to investigate railhead material failure mechanisms that might occur under dynamic wheel-rail rolling contact load environment.

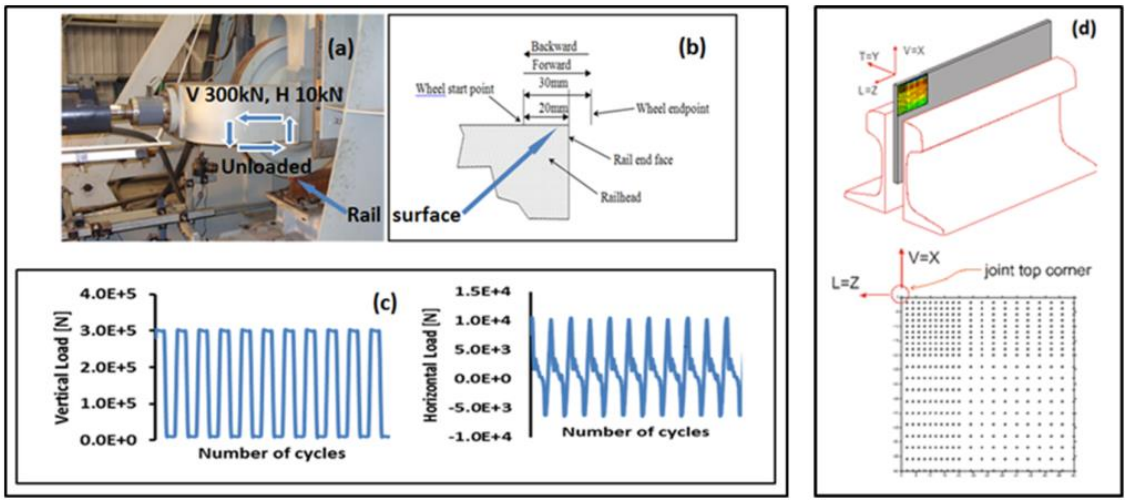

Figure 4-12 (a) Laboratory wheel-on-rail simulation rig (b) schematic diagram of wheel movement (c) In general, load-cycle plot for the rail sample carried out for both 600cycles and 1000 cycles using cyclic wheel-on-track simulation test rig (d) schematic of L-slice

The rail ends used are denoted as being in ‘as-manufactured’, condition, ‘low-cycle damaged’ and ‘high-cycle damaged’ rail end. Deformation employed a vertical wheel load of 300kN and 10kN in the horizontal direction. Load cycle data are displayed in Figure 4-12(c) which shows Load cycle data for Vertical Load (left) and Horizontal Load (right). The 300kN vertical and 10kN horizontal load was applied throughout the forward movement of the wheel stroke as it passed the free end Figure 4-12(a & b), the wheel then being unloaded and returned to the stroke start position.

Same experimental strategy as described in section 1 of this Chapter is used to investigate the residual stresses. As the rail surface has deformation only in the crown region of the rail head, which has obtained from controlled wheel-on-rail rig test. For this case, measurements are carried out in the central line of the rail head. By doing measurements in the central line, we assume symmetry of the stress and

only 3 principle directions can be measured for the full characterization of the stress tensor.

The target accuracy of strain (or d-spacing) determination is $0.7\text{-}0.9 \times 10^{-4}$ and should be sufficient for determining stress values with accuracy ±30 MPa.

4.5.3 Samples from Fish-plates

The fish-plates and track web sections were selected from the standard 4-bolt IRJs, both damaged ex-service and laboratory full-scale rig test rail joint samples. Lengths of the fishplates and track sections were 400mm, the IRJs were of type; AS1085.2 (Australian standard) with a 550MPa ultimate tensile strength for rail and 540-700MPa for fishplate bar. The thickness of the track web was 17 mm and the thickness of the fishplate 40 mm. If used as both 17 mm and 40 mm thickness would slow down or prevent efficient neutron stress measurements. Therefore, to accelerate measurements, 5 mm slices were cut using EDM, reducing individual measurement times and allowing high-resolution mapping with many measurement points around one hole. The reduction is not expected to have changed stress distributions significantly since the stress state was close to zero plane stress. Residual stress measurements for fishplates are carried out with the same instrument and strategy as explained earlier.

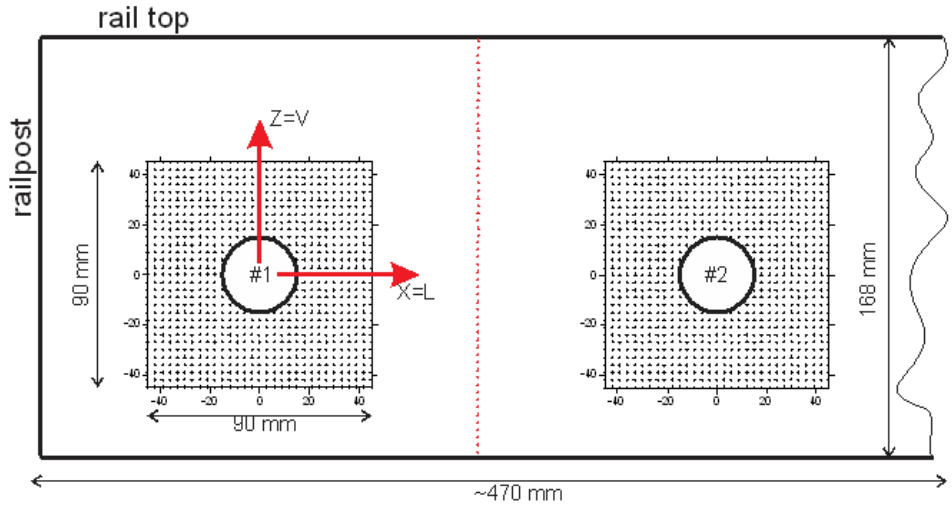

Figure 4-13 Schematic of sample geometry and mesh, left hole corresponds to Hole #1 near to rail end and right hole to Hole#2

Four directions were measured (longitudinal, transverse, vertical and shear) with an accuracy of 10MPa for approximately 870 mesh points as shown in Figure 6, and d0 were reconstructed using the σyy=0 condition.

5 MICROSTRUCTURAL CHARACTERISATION OF RAILHEAD DAMAGE IN INSULATED RAIL JOINTS

The first section of this Chapter is dedicated to coated rail approach to improvement of IRJ lifetimes, a comparison result of the uncoated and coated rail head damage samples are presented, starting with the changes in the rail head microstructure and hardness. The second section is dedicated to the development of improved coating design and selection of candidate material.

5.1 A coated rail approach to improvement of IRJ

In this part of the work the degradation mechanisms in two different angled cut IRJs, were investigated. One sample was made from head hardened rail and deemed to be a failed joint due to metal flow, and the second was a surface coated joint removed from service after the same period of operation under heavy haul rail traffic. Hereafter, the uncoated rail and the grade 431 martensitic stainless steel laser coated rail will be designated as Rail U and Rail C respectively. Both the coated and uncoated angle cut, 6-bolt, IRJs were fabricated from Australian standard 60 kg grade head-hardened steel. The test piece for surface coating with MSS was prepared by machining a “bathtub” shape into the head of the rail and then powder laser depositing of a 431 Martensitic Stainless Steel (MSS), as shown in Figure 5-1.

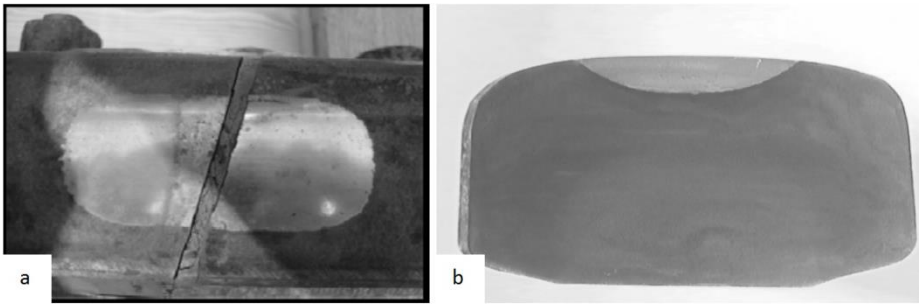

Figure 5-1 Martensitic stainless steel IRJ, (a) top view of ex-service IRJ fabricated with a 15-degree angle cut, (b) section showing bathtub shape of metal deposit.

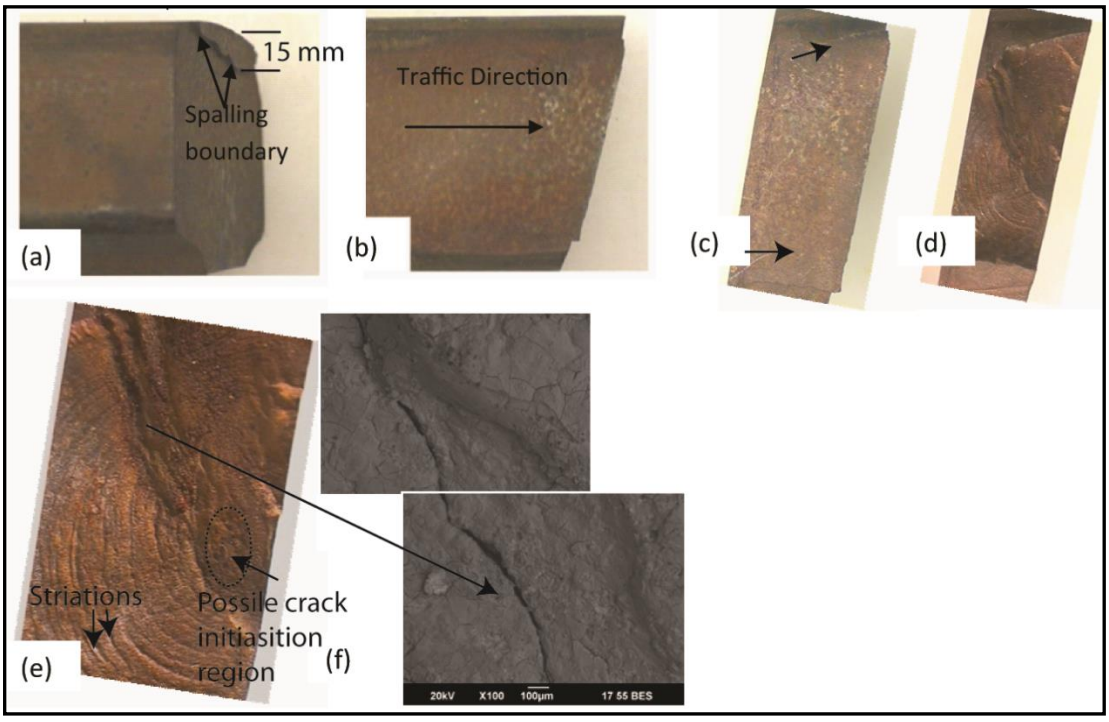

Figure 5-2 Head hardened rail - Damaged rail end with both spalling and metal flow. (a) side view, (b) top view, (c) top view of squat before removal showing crack directions (d) same region as (c) after removal of surface squat and (e) high mag suspected region.

5.2 Uncoated Raul (Rail U)

The rail ends of the failed uncoated joint showed severe deformation in the head hardened region, near the top rail surface, with microstructural evidence of both metal flow over the rail ends metal fracture, and in-service related fatigue mechanisms consistent with rolling contact fatigue. Macro metallographic results obtained from one rail end are described in Figure 5-2, which includes (a) side-on

and (b) top views of the damage rail end. The direction of travel of the rail traffic was in the direction of the metal flow. Top surface cracks in the feature protruding around 2 mm over the rail end are revealed in Figure 5-2 (c) and the whole feature was easily removed from the rail head ((compare Figure 5-2 (c) and (d)).

Collected evidence suggests strongly that a sub-surface-initiated crack propagated by rolling contact fatigue mechanism that has led to spalling of the hard surface of the head hardened. Beach/striation marks are evident on the fracture surface (Figure 5-2 (e)) which is attributed to the repeated rolling-sliding contact loading. Due to the uniformity of loading beach marks are fairly similarly spaced and fairly uniform in appearance. Fatigue failures occur due to high cyclic loading which initiates the crack and propagates until a stress much lower than that necessary to cause a fracture. The region inside the oval box contains the initial beach marks (the smallest elliptical features) and this is believed to be where the cracking has initiated. SEM-EDS investigations of regions below the rail surface (not shown) revealed inclusions including MnS which are likely sites for crack initiation.

5.3 Coated Rail (Rail C)

Damage to the IRJ ends of the stainless coated samples (Figure 5-3) was significantly different to that of the head-hardened rail. Plastic deformation of the top surface of the centre of the rail was less, consistent with expected mechanical property advantages of martensitic stainless steel over medium carbon rail steel (hardness, toughness, flow stress). However, there was notable plastic deformation in the coated sample in the vicinity of the interfaces between the rail steel and coating near at the top surface of the coating (Figure 5-3(a) – (c)). This, in part, could be related to mismatches in metal flow, being greater for the rail steel than for the

stainless steel. The type of cracking differed on each side of the track, with more oblique crack growth (Figure 5-3 (c)) on the gauge (wheel) side (wheel side) than near the field side. One approach to mitigating the problems near the top rail surfaces might be via re-design of the shape of the coating profile. The shallow angle of between the stainless steel rail steel interface and the top surface of the rail (<30 degrees) could be changed to a much steeper angle (near 90 degrees) to reduce the component of shear stresses acting on the interface.

Examination of both transverse sections (Figure 5-3 (d)) and longitudinal sections (not shown) located well below the top rail surface revealed cracks originating in regions of weld porosity and defects in the vicinity of the interface between the rail steel and the coating Figure 5-3 (d) & (e).

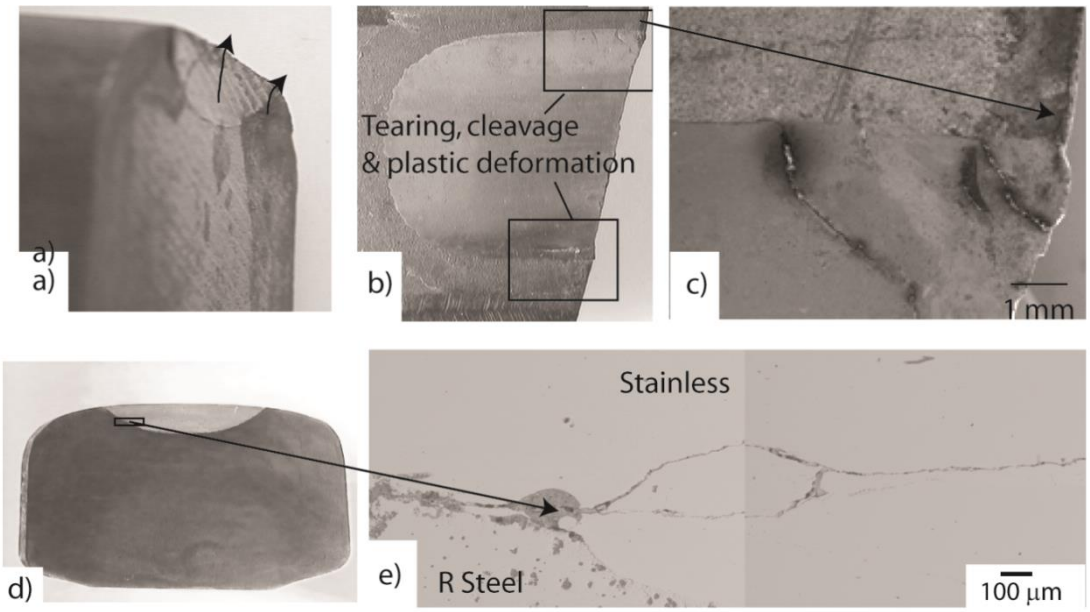

Figure 5-3 Laser surface coated rail – (a) rail end (b) top view, (c) SEM image of metal flow at rail end on wheel side of track (d) polished section 10 mm back from the rail end, (e) SEM image of void formation at interface between stainless and rail steel

Cracks associated with inclusions in the rail steel and in regions in the vicinity of the stainless steel rail steel interface were also observed but are not shown. It is

expected that complex residual stresses originating from the mismatches in thermal expansion coefficient of the two different types of steel contribute to the problem of interface cracking, crack initiation and crack growth both before and during service life. Based on these results, apart from the void formation, major issues to deal with during the initial laser cladding process include the management of defects initiated in the heat affected zone of the rail steel and the formation of Cr-rich precipitates on the interface.

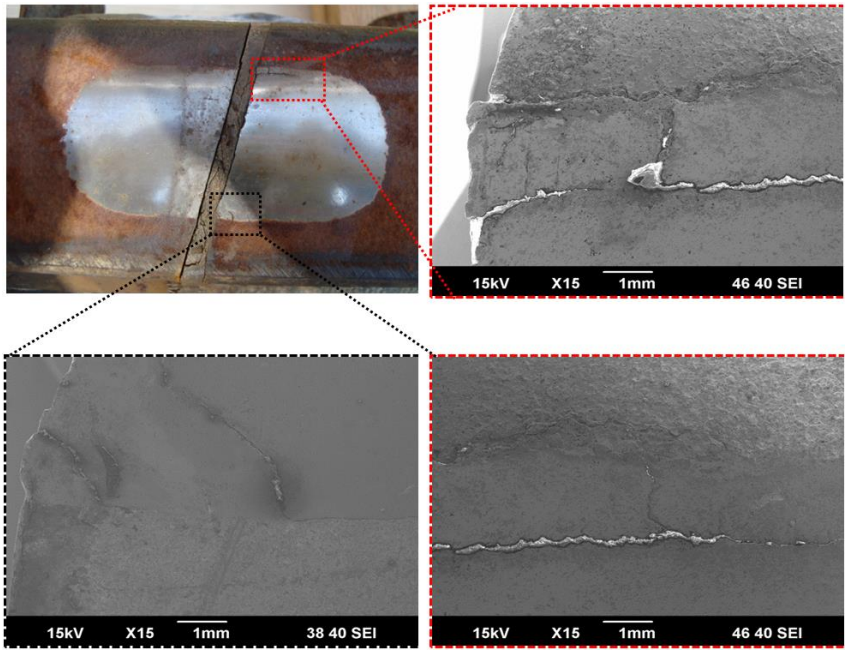

Figure 5-4 Cracks formation around the edges of the weld interfaces.

5.4 Hardness

Transverse cross-sections of the head hardened rail and weld inlay rail samples were examined with data obtained from the rail surfaces going down into the rail head. For a position around 10 cm back from the rail end the uncoated head hardened rail had a mean microhardness of; 430HV (500g), 350HV (500g), 267HV (500g) 1mm below the top surface, in the subsurface, and in regions below the head hardened surface, respectively.

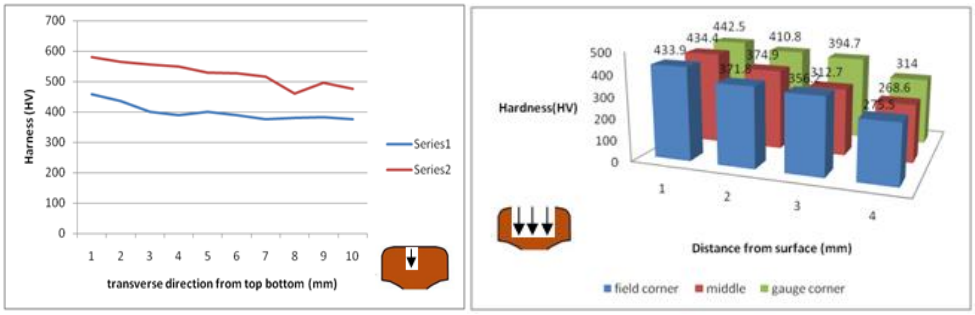

Figure 5-5 Surface hardness profiles for coated and uncoated head hardened rail for the first 10mm below the top surfaces and around 10 mm back from the rail ends.

There were in accordance with typical values for this grade of head-hardened rail. Trends in microhardness profiles close to the top surfaces of both samples, from the centre of rail head to a depth, of 10 mm, are shown in Figure 5-5. Factors contributing to these results include; (i) the higher hardness of the martensitic stainless steel over the rail steel, (ii) changes in head hardness of the head-hardened steel as a function of depth and (iii) surface strain hardening effects associated with deformation during service life.

5.5 Microhardness results

Both deformed rail samples exhibited similar hardness profile trends from the top surface down in the T-sections Figure 5-6 while the unused rail sample exhibited little variation in hardness values across the measuring line. The maximum hardness value of 490HV was found near the running surface while ~ 6 mm below the surface the hardness value changed to ~360HV, slightly higher than the bulk/unused rail hardness which falls in a range of 260-290HV. Hardness results obtained from longitudinal sections from the top down showed similar trends with lower values further away from the rail ends.

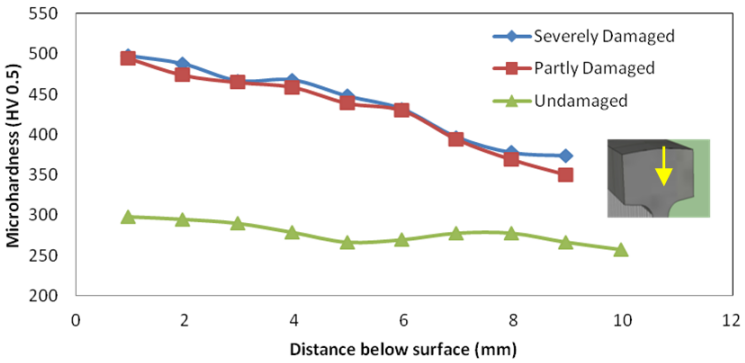

Figure 5-6 Micro hardness profiles as functions of depth below the surface near the rail end.

5.6 Summary and discussion

The interpretation of the latter requires data concerning complex stress and strain distributions in the railhead at and just below the rail surfaces at the rail ends. Because the rail end is free these will differ significantly from that occurring in the bulk rail. A series of experiments is currently underway using neutron diffraction to measure strain distributions in the immediate vicinity of IRJ rail ends. Further SEM-EBSD and advanced electron microscopy will be required to relate this to microstructure and properties. Alternative coating materials are also under investigation.

Compared to head-hardened rail, the laser coated IRJ suffered less damage for the same heavy haul lifecycle, apparently due to the superior mechanical properties of martensitic stainless steel over medium carbon rail steel. Damage to the IRJ ends of the laser coated samples was characterized by:

(i) Surface damage related to mismatches in metal flow of the two steel types, greater for the rail steel than the martensitic stainless and accentuated by the shallow angle of the interface to the rail surface and, (ii) Cracking associated with the laser

deposition procedure; the mismatch in thermal expansion properties of the two steel types, void formation during fabrication, defects and weakening of the heat-affected zone of the base steel.

5.7 Grounds for Follow-up investigations

Based on this initial investigation, two approaches were considered likely improve on the properties of a coated or hard-faced IRJ. These are (i) a simple redesign of the shape and position of the hard facing region in to reduce surface deformation mismatches during service and (ii) selection of a weld deposit material of compatibility of thermal expansion properties.

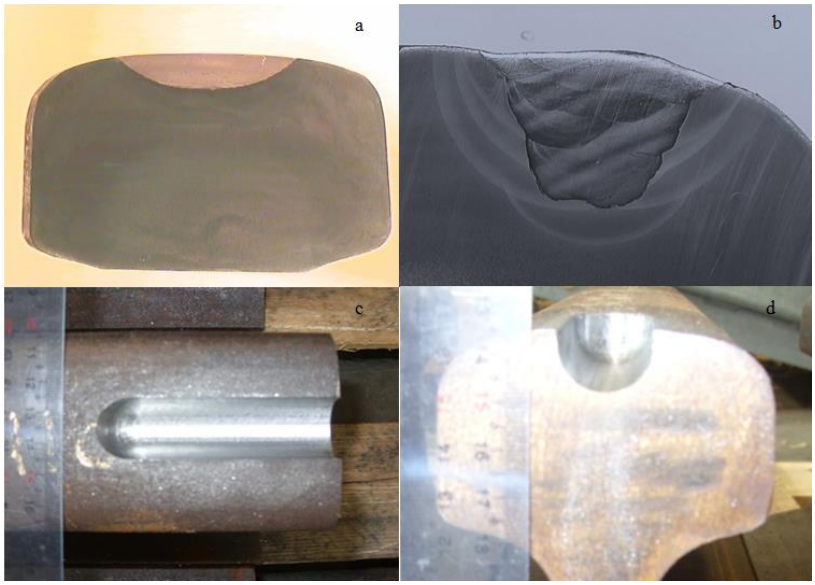

Figure 5-7 Different Weld profiles on the rail head surface; (a) profile for Martensitic stainless steel coating, (b) maraging steel weld deposit in a shallow groove, (c, d) redesigned bathtub groove on the rail head.

The weld test samples were prepared by machining a “bathtub” of set dimensions into the head of the rail and then weld deposition of maraging steel and hard facing steel was carried out. Photographs of the rail weld samples are shown in Figure 5-7, showing the location where the rail samples were sectioned to create a bathtub shape

groove. Transverse cross-section highlighting 431stainless steel weld inlays shown in Figure 5-7a were received from Jarvie Engineering, Australia.

5.7.1 Morphology of worn surfaces

The worn surfaces of three different steels were examined by scanning electron microscopy. The details of the worn surface morphology can be seen in the SEM images as shown in Figure 5-8 , which displays SEM micrographs of wore surfaces

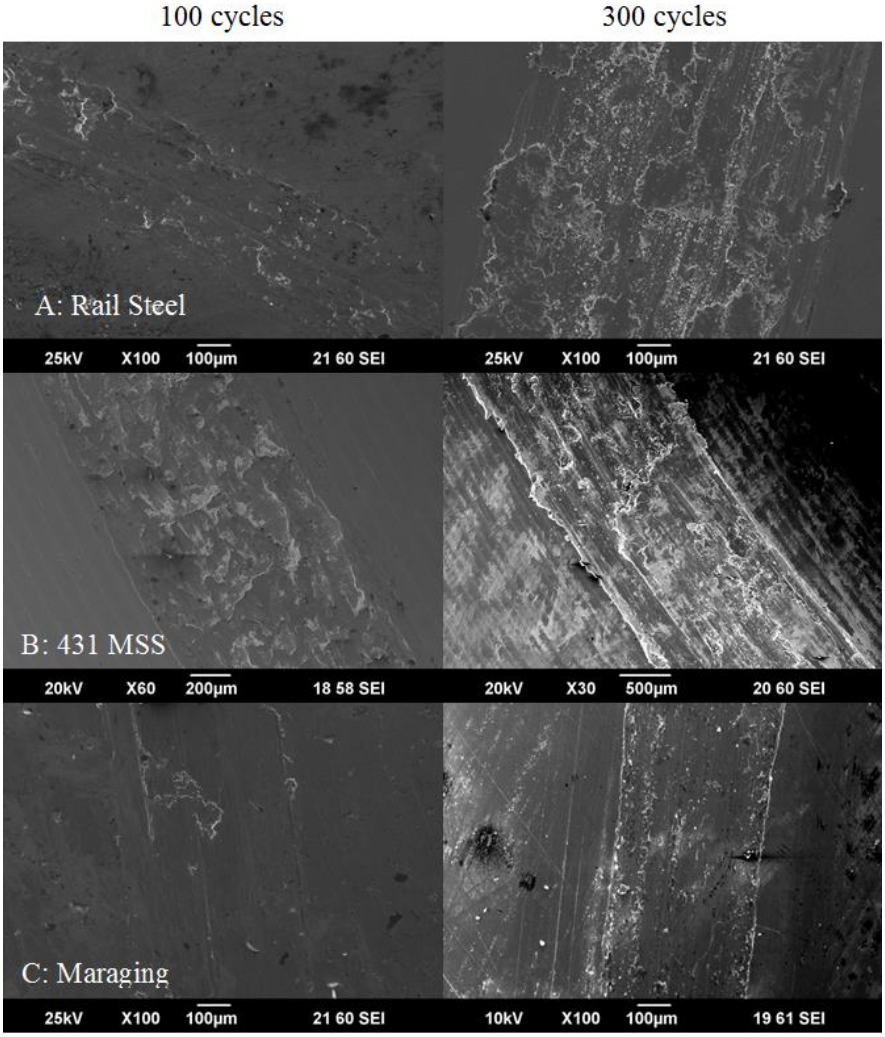

Figure 5-8 SEM micrographs of worn surface of (a) rail samples (b) martensitic stainless steel samples (c) maraging steel specimens undergone for two wear cycles

on rail steel at contact load of 60N for test speeds of 44 mm/s and 60 mm/s. Smooth wear track is found in the maraging sample with a few shear marks and small peel off regimes visible but substantial difference in wear track can be seen for rail steel at higher speed with a considerable adhesive wear and spalling off regimes. This could be attributable to the development of the oxide layer on the surface during the wear testing. It has been reported that the Fe_2O_3 oxide forms easily on the pearlitic steel (rail steel).

5.7.2 Wear response

Figure 5.9 presents a comparison of the coefficient of friction of rail steel (A), martensitic stainless steel (i) and maraging steel (a), under different unidirectional sliding wear parameters. Sliding under a normal load of 50N and 60N reached a COF value of 0.8 for martensitic stainless steel, which has a maximum among the three steel samples as shown in Figure 5-9 (ii).

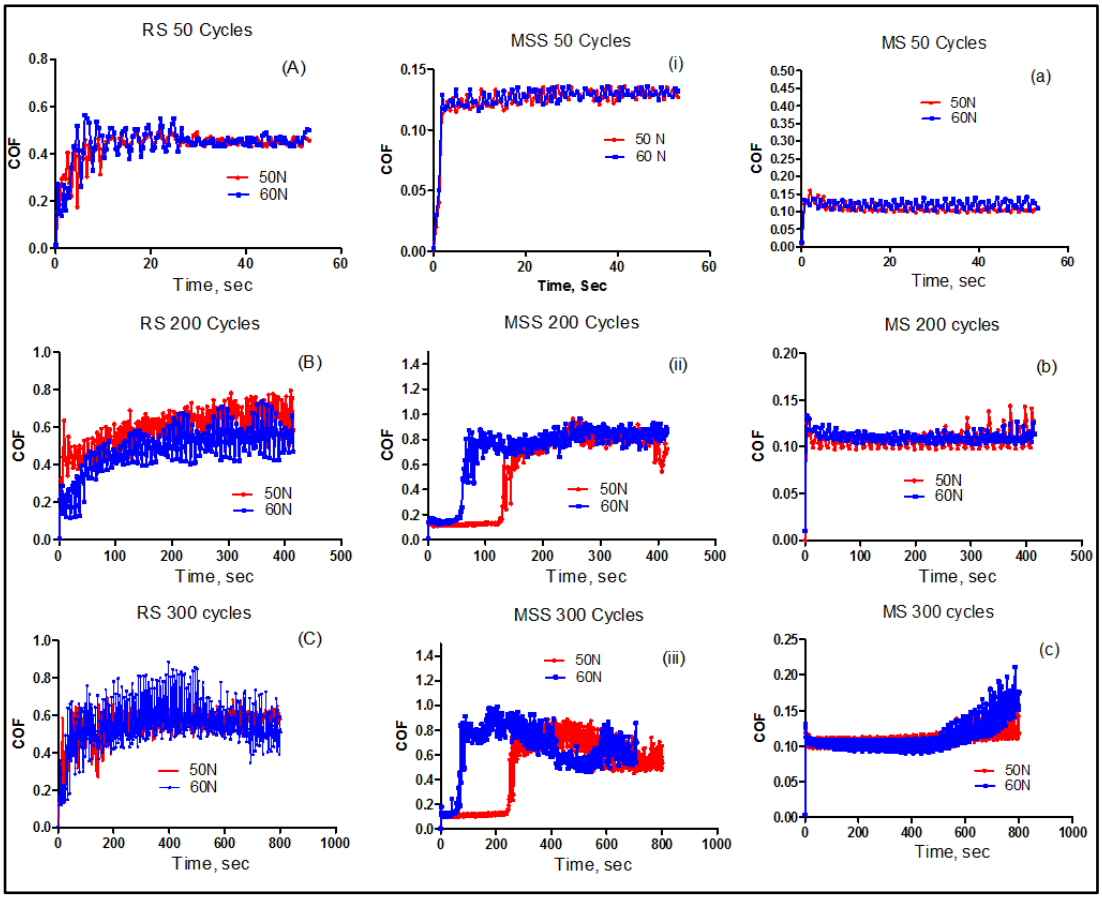

Figure 5-9 Coefficient of friction graph showing sliding friction coefficient vs sliding time for different cycle of wear test run (A, B, C) pearlitic rail steel (I, II, III) martensitic stainless steel (a,b,c) Maraging steel

The followers are around 0.6 and 0.5 COF value for rail steel as shown in Figure 5-9(A, B & C). When it comes to maraging steel, the COF value is from 0.10µm and remains constant throughout the completion of the test, expect for 300cycles the curve shows a slight increase after a period of wear period.

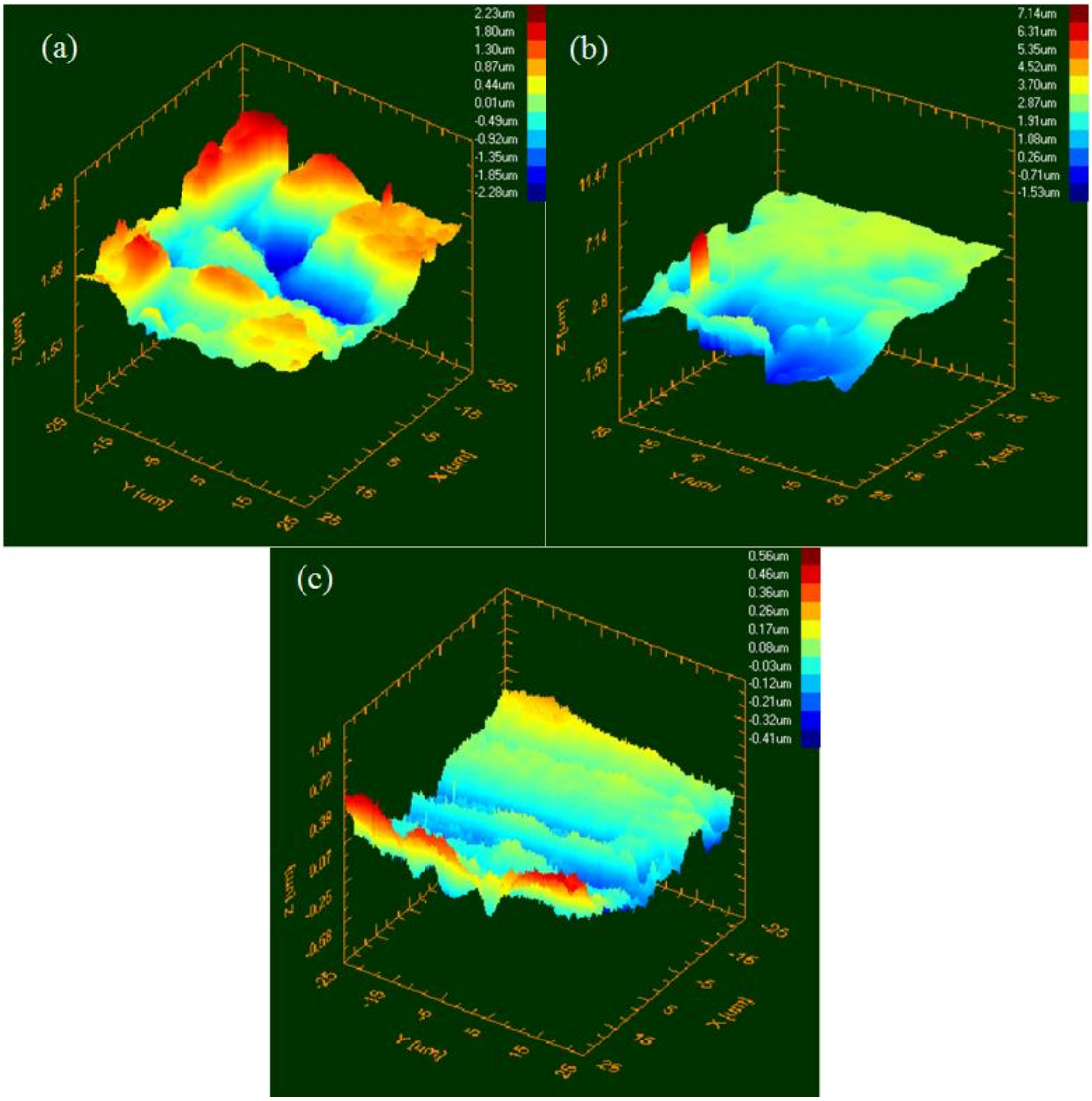

Figure 5-10 Surface roughness on the worn tracks of (a) pearlitic rail steel (b) maraging steel (c) martensitic stainless steel

Wear tracks profiles were measured using a surface Profilometer as shown in Figure 5-10. For rail steel, the surface profile shows a big surface variation with more bumps up and a few shallow groves on the wear track with an average wear track depth of 1.25μm. Track profile for stainless steel and maraging steel has minimum ups and grooves with an average wear track depth of 2.5μm and 0.20μm, respectively.

5.8 Conclusions and discussion

This research was concerned with the vicinity of rail ends and bolted connections in insulated rail joints and was performed in order to better understand the IRJ behaviour and failure mechanisms and to develop approaches to increasing IRJ lifetimes. Apart from track ballast work, IRJ inspection, maintenance, repair and replacement comprises the highest cost component maintenance of track work, and even modest improvements in IRJ lifetimes have the potential to provide significant cost savings to the rail industry. In this subsection and later in Chapter 7, conclusions are presented and recommendations for future research are discussed.

Conclusions are thus drawn from the respective Chapters in an orderly manner.

5.8.1 Initial comparison of ex-service head hardened Rail and ex-service Laser clad IRJs

Damage to the ex-service head hardened rail IRJ ends was characterized by metal flow, RCF, and microstructural features including spalling and cracking.

Compared to head-hardened rail, the laser coated IRJ suffered less damage for the same heavy haul lifecycle. This improvement was apparently due to the improved mechanical properties of the martensitic stainless steel cladding (hard facing) over that of head hardened medium carbon rail steel.

The 431 MSS clad sample was found to have a higher fatigue life cycle than the non-clad sample in this study. This initial result demonstrated the feasibility of rail surface cladding in the vicinity of rail joints to help in prolonging the service life of IRJs.

Damage to the laser clad IRJ ends was characterized by Surface damage related to mismatches in metal flow of the two steel types, greater for the rail steel than the martensitic stainless and accentuated by the shallow angle of the interface to the rail surface and,

Cracking associated with the laser deposition procedure; the mismatch in thermal expansion properties of the two steel types, void formation during fabrication, defects and weakening of the heat-affected zone of the base steel.

Two approaches might be considered to improve the properties of the coated IRJ; redesigning the shape and position of the hard facing region to reduce surface deformation mismatches during service and selection of a weld deposit material of compatibility of thermal expansion properties.

Design problems with the laser clad IRJs were identified as;

(i) the poor geometry of the cladding profile, with a shallow angle of the cladding profile promoting cracking at the rail surface/cladding interface and

(ii) Selection of a cladding material with different thermal expansion properties to that of the head-hardened rail.

5.8.2 Improved hard-facing design approaches and new hard-facing trials

On the basis of the identified design problems in the laser clad samples, two approaches were arrived at to improve the design of cladded IRJs:(i) redesigning the shape of the hard facing alloy profile so that the rail/hard-facing interface near perpendicular to the rail surface. This would minimise reduce deformation mismatches during service and (ii) selection of a weld deposit material of improved compatibility of thermal expansion properties with those of the base rail. In addition,

the approach of hard-facing by weld deposition was arrived at as a simple and practical approach to the cladding of IRJ rail ends.

5.8.2.1 Surface hard-facing experiments by weld deposition

Preliminary trail using surface deposition by stick welding of maraging weld inlays revealed an acceptable coating quality. Typical defects commonly associated with stick welding procedures were identified by ultrasonic and metallographic examination to be local regions of lack of fusion and porosity. These defects were minor and should have a very low deleteriously effect and it may affect the performance of the weld deposit during the rail service.

5.8.2.2 Follow-up trials of bathtub shaped claddings using MMAW (Maraging steel cladding) and GMAW (Commercial hard-facing steel)

Two different materials were used for MMAW and GMAW cladding the rail end samples to investigate the effect of cladding on the rolling contact fatigue properties of the clad samples. Samples were investigated by metallography, wear testing. GMAW clad rail samples were also investigated using a Simulated Wheel on Track Rig test. Commercially available hard facing steel was selected because of evidence of success in other active rail repair applications for worn railway components such as; switch blades, crossings, and bends. Maraging steel used because of its low thermal mismatch with pearlitic rail steel which has high mechanical properties and low carbon content.

5.8.3 Conclusions of Improved hard-facing design approaches and new hard-facing trials

Maraging steel deposited by stick weld deposition is a suitable material for application as a cladding material in the vicinity of the rail ends provided that the suitable cladding methods, cladding parameters, preheat and post-clad heat treatment is employed.

6 RESIDUAL STRESSES IN RAIL-ENDS FROM THE IN-SERVICE INSULATED RAIL JOINTS USING NEUTRON DIFFRACTION

Residual stresses often are crucial to the lifetime of components (Withers, 2007). Here, residual stress analyses were conducted on several rail joint samples both on serviced and laboratory test rail samples. The residual stresses were determined both in longitudinal and transverse direction across the sample surface and at certain distances to the sample surface.

6.1 Microstructures of damaged rail samples

Figure 6-1 shows representative reflected light and SEM micrographs Figure 6-2 of damaged rail samples. There was no evidence of white etching layer formation, but plastically deformed layers of depths ~25 μm and 60 μm below the running surface could be seen for the moderately deformed (Figure 6-1 (a)) and severely deformed (Figure 6-1 (b)) samples respectively. Below the deformed regions the bulk microstructures appeared free from any significant deformation.

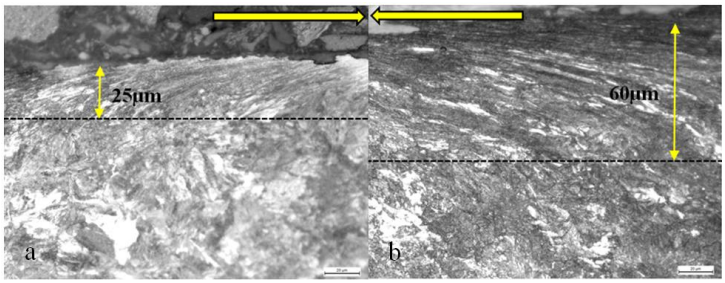

Figure 6-1 Optical images of (a) moderately deformed rail and (b) severely deformed rail ends

6.2 Microstructure

Scanning electron microscopy Figure 6-2 revealed deformation of the cementite lamellae and reorientation towards the direction of traffic movement. As indicated in Figure 6-2(c & d), features including lamellae kinking, bending, globularisation and thinning in the rolling direction were evident in the deformed microstructure regions near the rail surfaces. Previous results (Kelleher et al., 2003) reveal that rail head spalling and sub-surface cracks are noticeable within few mm from the rail surface. As discussed in (Rathod et al., 2012, Tillberg et al., 2009) crack originating subsurface regions tend to change direction, mostly either upward towards the rail surface or in some cases downwards. Because of this, the rail head material becomes detached from the surface resulting in spalling, causing failure of the rail.

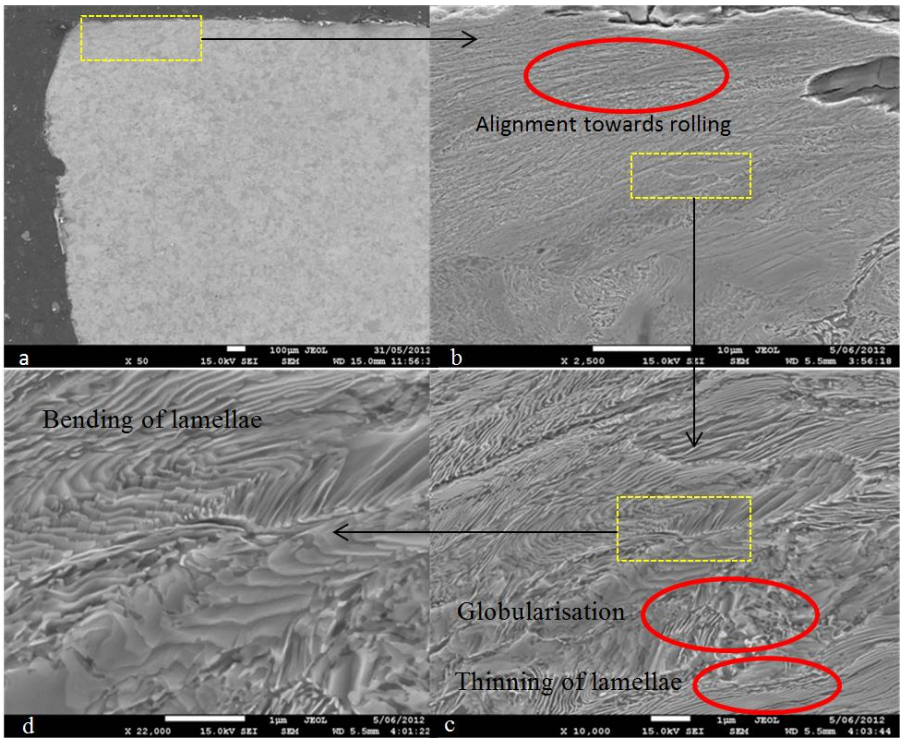

Figure 6-2 SEM images of rail end in longitudinal direction shows evolution of specifically deformed microstructures along the wheel rolling direction

6.3 Residual stress in longitudinal slice

The residual strain was measured in three directions Longitudinal (L), Transverse (T) and Vertical (V), two stresses were constructed in Longitudinal and vertical component and d0 were reconstructed using $\sigma_{yy}=0$ condition.

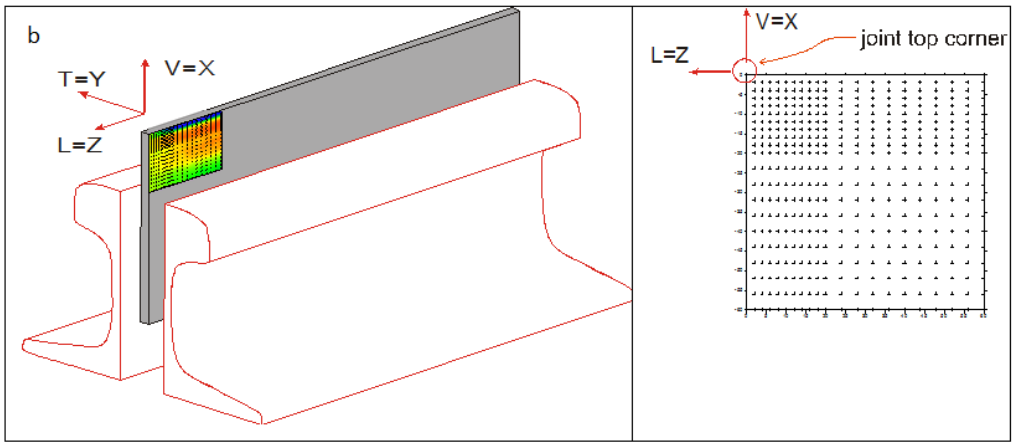

Figure 6-3 Schematics of sample section for neutron diffraction analysis longitudinal (L-Slice).

Evolution of the residual stresses longitudinal component in rail rails of different service history obtained on longitudinal slices. Patch size of 60x60mm^2 was measured, each patch maps top left corner corresponds to the top corner of the end post. In the stress maps, the red areas represent high tensile stress while the blue areas correspond to high compressive stress. In the lattice parameter maps, larger d-spacing are shown in red areas while small d-spacing values are in blue areas. Differential longitudinal stress component maps are obtained by subtracting stress values representing bulk material from the values representing material of IRJ.

For L slices, the stress distributions are dominated by compressive (~ -300 MPa) stresses at the running surface and up to ~5 mm into the rail, which is balanced by tensile stresses (~ 200 MPa) located around 5-15 mm beneath. Both after-service rail samples exhibited similar stress distributions, although these were accentuated for the badly damaged rail.

In the proximity of the rail end, the residual stress distributions and material damage are more and different to the continuous rail because of different loading conditions as wheel reaches the rail end post.

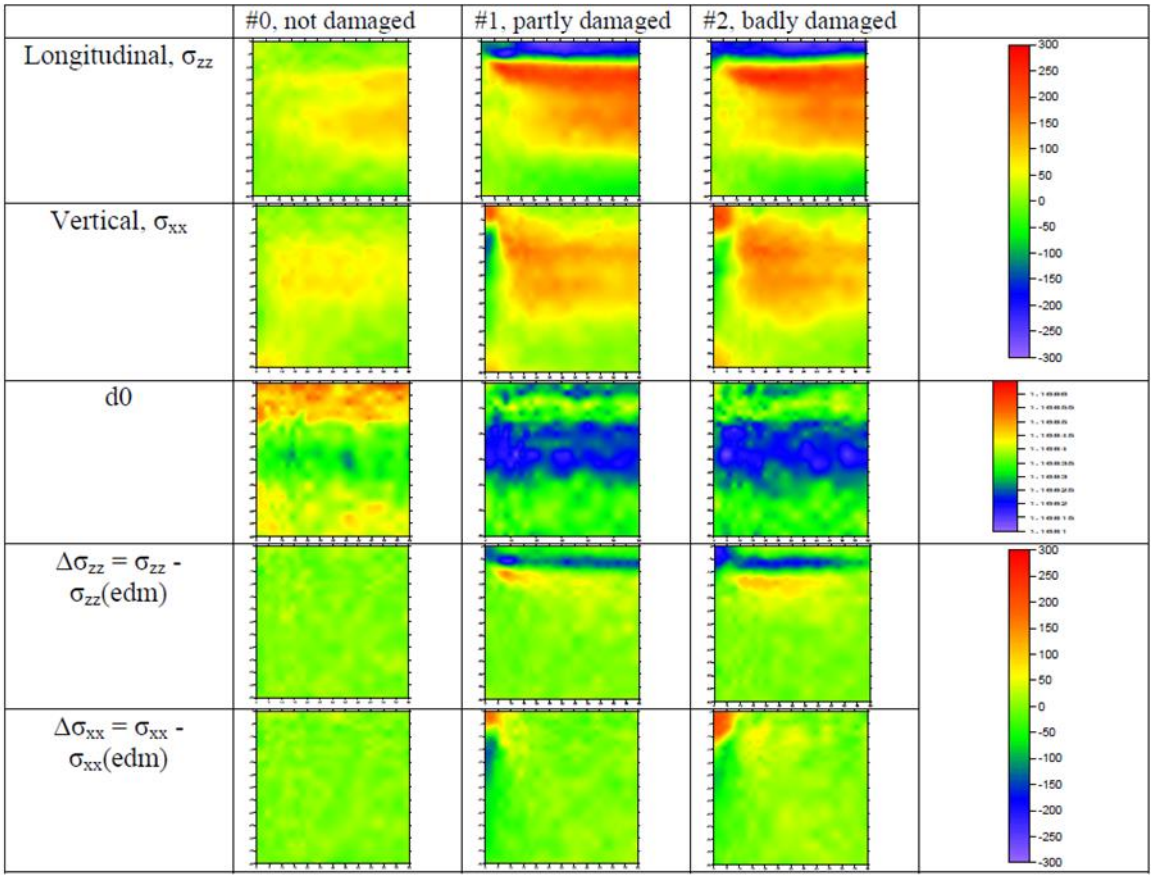

Figure 6-4 2D stress and d0 maps for the L-slices. Compressive forces are blue, tensile forces are red. Square L-slice patch is 60mm in size

6.3.1 Unused rail L-slice

The residual stress distribution from unused rail along the longitudinal direction across the surface of the rail is shown in Figure 6-5. The residual stresses studied in these samples are tensile in nature for both longitudinal and vertical component. In longitudinal component Line d=2 and 4 shows low compressive stresses value which rose during the manufacturing heat treatment and grinding process. On the rail end

surface, the stresses in the longitudinal component of the line d=12 to 20 tend to have low value compared to the value in longitudinal distance from x=0 to 60 mm (where x =horizontal axis) tensile residual stresses increases in a steady way reaching a maximum at x=60 by value 50-75MPa.

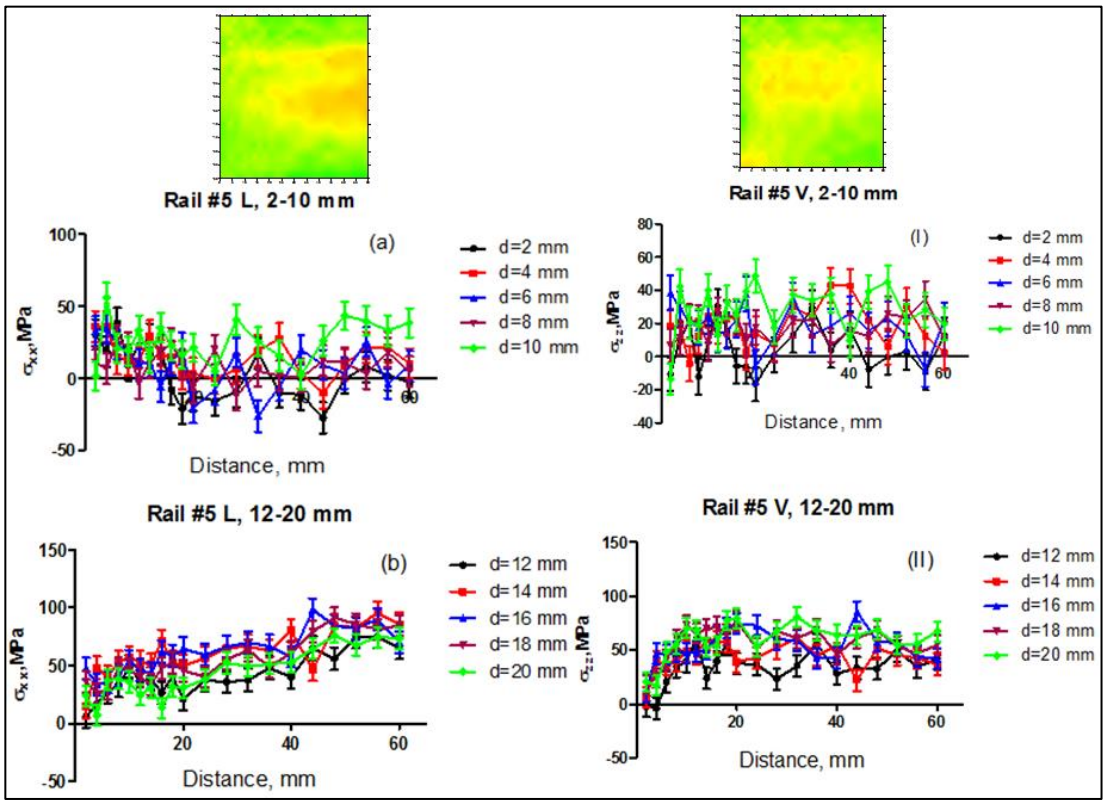

Figure 6-5 Residual stress variation for unused rail sample along the rail length of 60 mm. Measurements point from 2 mm from the rail surface to 20 mm in depth (a & b) – for Longitudinal (I & II) – for Vertical component

Residual stresses in the vertical component show similar trend compared to longitudinal component, with evenly distributed tensile stresses for line d=2 to 10, and increase in stress from line d=12 to 20.

6.3.2 Severely deformed rail L-slice

The residual stresses distribution for severely deformed rail obtained in the longitudinal rail sample is shown in Figure 6-6. The measurement was carried out

from line d=2 to 20mm in-depth for longitudinal distance up to x=60mm from the rail end.

Longitudinal component

In the region between line d=2 to 6, the rail running surface shows evenly distributed compressive stress along the longitudinal running direction ranging from -220MPa to -250MPa creating a valley at distance x=10 mm from the railend where stresses drop to -150MPa to-100MPa.

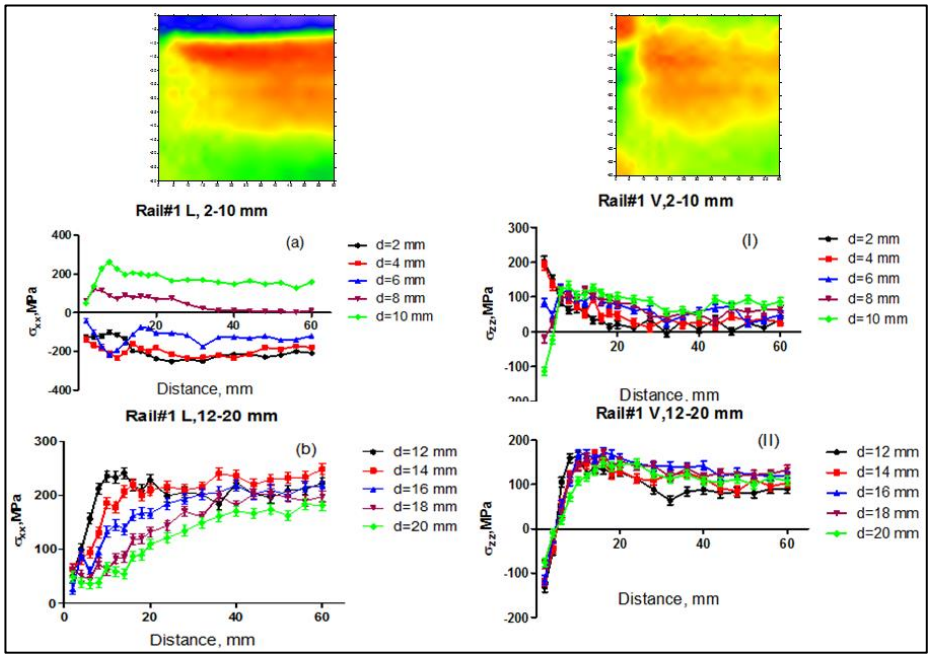

Figure 6-6 Rail #1, severely deformed used rail residual stress variation along the length of 60mm. Measurement points are from 2mm from the rail surface to 20mm in depth. (a& b) for the longitudinal component, (I & II) for the vertical component

For line d=8 and 10, the stresses changes to tensile with reaching a maximum of 280MPa for d=10 at location x= 5 mm from the rail end. For line d=12 to 20, the tensile stresses for all line at location x=2 mm from the rail end have very low stresses of magnitude 50-75MPa. With increasing distance from the rail end, first the tensile residual stresses increase with a strong gradient from 75MPa to 250MPa for a distance of 10 mm from the rail end and tends to remain constant throughout the

running surface. Then the tensile residual stresses tend to decrease with increase in depth from d=12 to d=20.

Vertical component

For the line d=2 to 6, the running surface shows tensile stresses along the longitudinal running direction for the vertical component with a maximum stress magnitude of 200MPa at the rail end. With increasing distance from the rail end, the stress value decreases with a strong gradient reaching a value as low as 25-50MPa for the remaining length of the rail.

For line d=8 to 20, shows the transition from compressive stresses at x=2 mm to tensile stresses at a distance of x=5 mm from the rail end with a gradient of -150MPa to 180MPa, respectively. Then the tensile stresses tend to remain constant stress value throughout the running rail surface.

6.3.3 Partially deformed rail L-slice

The residual stresses distribution for partially deformed rail obtained in the longitudinal rail sample is shown in Figure 6-7. Same measurements are carried out as with the severely damaged rail.

Longitudinal component

Residual stresses show similar stress distribution with a little variation. For line d=2 to 6, shows evenly distributed compressive stress with a maximum value of -250MPa. For location x=2 mm, all line from d=2 to 10 shows compressive stresses which did not occur in the severely deformed rail sample.

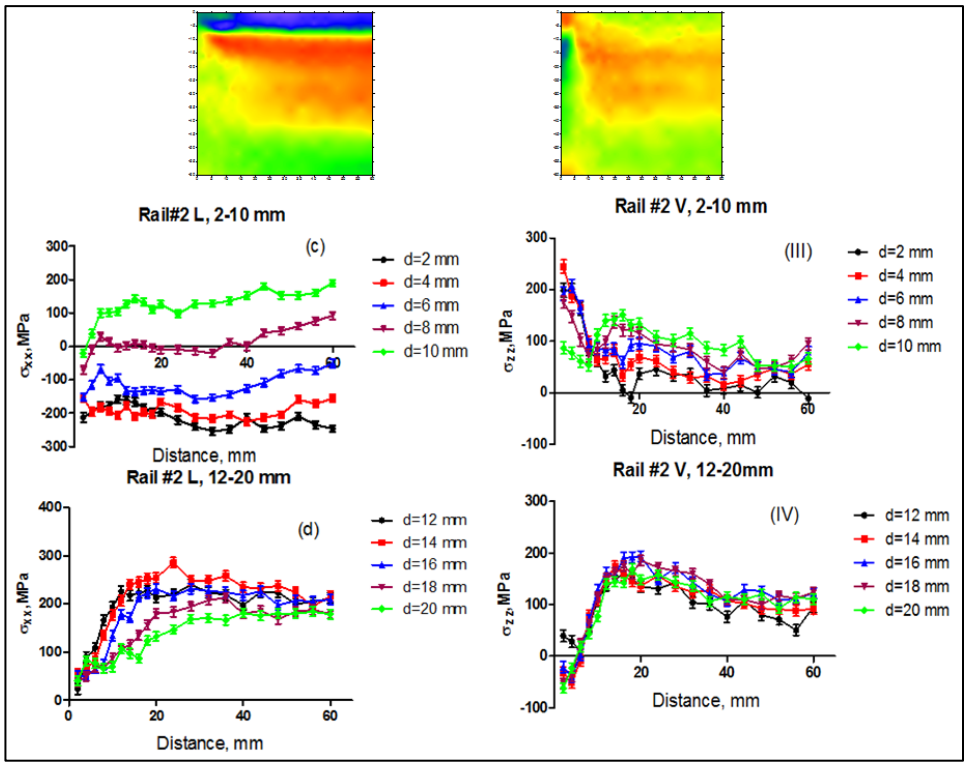

Figure 6-7 Rail #2 partially deformed rail. Residual stress variation for used rail sample along the rail length of 60mm. Measurement points from 2mm from the rail surface to 20mm in depth. (c& d) for the longitudinal component, (III & IV) for the vertical component

Vertical component

In the in-depth direction the residual stress distribution shows similar pattern with severely damaged rail with a maximum tensile stress of 250MPa at location x=2 mm, and decreases with a strong gradient reaching of constant stress level for the remaining length of the rail.

For line d=12 to 20, only three line shows compressive stresses at x=2 mm, with increasing distance from the rail end surface, first the residual stresses increase to a value of 200MPa at location x=18 mm then decreases with increase in distance from the rail end.

6.3.4 Residual stresses for centre line

Comparison of three rail end samples for residual stress distribution across the centre line of the rail head are represented in Figure 6-8.

For serviced rail end (Rail #1 and Rail 2) shows a higher value of compressive stresses at x=2 mm near the rail running surface of value -300MPa compared to unused rail (Rail #5) is about -75MPa for transverse component. The residual stress development in the in-depth direction shows a change in pattern from the surface until in-depth x=40 mm and remains same for larger depth from d=40 to 55. Further, the high value of tensile stresses is about 100MPa is developed in the unused rail sample at the depth of x=35 mm. For serviced rail transition from compressive stress to tensile stress occur at location x=10 mm from the rail surface.

A comparison in the vertical component shows a roughly similar residual stresses distribution between the three rail end samples, expect for the line d=6 for the serviced rails where the stresses maximum is -25MPa at location x=55 mm.

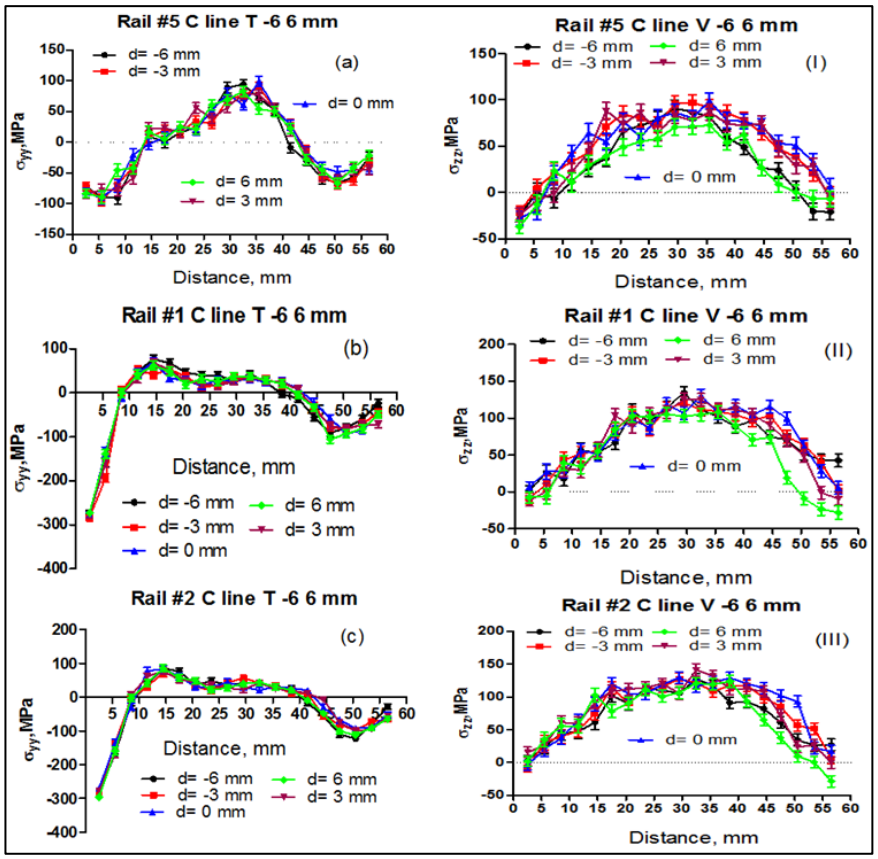

Figure 6-8 Comparison of residual stresses measured at central line from the rail end along the rail depth for Rail #5 unused rail (a, I), Rail #1 severely deformed rail (b, II) and Rail #2 partly deformed rail (c, III)

6.4 Residual stress in transverse slice

Evolution of the residual stress and material lattice parameter in transverse rail slice of different service history is shown in Figure 6-9. The railhead is 70mm across in the transverse direction, in the stress maps the red areas represents high tensile stress while the blues areas correspond to high compressive stress. In the lattice parameter maps, larger d-spacing are shown in red while small d-spacing values are blue.

Drastic changes in residual stress state were found in the rail head of the selected samples, see Figure 6-9. Compressive stress immediately under the top surface, which is induced due the service load from the train movement, is counterbalanced

by a wide zone of tension that potentially can cause defect growth. The rail material also undergoes a transformation as shown in lattice parameter changes in Figure 6-9 changing from harder steel as shown in read areas to softer as shown in blue areas. This happens differently across railhead and evolves noticeably with the service span.

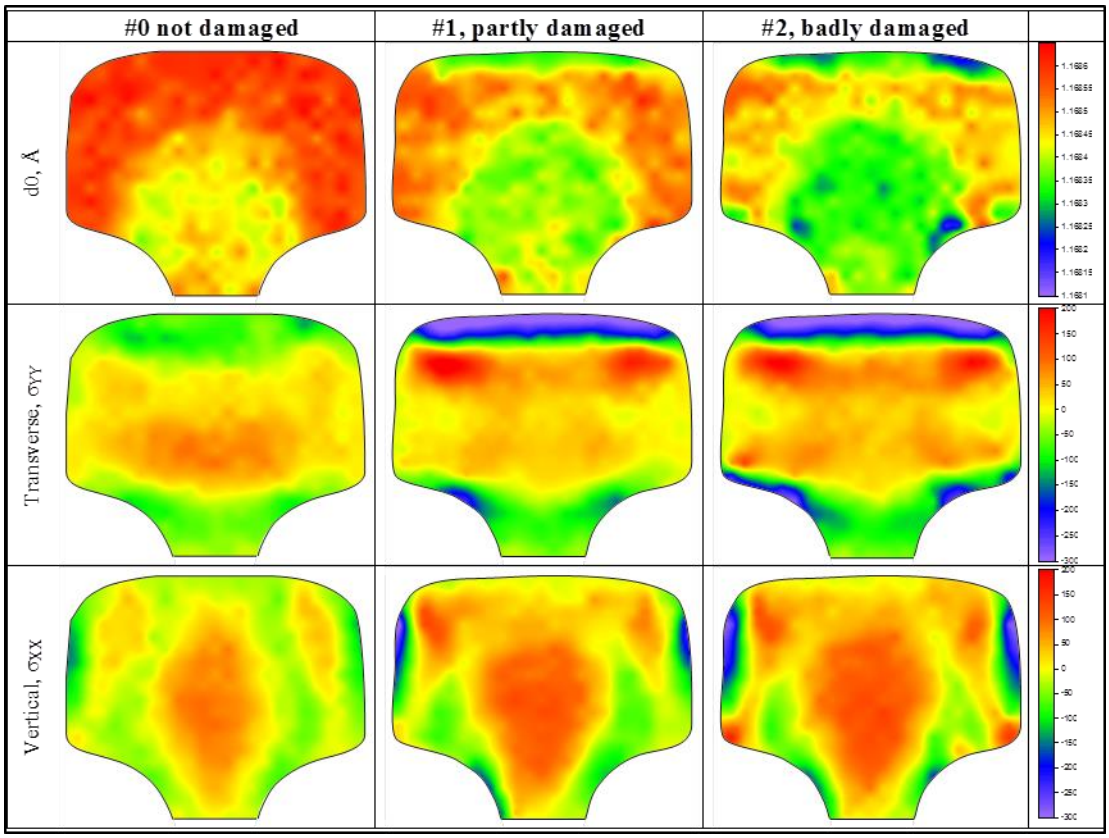

Figure 6-9 2D stress and d_0 maps for the T-slices. Compressive forces are blue, tensile forces are red

Figure 6-9 shows the distribution of 2D residual stress maps in the slices from rail samples in different conditions. For T slices, the stress distributions are dominated by compressive (~ -300 MPa) stresses at the running surface and up to ~5 mm into the rail, which is balanced by tensile stresses (~ 200 MPa) located around 5-15 mm beneath. Both after-service rail samples exhibited similar stress distributions, although these were accentuated for the badly damaged rail. While results for T-

slices characterize stress distributions of continuous sections of rail (samples are taken away from the rail joint), results for L-slices demonstrate stress gradients in the proximity of the rail joint. To separate the effect of stress redistribution due to the presence of the rail end from the effect purely due to the different regime of material deformation in IRJ, differential stress maps, $\Delta\sigma xx$ and $\Delta\sigma zz$, were produced by subtracting stresses measured in the rail ends produced by EDM cutting (a by-product of T-slice manufacturing) from stresses measured in the actual IRJ.

For the unused rail, the 2D maps also revealed moderate tensile stresses in the centre core of the rail head. These stresses are believed to be due to the roller straightening process during manufacturing.

Compressive stresses are observed near the running surface and these are believed to have a beneficial role in resisting the further plastic deformation and growth of Rolling Contact fatigue (RCF) cracks. A significant variation of d0 with depth near the top surface was detected and was attributed to decarburization in the top layer induced by cold work.

6.4.1 Unused rail T-Slice

The residual stress distribution for the transverse rail slice along the transverse component is shown in Figure 6-10.

In the area on the bottom side of the rail where d=0 the residual stresses have low compressive stresses. In the region between d=2.5 and d=14.5, the residual stress shows a tendency towards increasing compressive residual stresses with a magnitude of -150 MPa. In the line between d=17.5 to 29.5, the residual stresses shifts to tensile component with reaching a maximum magnitude of 90MPa.

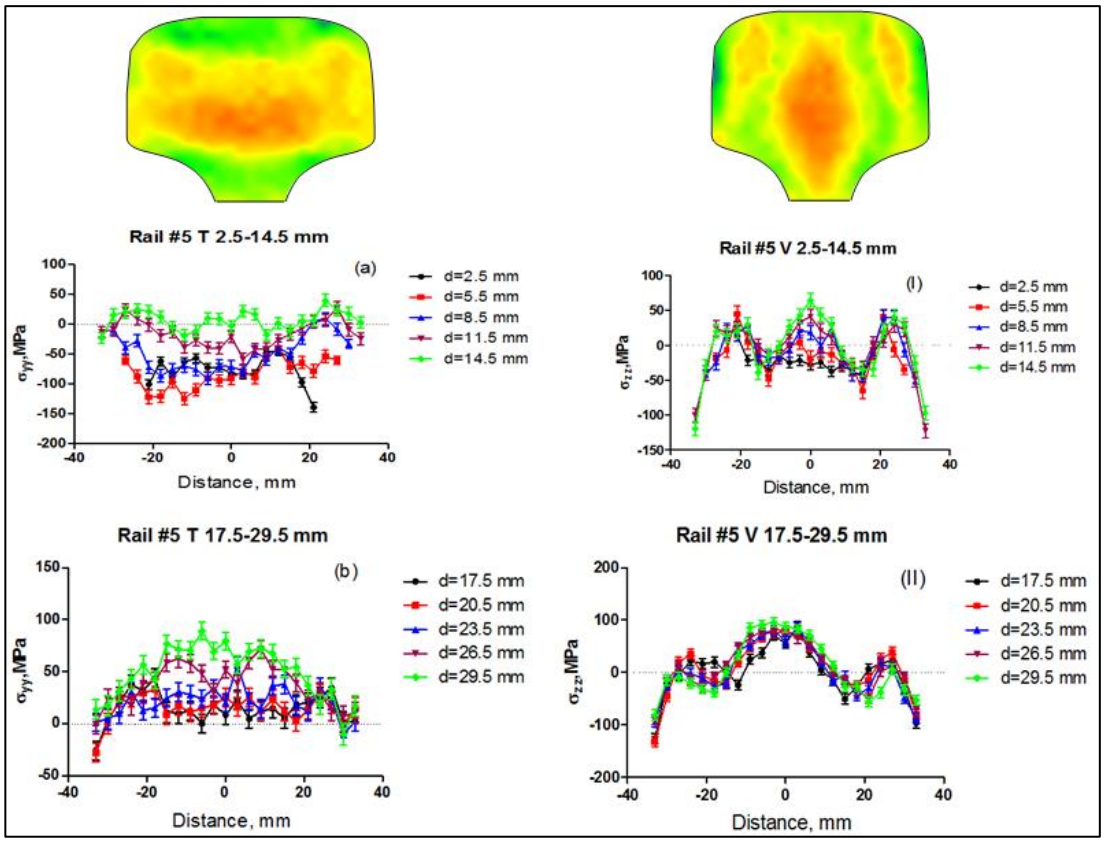

Figure 6-10 Residual stress variations for unused rail sample across the rail head for a transverse slice. Measurements point from 2.5 mm from the rail surface to 29.5 mm in depth (a & b) – for Transverse (I & II) – for Vertical component

6.4.2 Partially damaged rail T-Slice

For partially damaged rail the residual stress distribution is shown in Figure 6-11. In the region where d=2.5 and 5.5 the residual stress are high compressive stresses with a maximum magnitude of -380MPa near the running rail surface.

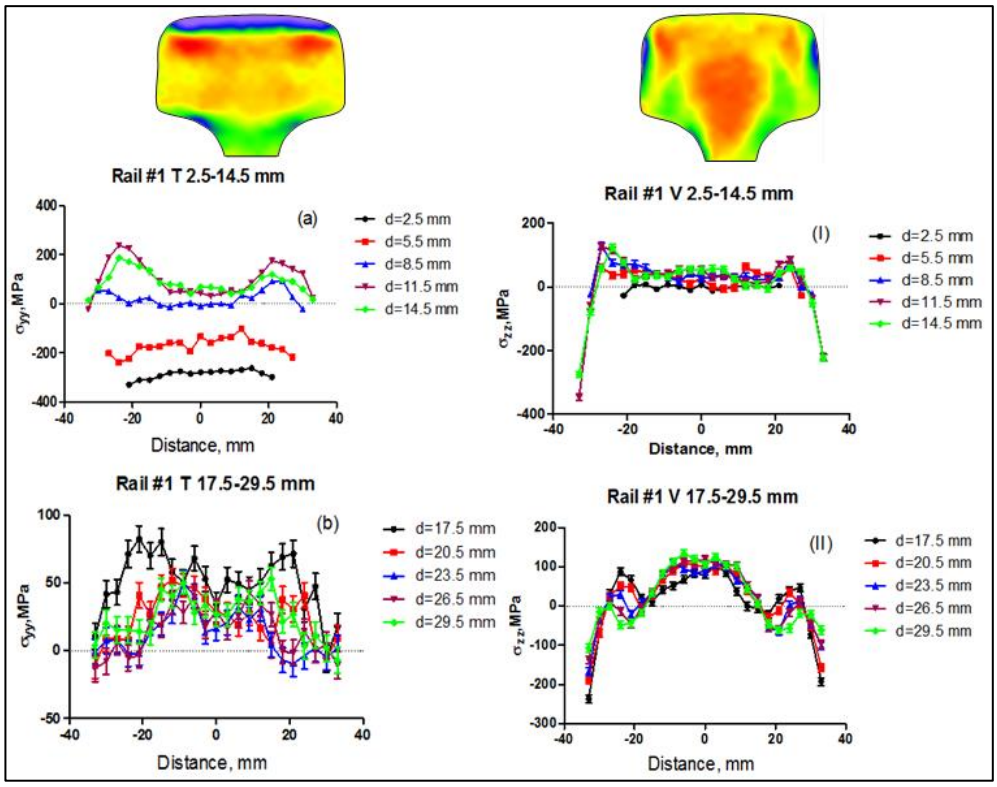

Figure 6-11 Residual stress variations for partially damaged rail sample across the rail head for a transverse slice. Measurements point from 2.5mm from the rail surface to 29.5mm in depth. (a & b) for the transverse component, (I & II) for the vertical component

In the region between d=8.5 to 14.5, line 8.5 is in the interface line where stresses cease to remain close to 0MPa, and line 11.5 reaches to maximum tensile stresses of magnitude 250MPa. In the region between d=14.5 to 29.5, shows a tendency towards decreasing tensile stresses with an increase in depth with a minimum magnitude of 20MPa.

6.4.3 Severely damaged rail T-Slice

For severely demerged rail the stress distribution is shown in Figure 6-12. The residual stresses show similar trends with the partially damaged rail \shown in Figure 6-11with a minimal change in the residual stress magnitude.

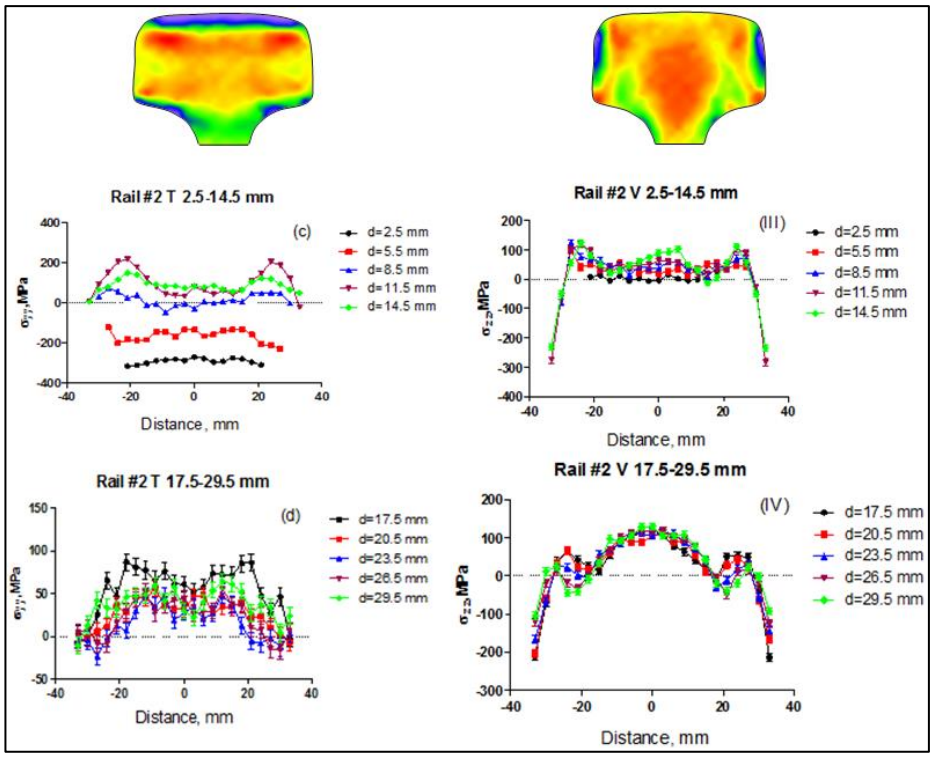

Figure 6-12 Residual stress variations for severely damaged rail sample across the rail head for a transverse slice. Measurements point from 2.5mm from the rail surface to 29.5mm in depth. (C & d) for the transverse component, (III & IV) for the vertical component

6.5 A neutron diffraction investigation of rail ends deformed in full-scale wheel on track rig testing device

Two samples with different load conditions were measured and an additional undamaged sample (labelled #1 free end) was also examined in order to differentiate stresses associated with loadings from stresses developed during the manufacturing process. The existence of compressive region near the rail surface with a balancing tensile stress below this confirmed similar results obtained from ex-service damage IRJs (Peltier and Barkan, 2009).

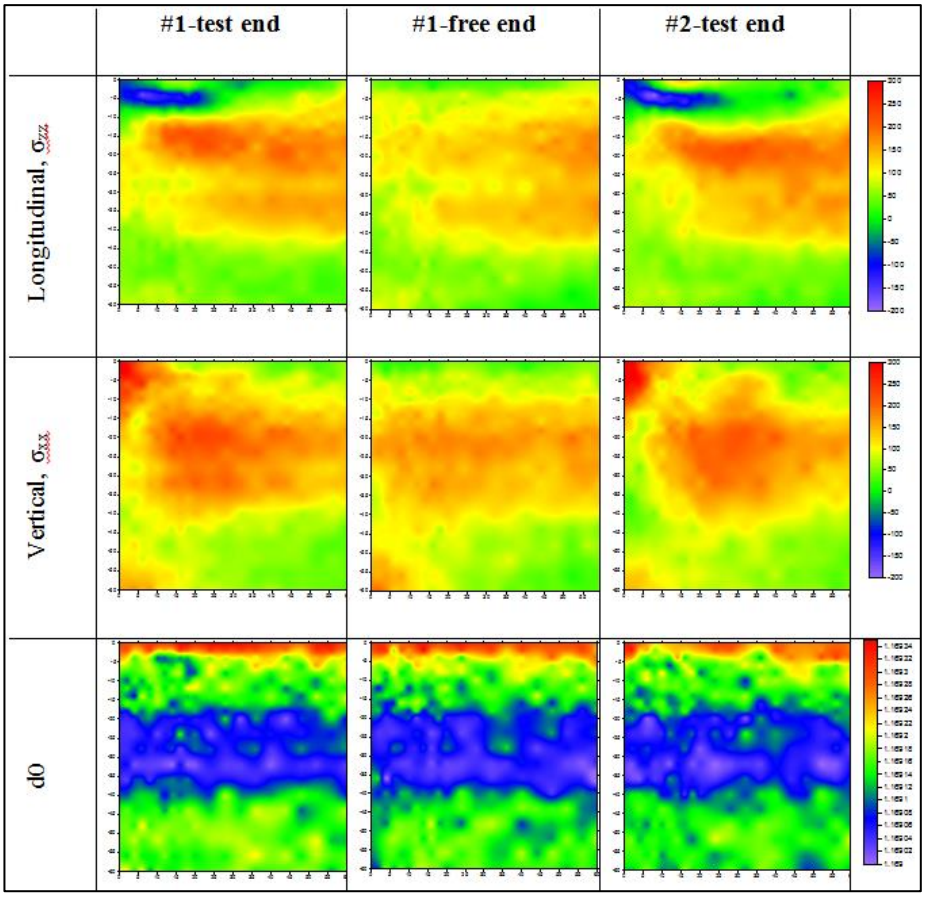

Figure 6-13 Residual stress maps in the longitudinal slices from the rails contact loaded in the rig tester. Variation in d0 is also shown in the bottom

Figure 6-13 shows 2D stress maps across the local railhead for two directions, namely longitudinal and vertical directions, and also shows the values of interplanar

d(211) spacing (i.e., the d0 values), as functions of the position in the rail sections. For the two rail samples that underwent wheel loadings in the rig tester for 600 and 1000 deformation cycles, similar longitudinal stress maps were obtained, with slight changes near the localised rail head. Compared to the undeformed sample, vertical stresses in both rig tested samples were particularly severe in the regions near the top free ends of the rail, with tensile stresses of around 200 MPa extending to a depth of around ~20 mm.

Local plastic deformation of rail head surface can arise when locally high contact stresses from the wheel rolling on rail exceed the material yield point. The contact stresses also leads to residual stress development which is created by the plastic deformation that builds up in rail during the wheel loading. The presence of significant compressive residual stresses zone of ~5mm deep from the rail surface was found to be counterbalanced by the tension zone underneath (~15mm deep), this tensile distribution zone is believed to be one of the critical regions for likely of crack initiation and propagation.

The maps in Figure 6-13 can be directly compared with the 2D stress maps that were obtained in the same way for the rails that were more heavily deformed in real service, as shown in Figure 6-4. Clearly, Figure 6-4 and Figure 6-13 show the similarity between the build-up of the longitudinal compressive residual stresses at the corner of the railhead; the obvious difference is their magnitude and the extent. For example, the maximum longitudinal compressive residual stress measured on the slices taken from the laboratory tested rail end was 200MPa whilst the from the ex-service loaded IRJs was 300MPa. The lab tested IRJ was subject to a maximum of only 1000 cycles of 300kN loaded wheels; this corresponds to approximately two coal trains of 250 wagons. In comparison, the slices taken from the ex-serviced IRJs

from the field were there for months (the actual traffic was not known). The lower residual stress is entirely acceptable-however, the feature that should be noted is the very high rate of build-up of residual stress 200MPa within 1000 load cycles. The very large accumulation of plastic strains is consistent with (Luzin et al., 2013a) observation. The other feature to note is the extent of residual stress build-up which is localised in the slices from the laboratory tested rail ends-whilst the slices from the ex-service IRJs show the entire length of the slice with maximum residual stress of 300MPa. Again, this is entirely logical as the load was only applied for a very local length of 20mm on the railhead.

The same inferences can be made for the vertical tensile residual stresses shown in Figure 6-4 and Figure 6-13. Interestingly, the vertical tensile residual stress magnitude is 300MPa for both the slices from the laboratory tested railends and the ex-serviced IRJs. This can be attributed to the rather comparable loads and the extreme stress singularity at the corner. The slices from the laboratory tested railends exhibited lower build-up of vertical tensile stresses on the body of the slice compared to the ex-serviced IRJs. Clearly, it can be seen that the build-up of the residual stresses and the associated accumulation of plastic strains in the IRJs are due to the manner in which the IRJs are designed; the contribution, if any, of the track moduli to these localised phenomena is negligible. Whilst the track modulus is a key parameter for the structural responses (deflection of sleepers, joint bars strains and ballast pressure), the localised ratchetting and the associated residual stress build-up are entirely due to the current design where the rail is cut normal to the axis of the rail making, the cut section is quite vulnerable to corner loading of the wheels.

Differences in results between the rig tested and ex-service samples may be attributed to (i) the fact that a rail end rather than a joint was loaded, so there was no

impact component of damage at the rail end and, (ii), the number of cycles associated with the rig testing was apparently less than that required to produce equivalent damage to that observed in the ex-service joints.

6.5.1 Tests of R1 & R2 for longitudinal component of accumulated residual stress

The residual stress distribution for laboratory tested rail samples are shown in Figure 6-14, accumulated stress for the laboratory test rail samples are practically same with the real service rail samples with a very minimal change in its value.

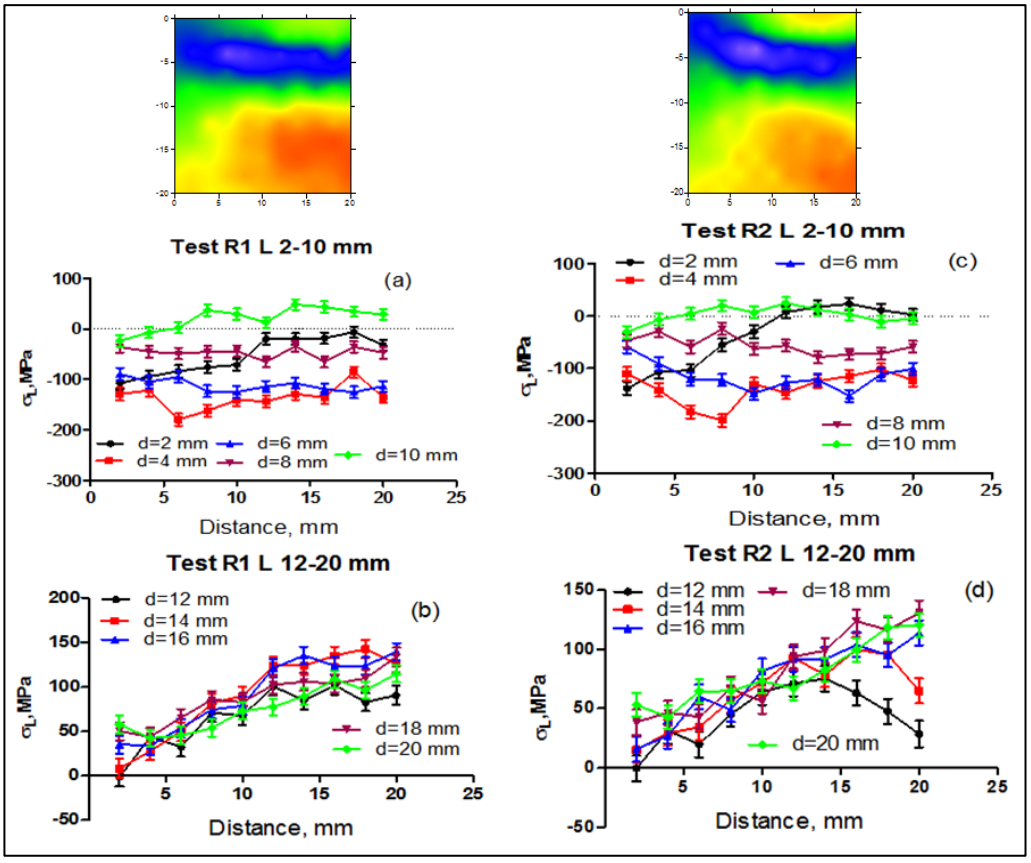

Figure 6-14 Longitudinal component for Rail #1 & Rail #2. Residual stress distributions on the rail head across the rail length to the depth of 20mm from the rail surface

For line d=2 to 8, the running surface shows compressive residual stresses throughout the rail surface with decreasing value with increase in depth from the rail end surface. For line d=10 to 20, the wheel loading on rail end sample has a marginal effect, the change in stress level from x=2 to 20 is due to the effect of rail manufacturing process.

6.5.2 Test R1 & R2 for vertical component

The residual stress distribution for laboratory tested rail samples are shown in Figure 6-15.

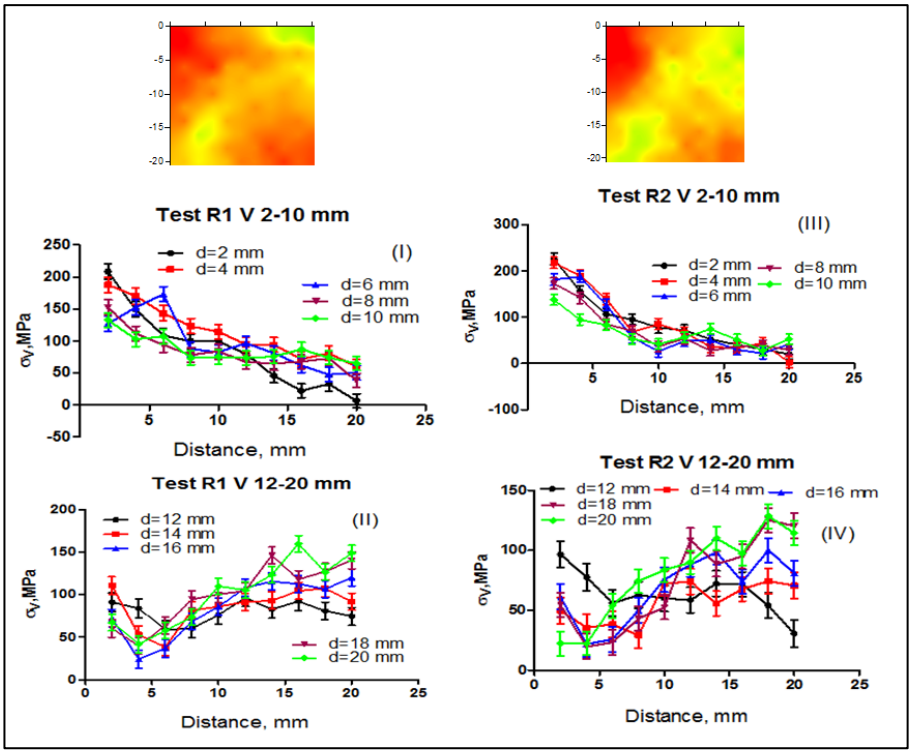

Figure 6-15 Vertical component for Rail #1 & Rail #2. Residual stress distributions on the rail head across the rail length to the depth of 20mm from the rail surface

In the in-depth direction, the residual stress distribution shows a maximum tensile stress of 220MPa at location x=2 mm for both rail end samples and decreases along the rail surface direction. The tensile stresses for rail #2 show a constant stress value

after x=10 mm. For line x=12 to 20 mm, tensile stresses are randomly distributed across the length of the rail which are developed due to the effect of the rail manufacturing process.

6.5.3 Unused rail for longitudinal and vertical component

The residual stress distribution for the longitudinal rail slice along the longitudinal and vertical component is shown in Figure 6-16.

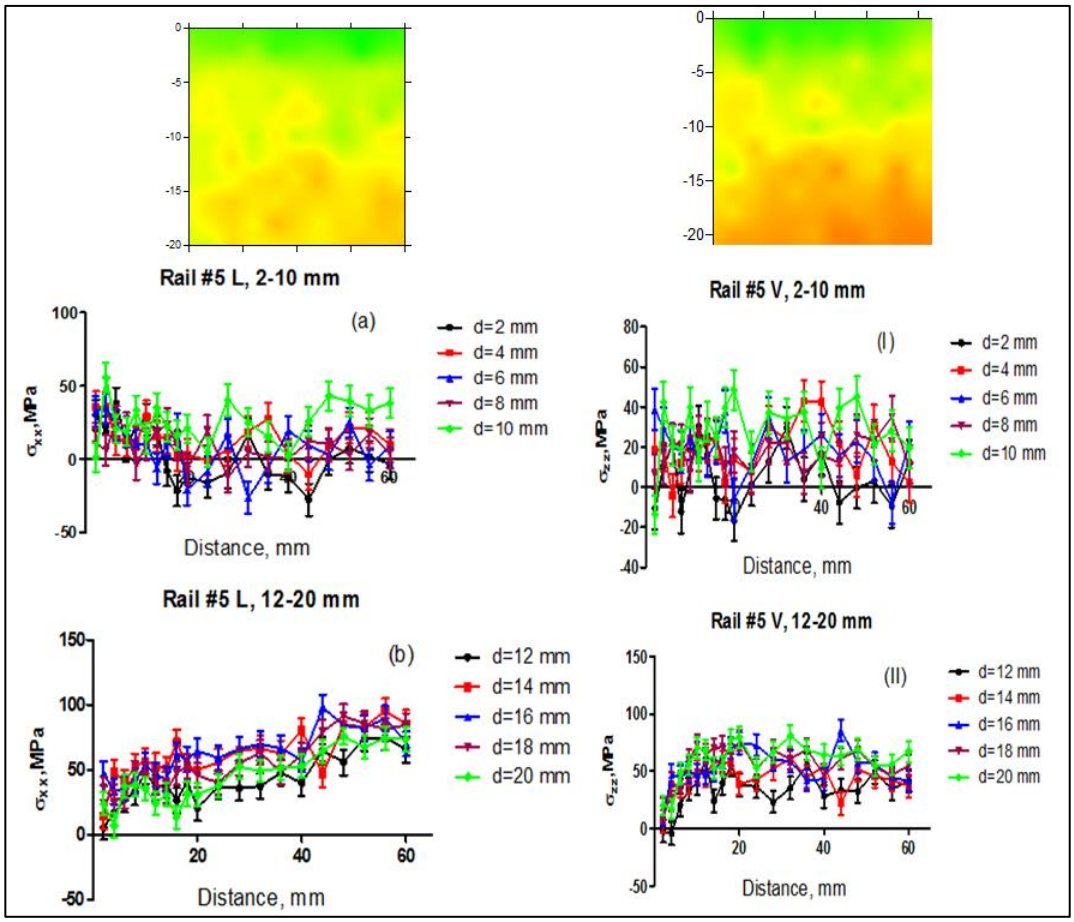

Figure 6-16 Residual stress variation for unused rail sample along the rail length of 60 mm. Measurements point from 2 mm from the rail surface to 20 mm in depth (a & b) – for Longitudinal (I & II) – for Vertical component

The residual stresses studied in these samples are tensile in nature for both longitudinal and vertical component. In longitudinal component Line d=2 and 4

shows low compressive stresses value which rose during the manufacturing heat treatment and grinding process. On the rail end surface, the stresses in the longitudinal component of the line d=12 to 20 tend to have low value compared to the value in longitudinal distance from x=0 to 60 mm (where x =horizontal axis) tensile residual stresses increases in a steady way reaching a maximum at x=60 by value 50-75MPa.

6.6 Residual stress summary

6.6.1 Residual stress for serviced rail

This research study has demonstrated of the value of using neutron diffraction as a non-destructive method for quantitative 3D residual stress analysis of large and heavy samples such as a rail track.

Desirable compressive residual stress was found close to the wheel running surface and followed by tensile stress acting in the subsurface region at a depth between (10 and 15mm). This residual stress investigation will provide valuable feedback to the FEM modellers of the rail manufacturing processes.

The influence of the wheel-rail service on track and in laboratory wheel-rail rig test for insulated rail joints on the residual stresses in the rail head and in the vicinity to boltholes was also examined. Two-dimensional stress distributions were determined in bulk and in slice samples by means of neutron diffraction. Results from this research are drawn out in the following conclusions.

The stress levels measured in the severely deformed, partially deformed and un-deformed rail joints are, however, small and so the sample preparation method of EDM sectioning is unlikely to have any significant influence on the results.

Under the cyclic loading service, a major part of the residual stresses are developed in different part of the rail joint sections, especially in the running surface region of rail head and in near boltholes of web and fishplate regions, with a significant compressive stress.

The narrow plastic deformation region is induced on the wheel-rail contact surface brings about the compressive residual stresses in longitudinal, vertical and in transverse directions. Depth and magnitude of compressive residual stresses depend on the loading on the rail surface and increases with increasing wheel loading. But the magnitude of the induced residual stresses is not directly proportional to the loading magnitude. Occurrences of residual stresses are more prominent near the rail end surface where maximum depth of the residual stress was situated.

The different loading conditions for the ex-service rail joint samples had a very little difference in the evolution of residual stresses of the deformed microstructure in the subsurface region.

As wheel-rail system undergoes not only mechanical stress but also thermal stress, the martensite formation develops through ferrite/pearlite-austenite-martensite phase transformation through repeated thermal phase. During this transformation, any severe pre-deformed austenite would bring about the ultra-fine grained martensite during the quick cooling process.

6.6.2 Deformation, Residual stresses and microstructural changes

Distinctive alterations of the microstructure are developed near the railhead surface because of the rolling contact of wheel loading along the rail surfaces. The microstructural results show a transformation of the microstructure of the rail surface and subsurface region during service loading, which was confirmed by the gradual

changes in the residual stress values, mainly in the railhead region. The rolling wheel introduces compressive stresses, with the higher values at the extreme running rail end surface for approximately (5-8mm) and reaches a maximum depth of (10-14mm) at the railend vertical surface.

Neutron diffraction of damaged IRJ samples revealed the significant evolution of residual stress fields in rails due to service. Stress evolution in the bulk and vicinity of rail ends was characterised by a compressive layer, approximately 5-10 mm deep, and a tension zone located approximately 10- 20 mm below the surfaces. A significant variation of d_0 with depth near the top surface was detected and was attributed to decarburization in the top layer induced by cold work. Around the IRJ, material is more heavily deformed than material in the bulk of the rail as demonstrated from the longitudinal stress component differential maps $\Delta\sigma_{zz}$ in the partially damaged rail the compression zone extends some 5 mm deeper than in the bulk areas, while for the badly damaged rail this effect even bigger and extend approximately 10 mm deeper than in a bulk part of the rail.

Thus, although stress distributions observed in longitudinal slices of the two differently deformed rail samples seem to be similar, the badly damaged rail demonstrates deeper and stronger changes in the stress (and damage) state. This is also consistent with evidence of larger material flow based on light and scanning electron microscopy studies. For the un-deformed rail, the stress distributions obtained could be attributed to variations associated with the thermo-mechanical history of the rail.

6.7 Residual stress for wheel rail rig test rails

The residual stress distributions on the 5mm thick slices of railhead samples were analysed both in longitudinal and vertical direction with certain distances from the rail surface.

The in-depth distributions of residual stresses were studied up to 60 mm2 from the rail surface in depth, with a nominal gauge volume of 3 x 3 x 3 mm3 for 400 mesh point measurements.

There was clear evidence of stress field evolution in all studied rails, for both tests cycled and ex-service samples. This was characterised by a compressive zone ~5 mm deep that is counterbalanced by a tension zone underneath (~15mm deep). The distribution of the residual stress in the rig tested rails indicates high local plastic deformations on the near surface of railhead near the rail end. The increase in tensile residual stress for the vertical component is nearly ~200MPa, twice the value of bulk material away from the rail end. There was an obvious evolution of d_0 in the ex-service rails while no evident evolution in the rig tested samples, probably due to the higher damage accumulated in ex-service samples than for the rig tested samples. Apparently, 600 or 1000 cycles during rig testing have not produced comparable damage as was achieved in ex-service samples. Longer duration cycling and cycling over real rail joint gaps rather than over rail ends would more accurately simulate metal flow over the insulated rail joints.

Using the full-scale rig equipment has proved, in general, to provide a considerable plastic strain resulting in microstructural deformation of the rail head. Longer duration cycling and cycling over real rail joint gaps rather than over rail ends would more accurately simulate metal flow over insulated rail joints.

6.8 Residual stress mapping for bolt holes

A 5 mm slice was cut using EDM from the 40 mm thick fishplate. Change in thickness has not altered but allowed high-resolution mapping (with respect to the given sample geometry) with many points as 872.

Four directions were measured in Longitudinal (L), Transverse (T), Vertical (V) and LV-shear, three stresses were constructed (L, V and LV-shear) and d_0 were reconstructed using $\sigma_{yy}=0$ condition.

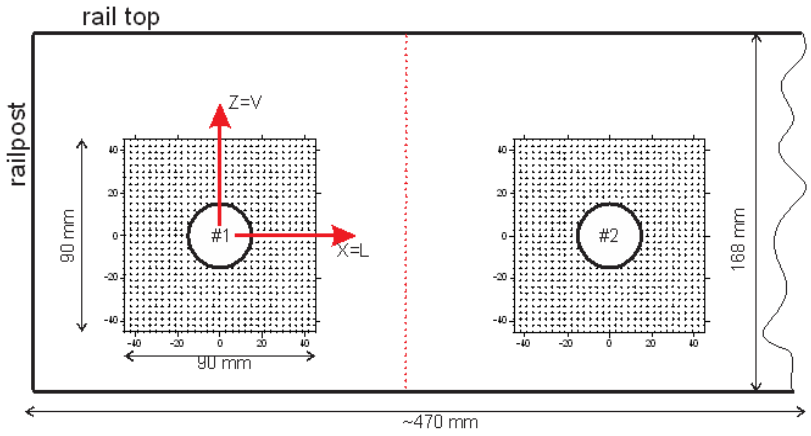

Figure 6-17 Schematic of sample geometry and mesh left hole corresponds to Hole #1 near to rail end and right hole to Hole#2

Stress accumulations near the bolt-hole surface are explained in two parts:

Firstly, low amplitude of stress introduction during installation of joints and during the high lateral load from wheel rolling service. The behaviour of jointed rails are complicated because of the rail is in contact with fishplates support and also because of its structural discontinuity in nature compared to a continuous rail.

The condition is further worsened by

(a) Loose joint sleepers.

(b) Loose or over tight fish bolts

(c) Wearing of the fishing planes

(d) Hogging and battering of rail ends

(e) Excessive expansion gaps.

Under such varied conditions, when stresses are introduced in the rail, fish-bolt holes act as stress raisers and act as critical point for the crack to initiate. 60 -65 % of total rail failures are accounted for rail end failures and quite a large number of these failures are due to bolt-hole failures.

It is not expected that the hole closest to the IRJ gap and the next hole, located 180 mm further away from the IRJ gap, experiences the same mechanical regime and stress accumulations. Therefore, we distinguish these two holes, performing measurements on holes, (i) nearest to rail end H#1, and (ii) the next away from the rail end H#2, to check the severity of the stress distribution across the rail length and fishplate length closest to the IRJ.

6.8.1 Results - Rail web bolt holes

Failure of rail web explained as

(1) During the passage of wheel, the joint undergoes a bending and flexural loading in particular bolts which react from pure shear to complex/combined shear and bending and with a significant deformation which changes the gap to wider. Due to this, there will be a development of stress concentration around the bolt-hole surface of the rail web, which will initiate cracks at 45^{o} (star crack) and grows during the reversal of loading when wheels pass the joint. Once this process begins, the benefits gained from an ideal support condition are lost and the system reverts back to the unsupported state.

(2) Bolt-hole cracks/cracks in the web region are also caused by loosening of ballast elasticity underneath, giving a higher vertical displacement at the joint which causes fretting between the fishplate and rail web. Eventually, leads to dislocation of rail web section by fracture. Understanding of stress accumulation in the vicinity of rail-web bolt-hole surface will help in predictions of IRJ lifetimes and improvements in design aspects as fatigue crack growth are sensitive to stress history.

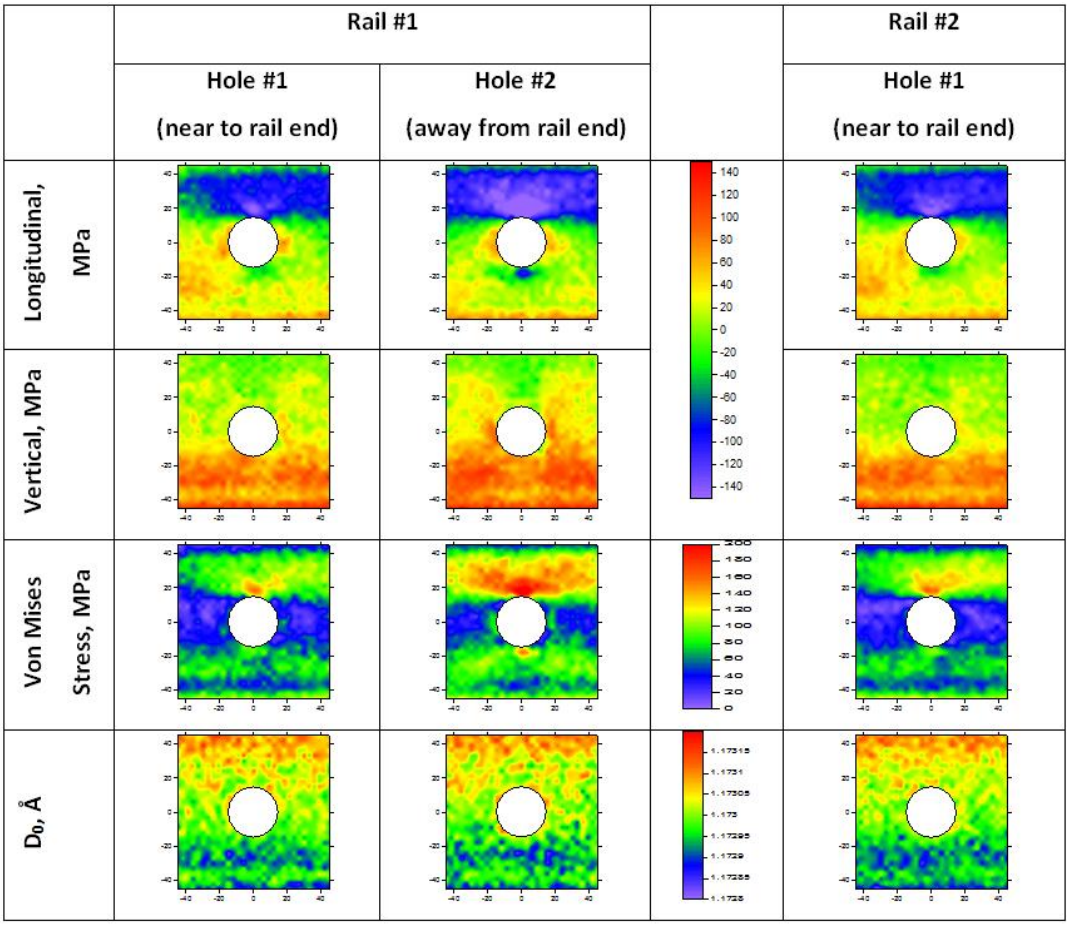

Figure 6-18 Residual stress maps from the rail web sections for rail #1 and rail #2. Compressive stress is blue, tensile stress is red. Map patch is 40mm in size

6.8.2 Rail web bolt holes

Figure 6-19 shows the distribution of 2D residual stress maps around two holes for longitudinal, vertical components in the slice taken from the rail web. Two rails were analysed: one is characterised as “partially damaged” (Rail#1) and the other one was assigned as “severely damaged” (Rail#2). The damage assessment was performed in terms of conditions of the steel of rail head adjacent to the IRJ gap. The stress pattern does not reveal any substantial changes for both Rail #1 and Rail #2. However, a closer look makes it possible to discern some areas where the shear stresses (von Mises stress) are concentrated around the top and bottom of the holes. For example, in the case of H#2/R#1, von Mises stresses can reach approximately to 150-200MPa occurring at the top of the bolt hole while much lesser von Mises stress of 60-80MPa can be found at the sides of the H#1/R#1. Moreover, there appears to be no significant difference in stress distribution for R#1 and R#2.

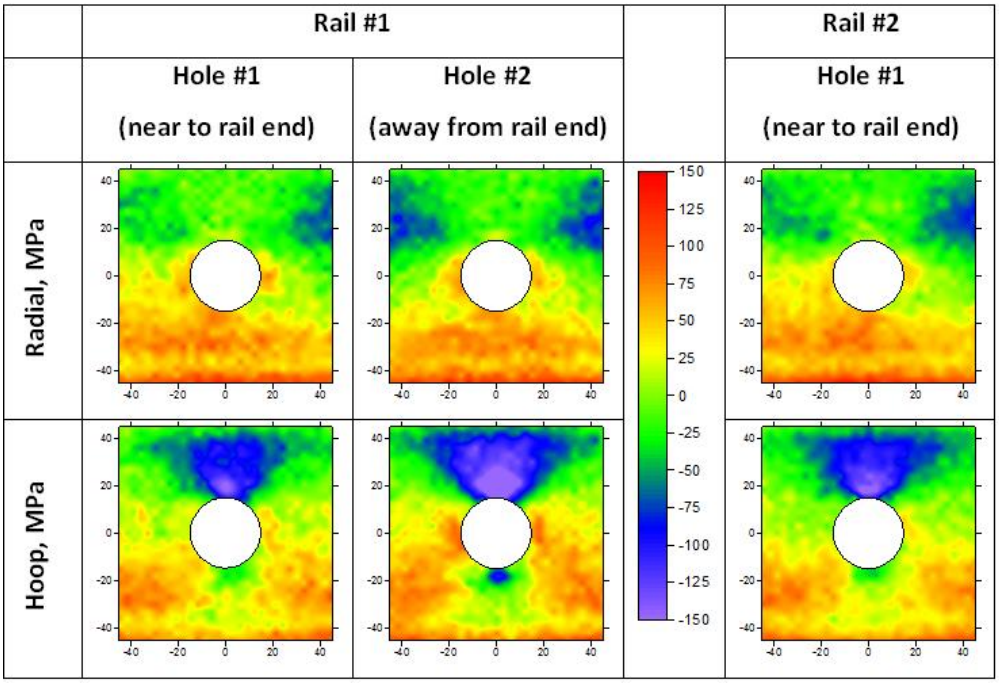

Figure 6-19 Radial and Hoop component stress map from the rail web sections for rail #1 and rail #2

6.8.3 Fishplate bolt holes

Fish plates were taken from the assembly of 3-bolt rail joint which had undergone controlled amounts of surface deformation using wheel-on-track simulation rig test with wheel loads and stroke cycles of 300kN and 1000kN, respectively. From this test, it is expected to produce a decent amount of accumulated residual stresses around the fishplate holes; the amount of load severity on each fishplate hole diminishes across the fishplate length. The measurement was carried out for the hole nearest the rail end shown in Figure 6-20. Stress distributions for fishplate are more prominent than for the rail web, as the fishplate substitutes for the rail discontinuity by providing missing vertical bending stiffness and so will subject to abnormally high dynamic bending forces when the wheels pass over it. However, it should be noted that the bending stiffness of fishplates is generally smaller than that of the rail and the yield point of the fishplate steel is lower due to the common practice of selecting a lower grade steel for the fishplates.

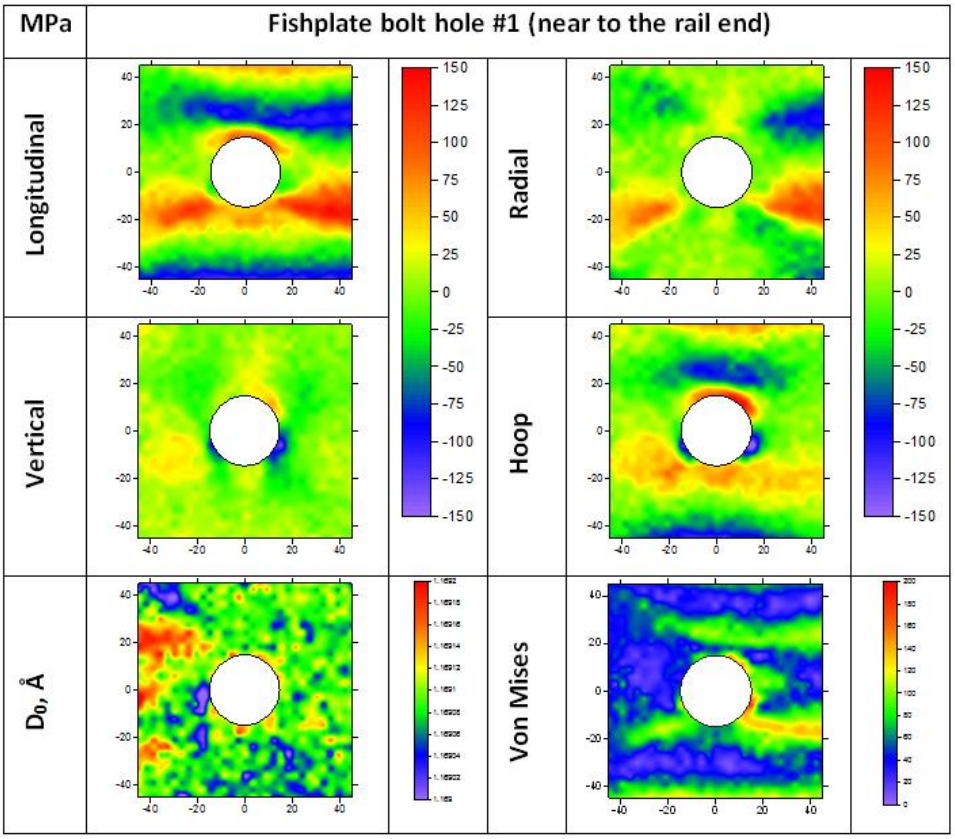

Figure 6-20 Residual stress maps for fishplate section. Stress representation across the lines as shown in schematic diagram

Examination of Figure 6-20 reveals that, the longitudinal component, away from the hole, i.e. the right side, the stress pattern that corresponds to the application of a large bending movement (to make it of a concave shape, viewed from the top), exceeds the yield point of the fishplate material, ~300 MPa. In the resultant stress, distribution stresses reach in extremes of ±150MPa and this is in agreement with similar stress accumulation reported in (Bandula-Heva et al., 2013). These stresses are modified in the vicinity of the hole during the service conditions and create stress concentration, judged by the von Mises stress in Figure 6-20 and, therefore, conditions for formation and propagation of 45° type of cracks from the bottom of the hole at an angle to the horizontal plane.

6.9 Conclusion and discussions

6.9.1 Residual stress for bolt holes

The residual stress distribution on the 5mm thick slices of fishplate and rail web section were experimentally obtained using neutron diffraction for both in longitudinal and vertical directions, for a measurement mesh area of 90×90 mm2 with a nominal gauge volume 3x3x3mm3 and 872 with mesh points. Measurements were carried out for both the hole near to the rail end H #1 and away from the rail end H #2, to check the severity of the stress distribution across the rail length.

6.9.2 Rail web bolt holes

Both rail #1 and rail #2 rail web stress distributions in the vicinity of the bolt holes were found to be similar. However, hole #2 demonstrates a more pronounced residual stress concentration: a compressive zone at the top of the bolt hole (minimum longitudinal stress) and tensile at the right and left side of the hole (maximum vertical stress). The residual stress will be superimposed on the applied load with stress concentration on the top and bottom of the hole (that will be partially cancelled by the residual stress) while having zero contribution to the sides positions.

Based on current understanding, if crack is initiated from the area of maximum tensile stress, which is a superposition of the residual and stress generated by external load, then it would start to emanate and grow from the right or left side of hole 2 and propagate horizontally or up to 45° up/down depending, on particular combination of the residual and applied stress as well as on whether rail is bent up/down due to the different sign of dynamic loading of the rail assembly (which is also dependent on the support system). Therefore, these observations suggest a scenario realized in Figure 6-18.

6.9.3 Fishplate bolt hole nearest to IRJ endpost

Compared to the rail web, stress distributions were more prominent with a typical zig-zag profile magnitude of stress levels reaching ~150MPa. This stress profile is consistent with plastic bending with the concave side being on top, in agreement with the kind of bending expected from contact with the loaded wheel. The bending moment and high deflection exerted on the bolt hole during the transverse cyclic loading can contribute to slip and loosening of bolted joints. This localised slip can accumulate stresses around the bolt hole and material flow at the rail head surface, especially when the stiffness of the joint has been compromised and eventually may also lead to fatigue failure of the insulated rail joints

Around the fishplate bolt holes, residual stress is modified by the presence of free surface and has a concentration of tensile stress at the top and bottom of the hole (maximum longitudinal stress). The applied load will have a concentration of the tensile stress in exactly the same positions and, therefore, superposition of the residual and applied load will aggravate crack initiation and crack propagation conditions.

If a crack is initiated from the area of this hole, then it will start to emanate and grow at the top and bottom of the hole and propagate in the vertical direction, therefore, realising a scenario shown in Figure 6-20.

The analyses of just a few examples do not exhaust all possible scenarios, as these depend on many factors including; the exact configuration of the rail support system, dynamical and static axle load parameters, the particular design and steel quality of the fishplate. However, a correlation with practically observed and reported cracks in IRJ fishplates and track webs near the rail end was certainly confirmed.

Overall, it was confirmed that as fatigue crack growth and accumulated stress are sensitive to the thermo-mechanical history of IRJ assemblies increased understanding of stress accumulation in the vicinity of rail-web bolthole surface will help in predictions of IRJ lifetimes and improvements in design aspects.

7 SUMMARY, CONCLUSIONS AND RECOMMENDATIONS FOR FUTURE WORK

Conclusions have been described in respective result Chapters 5 and 6. Several general and specific conclusions drawn from this thesis are reported in this section in the similar sequence of the Chapters presented.

7.1 From the results for the study of ex-service coated and uncoated rails it can be said that:

The stainless steel coated rail has exhibited higher hardness, less metal flow and less damage compared to the uncoated rail. For the Coated rail, cracks originated at the stainless steel rail steel interface, with significant cracking near the top rail surface. The origin of this cracking was the mismatch in metal flow rates- greater flow for the rail steel than the martensitic stainless steel. A second problem was related to welding defects at the base of "bathtub".

A significant design problem was the shallow angle at the two-material interface near the top of the rail. This was solved by the appropriate redesign of the coating profile.

7.2 Results and observations from the characterization of the head hardened rail and martensitic clad rail can be summarized as follows.

1. Damage of head hardened rail IRJ ends is characterized by metal flow, RCF, and microstructural features such as spalling and cracking

2. Compare to head-hardened rail, the laser coated IRJ suffered less damage for the same heavy haul lifecycle.

3. For cladding, cracks are developed at the interface between the coated and base material at the bottom of “bathtub”.

Damage to the IRJ ends of the stainless coated samples was significantly different to that of the head hardened rail and characterized by:

1. Mismatch in metal flow, greater for the rail steel than the martensitic stainless
2. This mismatch caused cracking in the vicinity of the rail steel and stainless steel interface
3. Type of cracking: two different cracking mechanisms occur at the interface on the top of railhead; oblique crack growth near gauge corner and straight/parallel crack near field side.
4. The problem was accentuated by the shallow angle of the interface to the rail surface.
5. Overall interface looks the good quality of bonding between the two steel, the surface shows promising resistance to RCF but can be further improved by specific railhead coating material.
6. Redesigning the shape and position of the hard facing region might reduce stress concentrations at the coating/rail interface and lead to increased IRJ lifetimes for the coated joint.

Maraging coated rail-ends

1. The approach avoided the cracking normally associated with the use of other coating materials with different thermal expansion properties
2. The simple technique of weld rod deposition resulted in coatings of very high hardness and toughness, characteristic of maraging steel.

7.3 Neutron residual stress for in-service rails

1. The first ever non-destructive determination of the stress distribution in an intact rail piece at the vicinity of rail joints was conducted.
2. Irrespective of loading conditions, both rail ends were observed to have a compressive layer, extending to of depths (8-10mm).
3. Results also differentiated between the change in d_0-value during rail fabrication and rail in-service.
4. The data may be useful as a practical way of the following metal degradation, but also as experimental verification of any modelling work related to deformation accumulation.

Neutron residual stress for rail end tested under laboratory rail rig test

1. There was a clear evolution of stress field in rails due to test cycling. Similar to those of rails being in service (see the previous report).There is compressive zone ~5 mm deep that is counterbalanced by a tension zone underneath (~15mm deep). But in contrast, to rails from real service the type of stress distribution is apparently different due to localized load.
2. There is no obvious evolution of d0, likely because the significant damage has not been accumulated yet to be visible.
3. Slices #1 Railend and #2 Railend are very similar though small differences can be found under close inspection.

Neutron residual stress for bolt-holes

1. The longitudinal stress component away from the hole demonstrates typical stress distribution after bending beyond yield point (from the plot is can be estimated as ~300 MPa).

2. This stress profile corresponds to bending with the concave side being on top, and this is in agreement with the kind of bending from contact with the loaded wheel.

3. Stresses around the hole are somehow modified and create conditions for formation and propagation of the vertical cracks on the top or bottom of the hole.

4. There are no apparent changes in d_0.

7.4 Scope of the Thesis Investigations

The first facet of this research addresses the topic of railhead surface coatings in the vicinity of rail joints and investigates feasibility this approach..

The second facet of the research analyses a comprehensive series in-depth investigations of residual stresses development in both ex-service IRJs and simulated tested rail ends of IRJs. A series of Neutron diffraction investigation supported by ANSTO, Australia are employed for these investigations.

Due to the complexity involved in this extensive IRJ project, the following aspects are identified as limitations on the scope of the research.

7.4.1 Selection and obtaining a desired damaged IRJs

The selection of damaged/rejected IRJs as reference sample was of particular value in this research project. Selection was limited by availability with large time delays associated with logistics of transfer to UOW (typically 5-6 months after sample selection), ex-service coated and uncoated samples were obtained from an

ARTC managed site in the Hunter Valley, NSW. Two additional IRJ samples of neutron investigations were obtained through a formal application for permission to visit a rail site and follow-up work to disassemble the rejected rail joints. Additional samples for rig testing were supplied by CQU Rockhampton. And, also due to the logistics situation project are affected by 5-6 months in time scale.

7.4.2 Scheduling requirements for of residual stress investigation at ANSTO

Neutron beam time allocation to carry out experiments is obtained through formal written proposals, twice a year, at ANSTO, Australia. The procedure for obtaining beam time and gathering results is often drawn out for this investigation involved the following.

i. Proposals are individually assessed via a competitive grant procedure involving external referees evaluating applications. Successful beam time proposals are allocated on the basis of urgency of the work and scientific excellence project. If the beam time allocation to a particular project is too short then an additional beam time are commonly made in the next 6 monthly rounds of beam time proposals.

ii. Overview of operation cost for conducting single proposal experiments which typically accommodated 6 rail samples over a one week time frame, with estimated of $AU65, 000-$AU73, 100.

7.4.3 Designing of welding schedules cost time and money

Choosing the optimum parameters to weld pearlitic rail steel with maraging steel and other steel metal can be difficult. Expensive experimental trials are required Section 4.2, which were time consuming and expensive.

7.5 Recommendations for Further Research Investigating on IRJs

The literature review of prior published work on rail joints showed that there is little detailed documentation of behaviour for surface coated rail joints under a controlled load conditions in simulated wheel-Rig tests. The present rail rig test investigations provide preliminary findings of rolling contact behaviour for surface coated half joint rail without joint bars. It is recommended that the wheel-rail rig facility is exploited to its fullest capacity for IRJ specimens consisting of two rails with joint bars in order to investigate the effect of incorporation of joint bars into the system on the results. Results could then be followed up by in-field testing of IRJs clad using the improved procedures developed in this investigation.

Further studies can be done in measuring residual stresses for surface cladded rail joint before and after undergoing wheel-rail simulation rig test.

Another interesting area to work will be to find the optimum bath-tub groove profile for surface hard facing a profile which results in minimum damage accumulation during IRJ service. Finite element modelling may assist in the design of the optimum hard facing profile. The preliminary designs used in this project represents pilot research project and are intended to lay down the ground work and to demonstrate the possibility of surface cladding on rail surface. In the future, a finite element optimization program should be carried out as a screening test to represent

comparatively realistic representations of typical residual stress rail samples, including those with different surface hard facing profiles.

Additional ball-on--disc fatigue tests are recommended for wheel and surface coated rails. Disc in lubricated and in a dry state should be used for the testing in order to study how a coated surface affects the rolling contact fatigue behaviour of these materials by measuring contact surface roughness, surface residual stress and topography and also to verify the existence of any defects, such as surface cracks, pits or spalls initiated by coated rail surface, and in the subsurface regions of the bodies in contact.

In addition, Computational modelling of welding should be carried out compliment weld trials. This modelling can complement experimental trials, improving reliability and consistency, and optimising welding parameters to a level of sophistication and accuracy.

This model can help predict in thermal histories and development of residual stresses and distortion. This plays a key role for a rail joint structural integrity. Carrying out a computational modelling before a real weld trails can potentially bring down the finance related to welding schedules.

Finally, Due to limitation in budget and time in this project, half section of the rail joints were tested in wheel rail simulator and no strain gauges were used to measure the predicated strain under varying depths from the railhead surface.

In addition to strain gauges, an image analysis technique known as Particle Image Velocimetry (PIV) can be possibly used to measure the highly stressed region close to rail head to examine the stress-strain characteristics using successive digital images.

It's important to conduct more experiments using the wheel rail simulator for rail surface coated full rail joint section to further investigate the effect of the rail end gap. In this way, failure development with number of cycles across the rail gap can be examined

List of Papers to be published

A. C Rathod, V Luzin, D Wexler. A neutron diffraction investigation of residual stresses in the vicinity of bolt holes of insulated rail joints (*In preparation*)

B. C.Rathod, D.Wexler Mitigation of rolling contact fatigue on rail head surface of insulated rail joint (*In preparation*)

C. C.Rathod, D.Wexler Investigation of sliding wear and its relationship with rolling contact fatigue in coated and uncoated rail steel (*In preparation*)

D. V.Luzin, C.Rathod D.Wexler Residual stress measurements in insulated rail joints by neutron diffraction (*In Preparation*)

8 REFERENCES

AKHTAR, M. & DAVIS, D. 2008. Preliminary results of prototype insulated joint tests at the Facility for Accelerated Service Testing. *US Department of Transportation, Federal Railroad Administration, RR08-11*.

AKHTAR, M., DAVIS, D. & O'CONNOR, T. Revenue service evaluation of advanced design insulated joints. AREMA Conference Proceedings, 2008.

AKHTAR, M. N. & DAVIS, D. D. 2011. Rail joint assembly using embedded load transfer keys and method therefor. Google Patents.

ASKARINJEJAD, H., DHANASEKAR, M. & SIMSON, S. 2010. Effect of vertical misalignment of adjacent sleepers on the increase in dynamic loads around rail joints.

AUSTRALIAN RAIL TRACK CORPORATION. 2010. *NIJ-721 installation guide* [Online]. Available: https://extranet.artc.com.au/docs/eng/waivers/Closed%20Waivers/200_TR_080410_271.pdf [Accessed 2010 2010].

BANDULA-HEVA, T., DHANASEKAR, M. & BOYD, P. 2013. Experimental investigation of wheel/rail rolling contact at railhead edge. *Experimental Mechanics*, 53**,** 943-957.

BARKAN, C. P. L., PELTIER, D. C. & BARKAN, C. P. L. 2009. Characterizing and inspecting for progressive epoxy debonding in bonded insulated rail joints. *Transportation research record*, 2117**,** 85-92.

BODNER, S. & PARTOM, Y. 1975. Constitutive equations for elastic-viscoplastic strain-hardening materials. *Journal of Applied Mechanics*, 42**,** 385-389.

BOGDANSKI S, B. M. W. 2002. Modelling the three dimensional behaviour of shallow contact fatigue cracks in rails. *Wear,* 253**,** 17-25.

BOGDAŃSKI, S., STUPNICKI, J., BROWN, M. W. & CANNON, D. F. 1999. A two dimensional analysis of mixed-mode rolling contact fatigue crack growth in rails. *European Structural Integrity Society,* 25**,** 235-248.

BOWER, A. 1988. The influence of crack face friction and trapped fluid on surface initiated rolling contact fatigue cracks. *Journal of Tribology,* 110**,** 704-711.

BOWER, A. & JOHNSON, K. 1989. The influence of strain hardening on cumulative plastic deformation in rolling and sliding line contact. *Journal of the Mechanics and Physics of Solids,* 37**,** 471-493.

BOWER, A. & JOHNSON, K. 1991. Plastic flow and shakedown of the rail surface in repeated wheel-rail contact. *Wear,* 144**,** 1-18.

CANNON, D., EDEL, K. O., GRASSIE, S. & SAWLEY, K. 2003. Rail defects: an overview. *Fatigue & Fracture of Engineering Materials & Structures,* 26**,** 865-886.

CANNON, D. & PRADIER, H. 1996. Rail rolling contact fatigue research by the European Rail Research Institute. *Wear,* 191**,** 1-13.

CHEN, Y. & KUANG, J. 2002. Contact stress variations near the insulated rail joints. *Proceedings of the Institution of Mechanical Engineers, Part F: Journal of Rail and Rapid Transit,* 216**,** 265-273.

CLAYTON, P. 1996. Tribological aspects of wheel-rail contact: a review of recent experimental research. *Wear,* 191**,** 170-183.

CLAYTON, P. & HILL, D. 1987. Rolling contact fatigue of a rail steel. *Wear,* 117**,** 319-334.

CLINTON, S. 2009. Preliminary study into fatigue of insulated rail joints. Institute of Railway Technology at Monash University.

COPE, G. H. 1993. *British railway track design, construction and maintenance,* Barnsley, UK, Permanent Way Institute.

DAVIS, D. D. & AKHTAR, M. 2005a. Improving the performance of bonded insulated joints. *Railway track and structures,* 101.

DAVIS, D. D. & AKHTAR, M. 2006. Reduced impact bonded insulated joint designs. *Railway Track and Structures,* 102.

DAVIS, D. D., AKHTAR, M., KOHAKE, E. & HORIZNY, K. Effects of heavy axle loads on bonded insulated joint performance. Proceedings of the AREMA 2005 Annual Conference, 2005.

DAVIS, D. D. & AKHTAR, M. N. 2005b. Improving the performance of bonded insulated joints. *RT&S: Railway Track & Structures,* 101**,** 14-17.

DHANASEKAR, M. & DING, K. 2013. Rolling Contact Fatigue in Rail–Insulated Rail Joints (IRJ). *Encyclopedia of Tribology.* Springer.

DHANASEKAR, M. W. B. 2009. Review of the insulated rail joints. *CRC for Rail Innovation,* R3 100.

DONZELLA, G., FACCOLI, M., GHIDINI, A., MAZZU, A. & ROBERTI, R. 2005. The competitive role of wear and RCF in a rail steel. *Engineering fracture mechanics,* 72**,** 287-308.

EDEN, H., GARNHAM, J. & DAVIS, C. 2005. Influential microstructural changes on rolling contact fatigue crack initiation in pearlitic rail steels. *Materials science and technology,* 21**,** 623-629.

EKBERG, A. & KABO, E. 2005. Fatigue of railway wheels and rails under rolling contact and thermal loading—an overview. *Wear,* 258**,** 1288-1300.

EKBERG, A., KABO, E. & ANDERSSON, H. 2002. An engineering model for prediction of rolling contact fatigue of railway wheels. *Fatigue & Fracture of Engineering Materials & Structures,* 25**,** 899-909.

EKBERG, A. & SOTKOVSZKI, P. 2001. Anisotropy and rolling contact fatigue of railway wheels. *International journal of fatigue,* 23**,** 29-43.

ESVELD, C. 2001. Modern railway track.

FISCHER, F. & DAVES, W. 2011. A possible origin of surface cracks in rails. *Proceedings of the Institution of Mechanical Engineers, Part F: Journal of Rail and Rapid Transit,* 225**,** 605-611.

FREDERICK, C. 1993. Future rail requirements. *Rail Quality and Maintenance for Modern Railway Operation.* Springer.

GNÄUPEL-HEROLD, T. C. 1999. Neutron diffraction investigation of residual stresses in transverse/oblique rail slices subjected to different grinding stratagies. *National Institute of Standards and Technology Internal Report 6305.* Gaithersburg MD: U.S. Dept. of Commerce Technology Administration.

GULLERS, P., ANDERSSON, L. & LUNDÉN, R. 2008. High-frequency vertical wheel–rail contact forces—Field measurements and influence of track irregularities. *Wear,* 265**,** 1472-1478.

HAMILTON JR WILLIAM, R. 1968. Insulated rail joints. Google Patents.

HECKL, M. A. & ABRAHAMS, I. 2000. Curve squeal of train wheels, part 1: mathematical model for its generation. *Journal of Sound and Vibration,* 229**,** 669-693.

HIMEBAUGH, A. K., PLAUT, R. H. & DILLARD, D. A. 2008. Finite element analysis of bonded insulated rail joints. *International Journal of Adhesion and Adhesives,* 28**,** 142-150.

HIRAKAWA, K. & KUBOTA, M. 2001. On the fatigue design method for high-speed railway axles. *Proceedings of the Institution of Mechanical Engineers, Part F: Journal of Rail and Rapid Transit,* 215**,** 73-82.

HOJO, T., UMEKUBO, S. & SEKIGUCHI, K. 1965. GLUED RAIL JOINT FOR INSULATION. *Railway Technical Research Institute, Quarterly Reports,* 6.

HUANG, S. W., BURGESS, S., WEHRMANN, L. N., NOLAN, D. & CHANDRA, T. 2007. Insulated rail joints for signalling applications. *Materials Science Forum,* 539-543**,** 4069-4074.

HUTCHINSON, J. W. & SUO, Z. 1992. Mixed mode cracking in layered materials. *Advances in applied mechanics,* 29**,** 191.

IGWEMEZIE, J. & NGUYEN, A. T. 2009a. Anatomy of joint bar failures. *RT&S: Railway Track & Structures,* 105**,** 31-37.

IGWEMEZIE, J. & NGUYEN, A. T. A. 2009b. Anatomy of joint bar failures II. *Railway Track & Structures,* 105**,** 43-48.

IGWEMEZIE, J. & NGUYEN, A. T. A. 2010. Anatomy of joint bar failures III. *Railway Track & Structures,* 106**,** 31-36.

JIANG, Y. & SEHITOGLU, H. 1996. Rolling contact stress analysis with the application of a new plasticity model. *Wear,* 191**,** 35-44.

JOHNSON, K. L. & JOHNSON, K. L. 1987. *Contact mechanics,* Cambridge university press.

JOHNSON, P. & WISE, S. 1970. Significance of a detection of defects in rails. *Non-Destructive Testing,* 3**,** 111-116.

KABO, E. 2002. Material defects in rolling contact fatigue—influence of overloads and defect clusters. *International journal of fatigue,* 24**,** 887-894.

KALOUSEK, J. & BETHUNE, A. 1978. Rail wear under heavy traffic conditions. *Rail Steels—Developments, Processing, and Use.* ASTM International.

KALOUSEK, J., SROBA, P. & HEGELUND, C. Analysis of rail grinding tests and implications for corrective and preventative grinding. Fourth International Heavy Haul Railway Conference 1989: Railways in Action; Preprints of Papers, The, 1989. Institution of Engineers, Australia, 193.

KAPOOR, A., FRANKLIN, F., WONG, S. & ISHIDA, M. 2002. Surface roughness and plastic flow in rail wheel contact. *Wear,* 253**,** 257-264.

KATAOKA, H., OIKAWA, Y., WAKATSUKI, O. & ABE, N. 2005. Dynamic analysis of stresses and evaluation of service life of jointed rails. *Quarterly Report of RTRI,* 46**,** 250-255.

KELLEHER, J., PRIME, M., BUTTLE, D., MUMMERY, P., WEBSTER, P., SHACKLETON, J. & WITHERS, P. 2003. The Measurement of Residual Stress in Railway Rails by Diffraction and other Methods*. *Journal of Neutron Research,* 11**,** 187-193.

KERR, A. D. & COX, J. E. 1999. Analysis and tests of boned insulted rail joints subjected to vertical wheel loads. *International Journal of Mechanical Sciences,* 41**,** 1253-1272.

KOH, C., CHUA, K., LO, K. & LEE, S. 1993. Impact noise at insulated rail joint.

KONDO, K., YOROIZAKA, K. & SATO, Y. 1996. Cause, increase, diagnosis, countermeasures and elimination of Shinkansen shelling. *Wear,* 191**,** 199-203.

KUMAR, S. 2006. *A study of the rail degradation process to predict rail breaks.* Division of Operation and Maintenance Engineering, Luleå University of Technology.

KUMAR, S., ESPLING, U. & KUMAR, U. 2008. Holistic procedure for rail maintenance in Sweden. *Proceedings of the Institution of Mechanical Engineers, Part F: Journal of Rail and Rapid Transit,* 222**,** 331-344.

LEWIS, R. & OLOFSSON, U. 2009. *Wheel-rail interface handbook,* Elsevier.

LI, Z., ZHAO, X., ESVELD, C., DOLLEVOET, R. & MOLODOVA, M. 2008. An investigation into the causes of squats—Correlation analysis and numerical modeling. *Wear,* 265**,** 1349-1355.

LIU C D, B. M. N., LAWRENCE S 1995. Dependence of the fatigue limit of rail steels on stress intensity factor near inclusions. *Engng Fract mech,* 50**,** 301-307.

LIU, X., SAAT, M. & BARKAN, C. 2012. Analysis of causes of major train derailment and their effect on accident rates. *Transportation Research Record: Journal of the Transportation Research Board***,** 154-163.

LIU, Y., LIU, L. & MAHADEVAN, S. 2007. Analysis of subsurface crack propagation under rolling contact loading in railroad wheels using FEM. *Engineering fracture mechanics,* 74**,** 2659-2674.

LONSDALE, C. & ENGINEER, M. 1999. Thermite rail welding: history, process developments, current practices and outlook for the 21st century. *The American Railway Engineering and Maintenance-of-way Association, Chicago, IL,* 2000.

LUZIN, V., GNAUPEL-HEROLD, T., GORDON, J. E. & PRASK, H. J. 2004. Neutron residual stress measurements on rail sections for different production conditions. *Rail Transportation,* 28**,** 117-122.

LUZIN, V., PRASK, H.-J., GNAUPEL-HEROLD, T., GORDON, J., WEXLER, D., RATHOD, C., PAL, S., DANIEL, W. & ATRENS, A. 2013a. Neutron residual stress measurements in rails. *Neutron News*, 24**,** 9-13.

LUZIN, V., RATHOD, C., WEXLER, D., BOYD, P. & DHANASEKAR, M. 2013b. Residual stresses in rail-ends from the in-service insulated rail joints using neutron diffraction. *Materials Science Forum*, 768-769**,** 741-746.

MAGEL, E., RONEY, M., KALOUSEK, J. & SROBA, P. 2003. The blending of theory and practice in modern rail grinding. *Fatigue & Fracture of Engineering Materials & Structures*, 26**,** 921-929.

MAGEL, E., SROBA, P., SAWLEY, K. & KALOUSEK, J. 2005. Control of rolling contact fatigue of rails. *Center for Surface Transportation Technology, National Research Council Canada*.

MAGEL, E. E. & KALOUSEK, J. 2002. The application of contact mechanics to rail profile design and rail grinding. *Wear*, 253**,** 308-316.

MANDAL, N. K. 2014. Ratchetting of railhead material of insulated rail joints (IRJs) with reference to endpost thickness. *Engineering Failure Analysis*, 45**,** 347-362.

MANDAL, N. K. & DHANASEKAR, M. 2013. Stress analysis of inserted rail joints.

MANDAL, N. K. & PEACH, B. 2010. An engineering analysis of insulated rail joints: a general perspective.

MASSE, T., CHASTEL, Y., MONTMITONNET, P., BOBADILLA, C., PERSEM, N. & FOISSEY, S. 2011. Impact of mechanical anisotropy on the geometry of flat-rolled fully pearlitic steel wires. *Journal of Materials Processing Technology*, 211**,** 103-112.

MASUMOTO, H., SUGINO, K., NISIDA, S., KURIHARA, R. & MATSUYAMA, S. 1978. Some features and metallurgical considerations of surface defects in rail due to contact fatigue. *Rail Steels—Developments, Processing, and Use*. ASTM International.

MAYVILLE, R. & STRINGFELLOW, R. 1995. Numerical analysis of a railroad bolt hole fracture problem. *Theoretical and applied fracture mechanics*, 24**,** 1-12.

MCDOWELL, D. 1995. Stress state dependence of cyclic ratchetting behavior of two rail steels. *International Journal of Plasticity*, 11**,** 397-421.

NELSON, A. D. & GOKEN, G. L. 1976. Adhesively bonded rail joint. Google Patents.

NICOLI, E., DILLARD, D., DILLARD, J., CAMPBELL, J., DAVIS, D. & AKHTAR, M. 2011. Using standard adhesion tests to characterize performance of material system options for insulated rail joints. *Proceedings of the Institution of Mechanical Engineers, Part F: Journal of Rail and Rapid Transit*, 225**,** 509-522.

OLOFSSON, U. & LEWIS, R. 2006. 5 Tribology of the Wheel–Rail Contact. *Handbook of railway vehicle dynamics***,** 121.

OLVER, A. 2005. The mechanism of rolling contact fatigue: an update. *Proceedings of the Institution of Mechanical Engineers, Part J: Journal of Engineering Tribology*, 219**,** 313-330.

ORRINGER, O. 1990. *Control of rail integrity by self-adaptive scheduling of rail tests,* Washington, DC., U.S. Department of Transportation, Federal Railroad Administration, Office of Research and Development ; National Technical Information Service distributor.

PAGE, D. R. 1903. Railway-rail joint. Google Patents.

PANG, T. 2007. *Studies on wheel / rail contact : impact forces at insulated rail joints.* Master Degree, Central Queensland University.

PANG, T. & DHANASEKAR, M. Dynamic finite element analysis of the wheel-rail interaction adjacent to the insulated rail joints. Proceedings of the International Conference, Contact Mechanics, 2006.

PAPAELIAS, M. P., ROBERTS, C. & DAVIS, C. 2008. A review on non-destructive evaluation of rails: state-of-the-art and future development. *Proceedings of the Institution of Mechanical Engineers, Part F: Journal of Rail and rapid transit,* 222**,** 367-384.

PELTIER, D. & BARKAN, C. 2009. Characterizing and inspecting for progressive epoxy debonding in bonded insulated rail joints. *Transportation Research Record: Journal of the Transportation Research Board***,** 85-92.

PELTIER, D., BARKAN, C. P., DOWNING, S. & SOCIE, D. 2004. Measuring degradation of bonded insulated rail joints. *Urbana.* University of Illinois

PLAUT, R. H., LOHSE-BUSCH, H., ECKSTEIN, A., LAMBRECHT, S. & DILLARD, D. A. 2007a. Analysis of tapered, adhesively bonded, insulated rail joints. *Proceedings of the Institution of Mechanical Engineers,* 221**,** 195-204.

PLAUT, R. H., LOHSE-BUSCH, H., ECKSTEIN, A., LAMBRECHT, S. & DILLARD, D. A. 2007b. Analysis of tapered, adhesively bonded, insulated

rail joints. *Proceedings of the Institution of Mechanical Engineers, Part F: Journal of Rail and Rapid Transit,* 221**,** 195-204.

PONTER, A., HEARLE, A. & JOHNSON, K. 1985. Application of the kinematical shakedown theorem to rolling and sliding point contacts. *Journal of the Mechanics and Physics of Solids,* 33**,** 339-362.

POPOVIC, O. & PROKIC-CVETKOVIC, R. 2012. *Surface welding as a way of railway maintenance,* INTECH Open Access Publisher.

RATHOD, C., WEXLER, D., CHANDRA, T. & LI, H. Microstructural characterisation of railhead damage in insulated rail joints. Materials Science Forum, 2012. Trans Tech Publ, 2937-2942.

RATHOD, C., WEXLER, D., LUZIN, V., BOYD, P. & DHANASEKAR, M. 2014. A neutron diffraction investigation of residual stresses in rail ends after severe deformation of rail surfaces. *Materials Science Forum,* 777**,** 213-218.

REDDY, V. 2004. *Modelling and analysis of rail grinding and lubrication strategies for controlling rolling contact fatigue (RCF) and rail wear.* Master by Research, Queensland University of Technology.

REDDY, V., CHATTOPADHYAY, G., LARSSON-KRAIK, P.-O. & ALLAHMANLI, T. Evaluation of technical vs economic decisions in rail grinding. Industrial Engineering and Engineering Management, 2008. IEEM 2008. IEEE International Conference on, 2008. IEEE, 496-500.

RINGSBERG J W, B. A. 2003. On propagation of short rolling contact fatigue cracks *Fatigue Fract Engng Mater Struct,* 26**,** 969-983.

RINGSBERG, J. W. 2000. Cyclic ratchetting and failure of a pearlitic rail steel. *Fatigue & Fracture of Engineering Materials & Structures,* 23**,** 747-758.

RINGSBERG, J. W. 2001. Life prediction of rolling contact fatigue crack initiation. *International Journal of fatigue,* 23**,** 575-586.

RINGSBERG, J. W. & LINDBÄCK, T. 2003. Rolling contact fatigue analysis of rails inculding numerical simulations of the rail manufacturing process and repeated wheel-rail contact loads. *International Journal of fatigue,* 25**,** 547-558.

SALEHI, I., KAPOOR, A. & MUTTON, P. 2011. Multi-axial fatigue analysis of aluminothermic rail welds under high axle load conditions. *International Journal of Fatigue,* 33**,** 1324-1336.

SANDSTRÖM, J. & EKBERG, A. 2009. Numerical study of the mechanical deterioration of insulated rail joints. *Proceedings of the Institution of Mechanical Engineers, Part F: Journal of Rail and Rapid Transit,* 223**,** 265-273.

SASAKI, T., TAKAHASHI, S., KANEMATSU, Y., SATOH, Y., IWAFUCHI, K., ISHIDA, M. & MORII, Y. 2008. Measurement of residual stresses in rails by neutron diffraction. *Wear,* 265**,** 1402-1407.

SATO, Y., MATSUMOTO, A. & KNOTHE, K. 2002. Review on rail corrugation studies. *Wear,* 253**,** 130-139.

SCHLEINZER, G. & FISCHER, F. 2001. Residual stress formation during the roller straightening of railway rails. *International Journal of Mechanical Sciences,* 43**,** 2281-2295.

SHENG, X., THOMPSON, D. J., JONES, C. J., XIE, G., IWNICKI, S. D., ALLEN, P. & HSU, S. S. 2006. Simulations of roughness initiation and growth on railway rails. *Journal of Sound and Vibration,* 293**,** 819-829.

SMITH, R. 2002a. Rolling contact fatigue of rails: what remains to be done? *China Railway Science,* 3**,** 001.

SMITH, R. 2002b. Rolling Contact Fatigue of Rails: What Remains to be Done?[J]. *China Railway Science,* 3**,** 001.

STEENBERGEN, M. J. M. M. 2008. *Wheel-rail interaction at short-wave irregularities*, TU Delft, Delft University of Technology.

SURESH, S. 1998. *Fatigue of materials*, Cambridge university press.

SUZUKI, T., ISHIDA, M., ABE, K. & KORO, K. 2005. Measurement on dynamic behaviour of track near rail joints and prediction of track settlement. *Quarterly Report of RTRI,* 46**,** 124-129.

TALAMINI, B., JEONG, D. Y. & GORDON, J. 2007. Estimation of the fatigue life of railroad joint bars.

TELLISKIVI, T. & OLOFSSON, U. 2001. Contact mechanics analysis of measured wheel-rail profiles using the finite element method. *Proceedings of the Institution of Mechanical Engineers, Part F: Journal of Rail and Rapid Transit,* 215**,** 65-72.

TILLBERG, J., LARSSON, F. & RUNESSON, K. 2009. A study of multiple crack interaction at rolling contact fatigue loading of rails. *Proceedings of the Institution of Mechanical Engineers, Part F: Journal of Rail and Rapid Transit,* 223**,** 319-330.

TOTTEN, G. E. 2002. *Handbook of residual stress and deformation of steel*, ASM international.

VITEZ, I., ORUČ, M., KRUMES, D. & KLADARIĆ, I. 2007. Damage to railway rails caused by exploitation. *Metalurgija,* 46**,** 123-128.

WEBSTER, G., WEBSTER, P., BOURKE, M., LOW, K., MILLS, G., MCGILLIVRAY, H., CANNON, D. & ALLEN, R. 1992. Neutron diffraction determinations of residual stress patterns in railway rails. *Residual Stress in Rails, ibid***,** 143-152.

WEBSTER, P., LOW, K., MILLS, G. & WEBSTER, G. Neutron measurement of residual stresses in a used railway rail. MRS Proceedings, 1989. Cambridge Univ Press, 311.

WEBSTER, P. J. L., K.S; MILLS, G; WEBSTER, G.A 1993. Neutron measurement of residual stresses in a used railway rail. *NDT & E International,* 26**,** 311-316.

WEN, Z., JIN, X. & ZHANG, W. 2005. Contact-impact stress analysis of rail joint region using the dynamic finite element method. *Wear,* 258**,** 1301-1309.

WILSON, A., KERR, M., MARICH, S. & KAEWUNRUEN, S. Wheel/rail conditions and squat development on moderately curved tracks. CORE 2012: Global Perspectives; Conference on railway engineering, 10-12 September 2012, Brisbane, Australia, 2012. Engineers Australia, 223.

WITHERS, P. 2007. Residual stress and its role in failure. *Reports on progress in physics,* 70**,** 2211.

WONG, S., BOLD, P., BROWN, M. & ALLEN, R. 2000. Fatigue crack growth rates under sequential mixed-mode I and II loading cycles. *Fatigue & fracture of engineering materials & structures,* 23**,** 667-674.

WU, T. & THOMPSON, D. 2003. On the impact noise generation due to a wheel passing over rail joints. *Journal of Sound and Vibration,* 267**,** 485-496.

YASUHARA, H. 1984. Development of a long life insulated rail joint. *Quarterly reports of the Railway Technical Research Institute,* 25**,** 79-84.

ZERBST, U., LUNDÉN, R., EDEL, K.-O. & SMITH, R. A. 2009. Introduction to the damage tolerance behaviour of railway rails–a review. *Engineering fracture mechanics,* 76**,** 2563-2601.

ZERBST, U., MÄDLER, K. & HINTZE, H. 2005. Fracture mechanics in railway applications—an overview. *Engineering Fracture Mechanics,* 72**,** 163-194.

ZONG, N. 2013. Development of optimal designs of insulated rail joints.

ZONG, N., WEXLER, D. & DHANASEKAR, M. 2013. Structural and material characterisation of insulated rail joints. *Electronic Journal of Structural Engineering,* 13**,** 75-87.

9 APPENDICES

9.1 Paper A: Microstructural characterisation of railhead damage in insulated rail joints

Materials Science Forum Vols. 706-709 (2012) pp 2937-2942
© (2012) Trans Tech Publications, Switzerland
doi:10.4028/www.scientific.net/MSF.706-709.2937

Microstructural characterisation of railhead damage in insulated rail joints

C.Rathod[1a], D.Wexler[1b], T. Chandra[1c] and H. Li[1d]

[1] Faculty of Engineering, University of Wollongong, Northfields Ave, Wollongong Australia 2522

[a]crr716@uowmail.edu.au, [b]davidw@uow.edu.au, [c]t.chandra@uow.edu.au, [d]huijun_Li@uow.edu.au

Keywords: Insulated rail joints, rail, head hardened, surface coated rail

Abstract

As an integral part the railway network infrastructure, insulated rail joints (IRJs) electrically isolate track segments providing critical feedback to both track signaling and train position detection systems. Because of the discontinuous nature of IRJs, accumulated damage at the railhead is high. Failure modes include plastic flow of metal across joints, bolt and fishplate failures, delamination of insulated material and, as a result of rolling contact fatigue, end post and endpost surface damage. In the current investigation, microstructural changes in the vicinity of endposts of IRJs made from both surface coated and uncoated rail are investigated using techniques of optical and scanning electron microscopy. Damaged IRJs made from pearlitic head hardened rail steel are compared with head hardened rail steel laser coated with martensitic stainless steel, the latter having an increased service life. Problems associated with the surface coating are identified and approaches to further improving IRJ resistance to rolling contact fatigue suggested.

Introduction and Background

Insulated Rail Joints (IRJs) play a key role in signaling systems in rail networks. End-to-end track sections are separated by a short insulating gap, often called an end post, while rigidity of IRJ components is obtained by bolted side joint bars, called fishplates, which are also electrically isolated from the track by a layer of composite resin [1, 2] (Fig. 1).

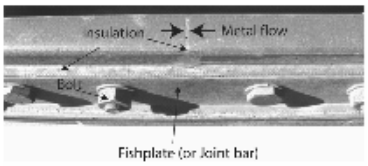

Figure 1, a straight cut IRJ displaying evidence of gap narrowing.

IRJ assemblies enable electrical isolation of track sections so that an electrical signal passing through a train's wheels can be used for a variety of functions including signaling the train's position and activate initiate of events such as the closing of level crossing boom gates. IRJs also play a secondary role as an aid to the detection of rail fractures in track segments. However, as one of the weakest components of the rail track systems [3], IRJ's pose a significant impact on maintenance costs due to their low and fluctuating service lives compared to continuously welded rail sections. The poor service reliability of IRJs is a particular problem in heavy haul rail corridors. Within Australia, 4-bolt and 6-bolt joint bars are the two most common IRJ assembly designs. The fishplate/bolt assemblies insulation is achieved by plastic liners for the fishplate, or by fully insulated fishplate encased by plastic liners/phenolic resins or/and by glued joints covered with epoxy resin/polyester and are subsequently welded into the track of desired short rail length.

A majority of IRJ failures in Australian heavy haul rail corridors are caused by flow of steel over the rail end-posts [4] High impact forces cause rail damage such as spalling, squashing, and saddle backed wear [5]. Deterioration of the integrity of the bolt, fishplate, epoxy bonding and support configurations, which themselves experience combined lateral and vertical bending stresses, leads to a vicious circle accelerating the failure at the joint [6-8]. Failure itself is generally characterised by either an unsafe gap or other evidence of defects which might result in catastrophic failure. Grinding out the track surface can mitigate problems associated with metal flow over the gap [9-10]. However, eventually the IRJ assembly must be replaced. This involves cutting out of a section of track, around 1.5-2.5 m in length, and rewelding a new length of track containing the new IRJ.

Various approaches have been employed to increase the lifetimes of IRJs. These include; decreasing the gap size, from 7-8 mm to around 5-6 mm, which results in less impact on rail ends; experimentation with the suspension and support configuration to give high deflections and lower impact loads [11, 12]; and altering the length of the joint bars according to whether they are 4-bolt or 6-bolt joints [13]. One to reducing the wheel-rail impact over joints has been to change from straight/conventional IRJs to 15 degree tapered cut IRJs (Fig. 2(a)). However, even after changing to tapered cut joint, metal flow at the surface was not completely eliminated [14]. A recent approach has involved use of a surface coating applied at the railhead with a hard tough material with high hardness, higher yield stress limit than the rail steel. It is expected that higher hardness and toughness of the rail might reduce the extent of rail-end flow leading to reducing maintenance and replacement.

As part of our effort to increase understanding of relationships between IRJ design and lifetime we compared degradation mechanisms in two different angled cut IRJs, one made from head hardened rail and deemed to be a failed joint due to metal flow, and second, a coated joint removed from service after the same period of operation under heavy haul rail traffic. Hereafter, the uncoated rail and grade 431 martensitic stainless steel laser coated rail will be designated as Rail U and Rail C respectively.

Experimental

Both the coated and uncoated angle cut, 6-bolt, IRJs were fabricated from Australian standard 60g grade head hardened steel AS 1085.12 with composition as listed in Table 1.

Table 1: Chemical Composition of Rail Steels.

Element	C	P	Mn	Si	S	Ni	Cr	Mo	Cu	Al	Sn
Wt%	0.64	0.031	0.75	0.15	0.027	0.024	0.062	<0.002	0.041	0.003	0.003

The test piece for surface coating with MSS was prepared by machining a "bathtub" shape into the head of the rail and then powder laser depositing of a 431 Martensitic Stainless Steel (MSS), as shown in Fig 2. Laser deposition has chosen over other deposition technique because of the finer microstructure and smaller heat affected zones compared to that resulting from deposition techniques such as hard facing by stick weld deposition. Full details are of the deposition methodology are commercial-in-confidence.

Macro optical imaging and both optical and scanning electron microscopies were used as the principal analytical techniques for this investigation. Specimens of rail head in the vicinity of the rail ends were sectioned in transverse and longitudinal directions to the long axis of the rail. Macro images were obtained from separated rail ends with no cleaning or chemical treatment. Samples

prepared for microscopy and hardness testing were ground and polished to a 1μm finish and etched with 2% nital solution and 10% oxalic acid. A Leica DMRM was used for optical microscopy. Microhardness in transverse section was performed using LECO M-400-H1 Hardness machine at 500gram load. Hardness values associated with a particular region were taken as an average of 8-10 readings. A JEOL JSM-6490LA model scanning electron microscope equipped with JEOL x-ray energy dispersive analysis system was used for secondary electron and backscattered electron SEM imaging.

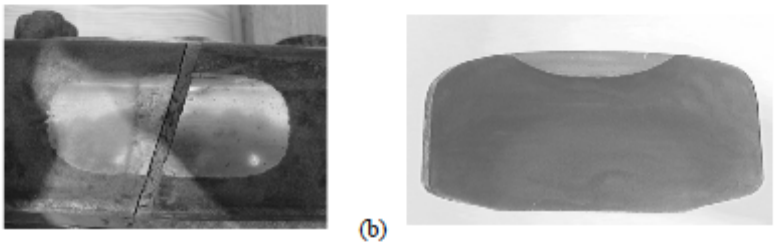

Figure 2 Martensitic stainless steel IRJ, (a) top view of ex-service IRJ fabricated with a 15 degree angle cut, (b) section showing bathtub shape of metal deposit,.

Results and Discussion

Uncoated rail (Rail U)

The rail ends of the failed uncoated joint showed severe deformation in the head hardened region, near the top rail surface, with microstructural evidence of both metal flow over the rail ends metal fracture, and in-service related fatigue mechanisms consistent with rolling contact fatigue [11]. Macro metallographic results obtained from one rail end are described in Fig 3, which includes (a) side-on and (b) top views of the damage rail end. The direction of travel of the rail traffic was in the direction of the metal flow. Top surface cracks in the feature protruding around 2 mm over the rail end are revealed in Fig 3(c) and the whole feature was easily removed from the rail head ((compare Fig 3(c) and 3(d)).

Collected evidence suggests strongly that sub-surface-initiated cracks are propagated by a rolling contact fatigue mechanism that has led to spalling of the hard surface of the head hardened. Beach/striation marks are evident on the fracture surface (Fig 3(e)) which is attributed by the repeated rolling-sliding contact loading. Due to uniformity of loading beach marks are fairly similarly spaced and fairly uniform in appearance. Fatigue failures occur due to high cyclic loading which initiates the crack and propagates until a stress much lower than that necessary to cause a fracture [12]. The region inside the oval box contains the initial beach marks (the smallest elliptical features) and this is believed to be where the cracking has initiated. SEM-EDS investigations of regions below the rail surface (not shown) revealed inclusions including MnS which are likely sites for crack initiation.

Uncoated rail (Rail U)

Damage to the IRJ ends of the stainless coated samples (Fig 4) was significantly different to that of the head hardened rail. Plastic deformation over the top surface of the centre of the rail was less, consistent with expected mechanical property advantages of martensitic stainless steel over medium carbon rail steel (hardness, toughness, flow stress). However, there was notable plastic deformation

in the coated sample in the vicinity of the interfaces between the rail steel and coating near at the top surface of the coating (Fig 4(a) – (c)). This, in part, could be related to mismatches in metal flow, being greater for the rail steel than for the stainless steel. The type of cracking differed on each side of the track, with more oblique crack growth (Fig 4(c)) on the gauge (wheel) side (wheel side) than near the field side. One approach to mitigating the problems near the top rail surfaces might be via re-design of the shape of the coating profile. The shallow angle of between the stainless steel-rail steel interface and the top surface of the rail (<30 degrees) could be changed to a much steeper angle (near 90 degrees) to reduce the component of shear stresses acting on the interface.

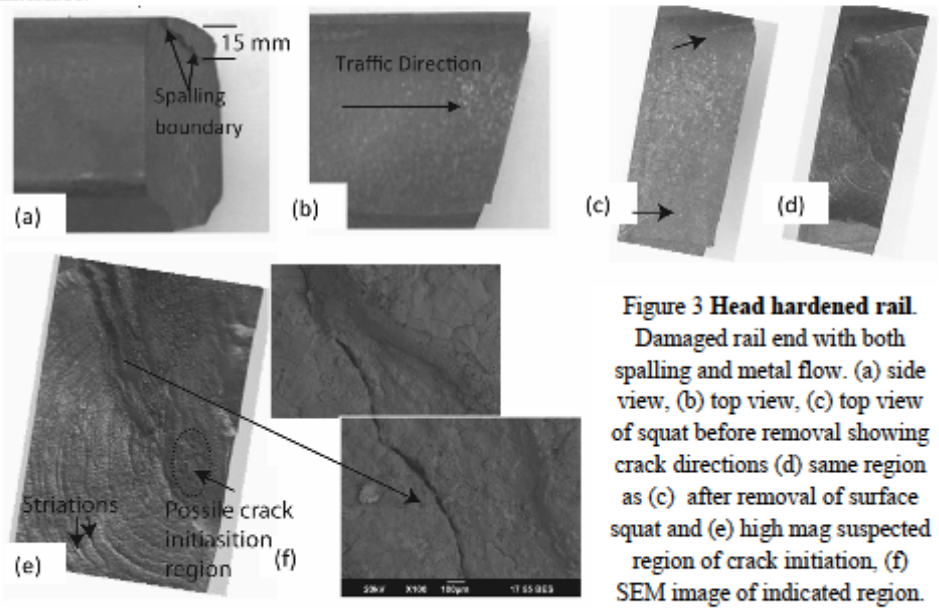

Figure 3 **Head hardened rail**. Damaged rail end with both spalling and metal flow. (a) side view, (b) top view, (c) top view of squat before removal showing crack directions (d) same region as (c) after removal of surface squat and (e) high mag suspected region of crack initiation, (f) SEM image of indicated region.

Examination of both transverse sections (Fig 4(d)) and longitudinal sections (not shown) located well below the top rail surface revealed cracks originating in regions of weld porosity and defects in the vicinity of interface between the rail steel and the coating (Fig 4(d) and SEM image, Fig 4(e)). Cracks associated with inclusions in the rail steel and in regions in the vicinity of the stainless steel-rail steel interface were also observed but are not shown. It is expected that complex residual stresses originating from the mismatches in thermal expansion coefficient of the two different types of steel contribute to the problem of interface cracking, crack initiation and crack growth both before and during service life. Based on these results, apart from void formation, major issues to deal with during the initial laser cladding process include the management of defects initiated in the heat affected zone of the rail steel and the formation of Cr rich precipitates on the interface.

Transverse cross-sections of the head hardened rail and weld inlay rail samples were examined with data obtained from the rail surfaces going down into the rail head. For a position around 10 cm back from the rail end the uncoated head hardened rail had mean microhardnesses of; 430HV (500g), 350HV (500g), 267HV (500g) 1mm below the top surface, in the subsurface, and in a regions below the head hardened surface, respectively. There were in accordance with typical values for this grade of head hardened rail. Trends in microhardness profiles close to the top surfaces of both samples, from the centre of railhead to a depth, of 10 mm, are shown in Fig. 5. Factors contributing to these results include; (i) the higher hardness of the martensitic stainless steel over the rail steel, (ii) changes in head hardness of the head hardened steel as a function of depth and (iii) surface strain hardening effects associated with deformation during service life.

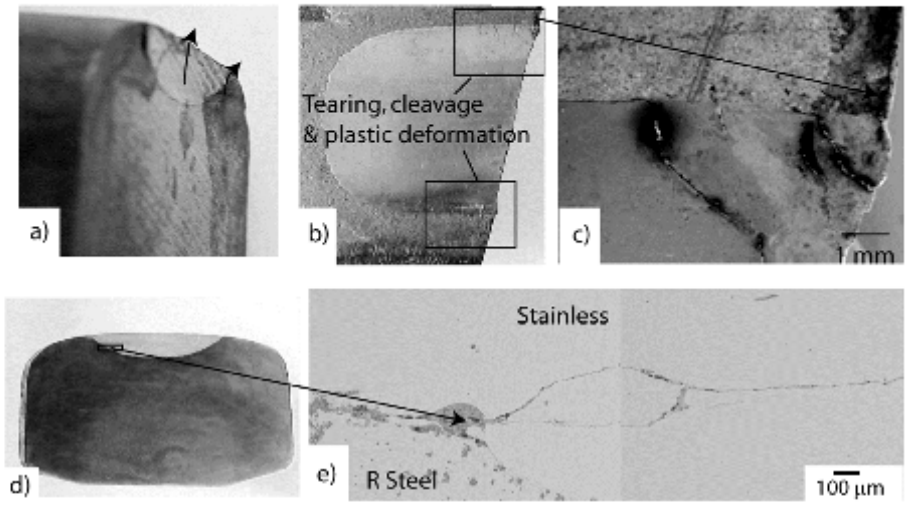

Figure 4 **Laser surface coated rail**. (a) rail end (b) top view, (c) SEM image of metal flow at rail end on wheel side of track (d) polished section 10 mm back from the rail end, (e) SEM image of void formation at interface between stainless and rail steel

Hardness results

Figure 5 Surface hardness profiles for coated and uncoated head hardened rail for the first 10 mm below the top surfaces and around 10 mm back from the rail ends.

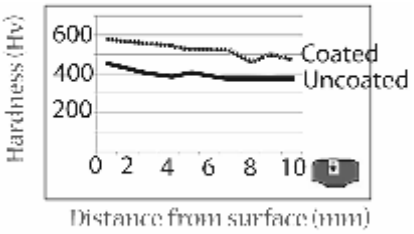

The interpretation of the latter requires data concerning complex stress and strain distributions in the railhead at and just below the rail surfaces at the rail ends. Because the rail end is free these will differ significantly from that occurring in the bulk rail. A series of experiments is currently underway using neutron diffraction to measure strain distributions in the immediate vicinity of IRJ rail ends. Further SEM-EBSD and advanced electron microscopy will be required to relate this to microstructure and properties. Alternative coating materials are also under investigation.

Conclusions and Suggestions

1. Damage to the head hardened rail IRJ ends was characterized by metal flow, RCF, and microstructural features such as spalling and cracking.

2. Compared to head hardened rail, the laser coated IRJ suffered less damage for the same heavy haul lifecycle, apparently due to the improved mechanical properties of martensitic stainless steel over medium carbon rail steel.

3. Damage to the IRJ ends of the laser coated samples was characterized by:

(i) Surface damage related to mismatches in metal flow of the two steel types, greater for the rail steel than the martensitic stainless and accentuated by the shallow angle of the interface to the rail surface and, (ii), cracking associated with the laser deposition procedure; the mismatch in thermal expansion properties of the two steel types, void formation during fabrication, defects and weakening of the heat affected zone of the base steel.

4. Two approaches might be considered to improve the properties of the coated IRJ; redesigning the shape and position of the hard facing region to reduce surface deformation mismatches during service and selection of a weld deposit material of compatibility of thermal expansion properties.

Acknowledgements

Financial support for this project comes from the Australian CRC for Rail Innovation, Proj. R3.100, Longer life insulated rail joints. Grateful thanks to Prof M. Dhanasekar of Queensland Univ. of Technology for expert guidance and Mr B Taylor from the Australian Track and Rail Coproation for arranging the procurement of damaged IRJ samples.

References

[1] D. Peltier, C.P.L.Barkan, S.Downing, D.Socie: *Measuring degradation of bonded insulated rail joints*, University of Illinois at Urbana-Champaign, Urbana,IL 61801.
[2] S.W. Huang, S. Burgess, L. N. Wehrmann, D. Nolan and T. Chandra; *Insulated rail joints for signalling applications*, Proc. THERMEC 2006 Int. Conf. on Processing & Manufacturing of Advanced Materials, Ed. T.Chandra et al., Trans Tech. (2006).
[3] Y. Hiroto: *Development of a long life Insulated Rail Joint*, Quarterly reports of the Railway Technical Research, Vol.25 (1984) p.79.
[4] C.Smalley: *Preliminary study into fatigue of Insulated Rail Joints*, Institute of Railway Technology at Monash University, (2009).
[5] Z. Wen, X. Jin, W. Zhang: *Contact-impact stress analysis of rail joint region using the dynamic finite element method*, Wear, Vol.258 (2005), p.1301.
[6] D.C. Peltier, C.P.L.Barkan: *Characterizing and inspecting for progressive epoxy*, Journal of the Transportation Research Record, Vol.11, (Dec 2009) p.85.
[7] J. Igwemezie, A.T. Nguyen: *Anatomy of joint bar failures II*, Railway Track & Structures, Vol. 105, Issue 10, (Oct 2009) p.43.
[8] J. Igwemezie, A.T. Nguyen: *Anatomy of joint bar failures III*, Railway Track & Structures, Information on http://www.rtsnds.com, (Feb 2010).
[9] V. Reddy : *Modelling and Analysis of Rail Grinding & Lubrication strategies for Controlling Rolling Contact fatigue(RCF) and Rail Wear*, Master of Applied Science Thesis, Queensland University of Technology, (May, 2004).
[10] J.J.Han, M. Dhanasekar: *A method for tracking internal crack propagation in railhead*, International Journal of Fracture, Vol.130, (2004) p.705.
[11] Tao. Pang: *Studies on Wheel/Rail contact-Impact forces at the Insulated rail Joints*, Master of Engineering Thesis, Central Queensland University, Australia (June, 2007).
[12] A.K. Himebaugh, R.H. P, D.A. Dillard: *Finite element analysis of bonded insulated rail joints*, International journal of Adhesion & Adhesives, Vol. 28, (2008), p. 142.
[13] B. Talamini, D.Y. Jeong, J. Gordon, *Estimation of the fatigue life of railroad joint bars*, Proceedings of Joint Rail Conference & Internal Combustion Engine Spring Technical Conference, Colorado, USA, (March,2007).
[14] R.H. Plaut, H.L.Busch, A. Eckstein, S. Lambrecht, D.A. Dillard: *Analysis of tapered, adhesively bonded, insulated rail joints*, Proceedings of the Institution of Mechanical Engineers, Vol. 221 (Jun 2007) p. 195.

9.2 Paper B: Residual stresses in rail ends from the in-service insulated rail joints using neutron diffraction

2014

Residual stresses in rail-ends from the in-service insulated rail joints using neutron diffraction

Vladimir Luzin
Australian Nuclear Science And Technology Organisation

Chandrahas Rathod
University of Wollongong, crr716@uowmail.edu.au

David Wexler
University of Wollongong, davidw@uow.edu.au

Paul Boyd
Central Queensland University

Manicka Dhanasekar
Queensland University of Technology

Publication Details

Luzin, V., Rathod, C., Wexler, D., Boyd, P. & Dhanasekar, M. (2014). Residual stresses in rail-ends from the in-service insulated rail joints using neutron diffraction. Materials Science Forum, 768-769 741-746.

Materials Science Forum Vols. 768-769 (2014) pp 741-746 *Online: 2013-09-23*
© (2014) Trans Tech Publications, Switzerland
doi:10.4028/www.scientific.net/MSF.768-769.741

Residual stresses in rail-ends from the in-service insulated rail joints using neutron diffraction

Vladimir Luzin[1, a], Chandrahas Rathod[2, b], David Wexler[2, c], Paul Boyd[3, d], Manicka Dhanasekar[4, e]

[1]Australian Nuclear Science & Technology Organisation, Lucas Heights, NSW, Australia

[2]Engineering faculty, Wollongong University, Northfields Ave, Wollongong, NSW, Australia

[3]Centre for Railway Engineering, Central Queensland University, Rockhampton, QLD, Australia

[4]Faculty of Built Environment & Engineering, QUT, Brisbane, QLD, Australia

[a]vll@ansto.gov.au, [b]crr716@uowmail.edu.au, [c]davidw@uow.edu.au, [d]p.boyd@cqu.edu.au, [e]m.dhanasekar@qut.edu.au,

Keywords: insulated rail joints, neutron diffraction, residual stress, accumulated stress, pearlitic steel, rail head.

Abstract

Insulated rail joints (IRJs) are an integral part of the rail track signaling system and pose significant maintenance and replacement costs due to their low and fluctuating service lives. Failure occurs mainly in rail head region, bolt- holes of fishplates and web-holes of the rails. Propagation of cracks is influenced by the evolution of internal residual stresses in rails during rail manufacturing (hot-rolling, roller-straightening, and head-hardening process), and during service, particularly in heavy rail haul freight systems where loads are high. In this investigation, rail head accumulated residual stresses were analysed using neutron diffraction at the Australian Nuclear Science and Technology Organisation (ANSTO). Two ex-service two head-hardened rail joints damaged under different loading were examined and results were compared with those obtained from an unused rail joint reference sample in order to differentiate the stresses developed during rail manufacturing and stresses accumulated during rail service.

Neutron diffraction analyses were carried out on the samples in longitudinal, transverse and vertical directions, and on 5mm thick sliceed samples cut by Electric Discharge Machining (EDM). Ex-service rail samples, irrespective of loading conditions and service times, were found to have similar depth profiles of stress distribution. Evolution of residual stress fields in rails due to service was also accompanied by evidence of larger material flow. Stress evolution in the vicinity of rail ends was characterised by a compressive layer, approximately 5 mm deep, and a tension zone located approximately 5- 15mm below the surfaces. A significant variation of d_0 with depth near the top surface was detected and was attributed to decarburisation in the top layer induced by cold work. Stress distributions observed in longitudinal slices of the two different deformed rail samples were found to be similar. For the undeformed rail, the stress distributions obtained could be attributed to variations associated with thermo-mechanical history of the rail.

Introduction

Insulated rail joint assemblies (Fig. 1) are primary components of rail track infrastructure and play a key role in track signaling systems and in the detection of rail fractures in track segments [1-3]. They generally comprise two rail ends separated by a narrow gap filled with insulator, and a fastening system including insulated side fishplates glued and bolted in place to improve rigidity [1]. IRJs have highly variable service lives with structural components failing under a range of modes, eventually resulting in overall failure of the joint. Metal flow is a key factor as the amount of surface rail deformation in the vicinity of rail ends is a generally greater than in continuous sections of rail. This can be attributed to a range of factors including; (i), that track sections comprising an IRJ are unbounded with a structural discontinuity across the rail joint and, (ii), that excessive interfacial friction is generated between the wheel and rail at the rail ends which

experience a notch/damping effect. This effect imposes severe stress concentrations and causes plastic deformation and metal flow across the joints which can eventually leads to malfunction of the electrical insulation [2-4]. For all these reasons, significant efforts have been made to improve life-span of rail joints either by optimizing the structural design or by improving the mechanical properties of rail steel. As pearlitic rail steel has reached its upper damage tolerance limit, there has also been effort in finding alternative rail surfacing materials which can reduce track degradation in the vicinity of the insulating gap [4].

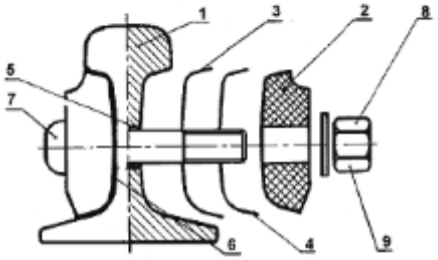

1. Rail, 2. Fishplate, 3. & 4. Insulators, 5. Bolt hole, 6. Insulator, 7. Bolt, 8. Nut, 9. Washer

Fig. 1. An Insulated Rail Joint assembly and its components.

As rail joints undergo plastic deformation during cyclic stress under rolling contact loading condition which results in a complex residual stress state near the surface and subsurface area of the rail head. Stresses are even more complex and intertwined near the rail joint due to its discontinuity in structure, and it is important to understand the stress development near the vicinity of rail joints and in subsurface region of the rail head. Stresses developed from a wheel/rail contact in service, exceeding the material yield point, can cause spalling fatigue cracking and can also produce head checking fatigue cracks.

Diffraction techniques are particularly suited to the non-destructive mapping of complex stress fields. Traditionally, neutron diffraction has been used to determine residual stresses internally in denser materials such as steel, where penetration depths are orders of magnitude greater than those of X-rays. Detailed 2-D and 3-D maps enable railway engineers to model and to better understand how residual stress fields are generated and to determine the most appropriate rail maintenance and replacement schedules for safe and economic operation. There are a handful of examples in the literature of use of neutron diffraction to investigate residual stresses in rail, including [5-8]. These investigations usually involve measurements of slices out of rails, like in the study on comparison of rails (slices) produced under different production conditions and investigations of residual stresses in wheel damaged track [8]. In this work, residual stresses in rail heads were analysed using the dedicated neutron residual stress diffractometer Kowari at the Australian Nuclear Science and Technology Organisation (ANSTO). In the current investigation, two IRJs with different rail service histories and accumulated damage were selected from the Queensland (Australia) heavy haul track service line. In addition, an unused IRJ fabricated from standard head hardened pearlitic steel track, was employed as a reference sample in order to differentiate the stresses developed during rail manufacturing and those developed during rail service.

Sample Preparation and Experimental

The end rail samples used for residual stress investigations comprised 400mm lengths of head hardened rail, obtained from disassembled 6-bolt square ended insulated rail joints. Three IRJs used are described as being in 'as-manufactured', condition, 'partly damaged' and 'badly damaged', the

latter having enough damage on inspection to require immediate removal from the Australian heavy haul rail track system. The 60 kg grade medium carbon rail steel is designated by Australian standard AS1085.12, with carbon content 0.65-0.82 wt.%

Measurements were made from intact rail ends in transverse (T) and longitudinal (L) directions at depths of 2, 4 and 6 mm from the top rail surfaces adjoining the rail ends. After that, 5mm thick slices were cut using electric discharge machining (EDM): transverse slices were cut from the middle part of the rail section while longitudinal slices were taken from ends of the rail section, as shown in Fig. 2. Residual stress measurements were carried out using the Kowari neutron residual stress scanner using 0.1672 nm neutron wavelength, Si(400) monochromator at $2\theta_M$ = 76°. In slices, the experiments were carried out using a gauge volume of 3×3×3 mm^3 and the Fe(211) reflection with the detector at the Bragg angle $2\theta_B$ of 90°. The measuring time of 30 secs per point was typical to achieve accuracy of ~$5x10^{-5}$ μstrains in strain scale and it was short enough to allow detailed stress mapping with large number of mesh points, 400 for L-slice and 355 for T-slices.

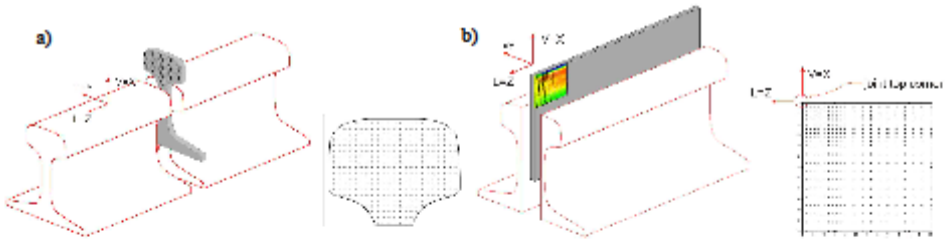

Fig. 2. Schematics of sample sections for neutron diffraction analysis, (a) T-slice and (b) L-slice.

Sectioned and polished samples were also examined unsig standard methods of reflected light microscopy, microhardness measurements (Leco Device) and secondary electron imaging (JEOL JSM 2001F instrument). Microhardness measurements were carried out along running surface of the rail head and across the gauge corner to access the extent of compressive stress shown in the transverse residual maps. A test load of 500g was selected, to measure the hardness distribution in the in-depth direction to about 20mm below the rail surface and at the gauge corner of the rail.

Results and Discussion

Microstructures of damaged rail samples Figure 3 shows representitative reflected light (Fig 3(a) - (b)) and SEM micrographs (Fig. 3(c)-(e)) of damaged rail samples. There was no evidence of white etching layer formation, but plastically deformed layers of depths ~25 μm and 60 μm below the running surface could be seen for the moderately deformed (Fig. 3(a)) and severely deformed (Fig. 3(b)) samples respectively. Below the deformed regions the bulk microstructures appeared free from any significant deformation.

Scanning electron microscopy (Fig. 3(c) – (e)) revealed deformormation of the cementite lamellae and reorientation towards the the direction of traffic movement. As indicated in Fig. 3(e), features including lamallae kinking, bending, globularisation and thinning in the rolling direction were evident in the deformed microstructure regions near the rail surfaces. Previous results [4] reveal that rail head spalling and sub-surface cracks are noticeable within few mm from the rail surface. As discussed in [9], crack originating subsurface regions tend to change direction, mostly either upward towards the rail surface or in some cases downwards. Because of this, the rail head material becomes detached from the surface resulting in spalling, causing failure of the rail.

Microhardness results Both deformed rail samples exhibited similar hardness profile trends from the top surface down in the T-sections (Fig. 4), while the unused rail sample exhibited little variation in hardness values across the measuring line. The maximum hardness value of 490HV were found near the running surface, while ~ 6 mm below the surface the hardness value changed to

~360HV, slightly higher than the bulk/unused rail hardness which falls in a range of 260-290HV. Hardness results obtained from longitudinal sections from the top down showed similar trands with a lower values further away form the rail ends.

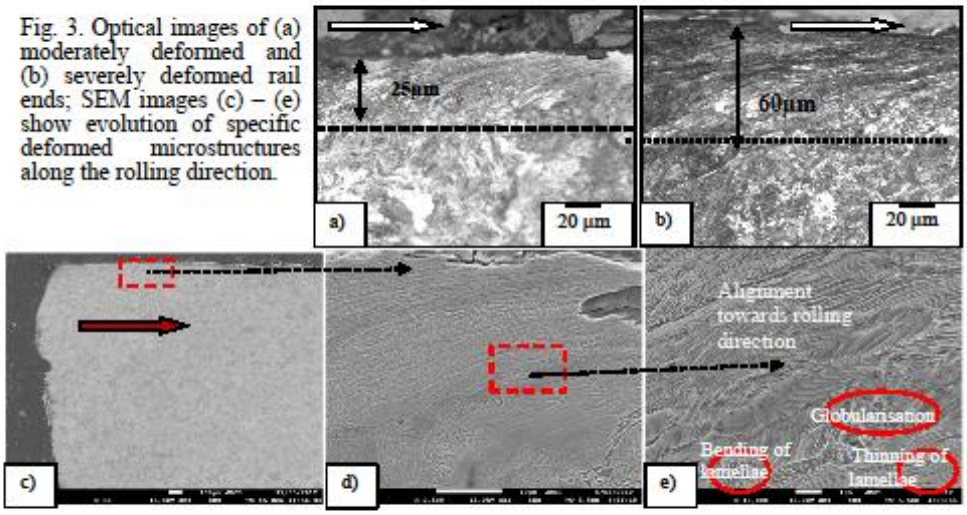

Fig. 3. Optical images of (a) moderately deformed and (b) severely deformed rail ends; SEM images (c) – (e) show evolution of specific deformed microstructures along the rolling direction.

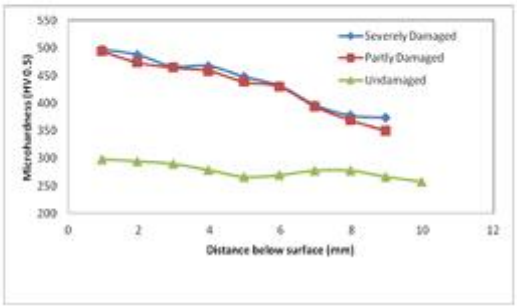

Fig. 4. Microhardness profiles as functions of depth below the suface near the rail end.

Residual stress maping.

Figure 5 shows the distribution of 2D residual stress maps in the slices from rail samples in different conditions. For both L and T slices, the stress distributions are dominated by compressive (~ -300 MPa) stresses (T component for the T-slices and L component for the L-slices) at the running surface and up to ~5 mm into the rail, which are balanced by tensile stresses (~ 200 MPa) located around 5-15 mm beneath. Both after-service rail samples exhibited similar stress distributions, although these were accentuated for the badly damaged rail.

While results for T-slices characterize stress distributions of continuous sections of rail (samples are taken away from the rail joint), results for L-slices demonstrate stress gradients in the proximity of the rail joint. To separate the effect of stress redistribution due to the presence of the rail end from the effect purely due to the different regime of material deformation in IRJ, diffirential stress maps, $\Delta\sigma_{xx}$ and $\Delta\sigma_{zz}$, were produced by subtracting stresses measured in the rail ends produced by EDM cutting (a byproduct of T-slice manufacturing) from stresses measured in the actual IRJ.

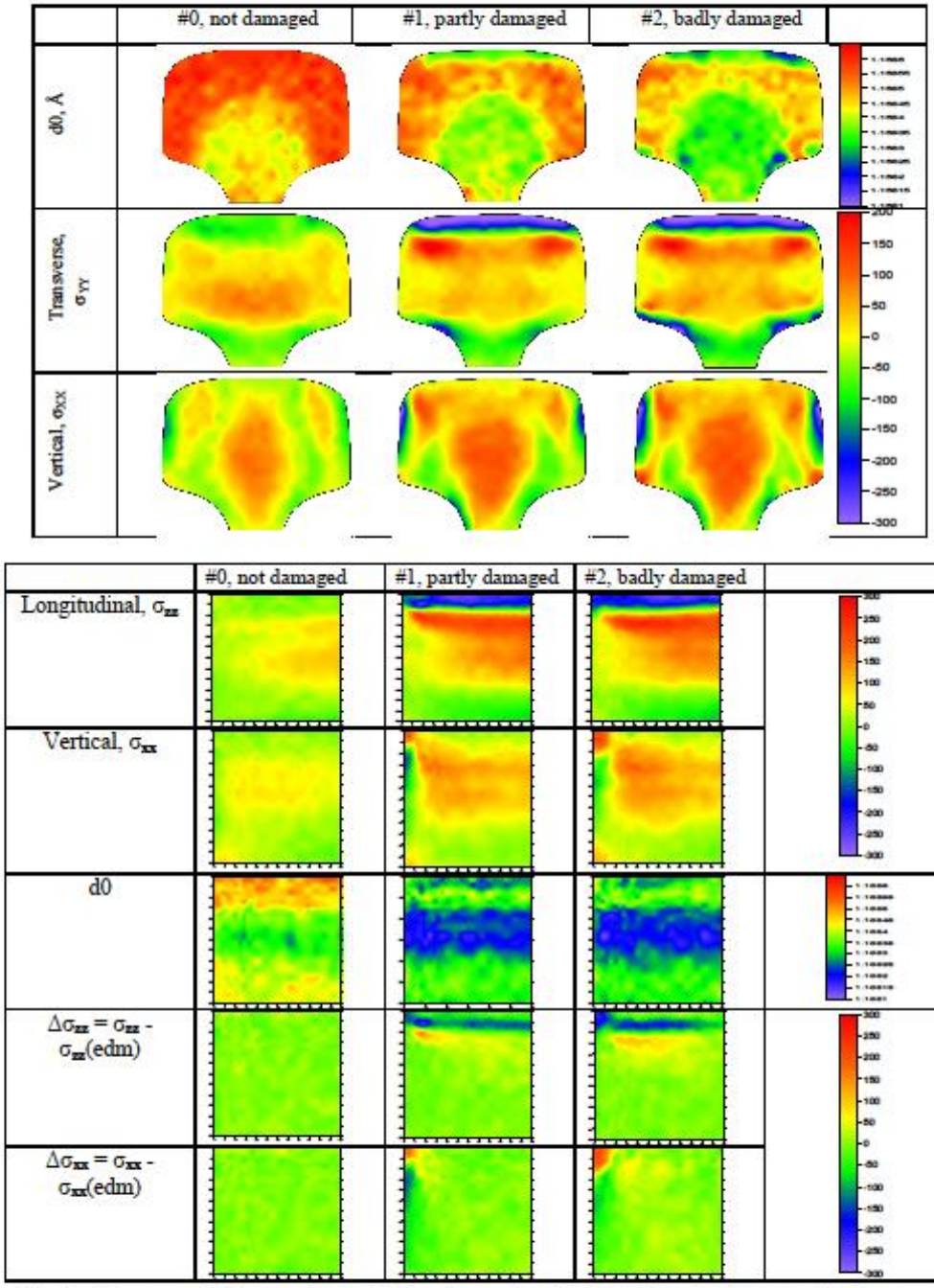

Fig. 5. 2D stress and d_0 maps for the T-slices (upper) and L-slices (lower). Compressive forces are blue, tensile forces are red. For the L slices both raw stress data and differential stress maps are shown. Square L-slice patch is 60 mm in size.

For the unused rail the 2D maps also revealed moderate tensile stresses in centre core of the rail head. These stresses are believed to be due to the roller straightening process during manufacturing. Compressive stresses are observed near the running surface and these are believed to have a beneficial role in resisting the further plastic deformation and growth of Rolling Contact fatigue (RCF) cracks. A significant variation of d_0 with depth near the top surface was detected and was attributed to decarburisation in the top layer induced by cold work.

Conclusions

Neutron diffraction of damaged IRJ samples revealed significant evolution of residual stress fields in rails due to service. Stress evolution in the bulk and vicinity of rail ends was characterised by a compressive layer, approximately 5-10 mm deep, and a tension zone located approximately 10-20 mm below the surfaces. A significant variation of d_0 with depth near the top surface was detected and was attributed to decarburisation in the top layer induced by cold work. Around the IRJ, material is more heavily deformed than material in the bulk of the rail as demonstrated from the longitudinal stress component differential maps $\Delta\sigma_{zz}$ in Fig.5: in the partially damaged rail the compression zone extends some 5 mm deeper than in the bulk areas, while for the badly damaged rail this effect even bigger and extend approximately 10 mm deeper than in a bulk part of the rail. Thus, although stress distributions observed in longitudinal slices of the two differently deformed rail samples seem to be similar, the badly damaged rail demonstrates deeper and stronger changes in the stress (and damage) state. This is also consistent with evidence of larger material flow based on light and scanning electron microscopy studies. For the undeformed rail, the stress distributions obtained could be attributed to variations associated with thermo-mechanical history of the rail.

Acknowledgements

This investigation forms a part of the Australian CRC for Rail Innovation research project, 'R3.100: longer life insulated rail joints' and was supported by an ANSTO in-kind grant for Beamtime proposal 1792. We also acknowledge the contribution of the Wollongong University Electron Microscopy Centre for provision of SEM services.

References

[1] Y. Hiroto: *Development of a long life Insulated Rail Joint*, Quarterly reports of the Railway Technical Research, Vol.25 (1984) p.79.
[2] C.Smalley: *Preliminary study into fatigue of Insulated Rail Joints*, Institute of Railway Technology at Monash University, (2009).
[3] J. Igwemezie, A.T. Nguyen: *Anatomy of joint bar failures II*, Railway Track & Structures, Vol. 105, Issue 10, (Oct 2009) p.43.
[4] C.Rathod, D.Wexler, T. Chandra, and H. Li, *Microstructural characterisation of railhead damage in insulated rail joints*, Materials Science Forum Vols. 706-709 (2012) p. 2937.
[5] T. Gnaupel-Herold, P.C. Brand, H.J. Prask, *Neutron Diffraction Investigation of Risidual Stresses in Transverse/Oblique Rail Slices Subjected to Different Grinding Stratagies*, Report NISTIR 6305, U.S. Department of Commerce, Technology Administration (1999).
[6] P.J. Webster, K.S. Low, G. Mills, and G.A. Webster, *Neutron Measurementsof Residual Stresses in a Used Raiway Rail*, Mat. Res. Soc Symp. Proc., 166, (1990) 311-316.
[7] G.A. Webster, P.J. Webster, M.A.M. Bourke, K.S. Low, G. Mills, H.J. McGillivray, D.F. Cannon and R.J. Allen, 1992, *Neutron Diffraction Determinations of Residual Stress Patterns in Railway Rails*, Mat. Res. Soc Symp. Proc 166, (1990) 143-152.
[8] V. Luzin, J.E. Gordon, T. Gnaupel-Herold and H.J. Prask, *Neutron residual stress measurements on rail sections for different production conditions*, Proc. IMECE04, 2004 ASME Int Mech Eng Congr. And Expn, Nov 13-20 (2004), Anaheim, CA, USA, 1-25.
[9] J. Tillberg, F.larson, K.Runesson, *A study of multiple crack interaction at rolling contact fatigue loading of rails*, Proc. I. Mech E Part F: J. Rail and Rapid Transit, 223 (2009) 319-330.

International Conference on Residual Stresses 9 (ICRS 9)
10.4028/www.scientific.net/MSF.768-769

Residual Stresses in Rail-Ends from the in-Service Insulated Rail Joints Using Neutron Diffraction
10.4028/www.scientific.net/MSF.768-769.741

DOI References
[9] J. Tillberg, F. larson, K. Runesson, A study of multiple crack interaction at rolling contact fatigue loading of rails, Proc. I. Mech E Part F: J. Rail and Rapid Transit, 223 (2009) 319-330.
http://dx.doi.org/10.1243/09544097JRRT242

9.3 Paper C: A neutron diffraction investigation of residual stresses in rail ends after severe deformation of rail surfaces

Materials Science Forum Vol. 777 (2014) pp 213-218
© (2014) Trans Tech Publications, Switzerland
doi:10.4028/www.scientific.net/MSF.777.213

A neutron diffraction investigation of residual stresses in rail ends after severe deformation of rail surfaces

Chandrahas Rathod[1, a], David Wexler[1, b], Vladimir Iuzin[2, c], Paul Boyd[3, d], Manicka Dhanasekar[4, e]

[1] Faculty of Engineering, University of Wollongong, Northfields Ave, NSW, Australia

[2] Australian Nuclear Science & technology Organisation, Lucas Heights, NSW, Australia

[3] The Centre for Railway Engineering, Central Queensland University, Rockhampton, QLD, Australia

[4] Faculty of Built Environment & Engineering, QUT, Brisbane, QLD, Australia
[a]crr716@uowmail.edu.au, [b]davidw@uow.edu.au,[c]vladimir.luzin@ansto.gov.au, [d]p.boyd@cqu.edu.au, [e]m.dhanasekar@qut.edu.au

Keywords: Insulated rail joint, residual stress, neutron diffraction, wheel-on-track simulation

Abstract. Insulated rail joints (IRJs) are a primary component of the rail track safety and signalling systems. Rails are supported by two fishplates which are fastened by bolts and nuts and, with the support of sleepers and track ballast, form an integrated assembly. IRJ failure can result from progressive defects, the propagation of which is influenced by residual stresses in the rail. Residual stresses change significantly during service due to the complex deformation and damage effects associated with wheel rolling, sliding and impact. IRJ failures can occur when metal flows over the insulated rail gap (typically 6-8 mm width), breaks the electrically isolated section of track and results in malfunction of the track signalling system.

In this investigation, residual stress measurements were obtained from rail-ends which had undergone controlled amounts of surface plastic deformation using a full scale wheel-on-track simulation test rig. Results were compared with those obtained from similar investigations performed on rail ends associated with ex-service IRJs. Residual stresses were measured by neutron diffraction at the Australian Nuclear Science and Technology Organisation (ANSTO). Measurements with constant gauge volume 3x3x3 mm^3 were carried in the central vertical plane on 5mm thick sliced rail samples cut by an electric discharge machine (EDM). Stress evolution at the rail ends was found to exhibit characteristics similar to those of the ex-service rails, with a compressive zone of 5mm deep that is counterbalanced by a tension zone beneath, extending to a depth of around 15mm. However, in contrast to the ex-service rails, the type of stress distribution in the test-rig deformed samples was apparently different due to the localization of load under the particular test conditions. In the latter, in contrast with clear stress evolution, there was no obvious evolution of d_0. Since d_0 reflects rather long-term accumulation of crystal lattice damage and microstructural changes due to service load, the loading history of the test rig samples has not reached the same level as the ex-service rails. It is concluded that the wheel-on-rail simulation rig provides the potential capability for testing the wheel-rail rolling contact conditions in rails, rail ends and insulated rail joints.

Introduction

Insulated rail joints (IRJs), Fig. 1(a) [2], are a primary component of the rail track system, electrically isolating separate track sections for both signalling purposes and as an aid to the rapid identification of track fractures. Typically, one rail is installed with a low voltage current and the other is used as a ground and the train wheel functions as a conductor between these two running rails within a track segment. IRJs represent a weak link in the heavy haul rail corridors and must be periodically repaired or replaced before they fail. In Australia, IRJs are generally replaced within

10%-20% of the useful life of other rail components due to evidence of railhead, bolt or fishplate damage, but particularly because of evidence of accumulated damage at the railhead suggesting that the IRJ insulating capacity may soon be compromised [1-5]. General factors which affect the failure of IRJs, include IRJ design, wheel load under both static and impact conditions, support stiffness, wheel defect, rail end dip, wheel passing speed. Some examples of IRJ failures are shown in Fig. 1 (b)-(f) [2]. These include, broken joint bars (Fig. 1(b), and failure associated with the progression of surface defects; battered end posts and metal flow (Fig 1(c)), rail end shelling, (Fig 1(d)), head spalling (Fig 1(e)) and crushing (Fig 1(f)) [6]. The majority of failures of IRJs in Australia are related to railhead surface defects in the crown or shoulder of the rail running surface. Two key factors relevant to the failure of Australian IRJs are wheel/rail contact impact force and metal plasticity.

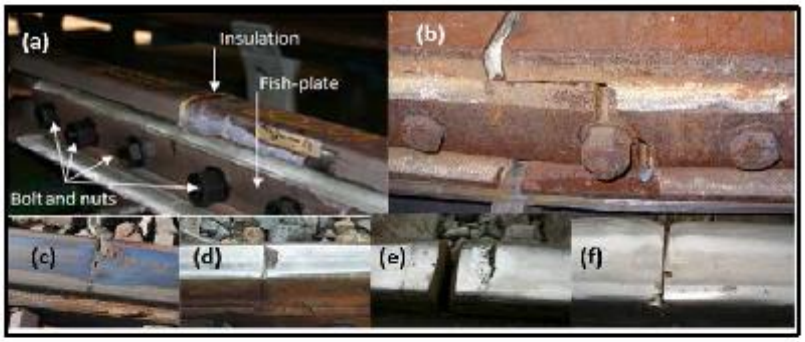

Fig.1 Insulated rail joints and some common failure modes, (a) IRJ assembly [Ref], (b) Fishplate fracture in vicinity of bolt hole, (c) – (f) failure modes associated with surface damage, (c) Rail end battering and metal flow, (d) rail end shelling, (e) rail head spalling and (f) railhead crushing to produce a surface dent.

Residual stress

Residual stresses in the subsurface region of the rail head are induced due to manufacturing processes and, subsequently, by train movement over the IRJ. Understanding the evolution of residual stresses in the vicinity of IRJ rail ends is a complex task as damage accumulates under different modes, with one aggravating to the other. The combination of cyclic stresses under rolling contact [3, 4], impact stresses associated with the structural discontinuity of the joint [5], and severe macroscopic rail deflections all contribute to the accumulation of stresses during service. Severe stress concentrations occurring at the rail-end and causes plastic deformation across the joint near the joint surface [4].

These stresses result in changes in atomic spacings of the α-Fe phase within the pearlitic matrix of medium carbon rail steel. With spatial resolutions of around 0.5 mm and penetration depths up to 60-100 mm compared to less than 3 µm for x-rays, neutron diffraction is an attractive option for internal strain measurements and subsequent calculation of residual stress in such steels. Compared to destructive relaxation methods that involve cutting and drilling, neutrons are also the preferred non-destructive method to determine the whole strain. The first reported neutron diffraction investigation of residual strain in full rail sections [6] involved significant beam time, and this has been followed up by less time consuming neutron diffraction investigations of strain in rail slices [7], including a recent investigation of strain in rail ends of ex-service IRJs [8, 9].

Experimental

Two sets of samples were studied: (i) Three IRJs comprising 400mm long sections of head hardened rail (60 kg grade, medium carbon rail pearlitic steel with carbon content 0.65-0.82 wt.%, Australian standard AS1085.12) obtained from disassembled 6-bolt square ended insulated rail joints. They are described as being in 'as-manufactured', condition, 'partly damaged' and 'badly damaged', the latter having enough damage on inspection to require immediate removal from the Australian heavy haul rail track system.

(ii) Rail ends of the same steel type as above, which had undergone controlled amounts of surface plastic deformation, using cyclic wheel-on-track simulation test rig illustrated in Fig. 2(a) and 2(b). This testing regime was carried out to investigate railhead material failure mechanisms that might occur under dynamic wheel-rail rolling contact load environment. The rail ends used are denoted as being in 'as-manufactured', condition, 'low-cycle damaged' and 'high-cycle damaged' rail end. Deformation employed a vertical wheel load of 300kN and 10kN in the horizontal direction. Load-cycle data are displayed in Fig 2(c) which shows Load cycle data for Vertical Load (left) and Horizontal Load (right). The 300kN vertical and 10kN horizontal load was applied throughout the forward movement of the wheel stroke as it passed the free end (Fig 2(a) and (b)), the wheel then being unloaded and returned to the stroke start position.

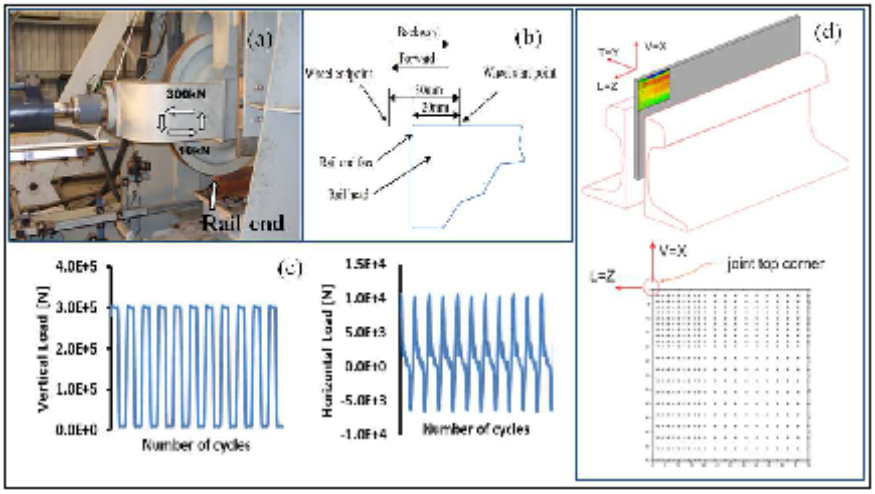

Fig 2: (a) Laboratory wheel-on-rail simulation rig (b) schematic diagram of wheel movement (c) In general, load-cycle plot for the rail sample carried out for both 600cycles and 1000 cycles using cyclic wheel-on-track simulation test rig (d) schematic of L-slice sample section from central part of the rail for neutron diffraction analysis.

Residual stress measurements were carried out using the ANSTO Kowari neutron residual stress scanner using 1.672 Å neutron wavelength from Si (400) monochromators at $2\theta_M$ = 76°. Measurements were performed on longitudinal rail slices abutting the rail end, cut by electric discharge machined (EDM) from the central part of the rail, 5 mm thick and parallel to the long axis of the rail, as shown in Fig.2(d). Based on previous experimentation on steels, we estimate that EDM cutting of the sample along the y-direction accounts for around 40-50 MPa stress changes. The experiments were carried out using a gauge volume of 3x3x3 mm^3 and Fe (211) reflection with the detector at the Bragg angle $2\theta_M$ of 90°. A measuring time of 30 secs per point provided accuracy of ~$5x10^{-5}$ μstarins in strain scale and was short enough to allow detailed stress mapping with 400 number of mesh points. Stress distributions away from rail ends abutting endposts and below the

surfaces of the rail are the focus of the experimental program, with the same measurement strategy will be applied to all rail pieces. By doing measurements in the central line we assume symmetry of the stress and only 3 principle directions can be measured for the full characterisation of the stress tensor. The target accuracy of strain (or d-spacing) determination is $0.7\text{-}0.9\text{x}10^{-4}$ and should be sufficient for determining stress values with accuracy ±30 MPa. The Iron (211) reflection was used since this is the strongest reflection and the instrument is optimized for using this reflection.

Results and Discussion

Two samples with different load conditions were measured and an additional undamaged sample (labelled 0 cycles) was also examined in order to differentiate stresses associated with loadings from stresses developed during the manufacturing process. The existence of compressive region near the rail surface with a balancing tensile stress below this confirmed similar results obtained from ex-service damage IRJs [8]. Figure 3 shows 2D stress maps across the local rail head for two directions, namely longitudinal and vertical directions, and also shows the values of interplannar d(211) spacing (i.e., the d_0 values), as functions of position in the rail sections. For the two rail samples that underwent wheel loadings in the rig tester for 600 and 1000 deformation cycles, similar longitudinal stress maps were obtained, with slight changes near the localised rail head. Compared to the undeformed sample, vertical stresses in both rig tested samples were particularly severe in the regions near the top free ends of the rail, with tensile stresses of around 200 MPa extending to a depth of around ~20 mm.

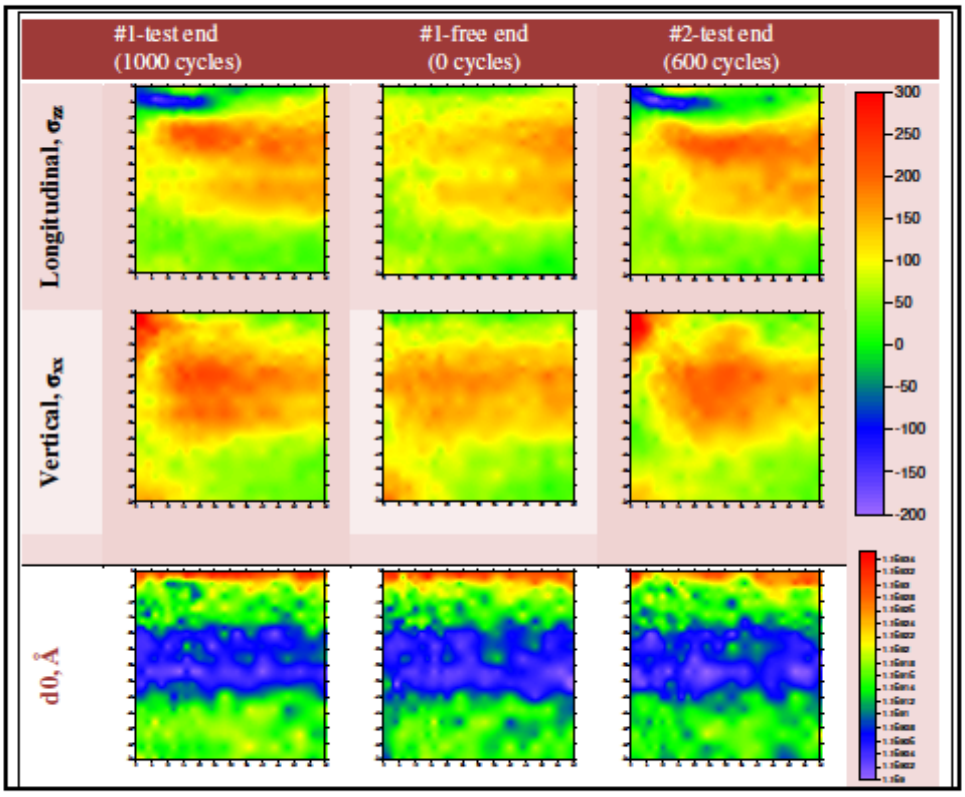

Fig 3. Residual stress maps in the longitudinal slices from the rails contact loaded in the rig tester. Variation in d0 is also shown in the bottom.

Local plastic deformation of rail head surface can arise when locally high contact stresses from the wheel rolling on rail exceed the material yield point. The contact stresses, also leads to residual stress development which are created by the plastic deformation that builds up in rail during the wheel loading. The presence of significant compressive residual stresses zone of ~5mm deep from the rail surface was found to be counterbalanced by the tension zone underneath (~15mm deep), this tensile distribution zone is believed to be one of the critical regions for likely of crack initiation and propagation.

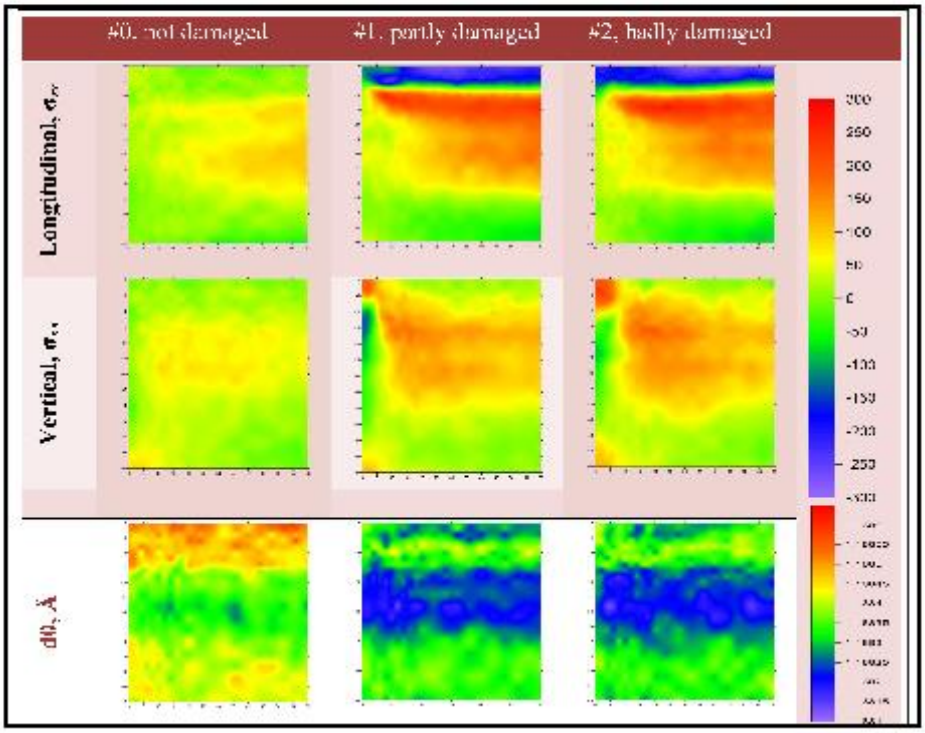

Fig 4. Residual stress maps in the longitudinal slices from the rails taken from the service (in two conditions and a no-service reference). Variation in d_0 is also shown.

The maps in (Fig 3) can be directly compared with the 2D stress maps that were obtained in the same way for the rails that were more heavily deformed in real service, as shown in (Fig 4). Clearly, there are similarities in the stress distributions, particularly the accumulation of damage near the top surfaces of the rails and, for the case of the vertical tensile and longitudinal compressive components, near the rail ends (top right). Differences in results between the rig tested and ex-service samples may be attributed to (i) the fact that a rail end rather than a joint was loaded, so there was no impact component of damage at the rail end and, (ii), the number of cycles associated with the rig testing was apparently less than that required to produce equivalent damage to that observed in the ex-service joints.

Conclusions

The residual stress distributions on the 5mm thick slices of railhead samples were analysed both in longitudinal and vertical direction with certain distances from the rail surface.

The in-depth distributions of residual stresses were studied up to 60 mm^2 from the rail surface in depth, with a nominal gauge volume of 3 x 3 x 3 mm^3 for 400 mesh point measurements.

There was clear evidence of stress field evolution in all studied rails, for both test cycled and ex-service samples. This was characterised by a compressive zone ~5 mm deep that is counterbalanced by a tension zone underneath (~15mm deep). The distribution of the residual stress in the rig tested rails indicates high local plastic deformations on the near surface of railhead near the rail end. The increase in tensile residual stress for the vertical component is nearly ~200MPa, twice the value of bulk material away from the rail end.

There was obvious evolution of d_0 in the ex-service rails, while no evident evolution in the rig tested samples, probably due to the higher damage accumulated in ex-service samples than for the rig tested samples. Apparently, 600 or 1000 cycles during rig testing have not produced comparable damage as was achieved in ex-service samples.

Using the full-scale rig equipment has proved, in general, to provide a considerable plastic strain resulting in microstructural deformation of rail head. Longer duration cycling, and cycling over real rail joint gaps rather than over rail ends would more accurately simulate metal flow over insulated rail joints.

Acknowledgements

This investigation forms a part of the Australian CRC for Rail Innovation research project, 'R3.100: longer life insulated rail joints' and was supported by an ANSTO in-kind grant for beam time proposals 1972 and 2206. We gratefully acknowledge the expertise and assistance of the Centre for Railway Engineering, Central Queensland University, Rockhampton, QLD, Australia.

References:

[1] Zachary, I.C "Innovative design concepts for insulated joints "*Master Thesis", Virginia Polytechnic Institute,* (2007).

[2] Nirmal, K.M "Failure of railhead material of insulated rail joints" *CQU Australia, PhD Thesis,* (2010).

[3] Davis, D.D & Akthar, M.N "Improving the performance of bonded insulating joints". *Railway track and structures*, 14-17, (2005)

[4] Kerr, A. D. & Cox, J. E "Analysis and tests of bonded insulated rail joints subjected to vertical wheel loads". *International Journal of Mechanical Sciences, 41*, 1253-1272, (1999)

[5] Wen, Z., Jin, X. & Zhang, W "Contact-impact stress analysis of rail joint region using the dynamic finite element method". *Wear, 258*, 1301-1309, (2005)

[6] Vladimir,L. Jeffrey,E,G. Thomas, G,H. Henry, J.P " Neutron residual stress measurements on rail sections for different production conditions" *Proceedings of IMECE04*, (2004)

[7] T. Gnaupel-Herold, P.C. Brand, H.J. Prask, "Neutron diffraction investigation of residual stresses in transverse/oblique rail slices subjected to different grinding strategies", *Report NISTIR 6305, U.S. Department of Commerce, Technology Administration,(1999)*

[8] Luzin, V., Prask,H.-J., Gnaupel-Herold, T., Gordon J., Wexler D., Rathod C., Pal S., Daniel, W. and Atrens, A "Neutron Residual Stress Measurements in Rails", *Neutron News* 24 (2013) 9-13.

[9] V.Luzin, C.Rathod, D.Wexler, H.Li, M.Dhanaseker, "Residual stresses in rail-ends from the in-service insulated rail joints using neutron diffraction". *Materials Science Forum*, [Accepted for publication, 2012].

9.4 Paper D: An investigation of residual stresses in insulated rail joints

An investigation of residual stresses in insulated rail joints

David Wexler[2], Chandrahas Rathod[2], Huijun Li[2], Manicka Dhanasekar[3], Vladimir Luzin[1]
[1]ANSTO, [2]University of Wollongong, [3]Queensland University of Technology, CRC for Rail Innovation

Insulated rail joints (IRJs) are an integral part of any rail track system, as they split a continuous rail track into electrically isolated sections for signalling and easy detection of rail track damage. Bonded IRJs are safety-critical components that must satisfy requirements for structural integrity as well as the isolation function for both railway signalling and track condition monitoring systems.

In heavy haul corridors in Australia and around the world, IRJs are periodically replaced due to accumulated damage in their railhead, often within 10-20% of the useful life of other rail components.

Their replacement is the single largest track maintenance cost in New South Wales, apart from track ballast work. Neutron diffraction can tell us what happens to material and residual stresses within used rails and trace down accumulation of damage caused by stresses throughout rail service history.

The study is helping railway engineers better understand how residual stress fields evolve in service and enable them to develop IRJs with longer service lives, as well as determine the most appropriate rail maintenance and replacement schedules for safe and economic operation.

Role of stress in rail damage

A number of serious incidents, including fatal derailments and train-on-train impacts, have been attributed to rail and rail-end failures resulting from rolling-contact fatigue. Most of the various mechanisms of rail failure are related to the interaction between defects and the residual stress field at and below the rail surface. Residual stresses are generated in rails first as a result of the manufacturing processes, which include hot-rolling (shaping rails from a billet), roller-straightening (final cold rolling through multiple rollers to achieve geometrical tolerance) and head-hardening (heat treatment to achieve high hardness). In service, the running surfaces of rails are subjected to repeated rolling-contact loading through interaction with train wheels, and the rail itself is subject to a variety of complex stresses and strains. Stresses are usually so high that they can cause plastic deformation around the contact surface and modify the stress field and material properties near the running line and internally in the railhead. Track fracture can result from one or more progressive defects, the propagation of which is also influenced by residual and contact stresses in the rail.

IRJs and their damage

The above mentioned effects change significantly in IRJs because they are somewhat different from continuous rail. Essentially IRJs comprise two rail ends and a narrow gap in the rail filled with insulator, and a support structure including bolted fishplates on both sides of the rails, which are electrically isolated from the track by a layer of glue and help add rigidity to the IRJ, as shown in Fig. 1. IRJs represent a different support structure to standard tracks as they endure an additional impact-forces distribution arising from the wheel-to-rail contact in special conditions of the rail gap and the rail ends. For example, failure can occur when metal flows over the insulated rail gap (typically 6-8 mm width) breaks the electrically isolated section of track and results in malfunction of the track signalling system. This can happen well before any other defects, such as cracks or surface voids, start to develop. Therefore, a significant amount of track maintenance work is dedicated to the inspection of rail ends. As a maintenance procedure the head of the rail may be ground periodically to restore the correct head profile, to remove surface cracks before they grow too big, or to move the wheel-rail contact position

Figure 1

Left: 4-bolt square ended IRJ: two rail sections are connected by means of bolted fishplates on both sides of the rail; an insulator, placed in the gap between two rail sections, forms a rail-post. Right: Metal flow in damaged end-post.

across the vicinity of the end-post in order to extend the life of the IRJs. In case of severe damage, when the rail is approaching an unsafe condition, rail sections containing IRJs are replaced. In heavy haul rail systems, IRJs' periodical replacement due to accumulated damage in their railhead may be necessary after only 2-3 years of service or within 10% of the useful life of other rail components. Apart from track ballast work, IRJ replacement represents the most significant track maintenance expense in the rail network.

Researching IRJs

A research project was initiated by the Cooperative Research Centre for Rail Innovation to address this problem and supported by industrial partners (the Australian Track and Rail Corporation, Queensland Rail) and academic institutions (University of Wollongong, Queensland University of Technology, University of Central Queensland). We use neutron diffraction to investigate the material stress accumulation at rail ends in the vicinity of the insulated gap in IRJs - this is the area of rail subjected to the most damage.

By selecting a series of samples with different service histories the investigation provided fundamental information about residual stresses accumulation, material properties evolution and how these might change during degradation of IRJs. The samples selected for this investigation are rail ends from square-ended IRJs made from the same steel type (Australian standard A1085.1 60 kg grade) and manufacturer. Rail ends from IRJs described as 'partly damaged' and 'badly damaged' will be compared with a rail end in the 'not damaged', as-manufactured, condition.

Neutron stress measurements

Neutron diffraction is particularly suited to the non-destructive mapping of complex internal stress fields within dense materials such as steel, because of the high penetration. For neutrons the penetration depth in steel is 100 times greater than that of X-rays. There are a handful of known examples of use of neutron diffraction to investigate residual stresses in rail and most of the studies have been performed on rail slices because the railhead thickness of 70 mm is still too great even for neutrons. Although stresses are partially eliminated by slicing, this approach allows stresses to be mapped much faster, more accurately and over larger areas. In our study one transverse slice and one longitudinal slice was machined out of each rail sample. They were studied in residual stress experiment with gauge volume (probing volume) of 2 x 2 x 2 mm³, accuracy of ±30 MPa and using the iron (211) Bragg reflection.

Mapping the stress

(1) Drastic changes in residual stress state were found in the rail head of the selected samples, see Fig. 2. Compressive stress (shown as blue areas) immediately under the top surface, which is induced due to the service load from train movement, is counteracted by a wide zone of tension (red areas) that potentially can cause defect growth (Fig. 2a). The rail material also undergoes transformation as shown in Fig. 2b changing from harder steel (shown in red) to softer (shown in blue). This happens differently across railhead and evolves noticeably with the service span.

(2) The distributions of stresses close to the end-posts are different from the bulk parts because of different loading conditions and this is demonstrated in Fig. 3a. The material close to the IRJ rail end-post is more damaged then material in the continuous rail as shown in Fig. 3b by a differential stress map for the longitudinal component. Damage accumulation is mostly happening 5-10 mm beneath the surface and progresses with rail service (can be seen as enhancement of the features in Fig. 3b).

Figure 2

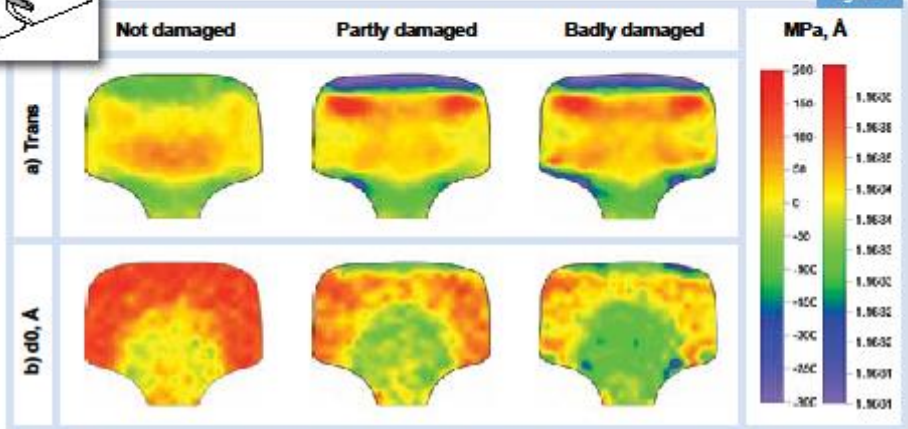

Evolution of the residual stress and material lattice parameter in rails of different service history. The railhead is 70 mm across. a) In the stress maps, the red areas represent high tensile stress while the blue areas correspond to high compressive stress. b) In the lattice parameter maps, larger d-spacing are shown in red while small d-spacing values are blue.

Figure 3

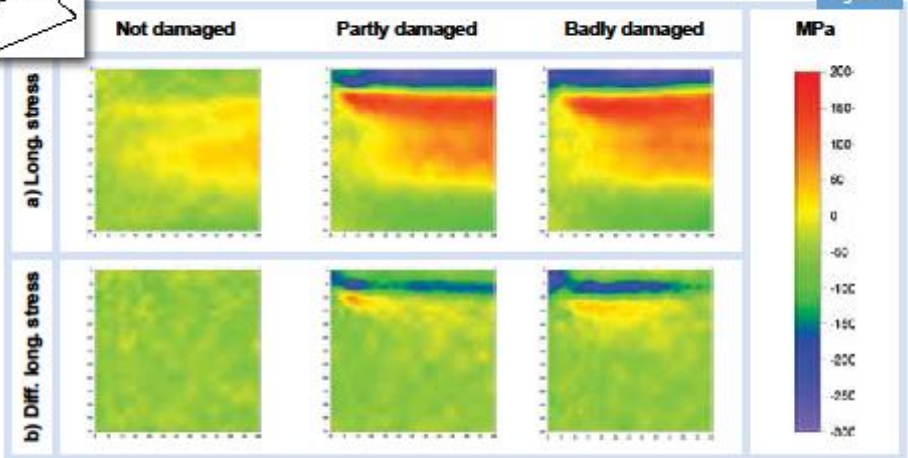

a) Evolution of the residual stress longitudinal component in rails of different service history obtained on longitudinal slices (maps top left corner corresponds to the top corner of the end-post). Patch size is 60 x 60 mm². b) Differential longitudinal stress component maps are obtained by subtracting stress values representing bulk material from the values representing material of IRJ.

Projected outcomes

The stress distributions determined experimentally can be used to validate finite-element simulations carried out at Queensland University of Technology to assess progressive damage accumulation in material of IRJ through elastic-plastic deformation history and residual stress evolution. Our detailed stress maps will allow us to narrow the selection of the correct material mechanical models and damage mechanisms. The combined experimental and modelling efforts will help railway engineers to better understand how residual stress fields evolve in service and enable them to develop IRJs with longer service lives, as well as to determine the most appropriate rail maintenance and replacement schedules for safe and economic operation.

9.5 Paper E: Neutron residual stress measurements in rails

Neutron News
Publication details, including instructions for authors and subscription information:
http://www.tandfonline.com/loi/gnnw20

Neutron residual stress measurements in rails

V. Luzin [a] , H.-J. Prask [b] , T. Gnaupel-Herold [b] , J. Gordon [c] , D. Wexler [d] , Ch. Rathod [d] , S. Pal [e] , W. Daniel [e] & A. Atrens [e]

[a] Bragg Institute, Australian Nuclear Science and Technology Organisation , Locked Bag 2001, Kirrawee , DC, NSW , 2232 , Australia

[b] NIST Center for Neutron Research , 100 Bureau Dr., MS 6102, Gaithersburg , MD , 20899-6102 , USA

[c] Volpe National Transportation Systems Center , Cambridge , MA , 02142 , USA

[d] Engineering Faculty , University of Wollongong, Northfields Ave. , Wollongong , NSW , 2522 , Australia

[e] School of Mechanical and Mining Engineering, University of Queensland , St. Lucia , QLD 4072 , Australia

Published online: 09 Jul 2013.

To cite this article: V. Luzin , H.-J. Prask , T. Gnaupel-Herold , J. Gordon , D. Wexler , Ch. Rathod , S. Pal , W. Daniel & A. Atrens (2013) Neutron residual stress measurements in rails, Neutron News, 24:3, 9-13, DOI: 10.1080/10448632.2013.804353

To link to this article: http://dx.doi.org/10.1080/10448632.2013.804353

Neutron residual stress measurements in rails

V. Luzin[1], H.-J. Prask[2], T. Gnaupel-Herold[2], J. Gordon[3], D. Wexler[4], Ch. Rathod[4], S. Pal[5], W. Daniel[5] and A. Atrens[5]

[1]Bragg Institute, Australian Nuclear Science and Technology Organisation, Locked Bag 2001, Kirrawee DC, NSW 2232, Australia

[2]NIST Center for Neutron Research, 100 Bureau Dr., MS 6102, Gaithersburg, MD 20899-6102, USA

[3]Volpe National Transportation Systems Center, Cambridge, MA 02142, USA

[4]Engineering Faculty, University of Wollongong, Northfields Ave., Wollongong, NSW 2522, Australia

[5]School of Mechanical and Mining Engineering, University of Queensland, St. Lucia, QLD 4072, Australia

Introduction

Rails were among the first objects of study by neutron diffraction strain measurement and the first experiments were done as early as the late 1980s [1, 2]. This interest is easy to explain: the problem of rail fracturing is critical from the public safety point of view and the penetrating ability of neutrons suggested the possibility of breakthrough experiments and fast progress in this field. It was well-established that residual stresses, both near-surface and interior, played a significant role in the development of defects which led to rail failure. This suggested three distinct approaches of neutron diffraction strain measurement that could contribute to various problems of the rail industry. The first method was to map the complete triaxial stress distribution non-destructively in the interior of an intact rail, ideally before and after significant service. Another approach was to use slices, for example to characterize how different processing methods produce favourable or detrimental stress distributions in rails. A third technique was to make non-destructive measurements, but in critical and not very deep portions of rails, for example, to examine defects and their relation to rail failure in the top running surface of rails, e.g. "white layer" formation.

In the case of the most direct and straightforward approach to measure stresses in the interior of an intact rail neutron beams would penetrate the whole thickness of the railhead (70–75 mm across) while the half-attenuation length in steel is only 6 mm. Therefore, neutron beam attenuation is critical so that experiment optimisation and planning become highly important issues even for the most intense neutron sources. Such optimisation would involve (i) adjustment of the neutron beam wavelength, scattering geometry and sample orientation to minimize the neutron beam flight path inside of the rail and (ii) balancing the choice of spatial resolution and number of mesh points and the available measurement time. Even with optimisation, measurement time is very significant (many hours) and the number of measurement points might not be great (a hundred) with low spatial resolution ($5 \times 5 \times 5$ mm^3).

An approximate solution would be to use slices cut out of the continuous rail sections and this approach was used in the milestone experiments by P. Webster that were published in *Neutron News* in 1991 [3]. Slices appropriate for neutron penetration, 5–20 mm thick, either transverse, longitudinal or sometimes oblique, can be cut out of long section and measured much faster (minutes), with high spatial resolution ($2 \times 2 \times 2$ mm^3) and covering larger rail cross-sections with large number of points (up to a thousand) than for an intact rail. This approach is suitable when there is a necessity to measure a long series of samples, i.e. providing important information on how different processes produce different initial stress distributions. However, the price for the convenience of working with thin (<10 mm) slices is that the stress component normal to the cut plane is completely eliminated, while all other stress tensor components are partially relaxed. Therefore, results of such measurements are not necessarily what railway engineers want to know: "what is the stress distribution in the original rail and how does it change with service?"

Attempts to recover the lost information have been made directly through combining contour-method results on a long rail with diffraction results on slices [4]. Attempts relying more heavily on modelling use combined measurements on transverse and oblique slices [5] and the eigenstrain approach [6] that infers the full stress distribution from strain measurements on a slice. Each relies on certain assumptions to recalculate the original triaxial distribution, but none has had the measured tri-axial distribution available to test the models.

For some rail failure problems only the near-surface layer is of interest, usually the top running surface of the railhead. An example of such a problem is the formation of a white layer and the role of stresses in its formation [7]. Although the laboratory x-ray $\sin^2\Psi$ method can examine the surface [8] and synchrotron experiments can also be used [9], still neutrons can penetrate significantly deeper (top 10 mm) while providing good spatial resolution (0.5 mm).

In the present paper, we describe recent results in the application of neutron diffraction to the long-standing problems described above.

Neutron stress measurements in a full rail

Neutron diffraction residual strain measurements on a full rail were made at NIST in 2003 [10]. To our knowledge none have been reported since. At NIST the major commitment was approximately 3 months of beamtime for non-destructive triaxial measurements on a long rail segment. The rail length chosen was 530 mm, which, according to finite element method (FEM), is enough to avoid edge effects and preserve the original stress state in the middle part of the specimen. The rail section was cut from a defect-free area adjacent to a detected transverse defect, so it was representative of the loading, fatigue history and stress conditions of the area where the defect occurred. The rail was provided by the High Tonnage Loop facility at the Transportation Technology Center after subjecting it to 39-ton axle load service as a part the Track System Research Program of the U.S. Federal Railroad Administration.

Optimizing scattering conditions to minimize neutron flight path and attenuation allowed utilization of a gauge volume of $5 \times 5 \times 5$ mm^3 (or $5 \times 5 \times 20$ mm^3 when expected stress gradients permitted) so that strains with an accuracy of $\Delta d/d = 5 \times 10^{-5}$ at 134 mesh points could be measured in acceptable times. The measurement time varied from 5 seconds, for the most shallow points, to 8 hours, for the deepest points. Five directions were measured, transverse, vertical, longitudinal and ±45° from vertical, and four stress components were reconstructed from the measured strains resulting in three normal and one shear components (Figure 1 shows only normal).

For comparison stress maps from a 6 mm thick slice are also presented in Figure 1, measured in the same experimental conditions. Statistically, the average longitudinal stress in the slice is zero. This kind of results is essentially the same as in the early works by P. Webster [1].

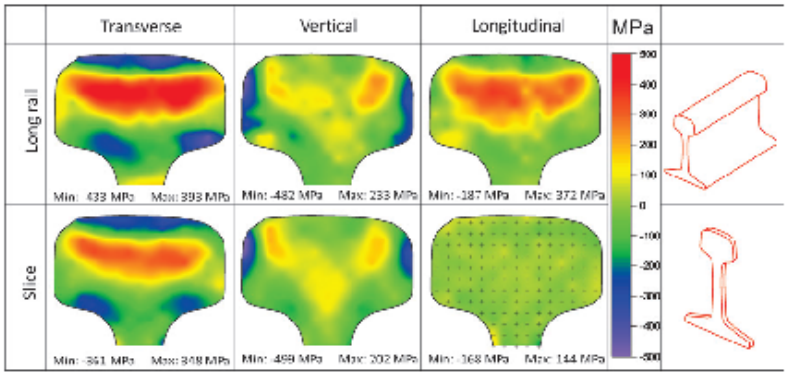

Figure 1. Stress maps of normal stress tensor components in the long section of the after-service rail (top). For comparison the same maps are given for the slice sample (bottom). Note that the longitudinal component in the slice is zero within statistical variations.

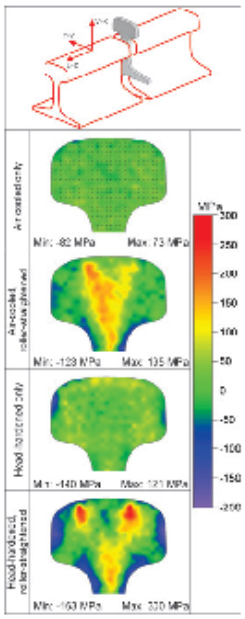

Figure 2. Maps of the vertical stress tensor component distributions for the rail slices of different production conditions.

Neutron stress measurements in slices from different production stages

The type of measurements described above, with measurement times of months, is not practical when extensive mapping measurements are required on many rail-specimen types. Thus, even losing information on one or another component, a research effort can be based on comparative studies of stress maps from thin slices. As demonstrated in the previous study (Figure 1), thin slices still preserve the main features of the original stress distribution in a long piece. Such research was carried out, within the same collaborative project between NCNR (NIST) and the Volpe National Transportation Center, on a series of rails from different production stages. These production steps include two different heat treatments (air-cooling or deep head-hardening) and two cold rolling post-processings (roller-straightened or not). Slices were cut by electric discharge machining (EDM) from the rails manufactured from the same commercial production line (but at different stages) from Rocky Mountain Steel Mills of the specification 132RE. They were cut to 6 mm thickness to minimize absorption of the neutron beam. In fact, two types of slices were studied: transverse or orthogonal slices, cut perpendicular to the rail longitudinal direction, and oblique slices, cut at 45° to the vertical direction.

A total of 366 locations arrayed in a 3×3 mm^2 mesh in the rail head, as shown in Figure 2, were the measurement sites. Four different directions for each point were measured in 90°-geometry with a nominal gauge volume of $3 \times 3 \times 3$ mm^3 and individual measurement times of 2 minutes. In contrast to the long-rail case, two days of neutron beamtime per sample provide excellent precision, are easily affordable, and allow measurement of many samples. In this case, four different production conditions were studied (Figure 2 shows vertical stress component only, while transverse and shear are omitted) in addition to the service rail slice (Figure 1, bottom). In a similar way, five different rails with different grinding conditions were studied [11].

Another good example of the application of the slicing technique is a research project on insulated rail joints (IRJs): IRJs are essentially an assembly of two rail ends with a narrow gap between them filled with insulator, and bolted "fishplates" on the sides of the rails, to add rigidity to the structure. They are designed to split continuous rail track into electrically isolated sections for position signalling and the detection of rail track damage. However, they accumulate structural damage faster than regular track, so that the lifespan of IRJs is often 5–10 times shorter than that of other rail components and subsequently, they have to be regularly replaced at considerable cost. For the case of IRJs, failure can occur when metal flows over the insulated rail gap (typically 6–8 mm width) breaking the electrically isolated section of track and resulting in malfunction of the track signalling system. Neutron diffraction can help reveal what happens to material and residual stresses during rail service and trace down accumulation of damage caused by stresses throughout rail service history. In practice, it is a big challenge since the stress state is no longer a function of the transverse cross-section coordinate (x,y), as in an long rail section, but at the vicinity of the gap all stress components also have z-dependence and in principle require three-dimensional mapping.

In this case longitudinal slices were studied. This was accomplished using the residual stress diffractometer Kowari at ANSTO [12]. IRJs in three conditions

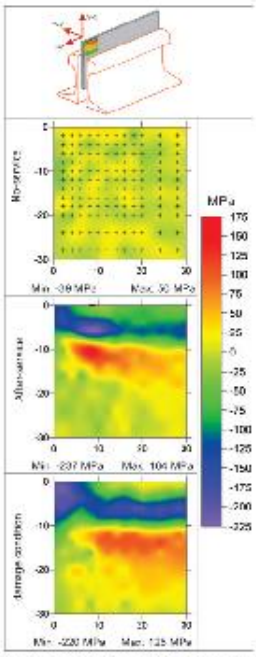

Figure 3. Differential maps of the longitudinal stress tensor component distributions for the longitudinal slices for three rail service conditions.

(no-service, after-service, and damaged) were chosen and longitudinal five-mm thick slices in the middle vertical plane of the rails were cut. Since the top corner of the rail joints is of interest, measurements were done in 400 locations (separated by 3 or 6 mm steps) in the area shown in Figure 3 with a nominal gauge volume of $3\times3\times3$ mm^3. A 90°-geometry and individual measurement times of 30 seconds were used to measure three normal directions for each mesh point. To study how damage accumulates in the area of the IRJ vs. in the bulk of the rail, the same measurements were done on the edges that were produced by EDM which represent the effect of service on the bulk portions of rails. To demonstrate the difference between the joint area vs. the bulk part of rails, the differential maps were produced as shown in Fig 3. Results suggest that the zone of the damaged material in the area of the IRJ extends deeper than in the bulk parts of the rail: some 5 mm deeper in the after-service condition and even deeper, 10 mm, in the damage-condition.

Near-surface stress measurements with high spatial resolution

In the case of rolling-contact fatigue damage in rails, the link between occurring defects (e.g. white etching layer, squats, etc.) and stresses is well established [7]. In spite of the fact that the first 100 µm is the most important region for the study of these defects and scanning and transmission electron microscope (SEM)/(TEM) or synchrotron radiation techniques seem to be the most appropriate, data up to 5–10 mm under the surface is also of interest since it is also linked to the overall thermo-mechanical history of rail material under the moving wheel-rail contact load. Without any slice cutting, residual stress measurements have been carried out using the Kowari residual stress neutron diffractometer with high spatial resolution of 0.5 mm to a depth of 5 mm from the top surface. Residual stress measurements were also conducted on (i) a service rail, in the area of a "squat," and (ii) a virgin rail. Significant compressive stresses were found in the service rail along the transverse and longitudinal directions: residual stress distributions below the surface in transverse and vertical directions are plotted for the virgin and service rails as a function of depth (Figure 4). The service rail showed a compressive stress of around –360 MPa from the surface of the rail head to at least a depth of 5mm, while there is almost no stress for the

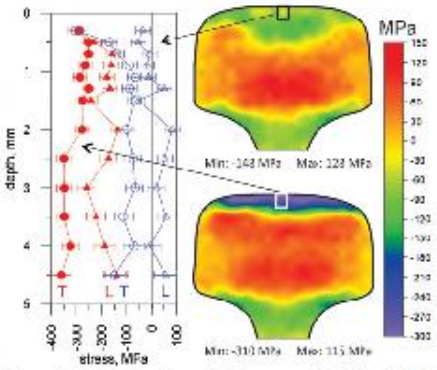

Figure 4. In-depth dependance of the transverse (T) and longitudinal (L) stress components for the virgin (solid symbols) and after service (empty symbols) rails that is associated with the maps of the transverse stress in the same virgin (top) and after-service (bottom) rail conditions.

virgin rail. These results provide important information about typical stress gradients existing at the near-surface region (or rather absence of gradient) – the kind of information that is missing from the low-resolution stress mapping experiments.

Conclusions

With P. Webster [3], we can re-state that the high penetration of neutrons enables unique non-destructive stress measurements in rail systems. In particular stress measurements in long rail sections, that cannot be matched by other non-destructive stress measurement techniques are challenging but possible. In addition, since 1991, increased neutron beam fluxes and better instrumentation (monochromators, detectors) make longer path-length as well as higher spatial resolution experiments possible. Altogether, these improvements make neutrons extremely useful for many important rail industry applications and stress problems in the future.

References

1. P. J. Webster, K. S. Low, G. Mills, G. A. Webster, *MRS Online Proceedings Library* **166**, 311 (1989).
2. P. J. Webster, X. Wang, G. Mills, in *Measurement of Residual and Applied Stress Using Neutron Diffraction*, M. Hutchings, A. Krawitz, Eds. (Springer Netherlands, 1992), vol. 216, pp. 517–524.
3. P. J. Webster, *Neutron News* 2, 19 (1991).
4. J. Kelleher, M. B. Prime, D. Buttle, P. M. Mummery, P. J. Webster, J. Shackleton, and P. J. Withers, *J. Neutr. Res.* **11**, 187 (2003).
5. O. Orringer, J. Orkisz, Z. Swiderski, *Residual Stress in Rails. Vol. 2: Theoretical and Numerical Analyses*. (Dordrecht, The Netherlands, Kluwer Academic, 1992).
6. T.-S. Jun, F. Hofmann, J. Belnove, X. Song, F. Hofmann, and A. M. Korsunsky, *The Journal of Strain Analysis for Engineering Design* **44**, 563 (2009).
7. A. Pyzalla, E. Wild, W. Reimers, in *Materials for Transportation Technology*. (Weinheim, Germany, Wiley-VCH Verlag GmbH & Co. KGaA, 2005), pp. 358–363.
8. T. Sasaki, O. Yaguchi, Y. Kobayashi, in *Mater. Sci. Forum*. (Trans Tech Publications, Switzerland, 2010), vol. 638–642, pp. 2458–2463.
9. T. Sasaki, Y. Miyazawa, S.I. Takahashi, R. Matsuyama, K. Sasaki, and K. Hiratsuka, in *Mater. Sci. Forum*. (Trans Tech Publications, Switzerland, 2008), vol. 571–72, pp. 249–254.
10. V. Luzin, J. E. Gordon, T. Gnaupel-Herold, H.-J. Prask, in *ASME 2004 International Mechanical Engineering Congress*. (Anaheim, California, USA, 2004), pp. 117–122.
11. T. Gnaupel-Herold, P. C. Brand, H.-J. Prask, *NISTIR 6305* (NIST, Gaithersburg, 1999).
12. O. Kirstein, V. Luzin, U. Garbe, *Neutron News* **20**, 34 (2009).

9.6 **Non**-destructive testing results from maraging cladded rail sample

BLUESCOPE STEEL

NON – DESTRUCTIVE TESTING
REQUEST & REPORT SHEET

Intranet Site:- http://www.ext.bluescopesteel.com/sites/pksw/105/Pages/default.aspx

PH: (02) 4275 4395
FAX: (02) 4275 4350

SAP Maint Work Centre: TEMTNDØØ

Report to:	David Wexler , Rathod Chandrahas			Report Sheet No:	1	of	3
Phone No:	4395	Fax No:	4449	Work Sheet No:	NA	of	NA
E-mail:				NDT No:	S10-069-07X		
Co:	Wollongong University			Work Order No:			
Copies to (if req):				Order No:			
Requested by:	James Hobbs	Phone No:	4395	Drawing No:			
Inquiry Date:	10/03/2010	Time:	12:00 PM				
ATW Required (circle)	Yes	No	Job Date /Time Confirmed (Initial)		Yes		JH

JOB DETAILS	**Date(s) Required:**	10/03/2010	**Time:**	1.00	pm
Item Identity:	<3> Of 60kg Rail Welds ID – A1 , A2 , A3				
Job Description:	Rail Head maraging weld deposits				
		For:	Wollongong University	Co	
Extent of Testing:	100% UT/MT of all nominated welds				
Welder Name(s):	N/A		Technique(s):	N/A	
Job Location:	Nth Gate SiS Lab				
Contact at Location:	James Hobbs		Phone:	4395	
Mfg History:	New Welds		Heat Treatment:	N/A	
Welded Items - Time period between welding & testing > 48 hrs?		Yes		hours : N/A	
Material/Grade:	60kg standard steel		Surface Condition:	As welded and machined	
Acceptance:	Report findings		Clause:	N/A	
Test Procedure (Aust Std Code):	AS1171 & AS2207				
Method:	Magnetic Flow/ UMA-Level 2		SP-ENG-NE-	1401,1201	
Variations:	Nil		Demagnetisation Required:		No
Test Required:	UT and MT				
Report Date Required:	A.S.A.P	Request Received By:	JH		

RESULTS (Include Statement of Compliance)

At the completion of ultrasonic testing all 3 samples had multiple areas lack of fusion at various depths lengths and heights throughout the weld and on all interfaces ranging from 3mm to 20mm in length.

Magnetic particle examination revealed detected various surface defects ranging from 3mm to 8mm in length.

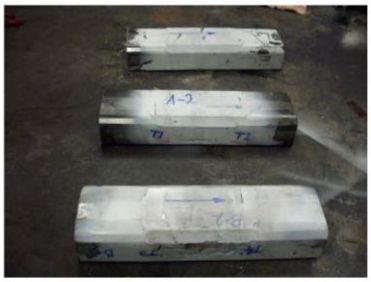

Showing the 3 off rail head weld samples tested.

Testing Officers:	G Nicholls,	Date(s)Tested:	10/03/2010
Signed:	J Hobbs	Date:	11/03/2010
Checked:	G Nicholls	Date:	11/03/2010

9.7 Welding procedure specification

Table 9-1 Gas metal Arc Welding procedure specification

PROJECT Rail Ends, Insulated joints defects		
	WELDING CODE/ Applicable standards	N/A guidelines AS/NZS 2576, DIN 8555, EN 14700, AS 1085.1, AWS D15.2
RAIL MATERIALS - 60 kg Standard and - Head Hardened Rail **SPECIFICATIONS:**	**Test Report:**	

MATERIAL THICKNESS	Length: 75mm Width: 20mm Depth: 13mm	**PREHEAT and MINIMUM INTERPASS TEMPERATURE:**	350 °C
		MAX INTERPASS TEMPERATURE	470 °C
JOINT TYPE	Flat and horizontal. weld overlay	Soaking Time at preheating temperature of 350 °C	30 minutes minimum.
JOINT POSITION	Flat and Horizontal	**Post Weld Treatment**:	Slow cooling after welding by wrapping in refractory blankets or vermiculite.
WELDING PROCESS	Flux Cored Arc Welding Self-Shielded	**Flux Cored Wire Self Shielded**:	OK Tubrodur 15.43 AS/NZS 2576 classification 1435-B7

OPERATORS	**IMPORTANT**: If the temperature during the repair drop below recommended preheats temperature of 350 °C, welding must be interrupted and temperature restored to the recommended minimum interpass of 350 °C. Maximum interpass temperature is 470 °C. Welding must be interrupted if the temperature exceeds 470 °C.
NOTICE: Prior to welding remove grease, rust and dirt.	**POWER SOURCE**: **WIRE FEEDER**:

Lay	**Weld Bead**	**ELECTRODE**	± DC	CV/VV	**AMPS**	**VOLTS**	**TRAVEL**	**Heat Input** kJ/mm

No.		**TYPE**	**SIZE** mm	AC				**SPEED** mm/min	
1	Stringer Bead	OK Tubrodur 15.43	1.6	DC +	CV	205-230	27-29		

MODULE RailWeldMod

An example of the robot generic programme language used for GMAW welding process utilising a flux-cored consumable. The program developed and written by Nathan Larkin.

PERS robtarget aaaTemp1:=[[967.24,-3868.80,1184.25],[0.499945,-0.499736,0.500299,-0.50002],[0,-1,-1,0],[3039.4,9E+09,9E+09,9E+09,9E+09,9E+09]];

PERS robtarget aaaTemp2:=[[716.25,-5517.33,1443.35],[0.300081,0.640296,0.300108,0.640241],[0,1,0,0],[4810.87,9E+09,9E+09,9E+09,9E+09,9E+09]];

proc RailWeld()

VAR robtarget OriginalPos:=[[850,-4423,652],[1.48262E-05,1.35713E-05,1,-3.19789E-06],[0,-1,0,0],[3000,9E+09,9E+09,9E+09,9E+09,9E+09]];

!VAR robtarget OriginalPos:=[[790,-4425,652],[1.48262E-05,1.35713E-05,1,-3.19789E-06],[0,-1,0,0],[3000,9E+09,9E+09,9E+09,9E+09,9E+09]];

VAR robtarget WeldStart:=[[792.6, -4129.4, 469.8],[0,0,1,0],[0,0,0,0],[3000,9E+09,9E+09,9E+09,9E+09,9E+09]];

VAR robtarget WeldEnd:=[[792.6, -4129.4, 469.8],[0,0,1,0],[0,0,0,0],[3000,9E+09,9E+09,9E+09,9E+09,9E+09]];

```
var pos initialpos{26}:=[[0,-11,0],[-3,-10,0],[3,-10,0],[0,-9,0],[-5,-
8,0],[+5,-8,0],
[0,-7,0],[-5,-6,0],[+5,-6,0],[0,-5,0],[-6,-4,0],[+6,-4,0],[0,-3,0],[-6,-
2,0],[+6,-2,0],
[0,-1,0],[-7,-0.5,0],[+7,-0.5,0],[0,+1,0],[-
7,+1.5,0],[+7,+1.5,0],[0,+2,0],[20,-11,-3],[15,-11,23],[15,-11,+13],[15,-11,+18]];
var pos finalpos{26}:=[[0,-11,75],[-3,-10,74.8],[+3,-10,74.8],[0,-
9,75],[-5,-8,74.3],
[+5,-8,74.3],[0,-7,75],[-5,-6,74.3],[+5,-6,74.3],[0,-5,75],[-6,-
4,74.0],[+6,-4,74.0],
[0,-3,75],[-6,-2,74.0],[+6,-2,74.0],[0,-1,75],[-7,-0.5,72.1],[+7,-
0.5,72.1],[0,+1,75],
[-7,+1.5,72.1],[+7,+1.5,72.1],[0,+2,75],[-20,-11,-3],[-15,-11,23],[-15,-
11,+13],[-15,-11,+18]];
var num PathNumber;
var num options;
var num WeldSpeed:=630/60;
confl \off;
confj \off;
While(TRUE) DO
    movej offs(OriginalPos,0,0,200),v200, fine, tWeldGun;
    !moveL offs(OriginalPos,0,0,0),v100, fine, tWeldGun;
    !waittime 1;
    !moveL offs(OriginalPos,0,0,200),v100, fine, tWeldGun;
    TPReadNum PathNumber, "Enter Path number (1 To 22)";
```

```
                    !if (PathNumber = 2) OR (PathNumber = 4) OR (PathNumber
= 6) OR (PathNumber = 8) OR
                    !(PathNumber = 10) OR (PathNumber = 12) OR (PathNumber
= 14) OR (PathNumber = 16) OR
                    !(PathNumber = 18) OR (PathNumber = 20) OR (PathNumber
= 22) THEN
                    !
        WeldEnd:=Offs(OriginalPos,initialpos{PathNumber}.z,-
initialpos{PathNumber}.x,initialpos{PathNumber}.y);
                    !       WeldEnd:=offs(WeldEnd,-20,0,0);
                    !
        WeldStart:=Offs(OriginalPos,finalpos{PathNumber}.z,-
finalpos{PathNumber}.x,finalpos{PathNumber}.y);
                    !       IF PathNumber > 12 THEN
                    !               WeldStart:=offs(WeldStart,10,0,0);
                    !       ENDIF
                    !else
                    WeldStart:=Offs(OriginalPos,initialpos{PathNumber}.z,-
initialpos{PathNumber}.x,initialpos{PathNumber}.y);


        WeldEnd:=Offs(OriginalPos,finalpos{PathNumber}.z,-
finalpos{PathNumber}.x,finalpos{PathNumber}.y);
                        if PathNumber < 23 then
                                WeldEnd:=offs(WeldEnd,15,0,0);
                                IF PathNumber > 12 THEN
```

```
                                        WeldStart:=offs(WeldStart,-10,0,0);
                                    ENDIF
                                endif
                            !endif
                            TPReadFK  options, NumToStr(PathNumber,0), "", "Weld -
x", "Weld +x", "Inact -x","Inact +x";
                            TEST options
                            CASE 2:
                                Weld WeldEnd,WeldStart , WeldSpeed,
\WeldActive:=1, \wtool:=tWeldGun;
                            CASE 3:
                                Weld WeldStart, WeldEnd, WeldSpeed,
\WeldActive:=1, \wtool:=tWeldGun;
                            CASE 4:
                                Weld WeldEnd,WeldStart , WeldSpeed,
\WeldActive:=0, \wtool:=tWeldGun;
                            CASE 5:
                                Weld WeldStart, WeldEnd, WeldSpeed,
\WeldActive:=0, \wtool:=tWeldGun;
                            endtest
                            moveL offs(OriginalPos,0,0,200),v100, fine, tWeldGun;
                        ENDwhile
                endproc
            ENDMODULE
```

MODULE Rail Weld Mod

An example of the robot programme used for investigation of the optimum interpass temperature of the five pass corner weldment welded with a flux-cored consumable.

PERS robtarget aaa

Temp1:=[[967.24,-3868.80,1184.25],[0.499945,-0.499736,0.500299,-0.50002],[0,-1,-1,0],[3039.4,9E+09,9E+09,9E+09,9E+09,9E+09]];

PERS robtarget aaa

Temp2:=[[716.25,5517.33,1443.35],[0.300081,0.640296,0.300108,0.640241],[0,1,0,0],[4810.87,9E+09,9E+09,9E+09,9E+09,9E+09]];

proc RailWeld()

VAR robtarget OriginalPos:=[[850,-4423,652],[1.48262E-05,1.35713E-05,1,-3.19789E-06],[0,-1,0,0],[3000,9E+09,9E+09,9E+09,9E+09,9E+09]];

!VAR robtarget OriginalPos:=[[790,-4425,652],[1.48262E-05,1.35713E-05,1,-3.19789E-06],[0,-1,0,0],[3000,9E+09,9E+09,9E+09,9E+09,9E+09]];

PERS robtarget

WeldStart:=[[792.6,-4129.4,

469.8],[0,0,1,0],[0,0,0,0],[3000,9E+09,9E+09,9E+09,9E+09,9E+09]];

WeldEnd:=[[792.6,-4129.4,

469.8],[0,0,1,0],[0,0,0,0],[3000,9E+09,9E+09,9E+09,9E+09,9E+09]];

```
    var pos initialpos{26}:=[[0,-11,0],[-3,-10,0],[3,-10,0],[0,-9,0],[-5,-8,0],[+5,-
8,0],[0,-7,0],[-5,-6,0],[+5,-6,0],[0,-5,0],[-6,-4,0],[+6,-4,0],[0,-3,0],[-6,-2,0],[+6,-
2,0],[0,-1,0],[-7,-0.5,0],[+7,0.5,0],[0,+1,0],[-7,+1.5,0],[+7,+1.5,0],[0,+2,0],[20,-11,-
3],[15,-11,23],[15,-11,+13],[15,-11,+18]];

    var pos finalpos{26}:=[[0,-11,75],[-3,-10,74.8],[+3,-10,74.8],[0,-9,75],[-5,-
8,74.3],[+5,-8,74.3],[0,-7,75],[-5,-6,74.3],[+5,-6,74.3],[0,-5,75],[-6,-4,74.0],[+6,-
4,74.0],[0,-3,75],[-6,-2,74.0],[+6,-2,74.0],[0,-1,75],[-7,-0.5,72.1],[+7,-
0.5,72.1],[0,+1,75],
    [-7,+1.5,72.1],[+7,+1.5,72.1],[0,+2,75],[-20,-11,-3],[-15,-11,23],[-15,-11,+13],[-
15,-11,+18]];
    var num PathNumber;
    var num options;
    var num WeldSpeed:=630/60;
    confl \off;
    confj \off;
    While(TRUE) DO
    movej offs(OriginalPos,0,0,200),v200, fine, tWeldGun;
    !moveL offs(OriginalPos,0,0,0),v100, fine, tWeldGun;
    !waittime 1;
    !moveL offs(OriginalPos,0,0,200),v100, fine, tWeldGun;
    TPReadNum PathNumber, "Enter Path number (1 To 22)";
    !if (PathNumber = 2) OR (PathNumber = 4) OR (PathNumber = 6) OR
(PathNumber = 8) OR
```

```
    !(PathNumber = 10) OR (PathNumber = 12) OR (PathNumber = 14) OR
(PathNumber = 16) OR
    !(PathNumber = 18) OR (PathNumber = 20) OR (PathNumber = 22) THEN
    !WeldEnd:=Offs(OriginalPos,initialpos{PathNumber}.z,-
initialpos{PathNumber}.x,initialpos{PathNumber}.y);!WeldEnd:=offs(WeldEnd,-
20,0,0);
    !WeldStart:=Offs(OriginalPos,finalpos{PathNumber}.z,-
finalpos{PathNumber}.x,finalpos{PathNumber}.y);
    !IF PathNumber > 12 THEN
    !WeldStart:=offs(WeldStart,10,0,0);
    !ENDIF
    !else
    WeldStart:=Offs(OriginalPos,initialpos{PathNumber}.z,-
initialpos{PathNumber}.x,initialpos{PathNumber}.y);
    WeldEnd:=Offs(OriginalPos,finalpos{PathNumber}.z,-
finalpos{PathNumber}.x,finalpos{PathNumber}.y);
    if PathNumber < 23 then
    WeldEnd:=offs(WeldEnd,15,0,0);
    IF PathNumber > 12 THEN
    WeldStart:=offs(WeldStart,-10,0,0);
    ENDIF
    endif
    !endif
    TPReadFK  options, NumToStr(PathNumber,0), "", "Weld -x", "Weld +x", "Inact
-x","Inact +x";
```

TEST options

CASE 2:

Weld WeldEnd,WeldStart , WeldSpeed, \WeldActive:=1, \wtool:=tWeldGun;

CASE 3:

Weld WeldStart, WeldEnd, WeldSpeed, \WeldActive:=1, \wtool:=tWeldGun;

CASE 4:

Weld WeldEnd,WeldStart , WeldSpeed, \WeldActive:=0, \wtool:=tWeldGun

CASE 5:

Weld WeldStart, WeldEnd, WeldSpeed, \WeldActive:=0, \wtool:=tWeldGun;

endtest

moveL offs(OriginalPos,0,0,200),v100, fine, tWeldGun;

ENDwhile

endproc

ENDMODULE